Field and Laboratory Studies of Atmospheric Organic Aerosol

Thesis by

Matthew Mitchell Coggon

In Partial Fulfillment of the Requirements

for the Degree of

Doctor of Philosophy

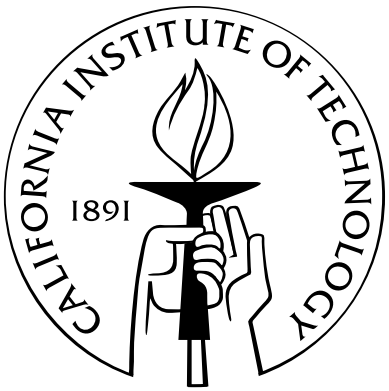

California Institute of Technology

Pasadena, California

2016

(Defended September 18, 2015)

To my siblings, Mark and Kara.

Thank you for teaching me how to overcome hardship.

Acknowledgements

There are many people who have played a role in my success at Caltech. First, I would like to thank my advisor, John Seinfeld, for his scientific guidance. I owe much of my professional growth to the trust and tremendous freedom that I was provided. John gave me many opportunities, and for those I am very grateful.

I would like to thank my co-advisor, Rick Flagan, for his valuable guidance both in and out of lab. I felt very lucky to have a resource whom I could turn to for field, instrument, and kayaking advice. His breadth of experience helped me through countless challenges.

I would like to thank my committee member, Armin Sorooshian, for his mentorship and encouragement over the past five years. I was fortunate to work with Armin on three field campaigns and soak in his scientific and life advice. His collaboration was crucial towards my success at Caltech. Thanks, Dutt.

I would also like to thank Paul Wennberg for serving on my committees and teaching me the basics of atmospheric science. He and his group have provided incredibly helpful discussions that have expanded my understanding of atmospheric chemistry.

When I first joined the Seinfeld Group, there were a number of students whose assistance, guidance, and mentorship were essential to setting my scientific groundwork. First, I must give enormous thanks to Jill Craven. In addition to being a phenomenal friend and kayaking buddy, Jill was my AMS mentor and big sib coach. In no way would I have made it through my first few years without her help and I'm looking forward to continued friendship and future paddling sessions in the Northwest and on the Colorado River. Many thanks to Andrew Metcalf, Scott Hersey, Christine Loza, and Lindsay Yee for being fantastic role models in the field and lab. Their wealth of knowledge and experience taught me a lot about how to approach atmospheric science research. Special thanks to Joey Ensberg for keeping the Schlinger office fun and intellectually stimulating. Prince, Michael Jackson, and Whitney Houston will always be in my karaoke repertoire.

I would also like to thank current Seinfeld members for their passionate pursuit of science. Many thanks to chamber folks: Xuan Zhang and Becky Schwantes for their positive attitudes and assistance on chamber studies, Tran Nguyen for her amazing insights into challenging chemistry, Renee McVay for her insights into the processes dictating chamber dynamics, Dandan Huang for her enthusiasm

and kindness, and Kate Schilling for her cheerfulness, expertise in mass spectrometry, and organized coffee breaks. I thank the Schlinger/Field crew for being great people to live with while away on campaign. Thank you Wilton/Vivasia for keeping it fun on the tarmac and Natasha for being a great model of work/life balance. Many thanks to Kelvin for being an phenomenal successor to the Caltech AMS line – I can't think of a person more fit to work with that instrument.

I would like to thank the flow tube crew for all the work put into designing and developing our lab's newest apparatus. Special thanks to Hanna Lignell for enthusiastically jumping into the project and working diligently to build a robust system. I'm incredibly impressed with our team effort and I'm incredibly grateful for her positivity and friendship. Many thanks to Yuanlong Huang, Michael Bauer, and Ran Zhao for taking on the challenge to model the flow tube dynamics and stepping up as the next flow tube users.

There are several collaborators and support staff to whom I extend my biggest thanks. At Caltech, I thank Yvette Grant and Martha Hepworth for their purchasing support, Nora Oshima and Kathy Young for laboratory and office maintenance, Suresh Guptha for instrument assistance, and Nathan Dalleska for detailed chemical analysis and boating discussions. I would like to thank the staff in the Athletics Department, especially John Carter, Betsy Mitchell, and Heather Morgan, for providing the Paddling Club with a space to practice and teach. Finally, I would also like to thank the team at CIRPAS, including Haflidi Jonsson, Roy Woods, Greg Cooper, Marko Jaakkola, Bryce Kujat, and Dennis Hamaker, for their unmatched professionalism and valued assistance in executing aircraft research. It was a pleasure working with them for three campaigns.

For three years, I worked as an Resident Associate in Dabney Hovse. I thank the entire RA group and student affairs office, especially Taso Dimitriadis, Portia Harris, Sue Chiarchiaro, Barbara Green, and Lesley Nye, for assistance during difficult student issues. I would also like to thank select students, including Jesse Salomon, Nick Schiefer, John Pharo, and Jomya Lei, for their incredible hovse leadership and collaboration. Finally, I would like to thank all of Dabney Hovse for providing an enriching experience at Caltech.

In addition to the assistance I've gained professionally, there are a number of people whose friendship I've valued over the past five years. First and foremost, I extend my biggest thanks to my girlfriend, Anna Chen, for her immense support and encouragement. She has been my greatest source of balance and my best adventure partner. I'm grateful for all she has provided me over the past three years and I thank her for tolerating my endless shenanigans. Thank you, Anna.

Many thanks to Anne Laraia for her outstanding friendship. In no small way, she have been a constant support and I will always look to her as a role model. I'll miss those early morning hikes up the San Gabriel Mountains, but look forward to hikes elsewhere. I thank Steve Gardner for being one of the most generous people I've ever met. I've always been impressed with his thoughtfulness, incredible humor, and bomb steak grilling. Steve and Anne make for one hell of a team.

I would like to especially thank my roommates, Matt Shaner, Chris Kempes, and Suzanne Kern for keeping my out-of-lab life fun and peaceful. To Matt, thanks for three years of adventures and RA madness – those years in Dabney are my most memorable. To Chris and Suzanne, thank you for sharing a year with me in RA retirement. It was the best detox I could ask for.

I thank my classmates, especially Ricardo, Charlie, Carissa, Wendy, and Kat, for all their support during first year classes. I thank my Paddling Club co-founder, Devin Wiley, for the opportunities to paddle in amazing locations. I thank other key Paddling Club members, including Bryan Jadot, Said Bogatyrev, Catie Blunt, Andrew Robbins, David Schuman, and Kelly Mauser, for sharing some great paddling adventures and assisting in club operations. I would like to thank the Kern River Valley for providing respite from LA city life.

Finally, I would like to thank my family and friends at home for their love from abroad. To my great friends, Greg, Adam, Conor, Dubby, Noelle, Caitlin, and Lindsay, thank you for your long-distance calls and visits to California. To my family, thank you for encouraging me to pursue engineering and supporting my decision to head to LA for graduate school. To my mom and dad, thank you for giving me perspective and constant reminders to maintain life balance. To my brother, thank you for serving as a role model of what it takes to overcome hardship and persist despite challenges. Thanks, and I love you.

Abstract

This thesis is the culmination of field and laboratory studies aimed at assessing processes that affect the composition and distribution of atmospheric organic aerosol. An emphasis is placed on measurements conducted using compact and high-resolution Aerodyne Aerosol Mass Spectrometers (AMS). The first three chapters summarize results from aircraft campaigns designed to evaluate anthropogenic and biogenic impacts on marine aerosol and clouds off the coast of California. Subsequent chapters describe laboratory studies intended to evaluate gas and particle-phase mechanisms of organic aerosol oxidation.

The 2013 Nucleation in California Experiment (NiCE) was a campaign designed to study environments impacted by nucleated and/or freshly formed aerosol particles. Terrestrial biogenic aerosol with $> 85\%$ organic mass was observed to reside in the free troposphere above marine stratocumulus. This biogenic organic aerosol (BOA) originated from the Northwestern United States and was transported to the marine atmosphere during periodic cloud-clearing events. Spectra recorded by a cloud condensation nuclei counter demonstrated that BOA is CCN active. BOA enhancements at latitudes north of San Francisco, CA coincided with enhanced cloud water concentrations of organic species such as acetate and formate.

Airborne measurements conducted during the 2011 Eastern Pacific Emitted Aerosol Cloud Experiment (E-PEACE) were aimed at evaluating the contribution of ship emissions to the properties of marine aerosol and clouds off the coast of central California. In one study, analysis of organic aerosol mass spectra during periods of enhanced shipping activity yielded unique tracers indicative of cloud-processed ship emissions (m/z 42 and 99). The variation of their organic fraction (f_{42} and f_{99}) was found to coincide with periods of heavy ($f_{42} > 0.15$; $f_{99} > 0.04$), moderate ($0.05 < f_{42} < 0.15$; $0.01 < f_{99} < 0.04$), and negligible ($f_{42} < 0.05$; $f_{99} < 0.01$) ship influence. Application of these conditions to all measurements conducted during E-PEACE demonstrated that a large fraction of cloud droplet (72%) and dry aerosol mass (12%) sampled in the California coastal study region was heavily or moderately influenced by ship emissions. Another study investigated the chemical and physical evolution of a controlled organic plume emitted from the R/V *Point Sur*. Under sunny conditions, nucleated particles composed of oxidized organic compounds contributed nearly an order of magnitude more cloud condensation nuclei (CCN) than less oxidized particles formed under cloudy

conditions. The processing time necessary for particles to become CCN active was short (<1 hr) compared to the time needed for particles to become hygroscopic at sub-saturated humidity (> 4 hr).

Laboratory chamber experiments were also conducted to evaluate particle-phase processes influencing aerosol phase and composition. In one study, ammonium sulfate seed was coated with a layer of secondary organic aerosol (SOA) from toluene oxidation followed by a layer of SOA from α-pinene oxidation. The system exhibited different evaporative properties than ammonium sulfate seed initially coated with α-pinene SOA followed by a layer of toluene SOA. This behavior is consistent with a shell-and-core model and suggests limited mixing among different SOA types. Another study investigated the reactive uptake of isoprene epoxy diols (IEPOX) onto non-acidified aerosol. It was demonstrated that particle acidity has limited influence on organic aerosol formation onto ammonium sulfate seed, and that the chemical system is limited by the availability of nucleophiles such as sulfate.

Flow tube experiments were conducted to examine the role of iron in the reactive uptake and chemical oxidation of glycolaldehyde. Aerosol particles doped with iron and hydrogen peroxide were mixed with gas-phase glycolaldehyde and photochemically aged in a custom-built flow reactor. Compared to particles free of iron, iron-doped aerosols significantly enhanced the oxygen to carbon (O/C) ratio of accumulated organic mass. The primary oxidation mechanism is suggested to be a combination of Fenton and photo-Fenton reactions which enhance particle-phase OH radical concentrations.

Contents

List of Figures

List of Tables

Chapter 1

Introduction

Aerosols are ubiquitous in Earth's atmosphere and significantly impact global climate and human health. In the context of climate science, aerosols strongly influence the global energy balance via the absorption/ reflection of solar radiation and modulation of cloud properties. These solar interactions, known as the direct and indirect effects, are the most uncertain of all anthropogenic forcings contributing to global climate change (IPCC 2014). In terms of human health, high concentrations of atmospheric particles, particularly in urban settings, are linked to pulmonary, cardiac, and other degenerative diseases (Pöloch 2005). Such issues extend far beyond the source; pollution from industrialized nations is known to impact countries downwind (e.g., Kwon et al. 2002, Lin et al. 2014). For example, one modeling study estimated that, at most, 12-24% of sulfate pollution over the Western United States can be attributed to emissions originating from Chinese production of exportable goods (Lin et al. 2014). Consequently, investigations into the formation, distribution, and fate of atmospheric aerosols are critical to assess anthropogenic impacts on regional and global scales.

Of the constituents that compose atmospheric aerosols, organic compounds, such as functionalized hydrocarbons, are the most diverse and typically contribute up to 50% of total particulate mass (Jimenez et al. 2009). Organic aerosol may be emitted directly from a source (referred to as "primary" emissions) or result from the atmospheric processing of a parent compound (referred to as a "secondary" source). The latter, also known as secondary organic aerosol (SOA), is particularly challenging to understand because of the number of processes and components contributing to its formation. Figure 1.1 demonstrates this complexity with respect to organic reactions with the OH radical. In general, a volatile organic compound (VOC) undergoes reaction to form an oxidized species. This species may also be volatile, or, because of functionalization, have the propensity to partition to the condensed phase. These semi-volatile compounds (SVOC) may contribute to secondary organic aerosol, or continue to undergo gas-phase reactions with additional oxidation species. As gas-phase reactions proceed, the original carbon backbone of the parent VOC may fragment, thus forming higher volatility products. Alternatively, continued functionalization may

lead to the formation of low-volatility organic compounds (LVOC) found exclusively in the particle phase.

In concert with this complex gas-phase chemistry, SOA is also formed from reactions occurring within the liquid fraction of the particle (Ervens et al. 2011). This aqueous-derived SOA (aqSOA) may undergo an additional suite of oxidation reactions to form new products, some of which partition out of the particle completely (aqueous-derived VOCs, aqVOC) and some that partition between the gas and particle phases (aqueous-derived SVOC, aqSVOC). Unlike gas-phase chemistry, which is primarily a means of SOA formation, particle-phase chemistry may act as both a source and sink of SOA depending on the oxidation pathway (Ervens et al. 2011, Sorooshian et al. 2013).

The chemical processes described above tend to generate oxidized organic species, which affects key physical properties such as particle hygroscopicity. For example, Lambe et al. (2011a) demonstrated that the organic hygroscopic parameter of laboratory-generated aerosol, κ_{org}, could be linearly parameterized to the elemental O/C ratio. Likewise, Wonaschütz et al. (2013) demonstrated that emissions of hydrophobic organics undergoing atmospheric processing in the marine atmosphere could generate cloud condensation nuclei (CCN) active particles. The number of CCN grew as the degree of organic oxidation increased. These studies demonstrate that the presence of organic aerosol affects a particle's chemio-physical state. Understanding the nature of these processes is especially important in order to gain better predictions of aerosol modifications to cloud microphysics (i.e., the indirect effect).

The following chapters outline a number of studies aimed at investigating the composition, distribution, and transformation of organic aerosol in field and laboratory settings. Central to these studies is the characterization of aerosol composition using the Aerodyne aerosol mass spectrometer (AMS). The AMS measures bulk aerosol mass spectra with fast time resolution. From these measurements, one can map out a particle's organic fingerprint and deduce properties about the particle. For example, the high-resolution AMS described by DeCarlo et al. (2006) employs technology capable of resolving the chemical formula of organic fragments, thus allowing one to calculate bulk elemental composition such as O/C, H/C, and N/C ratios.

Chapters 2-4 summarize results from the 2011 Eastern Pacific Emitted Aerosol Cloud Experiment (E-PEACE) and 2013 Nucleation in California Experiment (NiCE) field campaigns. These campaigns were based out of the Center for Interdisciplinary Remotely-Piloted Aircraft Studies (CIRPAS) in Marina, CA. E-PEACE was a multi-institutional effort to investigate aerosol-cloud interactions in the marine atmosphere while NiCE was designed to understand new particle formation in marine, urban, and agricultural regions. We refer readers to Russell et al. (2013) for details about the E-PEACE and NiCE platforms.

The studies described in Chapter 2-4 focus on measurements conducted in the marine atmosphere off the coast of California. This region is a compelling setting to study aerosol and clouds due to the

persistent presence of marine stratocumulus clouds that are susceptible to the aerosol modifications (Chaung et al. 2002). As demonstrated by Hegg et al. (2008, 2009, 2010), the marine aerosol budget (and consequently, bulk aerosol properties) is controlled by a soup of natural and anthropogenic emissions; however, the extent to which each of these sources impact the marine atmosphere remains uncertain. In Chapter 2, we present measurements conducted during E-PEACE and NiCE to demonstrate the mechanism by which continental biogenic emissions are transported into the free troposphere above marine stratocumulus. Periodically during the summer months, the North Pacific High ridges against the continental U.S. and induces offshore flow (Kloesel 1992, Crosbie et al. 2015). Consequently, emissions originating from heavily forested regions of the Northwestern U.S. are transported to the free troposphere immediately above the marine stratocumulus deck. In regions with the highest impact from continental sources, cloud water samples exhibit elevated concentrations of organic acids commonly found in biogenic emissions. These observations suggest that biogenic aerosol originating from the Northwestern U.S. has a noticeable influence on marine aerosol and cloud properties during periods of offshore flow.

Studies described in Chapters 3 and 4 focus exclusively on measurements conducted during E-PEACE. Unique to E-PEACE was the use of the R/V *Point Sur* to purposely emit aerosol into the marine stratocumulus deck. The CIRPAS Twin Otter aircraft probed these emissions, as well as those emitted from passing cargo ships, to characterize the impact of these sources on cloud microphysics. Utilizing AMS measurements, it is demonstrated that particles emitted into the marine atmosphere undergo extensive chemical evolution that affects both compositional markers and aerosol physical properties. In Chapter 3, we show that ship emissions that are subjected to aqueous processing yield a mass spectral fingerprint that is significantly different from the spectra of freshly emitted particles. This fingerprint was present in over 70% of cloud droplets and 12% of dry, background aerosol, whereas the fingerprint for freshly emitted emissions was primarily constrained to the immediate vicinity of the ship (consistent with measurements performed by Murphy et al. 2009). These results suggest that 1) ships have a strong influence on aerosol properties in the California shipping lanes and 2) fresh ship emissions quickly undergo atmospheric processing. In Chapter 4, we discuss measurements of organic aerosol plumes emitted from the R/V *Point Sur*. Under sunny conditions, new particles formed within an hour of atmospheric processing and led to a drastic increase in the number of CCN. Under cloudy conditions, no new particles were formed and CCN concentrations were lower by an order of magnitude. These two chapters demonstrate that atmospheric processing plays a major role in dictating aerosol properties in the marine atmosphere.

The remaining chapters describe laboratory studies aimed at understanding the properties and chemical transformation of organic aerosol under controlled, but atmospherically-relevant conditions. We conduct this research using two experimental platforms: the environmental chamber and the flow tube reactor. The environmental chamber is primarily used to study the time-dependent

oxidation of a precursor VOC and subsequent SOA formation. The chamber is operated as a batch reactor and is well-suited to study processes occurring on timescales equivalent to 1-2 days of atmospheric processing (e.g., Zhang et al. 2014). The flow tube reactor is operated at steady-state, and therefore product distributions measured in the effluent of the reactor reflect those of a single oxidant exposure time. Oxidant exposure times may be varied via changes in the residence time or oxidant concentration; as a result, flow reactors can simulate atmospheric processing on multi-day to week-long timescales (e.g., Kang et al. 2007, Lambe et al. 2011b, 2015, Li et al. 2015). Flow reactors are also more easily maintained due to a smaller surface area than typical environmental chambers; therefore, one can utilize a flow reactor to study chemical systems that would contaminate a teflon chamber.

Chapters 5 and 6 summarize SOA studies conducted using the environmental chamber. In Chapter 5, we study the evaporative properties of SOA formed by α-pinene and toluene photooxidation. In each experiment, SOA was generated via reaction with the OH radical. In mixed SOA experiments, SOA formed from one precursor was coated with a layer of SOA from the other precursor. After several hours of photochemical processing, SOA was heated under dark conditions to 42° C and changes in the particle size distribution and elemental composition were monitored. It was found that SOA produced by α-pinene oxidation was more volatile than that produced by toluene chemistry. In mixed SOA systems, the evaporative properties most resembled that of the second coating, suggesting that particles were structured with a core-and-shell morphology. These results suggest that multi-phase systems may influence key heterogeneous processes such as gas uptake and diffusion within the particle.

Chapter 6 is concerned with the formation of SOA resulting from the reactive uptake of isoprene epoxydiols (IEPOX). IEPOX is a product of isoprene photooxidation and is believed to significantly contribute to organic aerosol mass via heterogeneous chemistry (e.g. Froyd et al. 2010, McNeil et al. 2012). In this study, IEPOX was mixed with inorganic aerosol of different compositions under dry and humid conditions. IEPOX uptake was greatest in ammonium sulfate seed at high RH (60-85%), moderate for NH_4Cl, and substantially reduced for other seed compositions (NaCl and Na_2SO_4). Furthermore, IEPOX uptake into ammonium sulfate was independent of pH, indicating that the influence of pH may be weak due to the ability of NH_4^+ to act as a ring-opening catalyst. The enhancement in ammonium sulfate relative to NH_4Cl indicates that organic aerosol mass is likely limited by the availability of nucleophiles capable of generating low-volatility compounds (such as the reaction with SO_4^{-2} to form organosulfates). These results present a possible explanation for the weak correlation between pH and IEPOX-derived organic aerosol observed in field studies.

The final chapter describes a flow reactor study aimed at investigating the heterogeneous chemistry associated with particle-phase iron. Iron undergoes reactions involving H_2O_2, known collectively as the Fenton and photo-Fenton reactions, that are capable of substantially raising OH

concentrations beyond that resulting from hydrogen peroxide photolysis (e.g., Faust and Zepp 1993, Siefert et al. 1994). In this study, we photochemically age glycolaldehyde in the presence of ammonium sulfate particles doped with iron + H_2O_2 and compare the resulting SOA properties with those of experiments conducted with pure ammonium sulfate + H_2O_2. Glycolaldehyde is a water-soluble organic shown previously to form SOA in OH-driven aqueous systems (Perri et al. 2009, 2010); thus, we utilize AMS measurements to investigate aerosol composition as a result of OH oxidation. It is demonstrated that for a 45 minute plug-flow residence time, the systems containing iron exhibited substantially higher O/C ratios than systems only containing H_2O_2. The resulting SOA exhibits carboxylic acid functionalization, which is consistent with the OH mechanism proposed by Perri et al. (2009). These results suggest that iron chemistry may enhance aqueous OH levels and significantly contribute to SOA oxidation in atmospheric particles.

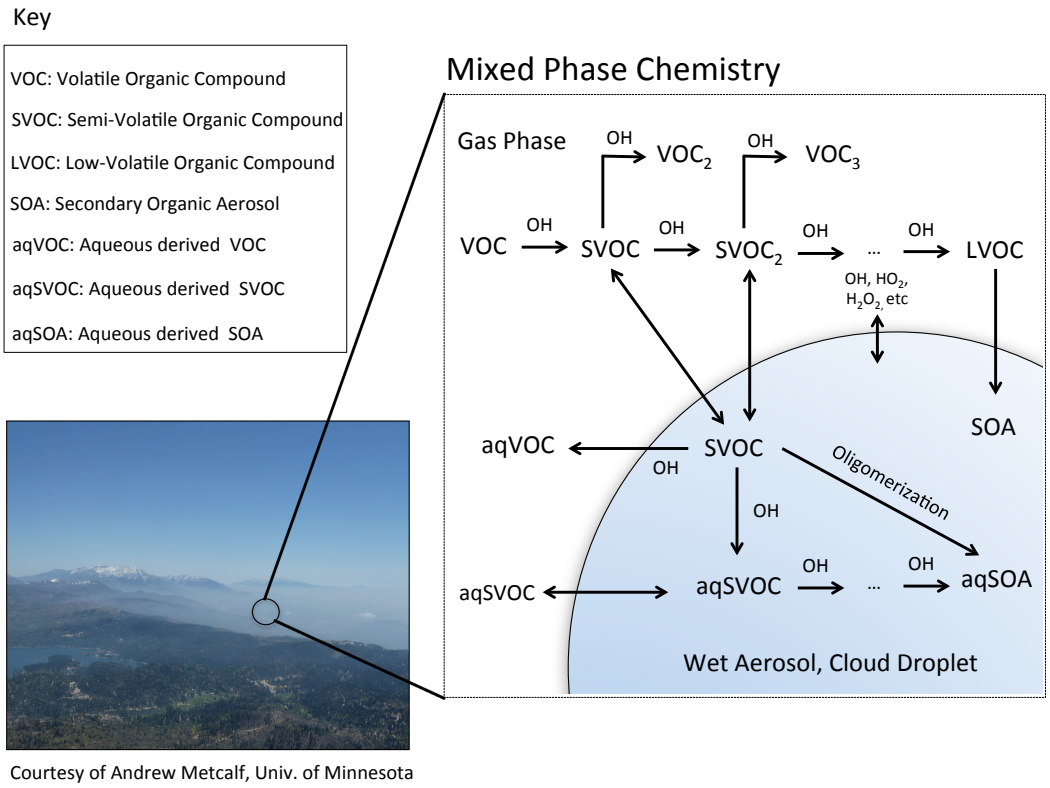

Figure 1.1: Overview of select processes leading to the formation and consumption of secondary organic aerosol (SOA).

1.1 References

1. Crosbie, E., Wang, Z., Sorooshian, A., Chuang, P.Y., Craven, J.S., Coggon, M.M., Brunke, M., Zeng, X., Jonsson, H.H., Woods, R.K., Flagan, R.C., and Seinfeld, J.H. (2015). Stratocumulus cloud clearings and notable thermodynamic and aerosol contrasts across the clear-cloudy interface. *J. Atmos. Sci.*. accepted.

2. Chaung, C.C., Penner, J.E., Prospero, J.M., Grand, K.E., Rau, G.H., Kawamoto, K. (2002). Cloud susceptibility and the first aerosol indirect forcing: Sensitivity to black carbon and aerosol concentrations. *J. Geophys. Res.* 107, D21. DOI: 10.1029/2000JD000215.

3. DeCarlo, P.F., Kimmel, J.R., Trimborn, A., Northway, M.J., Jayne., J.T., Aiken, A.C., Gonin, M., Fuhrer, K., Horvath, T., Docherty, K.S., Worsnop, D.R., and Jimenez, J.L. (2006). *Anal. Chem.* 78, 8281-8280. DOI: 10.1021/ac061249n.

4. Intergovernmental Panel on Climate Change (2014). Climate Change 2014: Synthesis Report. Contribution of Working Groups I, II and III to the Fifth Assessment Report of the Intergovernmental Panel on Climate Change [Core Writing Team, R.K. Pachauri and L.A. Meyer (eds.)]. IPCC, Geneva, Switzerland, 151 pp.

5. Ervens, B., Turpin, B.J., and Weber, R.J. (2011). Secondary organic aerosol formation in cloud droplets and aqueous particles (aqSOA): a review of laboratory, field and model studies. *Atmos. Chem. Phys.* 11, 11069-11102. DOI: 10.5194/acp-11-11069-2011.

6. Faust, B.C. and Zepp, R.G. (1993). Photochemistry of aqueous iron(III)-polycarboxylate complexes: the chemistry of atmospheric and surface waters. *Environ. Sci. Technol.* 27, 2517-2522.

7. Froyd, K.D., Murphy, S.M., Murphy, D.M., de Gouw, J.A., Eddingsaas, N.C., and Wennberg, P.O. (2010). Contribution of isoprene-derived organosulfates to free tropospheric aerosol mass. *Proc. Natl. Acad. Sci.* 107, 21360-21365. DOI:10.1073/pnas.1012561107.

8. Hegg, D.A., Covert, D.S., and Jonsson, H.H. (2008). Measurements of size-resolved hygroscopicity in the California coastal zone. *Atmos. Chem. Phys.* 8, 7193-7203. DOI: 10.5194/acp-8-7193-2008.

9. Hegg, D.A., Covert, D.S., Jonsson, H.H., and Woods, R. (2009). Differentiating natural and anthropogenic cloud condensation nuclei in the California coastal zone. *Tellus.* 61B, 669-676. DOI:10.1111/j.1600-0889.2009.00435.x

10. Hegg, D.A., Covert, D.S., Jonsson, H.H., and Woods, R.K. (2010). The contribution of anthropogenic aerosols to aerosol light-scattering and CCN activity in the California coastal zone. *Atmos. Chem. Phys.* 10, 7341-7351. DOI: 10.5194/acp-10-7341-2010.

11. Jimenez, J.L et al. (2009). Evolution of organic aerosols in the atmosphere. *Science*. 326 (5959), 1525-1529. DOI: 10.1126/science.1180353.

12. Kloesel, K. A. (1992). Marine stratocumlus cloud clearing episodes observed during FIRE. *Mon. Weather Rev.* 120, 565-578.

13. Kwon, H., Cho, S., Chun, Y., Lagarde, F., and Pershagen, G. (2002). Effects of the Asian dust events on daily mortality in Seoul, Korea. *Environ. Res. A.* 90, 1-5. DOI: 10.1006/enrs.2002.4377.

14. Lambe, A.T., Onasch, T.B., Massoli, P., Croasdale, D.R., Wright, J.P., Ahern, A.T., Williams, L.R., Worsnop, D.R., Brune, W.H., and Davidovits, P. (2011a). Laboratory studies of the chemical composition and cloud condensation nuclei (CCN) activity of secondary organic aerosol (SOA) and oxidized primary organic aerosol (OPOA). *Atmos. Chem. Phys.* 11, 8913-892. DOI:10.5194/acp-11-8913-2011.

15. Lambe, A.T., Ahern, A.T., Williams, L.R., Slowik, J.G., Wong, J.P.S., Abbatt, J.P.D., Brune, W.H., Ng, N.L., Wright, J.P., Croasdale, D.R., Worsnop, D.R., Davidovits, P., and Onasch, T.B. (2011b). Characterization of aerosol photooxidation flow reactors: Heterogeneous oxidation, secondary organic aerosol formation and cloud condensation nucleus (CCN) activity measurements. *Atmos. Meas. Tech.* 4, 445-461. DOI:10.5194/amt-4-445-2011

16. Lambe, A.T., Chhabra, P.S., Onasch, T.B., Brune, W.H., Hunter, J.F., Kroll, J.H., Cummings, M.J., Brogan, J.F., Parmar, Y., Worsnop, D.R., Kolb, C.E., and Davidovits, P. (2015). Effect of oxidant concentration, exposure time, and seed particles on secondary organic aerosol chemical composition and yield. *Atmos. Chem. Phys.* 15, 3063-3075. DOI:10.5194/acp-15-3063-2015

17. Lin, J., Pan, D., Davis, S.J., Zhang, Q., He, K., Wang, C., Streets, D.G., Wuebbles, D.J., and Guan, D. (2014) China's international trade and air pollution in the United States. *PNAS*, 11 (5), 1736-1741. DOI:10.1073/pnas.1312860111.

18. Li, R., Palm, B.B., Ortega, A.M., Hlywiak, J., Hu, W., Peng, Z., Day, D.D., Knote, C., Brune, W.H., de Gouw, J.A., and Jimenez, J.L. (2015). Modeling the radical chemistry in an oxidation flow reactor: Radical formation and recycling, sensitivities, and OH exposure estimation equation. *J. Phys. Chem. A.* 119, 4418-4432. DOI:10.1021/jp509534k.

19. McNeil, V.F., Woo, J.L., Kim, D.D., Schwier, A.N., Wanell, N.J., Summer, A.J., and Barakat, J.M. (2012). Aqueous-phase secondary organic aerosol and organosulfate formation in atmospheric aerosols: A modeling study. *Environ. Sci. Technol* 46, 8075-8081. DOI:10.1021/es3002986

20. Murphy, S.M., Agrawal, H., Sorooshian, A., Padro, L.T., Gates, H., Herset, S., Welch, W.A., Jung, H., Miller, J.W., Cocker III, D.R., Nenes, A., Jonsson, H.H., Flagan, R.C., and Seinfeld, J.H. (2009). Comprehensive Simultaneous shipboard and airborne characterization of exhaust from a modern container ship at sea. *Environ. Sci. Technol.*. 43 (13), 4626-4640. DOI: 10.1021/es802413j.

21. Perri, M.J., Seitzinger, S., and Turpin, B.J. (2009). Secondary organic aerosol production from aqueous photooxidation of glycolaldehyde: Laboratory experiments. *Atmos. Environ.* 43, 1487-1497. DOI:10.1016/j.atmosenv.2008.11.037

22. Perri, M.J., Lim, Y.B., Seitzinger, S.P, and Turpin, B.J. (2010). Organosulfates from glycolaldehyde in aqueous aerosols and clouds: Laboratory studies. *Atmos. Environ.* 44, 2658-2664. DOI:10.1016/j.atmosenv.2010.03.031

23. Pöschl, U. (2005). Atmospheric aerosols: composition, transformation, climate and health effects. *Angew. Chem. Int. Ed.* 44, 7520-7540. DOI: 10.1002/anie.200501122.

24. Russell, L.M. et al. (2013). Eastern Pacific Emitted Aerosol Cloud Experiment (E-PEACE). *B. Am. Meterol. Soc.* 94, 709-729. DOI: 10.1175/BAMS-D-12-00015.

25. Siefert, R.L., Pehkonen, S.O., Erel, Y., and Hoffman, M.R. (1994). Iron photochemistry of aqueous suspensions of ambient aerosol with added organic acids. *Geochim. Cosmochim. Acta* 58 (15), 3271-3279.

26. Sorooshian, A., Wang, Z., Coggon, M.M., Haflidi, J., Erven, B. (2013). Observations of Sharp Oxalate Reductions in Stratocumulus Clouds at Variable Altitudes: Organic Acid and Metal Measurements During the 2011 E-PEACE Campaign. *Environ. Sci. Technol.* 47, 14, 77477756. DOI: 10.1021/es4012383.

27. Wonaschütz,A. , Coggon, M.M., Sorooshian, A., Modini, R., Frossard, A., Ahlm, L., Mulmenstadt, J., Roberts G. C., Russell, L.M., Dey, S., Brechtel, F.J., Seinfeld, J.H. (2013). Hygroscopic properties of organic aerosol particles emitted in the marine atmosphere. *Atmos. Chem. Phys.* 13, 11919-11969. DOI:10.5194/acpd-13-11919-2013

28. Zhang, X., Schwantes, R., Coggon, M.M., Loza, C., Schilling, K., Flagan, R.C., Seinfeld, J.H. (2013). Role of ozone in SOA formation from alkane photooxidation. *Atmos. Chem. Phys.*, 14, 1,733-1,753, DOI:10.5194/acp-14-1733-2014.

Chapter 2

Observations of Continental Biogenic Impacts on Marine Aerosol and Clouds off the Coast of California

AGU PUBLICATIONS

JGR

Journal of Geophysical Research: Atmospheres

RESEARCH ARTICLE
10.1002/2013JD021228

Key Points:
- BOA is measured above marine stratocumulus off the coast of California
- BOA was observed to entrain into the marine boundary layer
- BOA has a wide area of impact off the coast of California

Supporting Information:
- Readme
- Supporting Information
- Figure S1
- Figure S2
- Figure S3
- Figure S4
- Figure S5
- Figure S6
- Figure S7
- Figure S8
- Figure S9
- Movie S1

Correspondence to:
J. H. Seinfeld,
seinfeld@caltech.edu

Citation:
Coggon, M. M., A. Sorooshian, Z. Wang, J. S. Craven, A. R. Metcalf, J. J. Lin, A. Nenes, H. H. Jonsson, R. C. Flagan, and J. H. Seinfeld (2014), Observations of continental biogenic impacts on marine aerosol and clouds off the coast of California, *J. Geophys. Res. Atmos.*, *119*, 6724–6748, doi:10.1002/2013JD021228.

Received 21 NOV 2013
Accepted 16 MAY 2014
Accepted article online 21 MAY 2014
Published online 11 JUN 2014

Observations of continental biogenic impacts on marine aerosol and clouds off the coast of California

M. M. Coggon[1], A. Sorooshian[2,3], Z. Wang[3], J. S. Craven[1], A. R. Metcalf[4], J. J. Lin[5], A. Nenes[5,6], H. H. Jonsson[7], R. C. Flagan[1,8], and J. H. Seinfeld[1,8]

[1]Division of Chemistry and Chemical Engineering, California Institute of Technology, Pasadena, California, USA, [2]Department of Chemical and Environmental Engineering, University of Arizona, Tucson, Arizona, USA, [3]Department of Atmospheric Sciences, University of Arizona, Tucson, Arizona, USA, [4]Department of Mechanical Engineering, University of Minnesota, Minneapolis, Minnesota, USA, [5]School of Earth and Atmospheric Sciences, Georgia Institute of Technology, Atlanta, Georgia, USA, [6]School of Chemical and Biomolecular Engineering, Georgia Institute of Technology, Atlanta, Georgia, USA, [7]Center for Interdisciplinary Remotely Piloted Aircraft Studies, Naval Postgraduate School, Monterey, California, USA, [8]Department of Environmental Science and Engineering, California Institute of Technology, Pasadena, California, USA

Abstract During the 2011 Eastern Pacific Emitted Aerosol Cloud Experiment (E-PEACE) and 2013 Nucleation in California Experiment (NiCE) field campaigns, a predominantly organic aerosol (> 85% by mass) was observed in the free troposphere over marine stratocumulus off the coast of California. These particles originated from a densely forested region in the Northwestern United States. The organic mass spectrum resolved by positive matrix factorization is consistent with the mass spectra of previously measured biogenic organic aerosol. Particulate organic mass exhibits a latitudinal gradient that corresponds to the geographical distribution of vegetation density and composition, with the highest concentration over regions impacted by densely populated monoterpene sources. Due to meteorological conditions during summer months, cloud-clearing events transport aerosol from the Northwestern United States into the free troposphere above marine stratocumulus. Based on the variation of meteorological variables with altitude, dry air containing enhanced biogenic organic aerosol is shown to entrain into the marine boundary layer. Fresh impacts on cloud water composition are observed north of San Francisco, CA which is consistent with fresh continental impacts on the marine atmosphere at higher latitudes. Continental aerosol size distributions are bimodal. Particles in the 100 nm mode are impacted by biogenic sources, while particles in the ~ 30 nm mode may originate from fresh biogenic emissions. Continental aerosol in the 100 nm mode is cloud condensation nuclei active and may play a role in modulating marine stratocumulus microphysics.

1. Introduction

Marine aerosol particles play an important role in modulating cloud microphysical properties, transmission of solar radiation, visibility, and the thermodynamic structure of the marine boundary layer. These effects are governed to a large extent by the physical, chemical, and optical properties of aerosol residing over the ocean surface. The eastern Pacific off the western coast of the United States is one of the world's major subtropical subsidence regions that exhibits persistent decks of stratocumulus, especially during summer months, making it an ideal location to study aerosol-cloud interactions. In addition to marine aerosol such as those resulting from sea spray, this region is heavily influenced by ship emissions, ocean biota, and transported and entrained air masses from both distant regions and coastal areas. The variety of these sources has the potential to result in strong spatial and temporal gradients in aerosol physicochemical properties.

Aerosol and clouds off the central coast of California have been studied in numerous field experiments [*Frick and Hoppel*, 2000; *Durkee et al.*, 2000; *Hudson et al.*, 2000; *Straub et al.*, 2007; *Lu et al.*, 2009; *Hegg et al.*, 2009, 2010; *Moore et al.*, 2012; *Benedict et al.*, 2012; *Coggon et al.*, 2012; *Russell et al.*, 2013]. One topic that has received considerable attention is the cloud condensation nuclei (CCN) properties of marine aerosol [*Roberts et al.*, 2006; *Sorooshian et al.*, 2009; *Hegg et al.*, 2009, 2010; *Langley et al.*, 2010; *Moore et al.*, 2012; *Coggon et al.*, 2012]. *Hegg et al.* [2009, 2010] apportioned CCN off the coast of California to anthropogenic and natural sources and determined that about 67% of CCN by number could be attributed to human activities, which included continental sources such as biomass burning. *Roberts et al.* [2006] found that continental sources from Asia and North America can modulate CCN properties over the eastern Pacific Ocean.

AGU Journal of Geophysical Research: Atmospheres 10.1002/2013JD021228

Ship emissions exert a strong influence on marine aerosol in regions of active ship traffic [*Langley et al.*, 2010]; in one study, *Coggon et al.* [2012] demonstrated that 72% of cloud droplet residuals measured in the California shipping lanes showed evidence of ship emissions.

Biogenic-derived compounds make up a significant fraction of volatile organic carbon and organic aerosol in forested regions of California [*Cahill et al.*, 2006; *Worton et al.*, 2011; *Setyan et al.*, 2012; *Shilling et al.*, 2013] and have been shown to be CCN active [e.g., *Asa-Awuku et al.*, 2009; *Gunthe et al.*, 2009; *O'Dowd et al.*, 2009; *King et al.*, 2010; *Poulain et al.*, 2010; *Shantz et al.*, 2010; *Creamean et al.*, 2011; *Engelhart et al.*, 2011; *Kerminen et al.*, 2012; *Kuwata et al.*, 2013; *Pierce et al.*, 2012; *Ruehl et al.*, 2012; *Tang et al.*, 2012; *Frosch et al.*, 2013]. Likewise, nucleation events in boreal forests could significantly contribute to the CCN budget in remote regions [*O'Dowd et al.*, 2009; *Yli-Juuti et al.*, 2011; *Kerminen et al.*, 2012; *Riipinen et al.*, 2012; *Crippa and Pryor*, 2013; *Schobesberger et al.*, 2013; *Westervelt et al.*, 2013]. The extent to which land-based biogenic aerosol impacts the marine atmosphere, including marine stratocumulus, off the coast of California is an open question that is examined in the present work.

In the following discussion, source apportionment by positive matrix factorization, satellite data, and forest surveys are used to establish that a large source of organic above marine stratocumulus off the coast of California originates from continental biogenic sources. The extent of this aerosol in the marine atmosphere, its properties, and its potential to act as CCN are evaluated based on case flights.

2. Methodology

The 2011 Eastern Pacific Emitted Aerosol Cloud Experiment (E-PEACE) was conducted between July and August to study aerosol-cloud interactions over the eastern Pacific Ocean [*Russell et al.*, 2013]. Measurements were performed onboard the Navy Twin Otter based out of the Center for Interdisciplinary Remotely-Piloted Aircraft Studies (CIRPAS) in Marina, CA. The focus of E-PEACE was to understand the extent to which different aerosol sources induce microphysical changes in cloud properties. The Twin Otter measured the response of stratocumulus to perturbations by three sources: an organic aerosol intentionally emitted by a specially outfitted ocean vessel, cargo ships of opportunity, and sea salt. In the present study, we focus on those flights in which continental aerosol was measured and investigate its influence on the chemical and physical properties of marine aerosol and clouds.

Follow-up flights designed to expand the findings from E-PEACE were conducted in 2013 during the Nucleation in California Experiment (NiCE). This experiment probed aerosol emitted from sources where new particle formation might occur, such as urban plumes, animal husbandry, forested regions, and ship exhaust. We focus here on those flights that specifically probe the impact of continental aerosol on the marine atmosphere.

2.1. Flight Descriptions: E-PEACE

The complete E-PEACE campaign consisted of 30 flights executed ~ 70 km off the coast of Monterey, CA [*Russell et al.*, 2013]. In the present study, we focus on four flights performed between Monterey and Oregon (Figure 1 and Table 1). The flight objectives were to characterize latitudinal gradients in marine and continental aerosol properties. During flights 27 and 28 (henceforth E27 and E28), we traversed along the coast and observed weak temperature inversions at 600 m and clear (cloudy) conditions for E27 (E28). During flight E29, we repeated a latitudinal gradient but also followed a longitudinal flight path to assess the properties of marine aerosol over the open ocean. Flight E29 was characterized by persistent cloud coverage and a strong temperature inversion at 500 m. The flight path for E30 was similar to those of flights E27 and E28; however, during this transect we performed long slant ascents and descents between 30 and 2500 m above sea level to sample the vertical composition of aerosol over ocean and land. Flight E30 was also characterized by persistent stratocumulus and a strong temperature inversion at 500 m.

Aside from flight E30 which sampled at many altitudes, the Twin Otter flew at 30 m above sea level or in the free troposphere above marine stratocumulus. The aircraft diverted 3 times to measure continental aerosol at various altitudes—the first samples were measured over Monterey, the second were measured 90 km north of San Francisco near Santa Rosa, CA, and the third were measured 250 km south of the Oregon border near Gaberville, CA. Five cloud water samples were collected north of San Francisco during flights E28 and E29 to characterize cloud water chemical composition.

Journal of Geophysical Research: Atmospheres 10.1002/2013JD021228

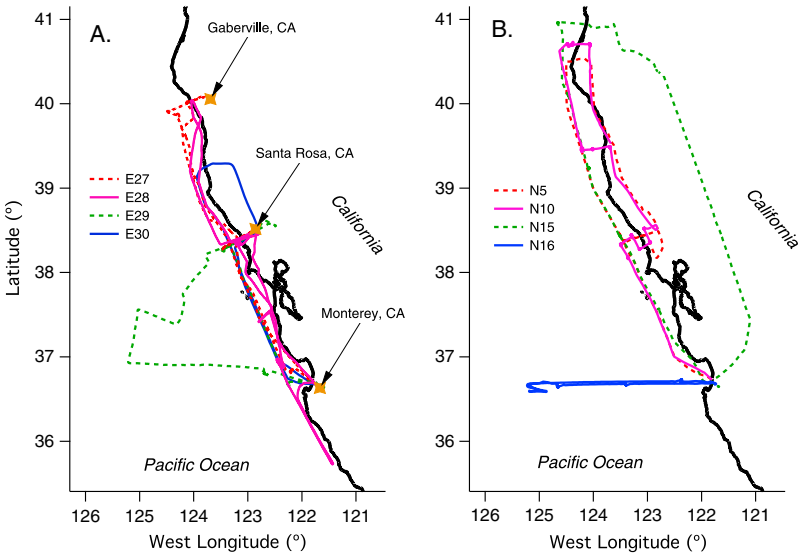

Figure 1. (a) Flight paths for E27, E28, E29, and E30. Gold makers indicate the locations where the Twin Otter diverted its coastal trajectory to measure aerosol over land. (b) Flight paths for N5, N10, N15, and N16.

2.2. Flight Descriptions: NiCE 2013

The NiCE campaign consisted of 23 flights conducted in various regions of California. Here we focus on four flights intended to measure free tropospheric aerosol over marine stratocumulus. In contrast to previous flight strategies, flights conducted during NiCE were designed to assess the vertical profile of aerosol properties utilizing deliberate maneuvers such as vertical spirals and slant ascents. Flights 5, 10, and 15 (henceforth N5, N10 and N15) were conducted along the coast to study latitudinal gradients, while flight N16 was carried out in an E-W fashion to assess properties over the open ocean (Figure 1). All flights encountered a mix of cloudy and clear conditions with strong marine temperature inversions at 500 m (N5), 500 m (N10), 350 m (N15), and 700 m (N16).

On 26 July 2013, the Big Windy and Whiskey Complex forest fires were first reported in southwest Oregon (http://www.inciweb.org). These fires were detected during flight N16 and subsequent flights. We use these data here as a tracer for biogenic sources; however, a more thorough treatment of these fires will be forthcoming.

2.3. Instrumentation

A nearly identical instrumentation payload was utilized onboard the CIRPAS Twin Otter during both campaigns [*Russell et al.*, 2013]. Cloud droplet residuals were selectively sampled using a counterflow virtual impactor (CVI) with a cut size of 11 μm [*Shingler et al.*, 2012]. Outside of cloud, particles were measured behind the main subisokinetic aerosol inlet. Under typical airspeeds, the main inlet samples aerosol < 3.5 μm diameter with 100% efficiency [*Hegg et al.*, 2005]. The focus of the present study is aerosol with diameters < 1 μm, for which losses due to particle sampling can be disregarded.

Submicrometer aerosol composition was measured using a compact time-of-flight Aerodyne aerosol mass spectrometer (AMS) [*Jayne et al.*, 2000; *Allan et al.*, 2004a; *Drewnick et al.*, 2005; *Aiken et al.*, 2008]; the data were collected and processed as described by *Coggon et al.* [2012]. Aerosol mass detection limits are taken to be twice the standard deviation of a species signal during filter sampling and are calculated to be 0.19 (organic), 0.032 (sulfate), 0.19 (ammonium), 0.04 (nitrate), and 0.06 (chloride).

Single-particle refractory black carbon mass was measured with a Droplet Measurement Technologies Single-Particle Soot Photometer (SP2, DMT, Boulder, CO, USA). The SP2 was calibrated and configured similar to a previous study [*Metcalf et al.*, 2012]. Fullerene soot is used to calibrate the SP2 following recommendations by *Laborde et al.* [2012] and *Baumgardner et al.* [2012]. The single-particle detection limits are 0.54–103 fg (83–478 nm volume-equivalent diameter, assuming a black carbon density of 1.8 g cm^{-3})

Journal of Geophysical Research: Atmospheres 10.1002/2013JD021228

Table 1. Summary of E-PEACE 2011 and NiCE 2013 Flight Objectives

	Flight[a]	Date	Conditions	Objective
E-PEACE				
	E27	15 Aug 2011	Clear	Measure latitudinal gradients in aerosol properties over ocean and land in the absence of clouds. Most measurements performed at low altitude except when over land.
	E28	16 Aug 2011	Cloudy	Measure latitudinal gradients in aerosol properties over ocean and land in the presence of clouds. Most measurements performed at low altitude except when over land.
	E29	17 Aug 2011	Cloudy	Measure longitudinal gradients in aerosol properties over ocean and land in the presence of clouds Most measurements performed at low altitude or in the free troposphere above marine stratocumulus.
	E30	18 Aug 2011	Cloudy	Measure latitudinal and vertical gradients in aerosol properties over ocean and land using slant ascents. Measurements performed at various altitudes over ocean and land.
NiCE				
	N5	12 July 2013	Clear/Cloudy	Measure latitudinal and vertical gradients in aerosol properties over ocean and land using slant ascents. Many measurements performed above cloud.
	N10	19 July 2013	Clear/Cloudy	Measure latitudinal and vertical gradients in aerosol properties over ocean and land using vertical spirals. Many measurements performed above cloud.
	N15	26 July 2013	Clear/Cloudy	Measure latitudinal and vertical gradients in aerosol properties over ocean and land using slant ascents and vertical spirals. Many measurements performed above cloud.
	N16	29 July 2013	Clear/Cloudy	Measure longitudinal and vertical gradients in aerosol properties over ocean and land using slant ascents and vertical spirals. Many measurements performed above cloud. This flight was influenced by biomass burning organic aerosol from Oregon forest fires.

[a]The designations E and N indicate flights from E-PEACE and NiCE, respectively.

AGU Journal of Geophysical Research: Atmospheres 10.1002/2013JD021228

with an absolute uncertainty of 30%. Black carbon mass concentrations are determined by summing the total mass of all single particles detected in a given sample period. These mass concentrations are typically 15–20% lower than mass calculated based on fitted distributions [*Metcalf et al.*, 2012].

Cloud water samples were collected using a modified Mohnen slotted cloud water collector [*Hegg and Hobbs*, 1986] and processed according to the procedures described by *Sorooshian et al.* [2013] and *Wang et al.* [2014]. Briefly, samples were treated with chloroform to minimize biological processing and stored at 5°C for off-line analysis. Chemical speciation was conducted by inductively coupled plasma mass spectrometry (ICP-MS) and ion chromatography (IC).

Cloud condensation nuclei (CCN) number concentrations were measured using a streamwise thermal-gradient cloud condensation nuclei counter (CCNC, Droplet Measurement Technologies) [*Roberts and Nenes*, 2005; *Lance et al.*, 2006]. A flow orifice and active control system was used to maintain instrument pressure at 700 mb independent of ambient pressure. The instrument was operated in scanning flow CCN analysis (SFCA) mode [*Moore and Nenes*, 2009]. SFCA produced CCN spectra over the range 0.15–0.85% supersaturation.

Absolute particle number concentrations were measured with an ultrafine CPC (UFCPC, $D_p \geq 2$ nm, model 3025, TSI). Aerosol size distributions were measured behind the subisokinetic inlet using a custom-built scanning mobility particle sizer (SMPS, $D_p \geq 10$ nm), which consists of a differential mobility analyzer (DMA, model 3081, TSI, Shoreview, MN) coupled to a condensation particle counter (CPC, model 3010, TSI). Size distributions and aerosol number concentrations were also measured outside the aircraft using a passive cavity aerosol spectrometer probe (PCASP, $D_p \geq 100$ nm).

Satellite imagery from the Geostationary Operation Environmental Satellite (GOES) and Moderate Resolution Imaging Spectoradiometer (MODIS) were used to visualize cloud coverage and vegetation density, respectively. Data were downloaded from the Naval Research Laboratory website (http://www.nrlmry.navy.mil/sat_products.html) and NASA (http://modis-atmos.gsfc.nasa.gov/NDVI/index.html).

2.4. Mass Spectra Deconvolution Using Positive Matrix Factorization

We use positive matrix factorization (PMF) [*Paatero and Tapper*, 1994; *Paatero*, 2007] to deconvolve the organic mass spectra into the contributions of its different sources. Details about the PMF solution can be found in the supporting information. Numerous studies have utilized PMF to analyze AMS data [e.g., *Ulbrich et al.*, 2009; *Slowik et al.*, 2010; *Chang et al.*, 2011; *Hildebrandt et al.*, 2011; *Hersey et al.*, 2011; *Ng et al.*, 2011; *Elsasser et al.*, 2012; *Garbariene et al.*, 2012; *Mohr et al.*, 2012; *Craven et al.*, 2013]. Spectra can often be separated into just two categories—hydrocarbon-like organic aerosol (HOA) and oxygenated organic aerosol (OOA) [*Ng et al.*, 2011]. HOA is representative of particles typically formed from gasoline or diesel emissions and is considered a tracer for anthropogenic pollution. In the marine environment, HOA is typically observed in the presence of fresh shipping exhaust [*Murphy et al.*, 2009; *Coggon et al.*, 2012]. OOA is formed when the products of volatile organic compound (VOC) oxidation partition to the aerosol phase and is often indicative of aged air masses. Depending on the degree of oxidation, OOA can be further categorized as low (LV-OOA) or semivolatile (SV-OOA). Low-volatility organic aerosol is more aged and typically exhibits a higher atomic oxygen-to-carbon ratio (O:C) than SV-OOA or HOA due to the presence of highly functionalized compounds such as carboxylic acids. Semivolatile aerosol is also oxygenated; however, it tends to be dominated by compounds with alcohol or ketone groups. For spectra measured with unit mass resolution, the fraction of mass at *m/z* 44 (typically CO_2^+) can be used to approximate the aerosol O:C ratio [*Aiken et al.*, 2008]. In remote regions, such as rural or marine atmospheres, OOA components may make up more than 95% of the organic mass [*Ng et al.*, 2011, and references therein].

3. Results and Discussion

3.1. Organic Aerosol From Continental Sources

Subcloud marine aerosol is dominated by sea spray and compounds resulting from the oxidation of marine precursors. Supermicrometer aerosol ($D_p > 1$ μm) is predominantly sea salt generated by mechanical processes [*McInnes et al.*, 1997], whereas aerosol in the submicrometer regime ($D_p \leq 1$ μm) is formed by both primary and secondary processes. Secondary chemical processing generates aerosol compounds by the gas-to-particle partitioning of low volatility compounds. Such compounds derive from the gas phase oxidation of biogenic (e.g., dimethyl sulfide) and anthropogenic precursors (e.g., ship emissions) and are

Journal of Geophysical Research: Atmospheres 10.1002/2013JD021228

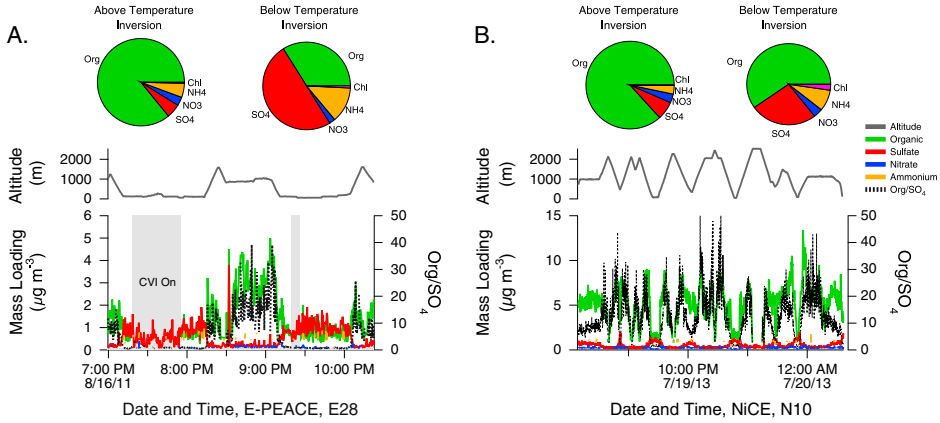

Figure 2. Summary of aerosol properties for (a) flight E28 from E-PEACE and (b) flight N10 from NiCE. Aerosol above the marine temperature inversion is highly organic (> 85%) whereas aerosol below the marine temperature inversion is a diverse mix of organic and inorganic species. Aside from organics, sulfate is the other dominant species measured by AMS. The Org/SO_4 ratio is used as a proxy to distinguish between aerosol above and below the marine temperature inversion.

predominantly composed of organics, sulfate, and ammonium. Sea spray has been observed to contribute large fractions of primary organics in the submicrometer regime in regions with high biogenic activity [e.g., *O'Dowd et al.*, 2004; *Keene et al.*, 2007; *Facchini et al.*, 2008; *Ovadnevaite et al.*, 2011; *Prather et al.*, 2013]. This is important in regions with large upwelling, such as along the western coast of the United States.

Figure 2 summarizes measurements made during flights E28 from E-PEACE and N10 from NiCE. In general, organic and sulfate are the dominant aerosol species. Below and within cloud, aerosol and cloud droplet residuals have organic to sulfate (Org/SO_4) ratios typical of marine aerosol measured during the E-PEACE and NiCE campaigns (range 0.34–4.07 with an average of 1.14, *Coggon et al.* [2012]). During all flights presented here, we observe a stark change in aerosol properties above cloud in which particles at high mass concentrations are dominated by organic material (> 85%). The bulk properties of these particles are nearly identical during both campaigns; however, higher mass concentrations were observed during NiCE.

In addition to variations in bulk aerosol composition, the organic mass spectra of aerosol measured above cloud differs from that measured below cloud. These differences are best illustrated in the triangular space defined by *Ng et al.* [2010] (Figure 3). The triangular space is a proxy to evaluate ambient aerosol oxidation based on the fraction of organic mass at *m/z* 44 and 43 (f_{44} and f_{43}, respectively). Fractions of organic at *m/z* 44 and 43 scattering about the top of the triangular region are typical of LV-OOA, those scattering about the middle of the triangle are typical of SV-OOA, while those scattering about the bottom of the triangle are typical of HOA. Aerosol with high Org/SO_4 exhibits f_{44} and f_{43} that scatter within the semivolatile region of the triangle plot while those with low Org/SO_4 exhibit fractions that scatter in regions of both semi volatility and low volatility (Figure 3). The source of aerosol with high Org/SO_4 above the marine temperature inversion is of particular interest in the present study. Similar observations were made during the other flights presented in Table 1.

In the present study, we evaluate the organic mass spectra of data collected during E-PEACE using PMF to infer the origin of the organic aerosol measured above cloud. As mentioned in section 2.4, a detailed description of the PMF solution is provided in the supporting information. In general, two factors are sufficient to describe the variation in organic mass spectra over the course of a flight. The mass spectra and time series for each factor are shown in Figure 4. Factor 1 is dominated by mass at *m/z* 44 (typically CO_2^+) and *m/z* 43 (typically $C_2H_3O^+$ or C_3H_7), whereas Factor 2 is dominated by mass at *m/z* 44 and *m/z* 29 (typically CHO^+). Both factors have spectra consistent with semivolatile organic aerosol (SV-OOA). In the triangle space, these factors exhibit f_{44} and f_{43} that scatter about regions coincident with aerosol of high and low Org/SO_4 ratio (Figure 3). As discussed in the supporting information, Factors 1 and 2 represent the profiles of aerosol measured above (high Org/SO_4) and below (low Org/SO_4) the marine temperature inversion, respectively. A HOA

Journal of Geophysical Research: Atmospheres 10.1002/2013JD021228

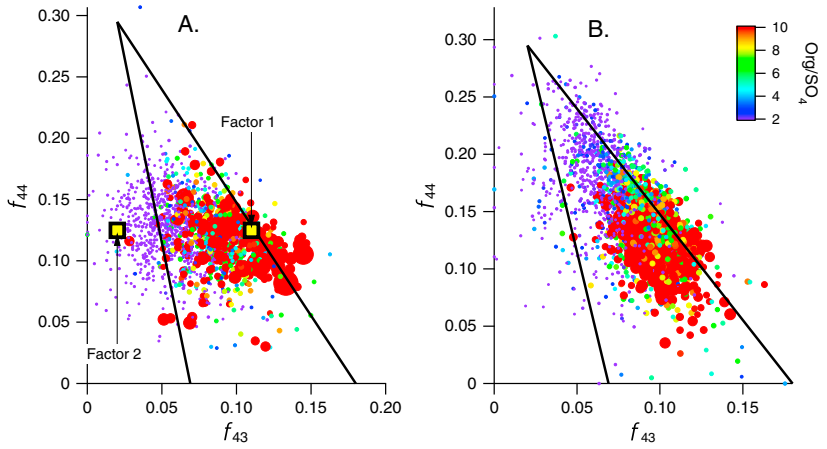

Figure 3. Triangle plot [*Ng et al.*, 2010] showing the relative contributions of organic mass at *m/z* 44 (f_{44}) and 43 (f_{43}) measured during (a) E-PEACE and (b) NiCE. Markers are colored and sized by the Org/SO_4 ratio. Red markers indicate Org/SO_4 ≥ 10; however, measurements as high as Org/SO_4 = 50 were observed above the marine temperature inversion.

factor is not resolved from the PMF solution, implying that fresh primary anthropogenic emissions did not impact measurements presented here.

The time series trends for Factors 1 and 2 are compared to external traces of sulfate and NaCl measured by AMS and black carbon measured by the SP2 (Figure 4). The NaCl trace is defined similarly to that from *Allan et al.* [2004b] and is the sum of mass at *m/z* 23 (Na^+), 35 (Cl^+), 36 (HCl^+), and 58 ($NaCl^+$). While NaCl is refractory and therefore not quantifiable by standard AMS operation, small amounts of NaCl fragments can be used as tracers for sea spray and primary marine organic aerosol.

Factor 2 varies positively with sulfate and NaCl and is constrained below cloud (Figure 4). Factor 2 variation is stronger with respect to sulfate ($R = 0.59$) than with NaCl ($R = 0.22$), implying that Factor 2 is not sea salt in

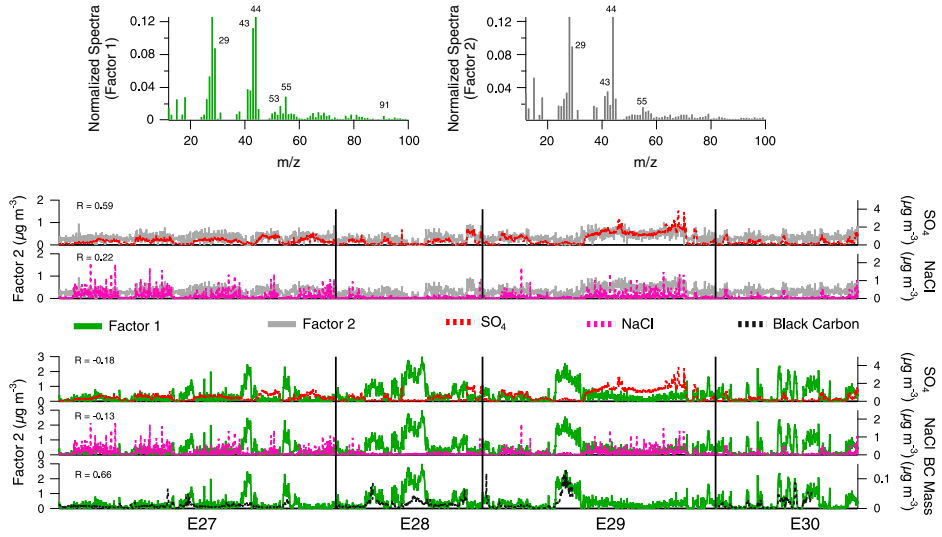

Figure 4. (top) Factors 1 and 2 spectra and time series profiles compared to (bottom) external traces of sulfate, NaCl, and black carbon. The NaCl trace is defined similarly to that from *Allan et al.* [2004b] and is the sum of mass at *m/z* 23 (Na^+), 35 (Cl^+), 36 (HCl^+), and 58 ($NaCl^+$). Note that factor profiles and external tracers presented here are uncorrected for collection efficiency.

Journal of Geophysical Research: Atmospheres 10.1002/2013JD021228

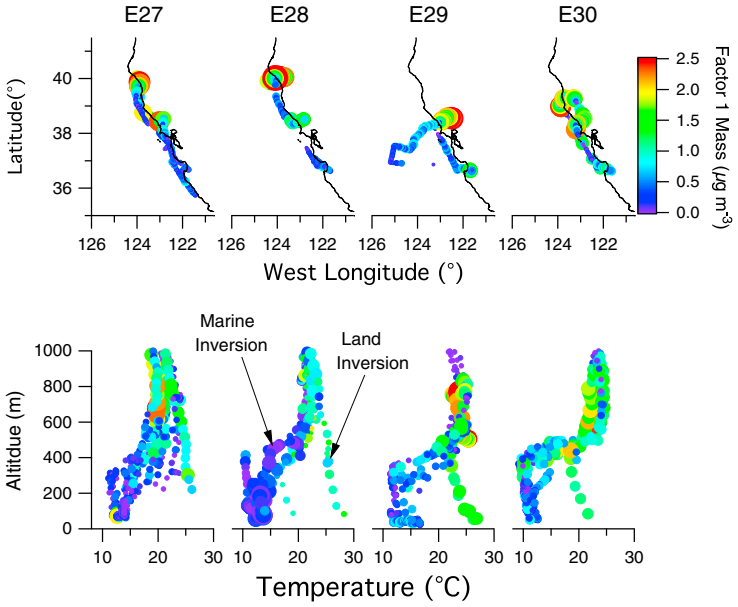

Figure 5. (top row) Map showing the spatial distribution of Factor 1 during E-PEACE flights. (bottom row) Temperature profile observed during each flight. Markers are colored and sized by the mass contribution of Factor 1.

nature. Positive variation with respect to NaCl is likely due to enhancement of both Factor 2 and NaCl within the marine boundary. Sulfate in this region could result from continental sources such as biomass burning and anthropogenic emissions or marine sources such as sea spray, dimethyl sulfide, and ship exhaust. During E-PEACE, most sulfate that was measured resulted from shipping emissions which often impact background marine aerosol off the coast of California [*Coggon et al.*, 2012]. Likewise, this is a region of strong oceanic upwelling; thus, biogenic emissions of dimethyl sulfide can strongly impact sulfate concentrations [e.g., *Gaston et al.*, 2010]. Consequently, sulfate observed in the present study likely results from sources originating within the marine boundary layer as opposed to continental sources. Given the positive variation between Factor 2 and marine species and Factor 2 enhancement within the boundary layer, we interpret Factor 2 as representative of marine boundary layer organic aerosol.

Factor 1 varies negatively with sulfate ($R = -0.13$) and NaCl ($R = -0.18$) making it unlikely to be a marine source. Figure 5 shows the Factor 1 spatial distribution for E-PEACE flights. Factor 1 exhibits low mass over ocean but rises sharply to values as high as 3 μg m^{-3} over land, suggesting that Factor 1 is a continental source. Measurements performed during NiCE show similarities to those from E-PEACE. Based on PMF analysis and measurements of bulk aerosol composition, continental aerosol (Factor 1), which is constrained above the marine temperature inversion, exhibits an Org/SO_4 ratio ≥ 3 and f_{44}/f_{43} of 0.125/0.11 (Figures 2a and 3a). Aerosol measured above the marine temperature inversion during N10 exhibits the same bulk properties and detailed organic mass spectra (Figures 2b and 3b), indicating a continental impact during NiCE. Further discussion about the continental sources contributing to Factor 1 is provided in section 3.2.

Measurements of the vertical temperature profiles suggest that meteorological conditions during E-PEACE may have facilitated transport of continental aerosol into the free troposphere above marine stratocumulus. Figure 5 illustrates that during most E-PEACE flights, a strong marine temperature inversion existed. The continental factor contributes little mass at low altitude but increases to values as high as 3 μg m^{-3} above the inversion. Measurements made over land show a weak inversion, and the contribution from continental factor is prominent at both low and high altitudes. Given that the continental factor originates from a region with a weak inversion, it is plausible that this aerosol is lifted into the free troposphere and subsequently transported over the ocean. This is consistent with the observation of aerosol with high Org/SO_4 ratio above the marine temperature inversion (Figure 2). In section 3.3, we will further investigate the mechanism by which continental aerosol is transported over marine stratocumulus using data from NiCE.

AGU Journal of Geophysical Research: Atmospheres 10.1002/2013JD021228

3.2. Biogenic Impact on the Continental Factor

The continental factor's mass spectral profile resembles SV-OOA, which is known to originate from many types of sources [*Ng et al.*, 2011]; thus, the continental factor is either natural, anthropogenic, or some combination of both. While previous studies have resolved separate anthropogenic and natural factors in continental regions [e.g., *Setyan et al.*, 2012; *Han et al.*, 2014], we find that additional factors do not exhibit meaningful correlations with external tracers, nor do they improve PMF goodness-of-fit criteria; therefore, a single factor is attributed to continental aerosol in this study (i.e., Factor 1. See supporting information). This limitation is reflected by the shortage of instruments capable of detailed chemical speciation that might elucidate factors corresponding to natural or anthropogenic continental sources. In the absence of instrumentation that could provide source specific tracers, we rely on black carbon (BC) data measured by the SP2, emission factor analysis, and satellite data to determine which sources (natural or anthropogenic) most likely contribute to the continental factor.

Figure 4 shows that the continental factor positively varies ($R = 0.66$) with black carbon (BC) which implies that some fraction of the organic may result from anthropogenic (e.g., vehicles) or natural (e.g., biomass burning) combustion. However, the organic variation with BC is not direct, which suggests that combustion may not be the only contribution to the continental factor. For example, measurements performed during flights E27 and E28 show that organic mass is enhanced relative to BC as compared to measurements performed during flights E29 and E30. We rule out biomass burning as a major source of aerosol given a lack of fires in this region during flights presented here (http://www.calfire.ca.gov); furthermore, aerosol does not exhibit typical biomass burning markers (high organic mass at *m/z* 60 and 73, *Ng et al.* [2011]).

Fossil fuel combustion could be a source of BC and, likewise, continental organic aerosol. Anthropogenic organic material may be emitted directly as primary organic aerosol (POA) or produced via secondary processes (secondary organic aerosol, SOA). To estimate an anthropogenic contribution due to fossil fuel consumption, we calculate the organic mass that might be associated with BC as either POA or SOA using organic carbon (OC) and organic mass (OM) ratios measured in urban environments.

POA is estimated using an OC/BC ratio of 2.08 reported by *Novakov et al.* [2005]. This ratio is typical for aerosol measured in United States urban environments and is assumed to represent OC from primary emissions [*Novakov et al.*, 2005]. Performing these calculations for the highest BC concentration observed in the present flights (0.13 μg m^{-3}) and assuming that total OM is approximately 1.4 times higher than OC [*Novakov et al.*, 2005], we estimate POA mass as

$$\mathrm{POA} = 0.13\,\mu\mathrm{g\,BC\,m^{-3}} \cdot 2.08\,\frac{\mu\mathrm{g\,OC}}{\mu\mathrm{g\,BC}} \cdot 1.4\,\frac{\mu\mathrm{g\,OM}}{\mu\mathrm{g\,OC}} = 0.38\,\mu\mathrm{g\,OM\,m^{-3}} \tag{1}$$

Accounting for uncertainties in BC (± 30%) measurements and OC/BC ratios (± 0.85), POA could contribute 0.38 (range 0.16–0.7) μg m^{-3} of organic mass to the continental factor. Secondary organic mass is calculated assuming that SOA produced by fossil fuels is primarily attributable to vehicular emissions. Here calculations are performed using emission factor analysis similar to the methods employed by *Ensberg et al.* [2014] to calculate vehicular SOA mass in the Los Angeles, CA Basin (Table 2). Equations (2) and (3) summarize these calculations.

$$R_{\mathrm{VOC/BC}} = \frac{\mathrm{EF_{VOC}}}{\mathrm{EF_{BC}}} \tag{2}$$

$$\mathrm{SOA_{Mass}} = \mathrm{BC_{Mass}} \cdot R_{\mathrm{VOC/BC}} \cdot \mathrm{SOA_{Yield}} \tag{3}$$

The inputs to equations (2) and (3) include the mass of gas phase organics (EF_{VOC}, g/kg) and BC (EF_{BC}, g/kg) emitted per kilogram of fuel consumed and SOA yield for bulk diesel or gasoline emissions (SOA_{Yield}). Emission factors and yields representative of the California vehicle fleet are provided by *Gentner et al.* [2012] and summarized in Table 2. The ratio $R_{VOC/BC}$ (equation (2)) is an estimation of the mass of gas phase organics emitted from diesel or gasoline emissions per gram of BC measured. Assuming that 100% of the VOCs emitted from vehicular sources undergo reaction, equation (3) yields an upper estimate of the total SOA mass attributable to gasoline or diesel activity (SOA_{Mass}).

Performing these calculations for the highest concentration of BC observed in Figure 4 (BC_{Mass}, 0.13 μg m^{-3}), we estimate that secondary processing of gasoline and diesel emissions could account for 0.09 (range

Journal of Geophysical Research: Atmospheres 10.1002/2013JD021228

Table 2. Results of Emission Factor Analysis Using Yields and BC, Gasoline, and Diesel Emission Factors From *Gentner et al.* [2012][a]

	EF^{b}_{VOC}	EF^{c}_{BC}	Yield	SOA Mass[d] μg m^{-3}
Gasoline	0.61 ± 0.24	0.02 ± 0.003	0.023 ± 0.007	0.09 (0.03–0.25)
Diesel	1.18 ± 0.47	0.54 ± 0.07	0.15 ± 0.05	0.04 (0.01–0.12)

[a]SOA mass is calculated using equations (2) and (3) with a maximum BC measurement of 0.13 (±30%) μg m^{-3}. Values in parentheses represent upper and lower estimates of SOA mass based on uncertainties in emission factors, yields, and BC mass.
[b]VOC emission factors are reported as grams of gas phase organic mass (gGPOM) per liter of fuel consumed [*Gentner et al.*, 2012]. Values listed here represent emission factors on a mass basis (gGPOM/kg fuel) assuming gasoline and diesel densities of 0.74 and 0.852 kg/L, respectively. Uncertainty ranges are calculated assuming ± 40% error [*Ensberg et al.*, 2014].
[c]BC emission factors are reported as gBC/kg fuel.
[d]SOA Mass is calculated assuming 100% VOC reaction.

0.03–0.25) and 0.04 (range 0.01–0.12) μg m^{-3} of organic mass, respectively. Assuming that gasoline emissions represent an upper estimate of fossil fuel SOA, total fossil fuel organic mass (POA + $SOA_{gasoline}$) could contribute as much as 0.47 (range 0.18–0.95) μg m^{-3} to the observed continental organic aerosol.

The mass estimated to be attributed to fossil fuel combustion is lower than organic mass measured during E-PEACE (3–4 μg m^{-3}, Figure 2) and NiCE (8–10 μg m^{-3}), suggesting that fossil fuel combustion is unlikely to be the sole source of continental organic aerosol measured in the present study. While anthropogenic BC could originate from nonvehicular emissions (e.g., ships, industrial activity, and human-induced biomass burning), there is little inorganic content and lack of tracers associated with biomass burning aerosol to support other anthropogenic sources (see above-cloud aerosol composition, Figure 2). Therefore, we reason that a fraction of the organic mass associated with the continental factor may be influenced by terrestrial biogenic sources.

Northern California is a region of densely populated coniferous forests. Figure 6a illustrates the flight path for E28 superimposed over a map of the normalized difference vegetation index (NDVI) for California during 13–28 August 2001. The NDVI, a product of the NASA MODIS satellite, is a measure of the relative amount of vegetation in a given region, with higher values indicating higher vegetation density. Though these data were collected 10 years earlier than E-PEACE, we presume that they reflect the same seasonal vegetation distribution as in August 2011. Data and details about NDVI can be found at http://modis-atmos.gsfc.nasa.gov/NDVI/index.html.

The continental factor is present preferentially in northern California, in correspondence with the NDVI which is highest at latitudes above 38°. Figure 6a suggests that the organic signature over land may be strongly influenced by biogenic sources that are more abundant at higher latitudes. Figure 6b shows that the continental factor's spatial gradient opposes that of human population density, which is consistent with our inferences of a limited anthropogenic impact.

The biogenic nature of the continental factor can be investigated further by examining its mass spectrum. Figure 7 compares the continental factor's mass spectrum to those of anthropogenic and biogenic SV-OOA previously resolved using PMF [*Ng et al.*, 2011; *Hersey et al.*, 2011; *Setyan et al.*, 2012; *Han et al.*, 2014]. The SV-OOA factor reported by *Ng et al.* [2011] is representative of an average SV-OOA profile from six data sets and could result from natural or anthropogenic emissions. The factor resolved by *Hersey et al.* [2011] represents anthropogenic SV-OOA measured in the Los Angeles Basin, CA. The profiles resolved by *Setyan et al.* [2012] and *Han et al.* [2014] are those of aerosol impacted by biogenic sources near the foothills of the Sierra Nevada Mountains, CA and in a Japanese boreal forest dominated by monoterpene emissions, respectively.

The continental factor shows close similarities to the factors resolved by *Setyan et al.* [2012] and *Han et al.* [2014] and exhibits high fractions of *m/z* 29, 43, and 44 with a distinguishable peak at *m/z* 55. All three factors exhibit similar features as organic spectra of aerosol generated from VOCs of monoterpene-emitting plants in chamber oxidation experiments (not shown, [*Kiendler-Scharr et al.*, 2009]). In contrast, the mixed

AGU Journal of Geophysical Research: Atmospheres 10.1002/2013JD021228

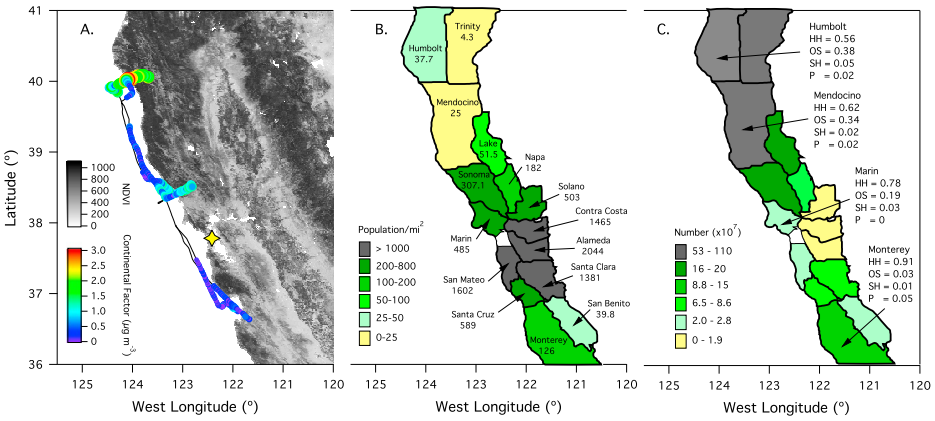

Figure 6. (a) Flight path for E28. Missing markers indicate periods removed from PMF analysis due to low organic mass or brief impacts by cloud-processed shipping emissions (see PMF description in supporting information). Markers are colored by the continental factor mass. The flight path overlays a satellite image of California. The map is colored by the normalized difference vegetation index (NDVI), which is a relative measure of the amount of vegetation in an area. Darker colors indicate higher vegetation. NDVI data can be found at http://modis-atmos.gsfc.nasa.gov/NDVI/index.html. The yellow star indicates the location of San Francisco, CA. (b) Map showing the human population density of a given California county. Numbers in each county represent the number of people per square mile as measured during the 2010 census and can be found at http://census.gov. (c) Map showing the total number of trees in a given California county. The composition (HH = hardwood, OS = other softwood, SH = soft hardwood, and P = pine) of the forests for four counties are shown. A breakdown of each category is provided in Table 3.

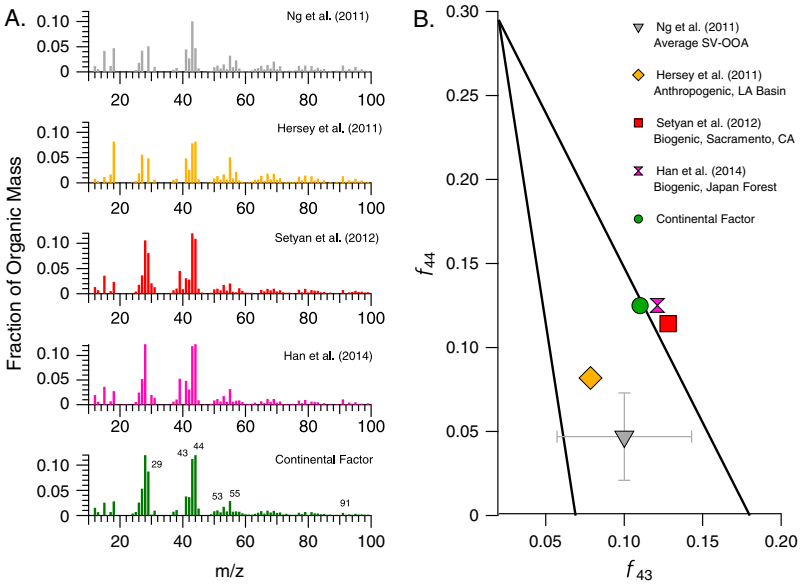

Figure 7. (a) Comparison of average SV-OOA [*Ng et al.*, 2011], anthropogenic SV-OOA measured in the Los Angeles Basin, CA [*Hersey et al.*, 2011], biogenic organic aerosol measured in Sacramento, CA [*Setyan et al.*, 2012], and biogenic organic aerosol measured in a Japanese boreal forest [*Han et al.*, 2014] to the continental factor resolved in this study. (b) Comparison of f_{44}/f_{43} for the continental factor resolved in this study to SV-OOA factors resolved previously [*Ng et al.*, 2011; *Hersey et al.*, 2011; *Setyan et al.*, 2012; *Han et al.*, 2014]. Note that f_{43} and f_{44} are calculated with the signal of 39 removed.

AGU Journal of Geophysical Research: Atmospheres 10.1002/2013JD021228

Table 3. Major Species (> 5% of Total Number) in the Tree Subgroups (HH = Hard Hardwood, OS = Other Softwood) Shown in Figure 6

	Common Name	Genus Species[a]	Group	%Total Number[b]	%α-Pinene[c]	REP[d]
Monterey County						
	Canyon live oak	*Quercus chrysolepis*	HH	24	34.8	1.176
	Coast live oak	*Quercus agrifolia*	HH	23	34.8	1.176
	California laurel	*Umbellularia californica*	HH	17	26	0.065
	Blue oak	*Quercus douglasii*	HH	11	34.8	1.176
Marin County						
	California laurel	*Umbellularia californica*	HH	47	26	0.065
	Tanoak	*Lithocarpus densiflorus*	HH	15	34.8	1.176
	Coast live oak	*Quercus agrifolia*	HH	11	34.8	1.176
	Redwood	*Sequoia sempervirens*	OS	10	25.7	0.016
Humbolt County						
	Tanoak	*Lithocarpus densiflorus*	HH	46	34.8	1.176
	Douglas-fir	*Pseudotsuga menziesii*	OS	23	64.2	9.909
	Redwood	*Sequoia sempervirens*	OS	12	25.7	0.016
Mendocino County						
	Tanoak	*Lithocarpus densiflorus*	HH	39	34.8	1.176
	Douglas-fir	*Pseudotsuga menziesii*	OS	21	64.2	9.909
	Redwood	*Sequoia sempervirens*	OS	11	25.7	0.016
	Pacific madrone	*Arbutus menziesii*	HH	7	—	—

[a] As listed by the National Forest Service (http://www.fs.fed.us).
[b] %Total Number is the percentage of the total number of trees in the given California county.
[c] %α-pinene is the percentage of alpha-pinene released relative to the total monoterpene flux [*Geron et al.*, 2000]. α-pinene fractions reported for the genus *Quercus* are an average of many species. Estimates are cited in *Geron et al.* [2000].
[d] REP is the relative emission potential, which is the product of the monoterpene emission factor, estimated percentage of the total crown coverage in the United States and the foliar density [*Geron et al.*, 2000, and references therein]. Higher values of REP suggest that a species is a greater contributor to monoterpene emissions. Estimates are cited in *Geron et al.* [2000].

and anthropogenic-influenced SV-OOA factors from *Ng et al.* [2011] and *Hersey et al.* [2011] exhibit lower fractions of *m/z* 44 and 43 and increased contributions from *m/z* 55 and 57. The continental factor resolved in this study and the biogenic factors resolved previously occupy roughly the same region of the triangle plot, which is in contrast to mixed or anthropogenic-influenced SV-OOA.

Analysis of the organic mass spectrum and spatial distribution leads us to conclude that the continental factor is linked to organic aerosol largely impacted by biogenic sources (Figures 6 and 7). Trees emit a complex mixture of biogenic volatile organic compounds (BVOCs) that can undergo atmospheric oxidation [*Geron et al.*, 2000; *Holzinger et al.*, 2005; *Steinbrecher et al.*, 2009; *Eddingsaas et al.*, 2012]. Isoprene is the globally dominant BVOC ($\sim$ 500 TgC yr^{-1}), and its emissions are strongly dependent on tree species [*Guenther et al.*, 1995; *Holzinger et al.*, 2005]. Monoterpenes (organics with chemical formula $C_{10}H_{16}$) may be the primary BVOC in coniferous forests [e.g., *Geron et al.*, 2000; *Yli-Juuti et al.*, 2011; *Riipinen et al.*, 2012]. For example, *Geron et al.* [2000] used the population of trees in California, a species emission factor, and the corresponding monoterpene composition profile to show that nearly 50% of the monoterpenes emitted by trees along the northern coastal regions could be attributed to α-pinene. The carbon flux due to α-pinene was estimated to be as high as 225 µg m^{-2} h^{-1}, making the northern Pacific coast one of the most concentrated emission sources of α-pinene in the United States.

The conclusions drawn by *Geron et al.* [2000] are analyzed further in Figure 6c and Table 3, which show the total estimated number of trees and bulk forest composition in California coastal counties. These data are from compiled surveys performed by the United States Forest Service from 2002 to 2011 and are available at http://www.fia.fs.fed.us/. While the latitudinal trends in tree populations mirror those observed in NDVI (Figure 6a), the composition of coastal forests also changes with latitude. Near Monterey County, CA, the

Journal of Geophysical Research: Atmospheres 10.1002/2013JD021228

majority of trees are hardwood, which are dominated by canyon live oak (24%), California live oak (25%), California-laurel (17%), and blue oak (11%). As shown in Table 3, these species emit a monoterpene composition that is roughly 30% α-pinene. The relative emission potential (REP) for these species, which is a ranking of the importance of a species as a monoterpene emitter [*Geron et al.*, 2000], is modest compared to those with high REP (*Pinus taeda*, REP = 11.77) and those with low REP (*Abies fraseri*, REP = 0.00). In contrast, Mendocino County in northern CA is home to a significant fraction of softwood species dominated by Douglas-fir (21%) and Redwood (11%). Douglas-fir, for example, has a monoterpene composition dominated by α-pinene (64.3%) and exhibits a REP of 9.909, making this species one of the most important monoterpene emitters nationally [*Geron et al.*, 2000]. Thus, it follows that the high flux of α-pinene in northern CA is not only attributable to the concentrations of trees but also to a shift toward trees that emit elevated concentrations of α-pinene.

The observation of elevated organic aerosol at latitudes with high emission of monoterpenes is consistent with previous studies that have observed enhanced biogenic SOA mass from boreal forest emissions [e.g., *Cahill et al.*, 2006; *Worton et al.*, 2011; *Pierce et al.*, 2012; *Riipinen et al.*, 2012; *Han et al.*, 2014]. One recent study by *Ehn et al.* [2014] has shown that extremely low-volatile compounds (referred to as ELVOCs) form at high yield from OH− and ozone-initiated photochemistry of α-pinene, suggesting that SOA from monoterpene oxidation could dominate the aerosol budget over boreal forest canopies. Thus, a strong biogenic impact on aerosol above northern California forests is not surprising.

3.3. The Impact of Continental Aerosol on the Marine Environment

Several studies have investigated biogenic organic aerosol (BOA) formation in California [e.g., *Cahill et al.*, 2006; *Worton et al.*, 2011; *Setyan et al.*, 2012; *Shilling et al.*, 2013]. The data presented here suggest that biogenic sources can give rise to strong latitudinal gradients and impact free tropospheric aerosol over the ocean (Figures 5 and 9). In section 3.1, we suggest that continental aerosol is lifted into the free troposphere and transported over marine stratocumulus, thus increasing organic aerosol concentrations above the marine temperature inversion. Here we expand upon this discussion and investigate the mechanisms by which continental plumes could impact the marine boundary layer.

Typically, air off the coast of California flows in a north-to-south direction with the predominant wind fields originating from the remote northeast Pacific Ocean; thus, aerosol in this region is typically marine in nature. These meteorological patterns are due to the North Pacific Subtropical High which is a semipermanent anticyclone over the Pacific Ocean [e.g., *Li et al.*, 2012]. However, as is common in the summer months, this high pressure system may shift toward the continental United States and induce offshore flow of continental air [*Kloesel*, 1992]. Previous studies have found that this flow of dry air along with large-scale subsidence can lead to persistent cloud-clearing events [*Kloesel*, 1992; *Koracin and Dorman*, 2001].

These "plumes" of dry continental air were routinely observed during NiCE. In the present study, we are interested in determining if such events transport continental aerosol, and thus BOA, into the marine atmosphere. Flights N5 and N10 were designed to contrast aerosol properties between air masses impacted by the plume to those with persistent stratocumulus. During N5, a large patch of dry air with features similar to the cloud-clearing events described by *Kloesel* [1992] developed over the course of the day and extended as far south as Santa Barbara, CA (Figure 8); at 19:00 UTC, it encompassed an approximate area of 145,000 km^2. As shown in Figure 8, aerosol sampled within the plume exhibited higher Org/SO_4 than aerosol measured over persistent marine stratocumulus. In section 3.1, we show that high Org/SO_4 is typical of continental BOA; therefore, Figure 8 suggests that the plume event during N5 led to enhancement of BOA above the marine temperature inversion.

A similar cloud-clearing event developed during flight N10 as air from the Northwestern United States was transported over marine stratocumulus (see Movie S1). As shown in Figure 9, measurements at low latitudes were executed over solid decks of marine stratocumulus and exhibit high Org/SO_4 ratio which suggests a continental BOA impact above cloud. The presence of these emissions likely resulted from a plume event that had transported continental aerosol into the marine atmosphere the previous day (see Movie S1). The area subsequently filled with clouds; however, the signature of continental impact remained high above cloud. Measurements performed at high latitudes were conducted inside the dry plume and exhibit enhancements in Org/SO_4 relative to those performed to the south. These observations complement those from flight N5 and further suggest that plume events described here are a means by which continental organic aerosol from the Northwestern United States is introduced into the marine atmosphere.

AGU Journal of Geophysical Research: Atmospheres 10.1002/2013JD021228

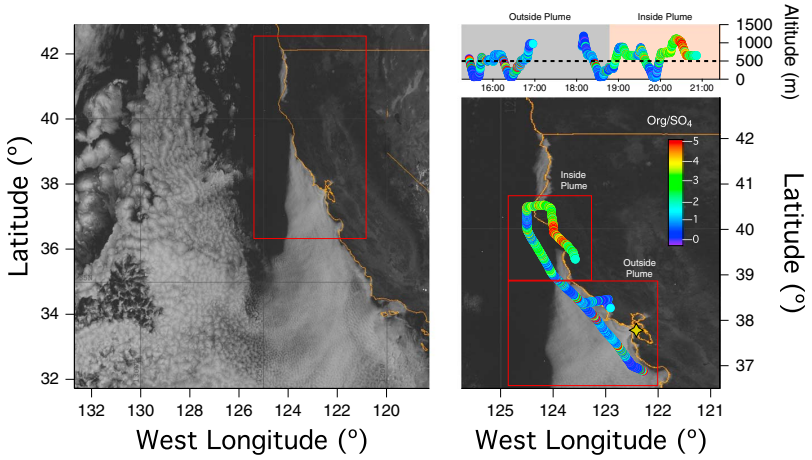

Figure 8. (left column) Satellite image taken at 18:30 UTC showing a dry air plume originating from the northwest United States. (right column) Expanded view of flight path and altitude profile for flight N5 overlaying the same satellite image (data downloaded at http://www.nrlmry.navy.mil/sat_products.html). The dotted line indicates the top of the marine boundary layer, and the yellow star indicates the location of San Francisco, CA. Markers are colored by the Org/SO_4 ratio. Data are separated into two regions: those that were measured within and outside of the dry air plume. In general, aerosol with high Org/SO_4 are dominant inside the plume. Likewise, measurements are constrained to altitudes above the marine inversion (500 m), which is consistent with Figures 5 and 9.

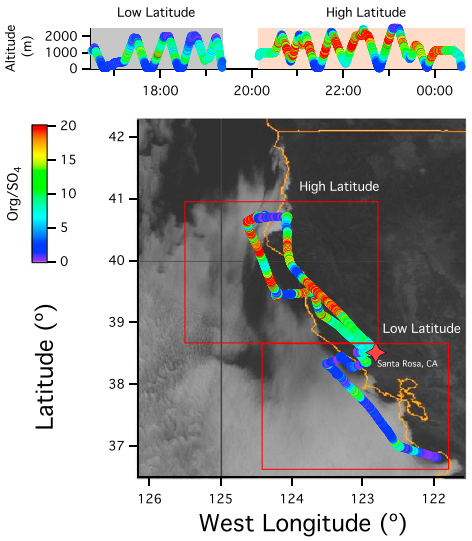

Figure 9. Flight path and altitude profile for flight N10 overlaying a satellite image showing cloud coverage at 23:15 UTC (data downloaded at http://www.nrlmry.navy.mil/sat_products.html). Markers are colored by the Org/SO_4 ratio. Data are separated into two regions: those that were measured south (low latitude) and north (high latitude) of Santa Rosa, CA. In general, aerosol with high Org/SO_4 are dominant north of Santa Rosa, CA, however particles in both regions exhibit higher Org/SO_4 than those of typical marine aerosol ($Org/SO_4 \sim 1$). Likewise, particles are constrained to altitudes above the marine inversion (500 m), similar to the results shown in Figure 5.

Given the observation of enhanced BOA above cloud, it leads to the question of the extent to which BOA also impacts the marine boundary layer and, subsequently, marine stratocumulus. As demonstrated by *Kloesel* [1992], cloud-clearing events may develop when dry continental air displaces the marine boundary layer. As the airmass is advected downwind over the ocean, the marine inversion redevelops and, given time, may refill with clouds. In the case of the N10 plume event, continental air is transported over a marine boundary layer that originated from the northeast Pacific (see supporting information, Figure S1), thus the formation of a dry plume would occur through mixing between air at the top of the marine boundary layer and the dry air in the free troposphere.

We illustrate that the mechanism described above plays a role in the development of the N10 plume using data collected from a suite of vertical spirals performed within (S5–S8) and outside (S1–S4) of the cloud-clearing event (Figure 10). Figures 10a and 10b show that boundary layer air inside the plume exhibits a lower water mixing

Journal of Geophysical Research: Atmospheres 10.1002/2013JD021228

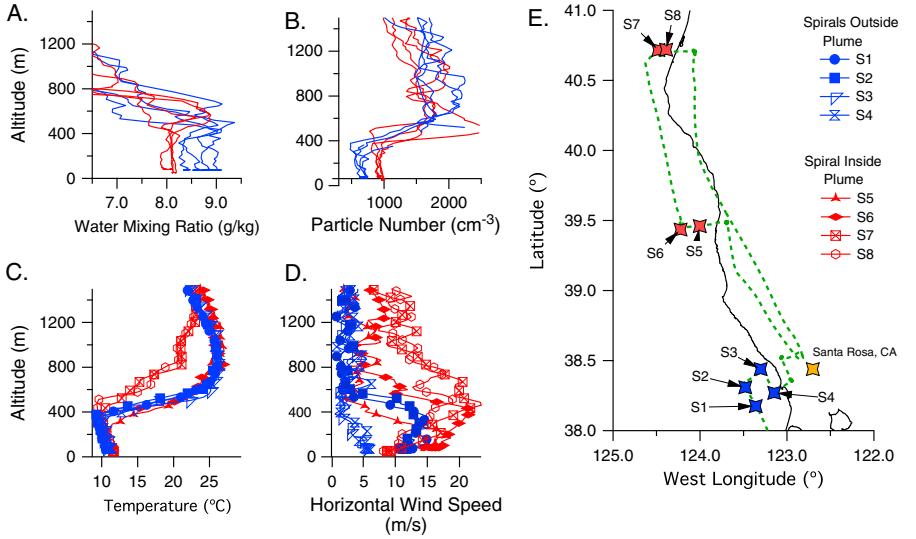

Figure 10. Summary of meteorological conditions from N10. Vertical profiles of (a) water mixing ratio, (b) particle number, (c) temperature, and (d) horizontal wind speed. Figure 10d summarizes the locations of each profile corresponding to the spirals (S) performed outside (blue) and inside (red) the plume. Figures 10c and 10d show individual spirals whereas Figures 10a and 10b show bulk vertical profiles segregated based on dry plume influence.

ratio and higher particle concentration than boundary layer air outside of the plume, indicating a recent impact by dry air with high particle number concentrations. This is consistent with the observation of enhanced dry, continental aerosol above cloud (Figure 9). Similarly, meteorological conditions within the plume suggest mixing with free tropospheric air (Figures 10c and 10d). Spirals S7 and S8 (latitude 40.7°) were performed in the heart of the cloud-clearing event (see Movie S1) and exhibit weakened temperature inversions relative to spirals S1-S6. This weakening is likely due to enhanced mixing with continental air. This is supported by faster horizontal wind speeds aloft and a higher inversion base (500 m) than spirals performed downwind of the plume (375 m). Spirals S5 and S6 (latitude 39.5°) were conducted at the leading edge of the cloud-clearing event and exhibited inversion profiles similar to those measured outside of plume influence (S1–S4). Thus, the evolution of the plume is consistent with a continental perturbation at high latitudes and redevelopment of the boundary layer as the air mass is advected southward over the ocean [*Kloesel*, 1992]. This mechanism would suggest a BOA impact on lower latitude clouds in Figure 9 given that this area had been impacted by a plume the previous day and filled with clouds overnight (see Movie S1).

Given the presence of BOA above cloud both within and outside of plume-impacted airspace, we question the extent to which the area of the dry plume in satellite data represents the general area of impact by continental BOA. From back trajectory analysis of the N10 event (see Movie S1), it is likely that a significant fraction of the plume is continental in nature; however, the Twin Otter did not measure aerosol near the plume's western boundary which may have cleared solely due to subsidence [*Kloesel*, 1992]. We suspect, however, that such plume events could carry BOA over a wide region of the marine atmosphere. Evidence for such an impact is provided by data collected during N16 (Figure 11). This flight was influenced by biomass burning organic aerosol (BBOA) originating from Oregon forest fires (Table 1). Similar to flight N10, a dry plume from the previous day had influenced measurements over regions of persistent stratocumulus. Based on enhancements of mass at m/z 60, which is a typical tracer for biomass burning due to its association with the mass spectrum of levoglucosan [e.g., *Alfarra et al.*, 2007; *Adler et al.*, 2011], BBOA was observed at distances farther than 100 km from the coast. Given the geographic commonality of the BBOA and BOA sources, Figure 11 provides additional support for the large area of impact by plume events.

Regardless of the plume's areal extent, we infer that cloud-clearing events such as those observed during flights N5 and N10 indicate the presence of continental aerosol in the free troposphere above the marine

AGU Journal of Geophysical Research: Atmospheres 10.1002/2013JD021228

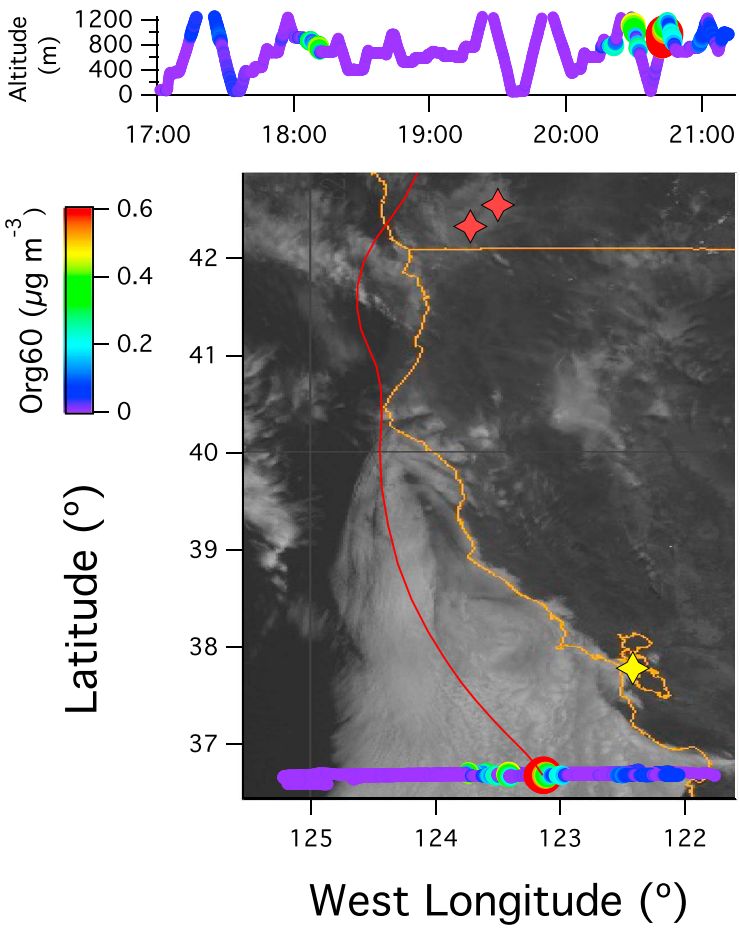

Figure 11. Flight path and altitude profile for flight N16 overlaying a satellite image showing cloud coverage at 21:00 UTC (data downloaded at http://www.nrlmry.navy.mil/sat_products.html). Measurements of biomass burning organic aerosol (BBOA) from Oregon fires were measured over marine stratocumulus. Markers are colored by the mass of organic at *m/z* 60 which is a typical tracer for BBOA. Markers are sized by the total organic loading, with the largest markers representing loadings of 150 μg m^{-3}. The red trace is a back trajectory ending at the location where the highest concentration of BBOA was measured. The back trajectory shows that measurements originated from a region impacted by Oregon fires (red stars). The yellow star indicates the location of San Francisco, CA.

temperature inversion and, moreover, its likely presence above and within cloud (Figure 9). The presence of BOA above marine stratocumulus leads us to inquire as to the degree to which this source could act as CCN or influence cloud water chemistry. We examine these questions in sections 3.4 and 3.5.

3.4. The Impact of Biogenic Organic Aerosol on Cloud Water Chemistry

Cloud water measurements demonstrate continental impacts on cloud chemistry. Figure 12 shows selected cloud water species measured over the course of the E-PEACE campaign together with 48 h HYSPLIT [*Draxler and Rolph*, 2012] back trajectories for aerosol measured in the free troposphere during flight E28. Back trajectories from flight E28 show that aerosol measured in the free troposphere above the location of the cloud water samples had been transported over land before impacting marine stratocumulus. *Wang et al.* [2014] showed that these cloud water samples exhibited the highest concentrations of crustal elements, such as Si, B, and Cs, of all samples collected during E-PEACE, implying a larger continental impact. These results are consistent with the observations of the BOA signature above marine stratocumulus (see section 3.3).

Journal of Geophysical Research: Atmospheres 10.1002/2013JD021228

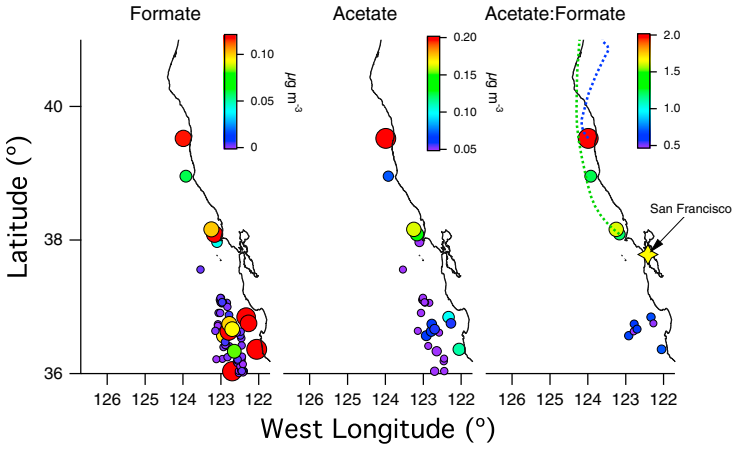

Figure 12. Spatial maps of cloud water species measured during the E-PEACE campaign. Markers are colored and sized by the air equivalent concentration, which is a concentration measure normalized by the cloud liquid water content. Dotted lines over the acetate:formate map are back trajectories for air masses above cloud during flight E28.

Acetate and formate (also shown in Figure 12) are the anions of monocarboxylic acids that are largely derived from the gas phase oxidation of vegetation sources [e.g., *Talbot et al.*, 1988; *Sanhueza et al.*, 1995; *Orlando et al.*, 2000; *Wang et al.*, 2007; *Paulot et al.*, 2011; *Stavrakou et al.*, 2011]. One recent study has shown that boreal forests may be a large source of formate and that biogenic sources in general account for ~ 90% of the global formic acid budget [*Stavrakou et al.*, 2011]. Acetate and formate may also come from combustion sources, and previous studies have observed these acids in cloud water samples impacted by ships [*Sorooshian et al.*, 2007]. Formate is also a common product formed by the cloud processing of compounds such as glyoxal and thus may be an indication of particle aging [e.g., *Ervens et al.*, 2003; *Carlton et al.*, 2006, 2007; *Sorooshian et al.*, 2007; *Lim et al.*, 2013; *Sorooshian et al.*, 2013].

Sorooshian et al. [2013] found that acetate and formate measurements from E-PEACE were well correlated ($R = 0.88$) and exhibited higher concentrations closer to the coast, suggesting primary influence from continental sources. We highlight these findings in Figure 12. The highest concentration of acetate (0.25 μg m^{-3}) during E-PEACE was measured north of San Francisco and is coincident with the highest concentrations of Si [*Wang et al.*, 2014], which may imply continental influence. Given that these air masses were transported over heavily forested regions (see back trajectories, Figure 12), it is likely that these enhancements result from biogenic sources.

Formate concentrations are more variable than those of acetate and are enhanced both north (0.12 μg m^{-3}) and south (0.15 μg m^{-3}) of San Francisco. Enhancement of formate to the north is likely due to impacts from continental sources given the high correlation with acetate. Enhancements of formate to the south could be the result of anthropogenic influence, however, this is unlikely given poor correlation with typical anthropogenic tracers such as vanadium, iron, nitrate, and sulfate [*Sorooshian et al.*, 2013].

Given a lack of evidence for strong anthropogenic impacts on cloud water formate, enhancement of formate at lower latitudes is consistent with aqueous phase processing. *Sorooshian et al.* [2013] found that cloud water samples to the south exhibited higher fractions of oxalate, a typical end product of aqueous phase oxidation. Similarly, the cloud water acetate to formate ratio, which is proposed to be a proxy for the relative impact of fresh emissions (higher values) to secondary production from cloud processing (lower values) [*Talbot et al.*, 1988; *Wang et al.*, 2007], exhibits a latitudinal gradient consistent with fresh impacts to the north (acetate to formate ratio ≥ 1.5) and aged cloud droplets to the south (acetate to formate ratio ≤ 1). These results agree with the conclusions drawn by *Sorooshian et al.* [2013] and this study that acetate and formate have a continental source at higher latitudes.

3.5. The Potential for Biogenic Organic Aerosol to Act as CCN

The observation of a fresh continental impact on cloud water at higher latitudes and the enhancement of compounds largely derived from biogenic sources provide additional support for BOA impacts on

AGU Journal of Geophysical Research: Atmospheres 10.1002/2013JD021228

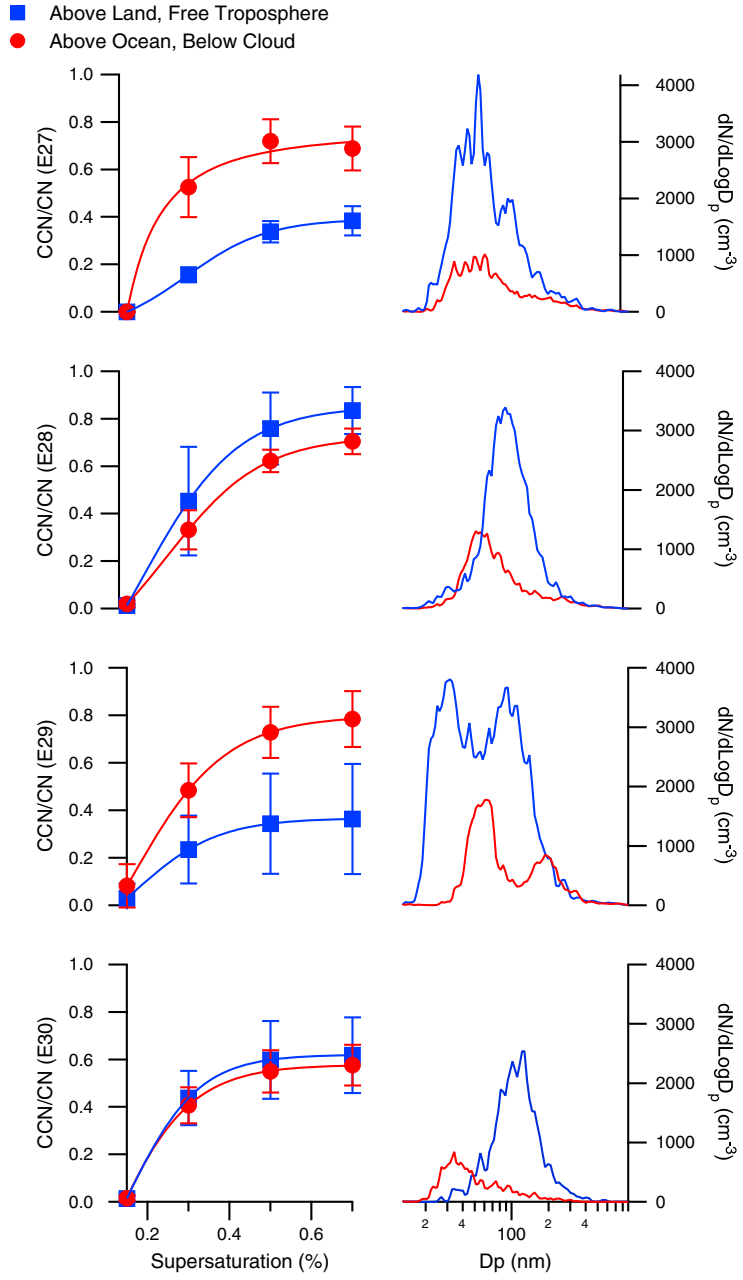

Figure 13. CCN spectra and SMPS distributions for aerosol measured over land (40° latitude) in the free troposphere (blue squares) and those measured over the ocean at 30 m (red circles). Error bars are the standard deviation in the measurement. The 100 nm mode observed in the free troposphere is consistent with that of biogenic aerosol. The appearance of a nucleation mode (~ 30 nm) likely results from fresh emissions. In the absence of chemical composition below 60 nm, we propose that this smaller mode is biogenic organic aerosol that has yet to grow to 100 nm.

Journal of Geophysical Research: Atmospheres 10.1002/2013JD021228

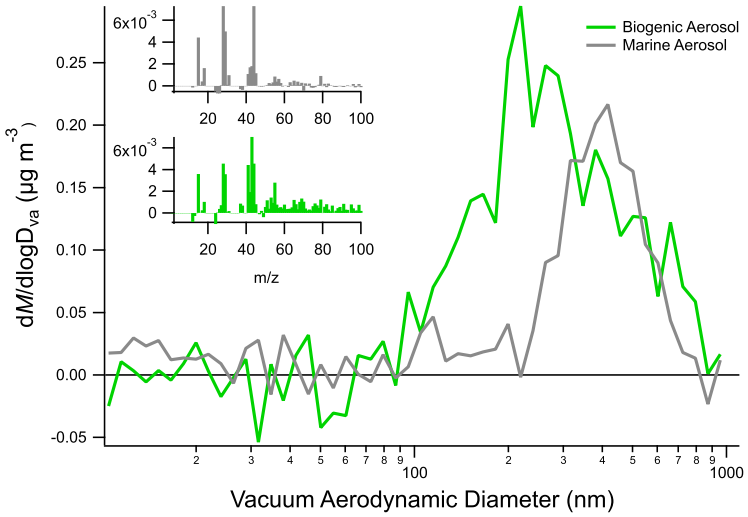

Figure 14. Organic mass distributions for *m/z* 43 (continental biogenic aerosol) and *m/z* 44 (marine aerosol), respectively, from flight E29. The corresponding mass spectra at the distribution peak are shown.

stratocumulus north of San Francisco. We can evaluate the CCN potential of BOA relative to other marine sources by comparing CCN and size distribution measurements of BOA in the free troposphere to those of subcloud marine aerosol (Figure 13). The size distribution of aerosol in the free troposphere is variable; flight E27 and E29 exhibit a bimodal distribution, whereas flight E28 and E30 each show a single mode. The larger peak at 100 nm appears to be consistent with biogenic SOA, a conclusion supported by the mass size distribution and size-resolved mass spectra measured by the AMS. Figure 14 shows organic mass size distributions of *m/z* 43 and *m/z* 44 for aerosol measured in the free troposphere and marine boundary layer, respectively, during E29. Note that particle sizes measured by the AMS are reported as vacuum aerodynamic diameters, which are typically larger than electrical mobility diameters measured by the SMPS by a factor corresponding to the particle density. The mass distributions in Figure 14 correspond to the larger mode aerosol, given that the mode below 100 nm lies outside the 100% transmission range (60 nm < D_{va} < 600 nm) of the AMS and accounts for only a small fraction of the total mass. The corresponding mass spectra at the distribution peaks are shown. The organic mass spectrum of the free tropospheric aerosol distribution is consistent with that of the continental factor, whereas, for comparison, the organic mass spectrum of the subcloud aerosol distribution is consistent with the marine factor. Thus, we conclude that the 100 nm mode in Figure 13 is primarily that of biogenic aerosol.

The BOA signature, as shown previously, is mostly organic. Previous field studies and chamber experiments have shown that organic aerosol originating from continental biogenic precursors may effectively act as CCN [*Shantz et al.*, 2008, 2010; *Lambe et al.*, 2011; *Pierce et al.*, 2012; *Ruehl et al.*, 2012; *Tang et al.*, 2012]. While organic aerosol often exhibits lower CCN activity relative to inorganic aerosol, the CCN activity of organics varies widely depending on the source or organic composition, such as the oxygen to carbon ratio [*Lambe et al.*, 2011; *Kuwata et al.*, 2013; *Wonaschütz et al.*, 2013]. For example, *Ruehl et al.* [2012] have shown that products from α-pinene ozonolysis reduce the surface tension of NaCl particles by 50–75%, implying that surface active products may enhance water uptake in certain aerosols. *Wonaschütz et al.* [2013] found that in the study region examined here, initially hydrophobic organics emitted from an ocean vessel yielded higher CCN after atmospheric aging.

Disregarding the smaller modes in Figure 13 for the moment, the CCN behavior of BOA can be inferred from the properties of the continental aerosol from flights E28 and E30, which exhibited a single, biogenic-influenced mode. BOA typically has an Org/SO_4 ratio > 3, whereas marine aerosol below cloud has an Org/SO_4 ratio ~ 1 (Figure2). Aerosol with a large fraction of inorganic substituents, such as subcloud marine aerosol, typically activate with greater efficiency, yet here we observe that BOA has a similar CCN activation spectrum as aerosol measured below cloud. These similarities are likely due to size effects.

Journal of Geophysical Research: Atmospheres 10.1002/2013JD021228

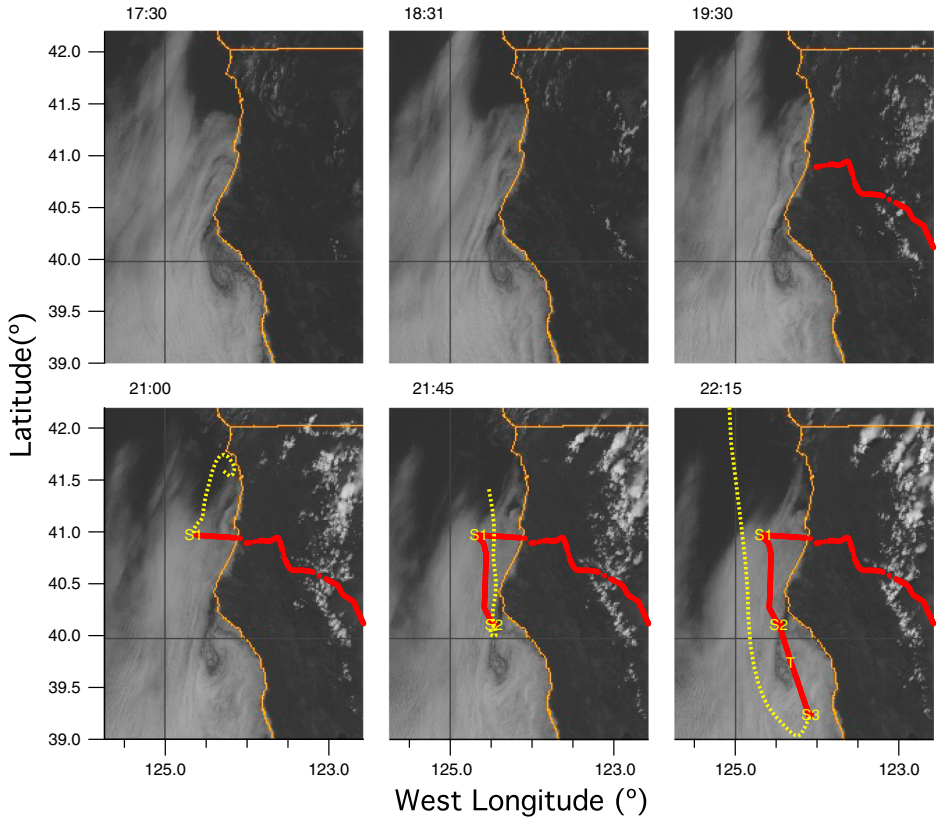

Figure 15. Time lapse showing the evolution of marine stratocumulus during flight N15 (26 July 2013). The time (UTC) above each panel indicates when the satellite image was recorded. The red trace is the Twin Otter flight path, and the labels S1, S2, and S3 indicate the location of a vertical spiral designed to sample a localized profile of marine aerosol. The area void of clouds (referred to as a plume of dry air) originated from the continent and moved south as time elapsed. Point T was a period where the Twin Otter briefly sampled aerosol above cloud top within the plume. The dotted yellow lines are 24 h back trajectories ending at the location of each spiral.

Calculations of the hygroscopicity parameter κ according to the procedure by *Moore et al.* [2011] indicates that BOA from flights E28 and E30 had κ of 0.08–0.12, which is consistent with BOA $\kappa \sim 0.1$ measured previously [*Engelhart et al.*, 2011; *Lambe et al.*, 2011; *Pierce et al.*, 2012; *Tang et al.*, 2012]. Marine aerosol below cloud exhibited κ of 0.15–0.58, which is expected to vary greatly depending on the sources affecting marine aerosol [*Pringle et al.*, 2010]. Given that BOA is less hygroscopic than particles within the marine boundary layer, it leads to reason that both sources have comparable CCN activation spectra because BOA had larger diameters than marine aerosol (Figure 13). These data suggest that the 100 nm mode observed in continental BOA could compete with marine CCN and impact the properties of marine stratocumulus in regions with enhanced entrainment.

The lower CCN fraction measured during flights E27 and E29 relative to flights E28 and E30 results from the presence of the 30 nm mode, which encompasses particles below the critical size for activation. This is clear because not all of the particles in the 100 nm mode act as CCN (see CCN spectra for flights E28 and E30, Figure 13). The 30 nm mode observed during flights E27 and E29 likely evolved from recently nucleated particles. Given that vegetation is prominent above 40° latitude, one possibility is that this mode is BOA that has yet to grow to 100 nm. Monoterpenes are suspected to play a major role in the growth of nucleated particles in coniferous forests given that these species are the major VOCs emitted by trees in these regions [*Laaksonen et al.*, 2011; *Yli-Juuti et al.*, 2011; *Riipinen et al.*, 2012]. For example, *Yli-Juuti et al.* [2011] found that seasonal variations in the growth rates of nucleated particles in Hyytiälä, Finland were strongly dependent

Journal of Geophysical Research: Atmospheres 10.1002/2013JD021228

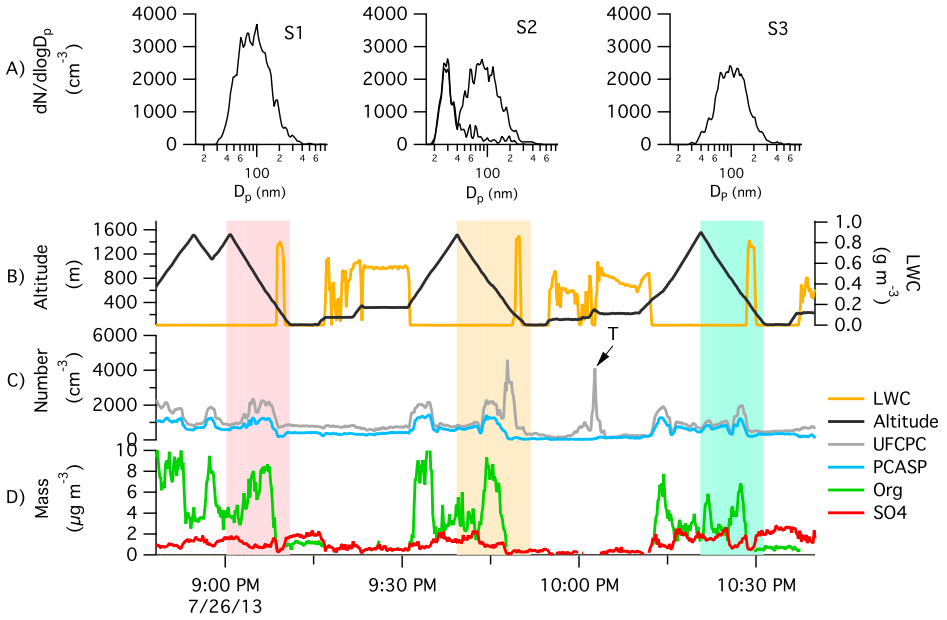

Figure 16. Summary of data from N15 corresponding to the flight path shown in Figure 15. (row a) Size distributions from each spiral (S1, S2, and S3). (row b)) Altitude and liquid water content (LWC). (row c) PCASP and ultrafine CPC (UFCPC) measurements. (row d) AMS measurements summarizing aerosol composition. Regions colored red, orange, and green correspond to S1, S2, and S3, respectively. PCASP concentrations apply to aerosol with diameters ≥ 100 nm, whereas UFCPC concentrations apply to aerosol with diameters ≥ 2 nm; thus, enhancements in UFCPC relative to PCASP are indications of enhanced concentrations of sub-100 nm small particles.

on the concentrations of monoterpenes. The composition of BOA measured here is most consistent with organic aerosol measured previously from boreal forests (section 3.2), implying that biogenic SOA likely impacts the 30 nm mode observed in this study.

The 30 nm mode is of particular interest because if it is transported into the marine environment, it could modulate cloud water chemistry via cloud scavenging or activate to cloud droplets if the particles grow to CCN sizes, thus influencing the microphysical properties of marine stratocumulus. Biogenic nucleation events from boreal forests in North America have been shown to yield CCN [e.g., *O'Dowd et al.*, 2009; *Creamean et al.*, 2011; *Kerminen et al.*, 2012; *Pierce et al.*, 2012] and may significantly impact the CCN budget in clean air masses [*Spracklen et al.*, 2008]. Given the predominant biogenic signature in continental aerosol transported to the marine atmosphere (section 3.3), it leads to the question whether particles in the 30 nm mode survive scavenging and impact the aerosol budget above marine stratocumulus.

Flight N15 afforded an opportunity to sample continental aerosol over the marine boundary layer close to the emission source when a small-scale dry plume developed near Cape Mendocino, CA (Figure 15). Three spirals and one vertical slant were conducted to sample the vertical profile of aerosol properties within (S2, T) and outside (S1, S3) of this dry plume (Figure 16). Spiral S1 was conducted north of the plume and exhibited an Org/SO_4 ratio typical of BOA above marine stratocumulus. The number size distribution exhibits a single, 100 nm mode. Furthermore, the difference between PCASP ($D_p \geq 100$ nm) and ultrafine CPC (UFCPC, $D_p \geq 2$ nm) number concentrations was small, implying that the diameters of most particles during S1 exceeded 100 nm. When the Twin Otter spiraled through the dry plume (S2), an enhancement in UFCPC appears relative to PCASP, indicating the presence of sub-100 nm particles. The number size distribution during S2 exhibits a bimodal distribution with a prominent sub-100 nm mode. At point "T," the Twin Otter briefly sampled aerosol above cloud within the dry plume and again observed an enhancement in UFCPC relative to PCASP. Measurements to the south of plume (S3) were similar to those to the north (S1).

These results indicate that the plume event observed during N15 contained small particles that could have nucleated from secondary processes. We suspect that more extensive plume events could transport

AGU Journal of Geophysical Research: Atmospheres 10.1002/2013JD021228

nucleated particles over a wide area of the marine atmosphere (Figure 8). Though we cannot deduce the extent to which these particles grow to the larger, CCN-active continental mode (100 nm), their presence above cloud is notable, and future studies might consider the role these particles play in modulating the chemical or physical properties of marine stratocumulus.

4. Conclusions

Organic aerosol layers above marine stratocumulus off the California coast are observed to originate from northwest United States continental sources. Positive matrix factorization analysis resolved a semivolatile oxygenated organic aerosol (SV-OOA) factor with a mass spectrum and spatial distribution consistent with organic aerosol derived from biogenic precursors. This biogenic organic aerosol (BOA) exhibits a latitudinal gradient that corresponds to changes in both vegetation density and forest composition. Summertime meteorological conditions induce offshore flow of continental air; subsequently, BOA is transported into the free troposphere via a plume of dry air and impacts aerosol over marine stratocumulus. Close to the plume source, we observe small particles that appear to be indicative of new particle formation, consistent with previous observations of nucleation events in North American coniferous forests [*O'Dowd et al.*, 2009; *Creamean et al.*, 2011; *Kerminen et al.*, 2012; *Pierce et al.*, 2012]. The measured vertical profile of meteorological variables indicates that BOA can be entrained into marine stratocumulus. This observations is supported by cloud water measurements that show a gradient in the acetate:formate ratio, which is a relative measure of the impacts of fresh emissions to secondary processes such as aqueous phase oxidation.

Sea spray, shipping exhaust, marine biota, biomass burning, anthropogenic sources, and continental dust all impact marine stratocumulus [*Roberts et al.*, 2006; *Straub et al.*, 2007; *Sorooshian et al.*, 2009; *Hersey et al.*, 2009; *Hegg et al.*, 2009, 2010; *Langley et al.*, 2010; *Benedict et al.*, 2012; *Coggon et al.*, 2012]. Here we show that relatively long-range transport of continental biogenic aerosol can also impact marine stratocumulus. BOA CCN activation spectra are comparable to those of boundary layer marine aerosol and is slightly hygroscopic ($\kappa \sim 0.1$); thus, it follows that this source can influence cloud microphysics in regions with entrainment.

Acknowledgments

This work was funded by ONR grants N00014-11-1-0783, N00014-14-1-0097, and N00014-10-1-0811, and NSF grants AGS-1008848 and AGS-1013381. A.N. acknowledges support from an NSF CAREER award. J.J.L. acknowledges support from a Georgia Tech President's fellowship and a NASA Graduate Student Researchers Program Fellowship. Conclusions drawn here reflect those of the authors and do not necessarily reflect the opinions of the Office of Naval Research or the National Science Foundation. We acknowledge Dean Hegg for providing the cloud water collector and Joseph Ensberg for helpful discussion. Please contact corresponding author for data requests. AMS mass spectra will be uploaded to the spectral database (http://cires.colorado.edu/jimenez-group/AMSsd/).

References

Adler, G., J. M. Flores, A. Abo Riziq, S. Borrmann, and Y. Rudich (2011), Chemical, physical, and optical evolution of biomass burning aerosols: A case study, *Atmos. Chem. Phys.*, *11*(4), 1491–1503, doi:10.5194/acp-11-1491-2011.

Aiken, A. C., et al. (2008), O/C and OM/OC ratios of primary, secondary, and ambient organic aerosols with high-resolution time-of-flight aerosol mass spectrometry, *Environ. Sci. Technol.*, *42*(12), 4478–4485, doi:10.1021/es703009q.

Alfarra, M. R., A. S. H. Prevot, S. Szidat, J. Sandradewi, S. Weimer, V. A. Lanz, D. Schreiber, M. Mohr, and U. Baltensperger (2007), Identification of the mass spectral signature of organic aerosols from wood burning emissions, *Environ. Sci. Technol.*, *41*(16), 5770–5777, doi:10.1021/es062289b.

Allan, J., et al. (2004a), A generalised method for the extraction of chemically resolved mass spectra from Aerodyne aerosol mass spectrometer data, *J. Aerosol Sci.*, *35*(7), 909–922, doi:10.1016/j.jaerosci.2004.02.007.

Allan, J., et al. (2004b), Submicron aerosol composition at Trinidad Head, California, during ITCT 2K2: Its relationship with gas phase volatile organic carbon and assessment of instrument performance, *J. Geophys. Res.*, *109*, D23S24, doi:10.1029/2003JD004208.

Asa-Awuku, A., G. J. Engelhart, B. H. Lee, S. N. Pandis, and A. Nenes (2009), Relating CCN activity, volatility, and droplet growth kinetics of β-caryophyllene secondary organic aerosol, *Atmos. Chem. Phys.*, *9*(3), 795–812, doi:10.5194/acp-9-795-2009.

Baumgardner, D., et al. (2012), Soot reference materials for instrument calibrations and comparisons, *Atmos. Meas. Tech.*, *5*, 2315–2362, doi:10.5194/amt-5-1869-2012.

Benedict, K. B., T. Lee, and J. L. Collett Jr. (2012), Cloud water composition over the southeastern Pacific Ocean during the VOCALS regional experiment, *Atmos. Environ.*, *46*(C), 104–114, doi:10.1016/j.atmosenv.2011.10.029.

Cahill, T. M., V. Y. Seaman, M. J. Charles, R. Holzinger, and A. H. Goldstein (2006), Secondary organic aerosols formed from oxidation of biogenic volatile organic compounds in the Sierra Nevada Mountains of California, *J. Geophys. Res.*, *111*, D16312, doi:10.1029/2006JD007178.

Carlton, A. G., B. J. Turpin, H. J. Lim, K. E. Altieri, and S. Seitzinger (2006), Link between isoprene and secondary organic aerosol (SOA): Pyruvic acid oxidation yields low volatility organic acids in clouds, *Geophys. Res. Lett.*, *33*, L06822, doi:10.1029/2005GL025374.

Carlton, A. G., B. J. Turpin, K. E. Altieri, S. Seitzinger, A. Reff, H.-J. Lim, and B. Ervens (2007), Atmospheric oxalic acid and SOA production from glyoxal: Results of aqueous photooxidation experiments, *Atmos. Environ.*, *41*(35), 7588–7602, doi:10.1016/j.atmosenv.2007.05.035.

Chang, R. Y. W., et al. (2011), Aerosol composition and sources in the central Arctic Ocean during ASCOS, *Atmos. Chem. Phys.*, *11*(20), 10,619–10,636, doi:10.5194/acp-11-10619-2011.

Coggon, M. M., et al. (2012), Ship impacts on the marine atmosphere: Insights into the contribution of shipping emissions to the properties of marine aerosol and clouds, *Atmos. Chem. Phys.*, *12*, 8439–8458, doi:10.5194/acp-12-8439-2012.

Craven, J. S., et al. (2013), Los Angeles Basin airborne organic aerosol characterization during CalNex, *J. Geophys. Res. Atmos.*, *118*, 11,453–11,467, doi:10.1002/jgrd.50853.

Creamean, J. M., A. P. Ault, J. E. Ten Hoeve, M. Z. Jacobson, and G. C. Roberts (2011), Measurements of aerosol chemistry during new particle formation events at a remote rural mountain site, *Environ. Sci. Technol.*, *45*, 8208–8216, doi:10.1021/es103692f.

Crippa, P., and S. C. Pryor (2013), Spatial and temporal scales of new particle formation events in eastern North America, *Atmos. Environ.*, *75*(C), 257–264, doi:10.1016/j.atmosenv.2013.04.051.

Draxler, R., and G. Rolph (2012), Hysplit (Hybrid Single-Particle Lagrangian Integrated Trajectory) model access via NOAA ARL ready website.

AGU Journal of Geophysical Research: Atmospheres 10.1002/2013JD021228

Drewnick, F., et al. (2005), A new time-of-flight aerosol mass spectrometer (TOF-AMS)—Instrument description and first field deployment, *Aerosol Sci. Technol.*, *39*(7), 637–658, doi:10.1080/02786820500182040.

Durkee, P. A., K. J. Noone, and R. T. Bluth (2000), The Monterey area ship track experiment, *J. Atmos. Sci.*, *57*, 2523–2541, doi:10.1175/1520-0469(2000)057<2523:TMASTE>2.0.CO;2.

Eddingsaas, N. C., C. L. Loza, L. D. Yee, J. H. Seinfeld, and P. O. Wennberg (2012), α-pinene photooxidation under controlled chemical conditions—Part 1: Gas-phase composition in low- and high-NO_x environments, *Atmos. Chem. Phys.*, *12*(14), 6489–6504, doi:10.5194/acp-12-6489-2012.

Ehn, M., et al. (2014), A large sources of low-volatility secondary organic aerosol, *Nature*, *506*, 476–479, doi:10.1038/nature13032.

Elsasser, M., et al. (2012), Organic molecular markers and signature from wood combustion particles in winter ambient aerosols: Aerosol mass spectrometer (AMS) and high time-resolved GC-MS measurements in Augsburg, Germany, *Atmos. Chem. Phys.*, *12*(14), 6113–6128, doi:10.5194/acp-12-6113-2012.

Engelhart, G. J., R. H. Moore, A. Nenes, and S. N. Pandis (2011), Cloud condensation nuclei activity of isoprene secondary organic aerosol, *J. Geophys. Res.*, *116*, D02207, doi:10.1029/2010JD014706.

Ensberg, J. J., et al. (2014), Emission factor ratios, SOA mass yields, and the impact of vehicular emissions on SOA formation, *Atmos. Chem. Phys.*, *14*, 2383–2397, doi:10.5194/acp-14-2383-2014.

Ervens, B., P. Herckes, G. Feingold, T. Lee, J. L. Collett, and S. M. Kreidenweis (2003), On the drop-size dependence of organic acid and formaldehyde concentrations in fog, *J. Atmos. Chem.*, *46*(3), 239–269, doi:10.1023/A:1026393805907.

Facchini, M. C., et al. (2008), Primary submicron marine aerosol dominated by insoluble organic colloids and aggregates, *Geophys. Res. Lett.*, *35*, L17814, doi:10.1029/2008GL034210.

Frick, G., and W. Hoppel (2000), Airship measurements of ship's exhaust plumes and their effect on marine boundary layer clouds, *J. Atmos. Sci.*, *57*, 2625–2648, doi:10.1175/1520-0469(2000)057<2625:AMOSSE>2.0.CO;2.

Frosch, M., M. Bilde, A. Nenes, A. P. Praplan, Z. Jurányi, J. Dommen, M. Gysel, E. Weingartner, and U. Baltensperger (2013), CCN activity and volatility of β-caryophyllene secondary organic aerosol, *Atmos. Chem. Phys.*, *13*(4), 2283–2297, doi:10.5194/acp-13-2283-2013.

Garbariene, I., K. Kvietkus, J. Šakalys, J. Ovadnevaitė, and D. Ceburnis (2012), Biogenic and anthropogenic organic matter in aerosol over continental Europe: Source characterization in the east Baltic region, *J. Atmos. Chem.*, *69*(2), 159–174, doi:10.1007/s10874-012-9232-7.

Gaston, C. J., K. A. Pratt, X. Qin, and K. A. Prather (2010), Real-time detection and mixing state of methanesulfonate in single particles at an inland urban location during phytoplankton bloom, *Environ. Sci. Technol.*, *44*, 1566–1572, doi:10.1021/es902069d.

Gentner, D. R., et al. (2012), Elucidating secondary organic aerosol from diesel and gasoline vehicles through detailed characterization of organic carbon emissions, *Proc. Nat. Acad. Sci.*, *109*(45), 18,318–18,323, doi:10.1073/pnas.1212272109.

Geron, C., R. Rasmussen, R. R. Arnts, and A. Guenther (2000), A review and synthesis of monoterpene speciation from forests in the United States, *Atmos. Environ.*, *34*, 1761–1781, doi:10.1016/S1352-2310(99)00364-7.

Guenther, A., et al. (1995), A global model of natural volatile organic compound emissions, *J. Geophys. Res.*, *100*, 8873–8892, doi:10.1029/94JD02950.

Gunthe, S. S., et al. (2009), Cloud condensation nuclei in pristine tropical rainforest air of Amazonia: Size-resolved measurements and modeling of atmospheric aerosol composition and CCN activity, *Atmos. Chem. Phys.*, *9*(19), 7551–7575, doi:10.5194/acp-9-7551-2009.

Han, Y., Y. Iwamoto, T. Nakayama, K. Kawamura, and M. Mochida (2014), Formation and evolution of biogenic secondary organic aerosol over a forest site in Japan, *J. Geophys. Res. Atmos.*, *119*, 259–273, doi:10.1002/2013JD020390.

Hegg, D. A., and P. V. Hobbs (1986), Sulfate and nitrate chemistry in cumuliform clouds, *Atmos. Environ.*, *20*(5), 901–909, doi:10.1016/0004-6981(86)90274-X.

Hegg, D., D. Covert, H. Jonsson, and P. Covert (2005), Determination of the transmission efficiency of an aircraft aerosol inlet, *Aerosol Sci. Technol.*, *39*(10), 966–971, doi:10.1080/02786820500377814.

Hegg, D., D. Covert, H. Jonsson, and R. Woods (2009), Differentiating natural and anthropogenic cloud condensation nuclei in the California coastal zone, *Tellus B*, *61*(4), 669–676, doi:10.1111/j.1600-0889.2009.00435.x.

Hegg, D., D. Covert, H. Jonsson, and R. Woods (2010), The contribution of anthropogenic aerosols to aerosol light-scattering and CCN activity in the California coastal zone, *Atmos. Chem. Phys.*, *10*, 7341–7351, doi:10.5194/acp-10-7341-2010.

Hersey, S., A. Sorooshian, S. M. Murphy, R. Flagan, and J. H. Seinfeld (2009), Aerosol hygroscopicity in the marine atmosphere: A closure study using high-time-resolution, multiple-RH DASH-SP and size-resolved C-ToF-AMS data, *Atmos. Chem. Phys.*, *9*, 2543–2554, doi:10.5194/acp-9-2543-2009.

Hersey, S., J. S. Craven, K. A. Schilling, A. R. Metcalf, A. Sorooshian, M. N. Chan, R. Flagan, and J. H. Seinfeld (2011), The Pasadena Aerosol Characterization Observatory (PACO): Chemical and physical analysis of the Western Los Angeles basin aerosol, *Atmos. Chem. Phys.*, *11*(15), 7417–7443, doi:10.5194/acp-11-7417-2011.

Hildebrandt, L., E. Kostenidou, V. A. Lanz, A. S. H. Prévôt, U. Baltensperger, N. Mihalopoulos, A. Laaksonen, N. M. Donahue, and S. N. Pandis (2011), Sources and atmospheric processing of organic aerosol in the Mediterranean: Insights from aerosol mass spectrometer factor analysis, *Atmos. Chem. Phys.*, *11*(23), 12,499–12,515, doi:10.5194/acpd-11-19639-2011.

Holzinger, R., A. Lee, K. T. Paw, and U. A. H. Goldstein (2005), Observations of oxidation products above a forest imply biogenic emissions of very reactive compounds, *Atmos. Chem. Phys.*, *5*, 67–75, doi:10.5194/acp-5-67-2005.

Hudson, J. G., T. J. Garrett, P. V. Hobbs, S. R. Strader, Y. Xie, and S. S. Yum (2000), Cloud condensation nuclei and ship tracks, *J. Atmos. Sci.*, *57*, 2696–2706, doi:10.1175/1520-0469(2000)057<2696:CCNAST>2.0.CO;2.

Jayne, J. T., D. C. Leard, X. Zhang, P. Davidovits, K. A. Smith, C. E. Kolb, and D. R. Worsnop (2000), Development of an Aerosol Mass Spectrometer for size and composition analysis of submicron particles, *Aerosol Sci. Technol.*, *33*(1), 49–70, doi:10.1080/027868200410840.

Keene, W. C., et al. (2007), Chemical and physical characteristics of nascent aerosols produced by bursting bubbles at a model air-sea interface, *J. Geophys. Res.*, *112*, D21202, doi:10.1029/2007JD008464.

Kerminen, V. M., et al. (2012), Cloud condensation nuclei production associated with atmospheric nucleation: A synthesis based on existing literature and new results, *Atmos. Chem. Phys.*, *12*(24), 12,037–12,059, doi:10.5194/acp-12-12037-2012.

Kiendler-Scharr, A., Q. Zhang, T. Hohaus, E. Kleist, A. Mensah, T. F. Mentel, C. Spindler, R. Uerlings, R. Tillmann, and J. Wildt (2009), Aerosol mass spectrometric features of biogenic SOA: Observations from a plant chamber and in rural atmospheric environments, *Environ. Sci. Technol.*, *43*, 8166–8172, doi:10.1021/es901420b.

King, S. M., T. Rosenoern, J. E. Shilling, Q. Chen, Z. Wang, G. Biskos, K. A. McKinney, U. Poschl, and S. T. Martin (2010), Cloud droplet activation of mixed organic-sulfate particles produced by the photooxidation of isoprene, *Atmos. Chem. Phys.*, *10*(8), 3953–3964, doi:10.5194/acp-10-3953-2010.

Kloesel, K. A. (1992), Marine stratocumulus cloud clearing episodes observed during FIRE, *Mon. Weather Rev.*, *120*, 565–578, doi:10.1175/1520-0493(1992)120<0565:MSCCEO>2.0.CO;2.

AGU Journal of Geophysical Research: Atmospheres 10.1002/2013JD021228

Koracin, D., and C. E. Dorman (2001), Marine atmospheric boundary layer divergence and clouds along California in June 1996, *Mon. Weather Rev.*, *129*, 2040–2056, doi:10.1175/1520-0493(2001)129<2040:MABLDA>2.0.CO;2.
Kuwata, M., W. Shao, R. Lebouteiller, and S. T. Martin (2013), Classifying organic materials by oxygen-to-carbon elemental ratio to predict the activation regime of Cloud Condensation Nuclei (CCN), *Atmos. Chem. Phys.*, *13*(10), 5309–5324, doi:10.5194/acp-13-5309-2013.
Laaksonen, A., et al. (2011), The role of VOC oxidation products in continental new particle formation, *Atmos. Chem. Phys.*, *8*, 2657–2665, doi:10.5194/acp-8-2657-2008.
Laborde, M. P., P. Mertes, P. Zieger, J. Dommen, U. Baltensperger, and M. Gysel (2012), Sensitivity of the single particle soot photometer to different black carbon types, *Atmos. Meas. Tech.*, *5*, 663–690, doi:10.5194/amtd-5-663-2012.
Lambe, A. T., et al. (2011), Laboratory studies of the chemical composition and cloud condensation nuclei (CCN) activity of secondary organic aerosol (SOA) and oxidized primary organic aerosol (OPOA), *Atmos. Chem. Phys.*, *11*(17), 8913–8928, doi:10.5194/acp-11-8913-2011.
Lance, S., A. Nenes, J. Medina, and J. N. Smith (2006), Mapping the operation of the DMT continuous flow CCN counter, *Aerosol Sci. Technol.*, *40*(4), 242–254, doi:10.1080/02786820500543290.
Langley, L., W. Leaitch, U. Lohmann, N. Shantz, and D. Worsnop (2010), Contributions from DMS and ship emissions to CCN observed over the summertime North Pacific, *Atmos. Chem. Phys.*, *10*, 1287–1314, doi:10.5194/acp-10-1287-2010.
Li, W., L. Li, M. Ting, and Y. Liu (2012), Intensification of Northern Hemisphere subtropical highs in a warming climate, *Nat. Geosci.*, *8*, 830–834, doi:10.1038/ngeo1590.
Lim, Y. B., Y. Tan, and B. J. Turpin (2013), Chemical insights, explicit chemistry, and yields of secondary organic aerosol from OH radical oxidation of methylglyoxal and glyoxal in the aqueous phase, *Atmos. Chem. Phys.*, *13*(17), 8651–8667, doi:10.5194/acp-13-8651-2013.
Lu, M.-L., A. Sorooshian, H. H. Jonsson, G. Feingold, R. C. Flagan, and J. H. Seinfeld (2009), Marine stratocumulus aerosol-cloud relationships in the MASE-II experiment: Precipitation susceptibility in eastern Pacific marine stratocumulus, *J. Geophys. Res.*, *114*, D24203, doi:10.1029/2009JD012774.
McInnes, L., D. Covert, and B. Baker (1997), The number of sea-salt, sulfate, and carbonaceous particles in the marine atmosphere:, *Tellus*, *49*(B), 300–313, doi:10.1034/j.1600-0889.49.issue3.6.x.
Metcalf, A. R., et al. (2012), Black carbon aerosol over the Los Angeles Basin during CalNex, *J. Geophys. Res.*, *117*, D00V13, doi:10.1029/2011JD017255.
Mohr, C., et al. (2012), Identification and quantification of organic aerosol from cooking and other sources in Barcelona using aerosol mass spectrometer data, *Atmos. Chem. Phys.*, *12*(4), 1649–1665, doi:10.5194/acp-12-1649-2012.
Moore, R. H., and A. Nenes (2009), Scanning flow CCN analysis—A method for fast measurements of CCN spectra, *Aerosol Sci. Technol.*, *43*(12), 1192–1207, doi:10.1080/02786820903289780.
Moore, R. H., R. Bahreini, C. A. Brock, K. D. Froyd, J. Cozic, J. S. Holloway, A. M. Middlebrook, D. M. Murphy, and A. Nenes (2011), Hygroscopicity and composition of Alaskan Arctic CCN during April 2008, *Atmos. Chem. Phys.*, *11*(22), 11,807–11,825, doi:10.5194/acp-11-11807-2011.
Moore, R. H., K. Cerully, R. Bahreini, C. A. Brock, A. M. Middlebrook, and A. Nenes (2012), Hygroscopicity and composition of California CCN during summer 2010, *J. Geophys. Res.*, *117*, D00V12, doi:10.1029/2011JD017352.
Murphy, S. H., et al. (2009), Comprehensive simultaneous shipboard and airborne characterization of exhaust from a modern container ship at sea, *Environ. Sci. Technol.*, *43*(13), 4626–4640, doi:10.1021/es802413j.
Ng, N. L., et al. (2010), Organic aerosol components observed in Northern Hemisphere datasets from Aerosol Mass Spectrometery, *Atmos. Chem. Phys.*, *10*, 4625–4641, doi:10.5194/acp-10-4625-2010.
Ng, N. L., M. Canagaratna, J. L. Jimenez, Q. Zhang, I. Ulbrich, and D. Worsnop (2011), Real-time methods for estimating organic component mass concentrations from Aerosol Mass Spectrometer data, *Environ. Sci. Technol.*, *45*(3), 910–916, doi:10.1021/es102951k.
Novakov, T., S. Menon, and T. W. Kirchstetter (2005), Aerosol organic carbon to black carbon ratios: Analysis of published data and implications for climate forcing, *J. Geophys. Res.*, *110*, D21205, doi:10.1029/2005JD00597.
O'Dowd, C., et al. (2004), Biogenically driven organic contribution to marine aerosol, *Nature*, *431*, 676–680, doi:10.1038/nature02959.
O'Dowd, C., Y. J. Yoon, W. Junkermann, P. Aalto, M. Kulmala, H. Lihavainen, and Y. Viisanen (2009), Airborne measurements of nucleation mode particles II: Boreal forest nucleation events, *Atmos. Chem. Phys.*, *9*, 937–944, doi:10.5194/acp-9-937-2009.
Orlando, J. J., B. Noziere, G. S. Tyndall, G. E. Orzechowska, S. E. Paulson, and Y. Rudich (2000), Product studies of the OH- and ozone-initiated oxidation of some monoterpenes, *J. Geophys. Res.*, *105*, 11,561–11,572, doi:10.1029/2000JD900005.
Ovadnevaite, J., C. O'Dowd, M. Dall'Osto, D. Ceburnis, D. R. Worsnop, and H. Berresheim (2011), Detecting high contributions of primary organic matter to marine aerosol: A case study, *Geophys. Res. Lett.*, *38*, L02807, doi:10.1029/2010GL046083.
Paatero, P. (2007), *User's Guide for Positive Matrix Factorization Programs PMF2.EXE and PMF3.EXE*, University of Helsinki, Finland.
Paatero, P., and U. Tapper (1994), Positive Matrix Factorization: A non-negative factor model with optimal utilization of error estimates of data values, *Environmetrics*, *5*, 111–126, doi:10.1002/env.3170050203.
Paulot, F., et al. (2011), Importance of secondary sources in the atmospheric budgets of formic and acetic acids, *Atmos. Chem. Phys.*, *11*(5), 1989–2013, doi:10.5194/acp-11-1989-2011.
Pierce, J. R., et al. (2012), Nucleation and condensational growth to CCN sizes during a sustained pristine biogenic SOA event in a forested mountain valley, *Atmos. Chem. Phys.*, *12*(7), 3147–3163, doi:10.5194/acp-12-3147-2012.
Poulain, L., Z. Wu, M. D. Petters, H. Wex, E. Hallbauer, B. Wehner, A. Massling, S. M. Kreidenweis, and F. Stratmann (2010), Towards closing the gap between hygroscopic growth and CCN activation for secondary organic aerosols–Part 3: Influence of the chemical composition on the hygroscopic properties and volatile fractions of aerosols, *Atmos. Chem. Phys.*, *10*(8), 3775–3785, doi:10.5194/acp-10-3775-2010.
Prather, K. A., et al. (2013), Bringing the ocean into the laboratory to probe the chemical complexity of sea spray aerosol, *Proc. Nat. Acad. Sci.*, *110*(19), 7550–7555, doi:10.1073/pnas.1300262110.
Pringle, K. J., H. Tost, A. Pozzer, U. Poschl, and J. Lelieveld (2010), Global distribution of the effective aerosol hygroscopicity parameter for CCN activation, *Atmos. Chem. Phys.*, *10*(12), 5241–5255, doi:10.5194/acp-10-5241-2010.
Riipinen, I., T. Yli-Juuti, J. R. Pierce, T. Petäjä, D. R. Worsnop, M. Kulmala, and N. M. Donahue (2012), The contribution of organics to atmospheric nanoparticle growth, *Nat. Geosci.*, *5*(7), 453–458, doi:10.1038/ngeo1499.
Roberts, G., G. Mauger, O. Hadley, and V. Ramanathan (2006), North American and Asian aerosols over the eastern Pacific Ocean and their role in regulating cloud condensation nuclei, *J. Geophys. Res.*, *111*, D13205, doi:10.1029/2005JD006661.
Roberts, G. C., and A. Nenes (2005), A continuous-flow streamwise thermal-gradient CCN chamber for atmospheric measurements, *Aerosol Sci. Technol.*, *39*(3), 206–221, doi:10.1080/027868290913988.
Ruehl, C. R., P. Y. Chuang, A. Nenes, C. D. Cappa, K. R. Kolesar, and A. Goldstein (2012), Strong evidence of surface tension reduction in microscopic aqueous droplets, *Geophys. Res. Lett.*, *39*, L23801, doi:10.1029/2012GL053706.

AGU Journal of Geophysical Research: Atmospheres 10.1002/2013JD021228

Russell, L. M., et al. (2013), Eastern Pacific emitted aerosol cloud experiment (E-PEACE), *Bull. Am. Meteorol. Soc.*, *94*(5), 709–729, doi:10.1175/BAMS-D-12-00015.1.

Sanhueza, E., L. Figueroa, and M. Santana (1995), Atmospheric formic and acetic acids in Venezuela, *Atmos. Environ.*, *30*, 1861–1873, doi:10.1016/1352-2310(95)00383-5.

Schobesberger, S., et al. (2013), Airborne measurements over the boreal forest of southern Finland during new particle formation events in 2009 and 2010, *Boreal Environ. Res.*, *18*(2), 145–163.

Setyan, A., et al. (2012), Characterization of submicron particles influenced by mixed biogenic and anthropogenic emissions using high-resolution aerosol mass spectrometry: Results from CARES, *Atmos. Chem. Phys.*, *12*(17), 8131–8156, doi:10.5194/acp-12-8131-2012.

Shantz, N., W. Leaitch, L. Phinney, M. Mozurkewich, and D. Toom-Sauntry (2008), The effect of organic compounds on the growth rate of cloud droplets in marine and forest settings, *Atmos. Chem. Phys.*, *8*, 5869–5887, doi:10.5194/acp-8-5869-2008.

Shantz, N., R. Y. W. Chang, J. G. Slowik, A. Vlasenko, J. P. D. Abbatt, and W. Leaitch (2010), Slower CCN growth kinetics of anthropogenic aerosol compared to biogenic aerosol observed at a rural site, *Atmos. Chem. Phys.*, *10*(1), 299–312, doi:10.5194/acp-10-299-2010.

Shilling, J. E., et al. (2013), Enhanced SOA formation from mixed anthropogenic and biogenic emissions during the CARES campaign, *Atmos. Chem. Phys.*, *13*, 2091–2113, doi:10.5194/acp-13-2091-2013.

Shingler, T., et al. (2012), Characterization and airborne deployment of a new counterflow virtual impactor, *Atmos. Meas. Tech.*, *5*, 1515–1541, doi:10.5194/amtd-5-1515-2012.

Slowik, J. G., A. Vlasenko, M. McGuire, G. J. Evans, and J. P. D. Abbatt (2010), Simultaneous factor analysis of organic particle and gas mass spectra: AMS and PTR-MS measurements at an urban site, *Atmos. Chem. Phys.*, *10*(4), 1969–1988, doi:10.5194/acp-10-1969-2010.

Sorooshian, A., N. L. Ng, A. W. H. Chan, G. Feingold, R. C. Flagan, and J. H. Seinfeld (2007), Particulate organic acids and overall water-soluble aerosol composition measurements from the 2006 Gulf of Mexico Atmospheric Composition and Climate Study (GoMACCS), *J. Geophys. Res.*, *112*, D13201, doi:10.1029/2007JD008537.

Sorooshian, A., et al. (2009), On the link between ocean biota emissions, aerosol, and maritime clouds: Airborne, ground, and satellite measurements off the coast of California, *Global Biogeochem. Cycles*, *23*, GB4007, doi:10.1029/2009GB003464.

Sorooshian, A., Z. Wang, M. M. Coggon, H. H. Jonsson, and B. Ervens (2013), Observations of sharp oxalate reductions in stratocumulus clouds at variable altitudes: Organic acid and metal measurements during the 2011 E-PEACE campaign, *Environ. Sci. Technol.*, *47*, 7747–7756, doi:10.1021/es4012383.

Spracklen, D. V., B. Bonn, and K. S. Carslaw (2008), Boreal forests, aerosols and the impacts on clouds and climate, *Philos. Trans. R. Soc. A*, *366*, 4613–4625, doi:10.1098/rsta.2008.0201.

Stavrakou, T., et al. (2011), Satellite evidence for a large source of formic acid from boreal and tropical forests, *Nat. Geosci.*, *5*(1), 26–30, doi:10.1038/ngeo1354.

Steinbrecher, R., G. Smiatek, R. Koble, G. Seufert, J. Theloke, K. Hauff, P. Ciccioli, R. Vautard, and G. Curci (2009), Intra- and inter-annual variability of VOC emissions from natural and semi-natural vegetation in Europe and neighbouring countries, *Atmos. Environ.*, *43*(7), 1380–1391, doi:10.1016/j.atmosenv.2008.09.072.

Straub, D. J., T. Lee, and J. L. Collett Jr. (2007), Chemical composition of marine stratocumulus clouds over the eastern Pacific Ocean, *J. Geophys. Res.*, *112*, D04307, doi:10.1029/2006JD007439.

Talbot, R. W., K. M. Beecher, R. C. Harriss, and W. R. Cofer III (1988), Atmospheric geochemistry of formic and acetic acids at a midlatitude temperate site, *J. Geophys. Res.*, *93*, 1638–1652, doi:10.1029/JD093iD02p01638.

Tang, X., D. R. Cocker III, and A. Asa-Awuku (2012), Are sesquiterpenes a good source of secondary organic cloud condensation nuclei (CCN)? Revisiting β-caryophyllene CCN, *Atmos. Chem. Phys.*, *12*(18), 8377–8388, doi:10.5194/acp-12-8377-2012.

Ulbrich, I., M. Canagaratna, Q. Zhang, D. Worsnop, and J. L. Jimenez (2009), Interpretation of organic components from Positive Matrix Factorization of aerosol mass spectrometric data, *Atmos. Chem. Phys.*, *9*, 2891–2918, doi:10.5194/acp-9-2891-2009.

Wang, Y., G. Zhuang, S. Chen, Z. An, and A. Zheng (2007), Characteristics and sources of formic, acetic and oxalic acids in PM2.5 and PM10 aerosols in Beijing, China, *Atmos. Res.*, *84*, 169–181, doi:10.1016/j.atmosres.2006.07.001.

Wang, Z., A. Sorooshian, G. Prabhakar, M. M. Coggon, and H. H. Jonsson (2014), Impact of emissions from shipping, land, and the ocean on stratocumulus cloud water elemental composition during the 2011 E-PEACE field campaign, *Atmos. Environ.*, *89*, 570–580, doi:10.1016/j.atmosenv.2014.01.020.

Westervelt, D. M., J. R. Pierce, I. Riipinen, W. Trivitayanurak, A. Hamed, M. Kulmala, A. Laaksonen, S. Decesari, and P. J. Adams (2013), Formation and growth of nucleated particles into cloud condensation nuclei: Model–measurement comparison, *Atmos. Chem. Phys.*, *13*(15), 7645–7663, doi:10.5194/acpd-13-8333-2013.

Wonaschütz, A., et al. (2013), Hygroscopic properties of smoke-generated organic aerosol particles emitted in the marine atmosphere, *Atmos. Chem. Phys.*, *13*, 9819–9835, doi:10.5194/acp-13-9819-2013.

Worton, D. R., et al. (2011), Origins and composition of fine atmospheric carbonaceous aerosol in the Sierra Nevada Mountains, California, *Atmos. Chem. Phys.*, *11*(19), 10,219–10,241, doi:10.5194/acp-11-10219-2011.

Yli-Juuti, T., et al. (2011), Growth rates of nucleation mode particles in Hyytiälä during 2003–2009: Variation with particle size, season, data analysis method and ambient conditions, *Atmos. Chem. Phys.*, *11*(24), 12,865–12,886, doi:10.5194/acp-11-12865-2011.

Chapter 3

Ship Impacts on the Marine Atmosphere: Insights into the Contribution of Shipping Emissions to the Properties of Marine Aerosol and Clouds

Atmos. Chem. Phys., 12, 8439–8458, 2012
www.atmos-chem-phys.net/12/8439/2012/
doi:10.5194/acp-12-8439-2012

Atmospheric Chemistry and Physics

Ship impacts on the marine atmosphere: insights into the contribution of shipping emissions to the properties of marine aerosol and clouds

M. M. Coggon[1], A. Sorooshian[2,3], Z. Wang[2], A. R. Metcalf[4], A. A. Frossard[5], J. J. Lin[6], J. S. Craven[1], A. Nenes[6,7], H. H. Jonsson[8], L. M. Russell[5], R. C. Flagan[1,4], and J. H. Seinfeld[1,4]

[1]Department of Chemical Engineering, California Institute of Technology, Pasadena, CA, USA
[2]Department of Chemical and Environmental Engineering, University of Arizona, Tucson, AZ, USA
[3]Department of Atmospheric Sciences, University of Arizona, Tucson, AZ, USA
[4]Department of Environmental Science and Engineering, California Institute of Technology, Pasadena, CA, USA
[5]SCRIPPS Institution of Oceanography, University of California, San Diego, CA, USA
[6]School of Earth and Atmospheric Sciences, Georgia Inst. of Technology, Atlanta, GA, USA
[7]School of Chemical and Biomolecular Engineering, Georgia Institute of Technology, Atlanta, GA, USA
[8]Naval Postgraduate School, Monterey, CA, USA

Correspondence to: J. H. Seinfeld (seinfeld@caltech.edu)

Received: 22 May 2012 – Published in Atmos. Chem. Phys. Discuss.: 7 June 2012
Revised: 1 September 2012 – Accepted: 3 September 2012 – Published: 20 September 2012

Abstract. We report properties of marine aerosol and clouds measured in the shipping lanes between Monterey Bay and San Francisco off the coast of Central California. Using a suite of aerosol instrumentation onboard the CIRPAS Twin Otter aircraft, these measurements represent a unique set of data contrasting the properties of clean and ship-impacted marine air masses in dry aerosol and cloud droplet residuals. Below-cloud aerosol exhibited average mass and number concentrations of 2 µg m^{-3} and 510 cm^{-3}, respectively, which are consistent with previous studies performed off the coast of California. Enhancements in vanadium and cloud droplet number concentrations are observed concurrently with a decrease in cloud water pH, suggesting that periods of high aerosol loading are primarily linked to increased ship influence. Mass spectra from a compact time-of-flight Aerodyne aerosol mass spectrometer reveal an enhancement in the fraction of organic at m/z 42 (f_{42}) and 99 (f_{99}) in ship-impacted clouds. These ions are well correlated to each other ($R^2 > 0.64$) both in and out of cloud and constitute 14 % (f_{44}) and 3 % (f_{99}) of organic mass during periods of enhanced sulfate. High-resolution mass spectral analysis of these masses from ship measurements suggests that the ions responsible for this variation were oxidized, possibly due to cloud processing. We propose that the organic fractions of these ions be used as a metric for determining the extent to which cloud-processed ship emissions impact the marine atmosphere where ($f_{42} > 0.15$; $f_{99} > 0.04$) would imply heavy influence from shipping emissions, ($0.05 < f_{42} < 0.15$; $0.01 < f_{99} < 0.04$) would imply moderate, but persistent, influences from ships, and ($f_{42} < 0.05$; $f_{99} < 0.01$) would imply clean, non-ship-influenced air.

1 Introduction

Ship exhaust is estimated to account for 14 and 16 % of global NO_x and SO_x emissions, respectively (Corbett and Fischbeck, 1997). Models show that ship emissions also contribute 1.67 Tg yr^{-1} to global particulate matter, which is nearly equivalent to current estimates of particulate matter emitted by all on-road vehicles (Eyring et al., 2005; Yan et al., 2011). Because many shipping lanes are located along coastal regions where marine stratocumuli persist, ship emissions have the potential to directly affect cloud microphysics. Studies of cargo ship exhaust/cloud interactions have shown distinct cloud responses to these perturbations (e.g., Coakley

et al., 1987; Ackerman et al., 1995; Frick and Hoppel, 2000; Durkee et al., 2000; Hudson et al., 2000; Noone et al., 2000; Lu et al., 2009; Christensen and Stephens, 2011). Satellite imagery shows that ship tracks can exist hours after initial emission (Coakley et al., 1987; Durkee et al., 2000; Christensen and Stephens, 2011) and therefore have the potential to exert a significant effect on local radiative fluxes.

Ship emissions mix with marine aerosol and subsequently with cloud droplets, however the extent of this effect is not well established. Marine aerosol is a complex mixture of natural and anthropogenic sources, and thus the signature from shipping emissions is difficult to detect. Natural marine aerosol comprises particles resulting from sea-spray (e.g., NaCl, KCl, organics), marine biological activity (e.g., dimethylsulfide and subsequent oxidation products), and those from continental origins (e.g., dust, secondary products from biogenic oxidation). Anthropogenic sources include ship emissions, continental pollution, and biomass burning. Sea-salt typically dominates the super micrometer aerosol ($D_p > 1\,\mu m$), whereas organics, sulfate, and ammonium from natural and anthropogenic sources constitute a large portion of mass in the submicrometer regime ($D_p \leq 1\,\mu m$) (Cunningham and Zoller, 1981; McInnes et al., 1996).

With its location along busy shipping lanes and near heavily populated areas, the California coastal zone is an especially advantageous region to evaluate the anthropogenic contribution to marine aerosol and cloud condensation nuclei (CCN). Table 1 summarizes studies conducted in the vicinity of the California coastal zone on marine aerosol and cloud droplets. Important studies by Hegg et al. (2008, 2009, 2010) have utilized source apportionment models to attribute size-resolved hygroscopicity, light scattering coefficient, and CCN activity of marine aerosol to natural and anthropogenic sources. They estimated that 50 % of the measured CCN concentrations and 57 % of the light-scattering coefficient of marine aerosol in the California coastal region originated from anthropogenic sources. Though anthropogenic signatures contribute significantly to measured aerosol properties, the extent to which ship emissions contribute to this signal remains uncertain.

Few studies along the California coast have investigated marine aerosol and cloud properties simultaneously (Table 1). In this study, we utilize state-of-the-art aerosol measurements to build upon the knowledge of marine aerosol and cloud properties, with special attention to the contribution from ship emissions.

2 Methodology

2.1 Field mission description

From July–August 2011, the Eastern Pacific Emitted Aerosol Cloud Experiment 2011 (E-PEACE) was operated out of the Center for Interdisciplinary Remotely-Piloted Aircraft Studies (CIRPAS) in Marina, CA (Russell et al., 2012). The purpose of the field mission was to study the effect of ship emissions, sea-salt and organic aerosol on Eastern Pacific marine stratocumulus commonly found off the coast of Central California. Thirty flights were conducted by the CIRPAS Twin Otter aircraft to probe the emissions of cargo and tanker ships and their effects on marine stratocumulus. The focus of this study is a set of measurements made during twenty-six flights conducted in a sampling region between San Francisco and Monterey Bay (Fig. 1). Four additional flights were performed outside of this sampling region and are analyzed in Sect. 4.1 to compare aerosol properties during cloudy and clear conditions, however a more extensive analysis of these flights will be forthcoming. In addition to sampling direct ship emissions, measurements of aerosol and cloud properties were made below, within, and above cloud during each flight. Simultaneous measurements of marine aerosol properties were conducted onboard the R/V *Point Sur*. Averaged measurements made outside direct ship fumigation were taken to reflect the variation of marine aerosol and cloud properties over the course of the campaign.

2.2 Aerosol and cloud droplet measurement methodology

Cloud and aerosol properties were measured by ship and aircraft using a suite of aerosol instruments (Table 2). A detailed description of the instrumentation used in this study can be found in the Appendix. Cloud droplet residuals were measured downstream of a counterflow virtual impactor (CVI) inlet with a cut size of 11 µm (Shingler et al., 2012).

In the following discussion, we report cloud residual mass concentrations measured behind the CVI inlet. Despite the improved CVI design that can accommodate high sample flow and thus reduce the need for large counterflow and dilution (Shingler et al., 2012), uncertainties remain in total mass and number concentrations that are common among all CVI inlets. Primarily, the transmission efficiency (TE) of the CVI is a function of several parameters, including aircraft speed, sample-flow dilution, and particle diameter. In addition, the instrument is characterized by a cut size that restricts the smallest particle that can be sampled; thus, the cloud residual mass concentrations reported in this study (Table 3) are less than the total cloud residual mass. However, there are relative differences between periods of low and high concentration that suggest a qualitative difference between flights.

An altitude-dependent, zig-zag aircraft sampling pattern was utilized to measure unperturbed and perturbed air masses. Upon locating a ship, the Twin Otter sampled below, within and above cloud in close proximity to the ship's plume. While in cloud, measurements were made behind the CVI, thus sampling only cloud droplet residuals. Measurements made out of cloud were sampled through the main sub-isokinetic aerosol inlet. The main inlet is designed to

Table 1. Previous studies on the properties of marine aerosol over the Northeastern Pacific Ocean. Footnotes define instrument abbreviations.

Author	Research Location	Instruments	Type of Mission	Sources Sampled	CCN Properties	Hygroscopicty	Size Properties	Chemical Properties	Species Analyzed	Summary
Hegg et al. (1996)	Pacific Coast	nephelometer PCASP, SMPS, DNH	Aircraft	Dry Aerosol	–	yes	–	–	–	Authors report the optical and hygroscopic properties of marine aerosol in the vicinity of the California coast. The hygroscopic growth factor was shown to be 1.7 while the ratio of backscatter to total scattering was found to be 0.13.
McInnes et al. (1996)	E. Pacific	Filter Sampling and off-line analytical chemistry	Ground, Ship	Dry Aerosol	–	–	–	yes	sea salt ions, sulfate, ammonium, water	This study investigated the composition of sub-micrometer aerosol. Gravimetric measurements showed that a significant amount of mass (0–76 %) was unaccounted for in filter measurements. Water uptake on the filter samples made up 29 % of the mass and the remaining mass was likely to be organic in nature.
Phinney et al. (2006)	N.E. Pacific	SMPS, PCASP, MOUDI, AMS, GC	Ship	Dry Aerosol	–	–	yes	yes	MSA, sulfate, organics, nitrate, ammonium, sea salt	Marine aerosol off the coast of British Columbia was measured for size and composition. MSA was found to be an order magnitude higher than previously observed in the N.E. Pacific. AMS organic spectra showed that ship emissions may play a role in contributing to the organic signature of marine aerosol.
Straub et al. (2007)	California Coast	Cloud water collector inlet and off-line analytical chemistry, FSSP, PCASP, PVM (LWC)	Aircraft	Cloud Particles	–	–	–	yes	TOC, inorganic ions, sulfate, nitrate, hydrogen peroxide, formaldehyde	Cloud water off the coast of California was analyzed for ionic, TOC, trace ion, soluble organics and formaldehyde concentrations. The measurements represent a unique compilation of remote marine cloud water chemistry.
Sorooshian et al. (2007a)	California Coast	PILS, LWC, CVI	Aircraft	Cloud Particles	–	–	–	yes	oxalate, sulfate	Oxalate: SO_4 measurements tended to increase with altitude, suggesting that cloud processing of below-cloud aerosols generated a higher fraction of oxalate. LES simulations showed that particles above cloud were likely generated due to cloud evaporation; thus, the high fractions of oxalate observed above cloud were partially due to cloud processing.
Hegg et al. (2008)	California Coast	Filter Sampling and off-line analytical chemistry, AHS, Light-scattering humidigraph, PSAP	Aircraft	Dry Aerosol	–	yes	–	yes	organics, inorganic ions, BC, sulfate, lead	Aerosol hygroscopicity was observed to increase with altitude. Given that the MBL is a well mixed system, changes in aerosol properties with altitude plausibly resulted from oxidation of organic films. No evidence for the accumulation of inorganics was observed.
Hegg et al. (2009)	California Coast	Filter Sampling and off-line analytical chemistry, AHS, PSAP, CCN, PCASP	Aircraft	Dry Aerosol	yes	–	yes	yes	organics, inorganic ions, BC, sulfate, lead	CCN measurements off the coast of California are attributed to natural and anthropogenic sources using receptor modeling. Roughly 50 % of the samples measured in the study were anthropogenic in nature.
Hersey et al. (2009)	California Coast	AMS, DASH-SP	Aircraft	Dry Aerosol	–	yes	–	–	organics, sulfate	DASH-SP and AMS measurements are coupled to characterize the chemical dependence of aerosol growth factors. It was found that higher organic fractions yielded lower growth factors at high RH. High organic fractions are correlated with continental sources from back trajectory modeling.
Sorooshian et al. (2009)	California Coast	PILS-IC, LWC, FSSP, SMPS, CCN, DASH-SP	Aircraft, ground, satellite	Aerosol, Clouds	yes	yes	yes	yes	DEA, MSA	The link between chlorophyll *a* concentrations and the fraction of MSA and DEA in aerosol suggests that ocean biota have significant influence over marine aerosol properties including CCN and hygroscopicity. A link between cloud properties and chlorophyll *a* is not shown as cloud properties were heavily influenced by meteorological conditions.
Hegg et al. (2010)	California Coast	Filter Sampling and off-line analytical chemistry, AHS, PSAP, CCN, PCASP	Aircraft	Dry Aerosol	yes	yes	yes	yes	organics, inorganic ions, BC, sulfate, lead	A receptor based model is used to investigate the extent of anthropogenic sources on CCN in the marine environment. The authors report that 63–74 % of the aerosols are anthropogenic in nature.
Langley et al. (2010)	N.E. Pacific	AMS, SMPS, CCN, gas phase SO_2	Ship	Dry Aerosol	yes	–	yes	yes	MSA, SO_2, organics	Ship measurements of marine aerosol showed that periods of high sub-micron CCN activity were consistent with increased concentrations of MSA. CCN and MSA/sulfate were strongly correlated. Organics (primarily anthropogenic) are important as acting as a site for sulfate condensation and subsequent CCN activation.
Moore et al. (2012)	N.E. Pacific	AMS, SMPS, CCN	Aircraft	Dry Aerosol	yes	yes	yes	yes	organic, nitrate, sulfate, ammonium	Detailed characterization of CCN off the coast of California are made and compared to CCN in urban and rural areas. CCN-derived hygroscopicity parameter was highest in marine outflow compared to urban or rural areas.

PCASP – Passive Cavity Aerosol Sizing Probe; FSSP – Forward Scatter Spectrophotometer Probe; PSAP – Particle Soot Absorption Photometer; SMPS – Scanning Mobility Particle Sizer; PVM – Particle Volume Monitor; CCN – Cloud Condensation Nuclei; AMS – Aerosol Mass Spectrometer; LWC – Liquid Water Content; DASH-SP – Differential Aerosol Sizing and Hydroscopicity Spectrometer Probe; DNH – dual-nephelometer humidigraph; CVI – Counter-Flow Virtual Impactor; PILS-IC – Particle Into Liquid Sampler – Ion Chromatography; MOUDI – Micro-Orifice Uniform-Deposit Impactor; AHS – Aerosol Hydration Spectrophotometer

Table 2. Instruments onboard the Twin Otter aircraft and R/V *Point Sur*.

Parameter	Instrument	Time Resolution	Detection Limit	Size Range	Twin Otter	Point Sur
Particle Number Concentration	Condensation Particle Counter (TSI CPC 3010)	1 s	$< 50\,000\,cm^{-3}$	$\geq$ 10 nm	✓	✓
Aerosol Size Distribution	Scanning Mobility Particle Sizer (SMPS)	110 s	N/A	10–700 nm	✓	✓
Cloud Droplet Residuals	Counterflow Virtual Impactor (CVI)	N/A	N/A	$> 11\,\mu m$	✓	
Bulk Cloud Water Composition	Modified Mohen Slotted Cloud Water Collector	N/A	N/A	N/A	✓	
Cloud and Aerosol Size Distribution	Cloud and Aerosol Spectrometer Probe (CAS)	1 s	N/A	0.65–55 µm	✓	
Cloud Droplet Liquid Water Content	Light Diffraction (Gerber PVM-100 probe)	1 s	N/A	5–50 µm	✓	
Aerosol Bulk Composition	High Resolution Time-of-Flight Aerosol Mass Spectrometer (HiRes-ToF-AMS)	2 min	$\leq 1\,\mu g\,m^{-3}$	60–600 nm		✓
Aerosol Bulk Composition	Compact Time-of-Flight Aerosol Mass Spectrometer (C-ToF-AMS)	8–12 s	$\leq 1\,\mu g\,m^{-3}$	60–600 nm	✓	
Cloud Condensation Nuclei (CCN) Number Concentration	Continuous Flow Streamwise Thermal Gradient CCN chamber	1–20 s	$< 20\,000\,cm^{-3}$	s.s 0.2–0.7 %	✓	✓

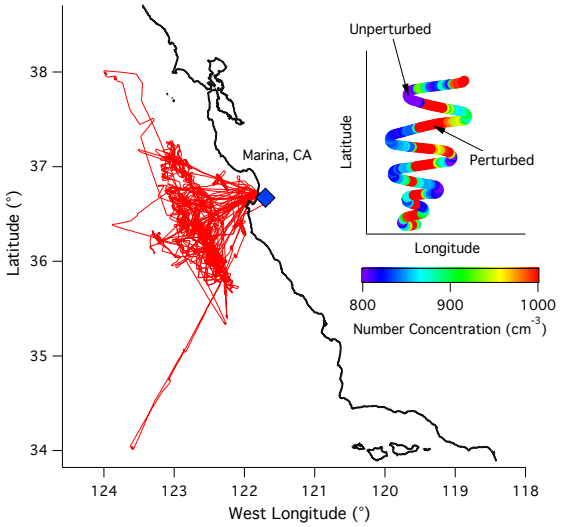

Fig. 1. Twin Otter flight paths for RF 1-26 during the E-PEACE mission. Inset shows a typical sampling pattern when encountering a ship exhaust plume. The color bar indicates the total aerosol number concentration as measured by the Twin Otter CPC.

decelerate airstream velocities outside the cabin ($\sim 50\,m\,s^{-1}$) to lower velocities that can be effectively sampled by aircraft instruments ($\sim 7\,m\,s^{-1}$). Under normal airspeed, the inlet on the Twin Otter samples aerosol below 3.5 µm with 100 % efficiency (Hegg et al., 2005). Thus, for the results reported here, there was no appreciable loss of particles due to aircraft sampling.

3 Aerosol and cloud droplet properties

In the following discussion, we use terminology such as "background" and "perturbed" to define aerosol conditions of the marine atmosphere. We acknowledge, however, that the assignment of these terms is not without ambiguity. A solely background signal in the remote marine atmosphere is a condition that occurs only when natural marine processes contribute to the aerosol. Without anthropogenic or continental influences, one might presume that a true baseline marine signal exists. However, even in a total absence of anthropogenic influence, such a signal is likely not unique and constant throughout the remote marine atmosphere. Varying wind speeds that generate sea spray, or biological production of dimethyl sulfide (DMS), which leads to homogeneously nucleated particles, can increase local "background" signal. On the other hand, varying wind speeds can dilute particles and lead to evaporation or ventilate DMS and inhibit new particle formation. Furthermore, particles can be lost due to wet or dry deposition. Even in the absence of non-marine sources, the natural background marine aerosol is dynamic.

Rather than relying on a definition of "background" aerosol, we choose to distinguish between "clean" and "perturbed" conditions based on the extent to which the marine atmosphere is impacted by shipping emissions. We define "perturbed" air masses as being pockets of the marine atmosphere that have been directly impacted by local ship emissions. This would comprise relatively small spatial regions in which the aerosol number concentration has increased, the aerosol number size distribution has shifted in mean diameter, and the aerosol composition has changed relative to the surrounding region. The atmosphere unperturbed by ship emissions, which we take to be synonymous with the term "clean", can be broken into a spectrum of conditions with varying degrees of non-ship related influences. Here, we are interested in comparing properties of the marine aerosol

Table 3. Summary of average aerosol and cloud properties over the course of the E-PEACE campaign. Bottom table summarizes key aerosol properties from previous studies of marine aerosol and cloud droplets off the coast of Central California. Values in brackets represent standard deviations of the average. Values in parenthesis list the range of measurements. Values below detection limit (DL) are noted.

		Below Cloud Aerosol Measurements						Cloud Measurements[g]				Air Equivalent Cloud Water Chemistry					
Research Flight (RF)	Date	Total Mass[a] ($\mu g\,m^{-3}$)	Organic[a] ($\mu g\,m^{-3}$)	Sulfate[a] ($\mu g\,m^{-3}$)	CPC (cm^{-3})	CCN (0.15 %) (cm^{-3})	CCN (0.3 %) (cm^{-3})	Total Mass[a] ($\mu g\,m^{-3}$)	Organic[a] ($\mu g\,m^{-3}$)	Sulfate[a] ($\mu g\,m^{-3}$)	N_d[b] (cm^{-3})	pH	Na (10^4) ($\mu g\,m^{-3}$)	Fe (10^4) ($\mu g\,m^{-3}$)	Mn (10^4) ($\mu g\,m^{-3}$)	V (10^4) ($\mu g\,m^{-3}$)	LWC[b] ($g\,m^{-3}$)
1	8 Jul	0.96	0.65	0.28	665	–	349	1.37	0.76	0.41	208	4.02	87 182	51.41	4.72	0.59	0.10
2	9 Jul	1.32	0.70	0.51	892	–	238	2.06	1.01	0.84	235	4.23	16 956	26.63	2.12	2.12	0.09
4	14 Jul	1.04	0.60	0.45	968	–	131	1.68	0.84	0.69	93	4.32	7757	< (DL)	< (DL)	1.29	0.15
5	15 Jul	0.86	0.75	0.20	364	–	78	0.92	0.49	0.20	23	4.63	688	0.19	0.07	0.31	0.01
6	16 Jul	0.90	0.58	0.31	329	–	–	1.06	0.67	0.22	27	4.50	127	< (DL)	< (DL)	2.02	0.11
7[c]	17 Jul	0.77	0.72	0.18	341	–	–	–	–	–	–	–	–	–	–	–	–
8	19 Jul	0.88	0.44	0.40	323	–	–	1.24	0.68	0.54	145	4.21	3671	11.78	0.52	4.25	0.19
9	21 Jul	1.83	0.70	0.78	578	217	–	1.08	0.63	0.39	127	5.16	17 662	4.85	3.11	1.50	0.23
10	22 Jul	1.80	0.49	1.02	376	213	–	1.81	0.79	0.78	116	4.67	15 212	7.58	1.08	2.46	0.25
11	23 Jul	2.83	0.86	1.56	976	300	400	1.84	0.88	0.81	169	4.30	13 881	17.61	1.55	3.28	0.18
12	24 Jul	2.81	0.92	1.57	736	226	355	1.90	0.87	0.85	170	3.99	5362	15.95	1.36	3.12	0.10
13	26 Jul	0.99	0.60	0.34	221	75	116	1.04	0.56	0.32	87	4.95	11 702	5.13	0.41	4.11	0.23
14[d]	27 Jul	2.99	0.81	1.91	425	207	–	1.53	0.64	0.80	199	3.86	4587	34.05	2.29	16.78	0.22
15	28 Jul	4.74	1.06	3.14	589	101	406	4.98	2.21	2.50	327	2.92	10 772	86.28	4.89	43.08	0.12
16	29 Jul	2.62	0.70	1.59	465	96	304	2.14	0.89	1.13	252	3.84	3664	164.63	17.47	19.99	0.28
17	1 Aug	2.22	0.58	1.44	400	78	352	1.86	0.62	1.10	212	3.77	978	47.07	2.71	7.35	0.10
18	2 Aug	2.55	0.80	1.47	587	184	335	2.34	1.00	1.13	269	4.07	2777	27.67	1.98	8.92	0.21
19	3 Aug	1.41	0.57	0.70	346	167	173	1.11	0.60	0.38	120	4.80	11 406	< (DL)	0.45	3.63	0.19
20[c]	4 Aug	1.08	0.52	0.55	229	44	83	–	–	–	–	–	–	–	–	–	–
21	5 Aug	2.06	0.65	1.17	561	63	254	1.13	0.57	0.48	163	4.65	8376	19.06	1.69	1.03	0.19
22	8 Aug	3.75	1.01	2.24	737	328	333	2.03	0.52	1.30	323	3.66	42 794	26.45	1.31	4.17	0.11
23	9 Aug	2.97	0.92	1.73	428	28	294	1.79	0.75	0.80	226	4.06	34 543	13.77	1.01	1.24	0.11
24	10 Aug	1.57	0.83	0.79	296	49	296	0.99	0.65	0.41	150	4.54	27 015	31.42	1.76	7.64	0.25
25	11 Aug	1.18	0.53	0.46	252	157	91	0.86	0.58	0.21	41	5.07	1538	1.86	0.59	3.97	0.13
26	12 Aug	3.49	1.24	1.94	670	–	459	1.80	0.71	0.97	257	3.90	32 109	17.24	1.07	3.56	0.14
	Min	0.77	0.44	0.18	221	28	78	0.86	0.49	0.20	23	2.92	127	0.19	0.07	0.31	0.01
	Max	4.74	1.24	3.14	976	328	459	4.98	2.21	2.50	327	5.16	87 182	164.63	17.47	43.08	0.28

		Below Cloud Aerosol Measurements						Cloud Measurements[g]				Air Equivalent Cloud Water Chemistry					
Author/ Mission	Date	Total Mass[a] ($\mu g\,m^{-3}$)	Organic[a] ($\mu g\,m^{-3}$)	Sulfate[a] ($\mu g\,m^{-3}$)	CPC (cm^{-3})	CCN (0.15 %) (cm^{-3})	CCN (0.3 %) (cm^{-3})	Total Mass[a] ($\mu g\,m^{-3}$)	Organic[a] ($\mu g\,m^{-3}$)	Sulfate[a] ($\mu g\,m^{-3}$)	N_d[b] (cm^{-3})	pH	Na (10^4) ($\mu g\,m^{-3}$)	Fe (10^4) ($\mu g\,m^{-3}$)	Mn (10^4) ($\mu g\,m^{-3}$)	V (10^4) ($\mu g\,m^{-3}$)	LWC[b] ($g\,m^{-3}$)
E-PEACE Average	Jul–Aug 2011	1.98 [1.07]	0.73 [0.19]	1.07 [0.76]	510 [225]	148 [91]	266 [120]	1.67 [0.85]	0.78 [0.34]	0.75 [0.50]	171 [86]	4.48 [0.72]	13 227 [15 531]	23 [37]	2.3 [4.1]	5.4 [7]	0.16 [0.07]
Hegg et al. (2010)[e]																	
CARMA II	Jul 2004	3.12	–	1.34	–	–	100–825	–	–	–	–	–	–	–	–	–	–
CARMA III	Aug 2005	3.93	–	1.3	–	–	75–1150	–	–	–	–	–	–	–	–	–	–
CARMA IV	Aug 2007	16.3	–	1.04	197–6104	–	50–700	–	–	–	–	–	–	–	–	–	–
Sorooshian et al. (2009) MASE II	Jul 2007	–	–	0.78 [0.59]	307 [239]	–	73 [27]	– –	–	– –	104 [56]	–	–	–	–	–	0.15 [0.07]
McInnes et al. (1996)[f]	Apr–Jun 1994	2.21 [1.16]	–	–	–	–	–	–	–	–	–	–	–	–	–	–	–
Straub et al. (2007) DYCOMS-II	Jul 2001	–	–	–	–	–	–	–	–	–	174 [79]	3.26–4.82	38 900 (3900–133 900)	71 (0–369)	2.3 (0–11.6)	–	0.33 [0.17]

[a] Measurements from AMS.
[b] Averaged cloud probe data during cloud water sampling period.
[c] No clouds (7/17), few cloud measurements by probes (8/4).
[d] AMS Failure – limited measurements available below cloud (7/27).
[e] Filter samples for aerosol > 0.2 µm in diameter.
[f] Filter samples for aerosol < 1 µm in diameter.
[g] Organics, sulfate and total mass concentrations measured behind the CVI are a fraction of the total loading and may not reflect absolute mass concentrations. See text for details.

during periods of high aerosol mass loading owing to ship emissions (defined here as "perturbed") with properties in adjacent air masses not directly impacted by ship emissions (defined here as "clean"). The nature of non-refractory marine aerosol (i.e., non sea salt components such as organics and sulfate) can be consistently categorized using data from the aerosol mass spectrometer (AMS), which transmits particles with vacuum diameters ranging between 60–600 nm with 100 % transmission efficiency. Initially we will rely on bulk AMS mass concentrations as the basis on which to identify and define "clean" and "perturbed" conditions, but subsequently, we will derive conditions that more concretely define air masses directly impacted by shipping emissions.

Table 3 reports average aerosol properties for each flight compared to measurements reported by other studies conducted in the Eastern Pacific. We note that observations from this study agree broadly with previous findings. Notably, aerosol mass measured by the AMS agrees well with that measured by filter sampling reported in McInnes et al. (1996). Mass loadings from this study reflect submicrometer, non-refractory aerosol, whereas loadings reported by McInnes et al. (1996) reflect total submicrometer mass. The close agreement suggests that the mass measured in the submicrometer regime is dominated by non-sea salt components. This is consistent with McInnes et al. (1997) who show that 87–96 % of the total number concentration of submicrometer particles in the remote marine atmosphere are non-sea salt.

We can use the results from Table 3 to identify flights that were clean and perturbed during the E-PEACE campaign. Figure 2 shows the mass contributions of bulk AMS

species to dry marine aerosol and cloud droplet residuals over the course of the study. As is also shown in Table 3, submicrometer aerosol mass concentrations strongly varied between flights. In the beginning of the study, a continual period of low aerosol loading was observed between 15–19 July (RF 5–8). These measurements yielded aerosol mass concentrations below 1 µg m^{-3} and were among the lowest aerosol concentrations observed during E-PEACE. In the present study, these were likely to have been the least influenced by shipping emissions and are therefore defined as "clean".

Clean conditions have been previously observed in the marine atmosphere and are known to vary greatly (e.g., McInnes et al., 1996; Phinney et al., 2006; Straub et al., 2007; Langley et al., 2010; Ovadnevaite et al., 2011). For example, using an AMS, Phinney et al. (2006) measured submicrometer aerosol mass concentrations of 1.4 µg m^{-3} in the remote sub-arctic Pacific Ocean. The majority of the mass was sulfate (0.74 µg m^{-3}), of which MSA was found to contribute significantly, however organics were also a large fraction of the total signal (0.3 µg m^{-3}). Ammonium and nitrate were present in low amounts, which is consistent with the results from this study (see Fig. 2). In contrast, Ovadnevaite et al. (2011) observed organic aerosol mass concentrations as high as 3.8 µg m^{-3} during high wind events from clean marine air masses. The organic mass spectra and the observation of high biological activity suggested a primary organic source. In Sect. 3.5, we show that the origin of air masses sampled during RF 5–8 was remote marine. Of the previous studies that we have discussed, the clean conditions in this study are most consistent with measurements by Phinney et al. (2006) and McInnes et al. (1996). However, as has been shown, for example, by authors like Ovadnevaite et al. (2011), clean marine environments can exhibit a large range of aerosol mass concentrations.

Of particular interest in the present study are flights with elevated sulfate concentrations. Sulfate in the marine atmosphere is primarily attributed to DMS, continental pollution, and shipping exhaust. Flights conducted between 27 July–2 August (RF 14–18) exhibited enhancements in total aerosol mass concentrations that were nearly double the amount observed during clean conditions. These flights also had some of the highest concentrations of sulfate below cloud and in residual cloud droplets. Though there were other flights in which the total aerosol mass concentration was high, the period during RF 14–18 represents nearly a week of uninterrupted enhancements in aerosol mass. Thus, we focus our attention to these flights and define them as "perturbed".

3.1 Cloud-processed aerosol

Figure 3 shows typical marine aerosol number size distributions as measured by the scanning mobility particle sizer (SMPS). In general, marine aerosol exhibits two modes at approximately 60 and 200 nm, respectively. The peak at

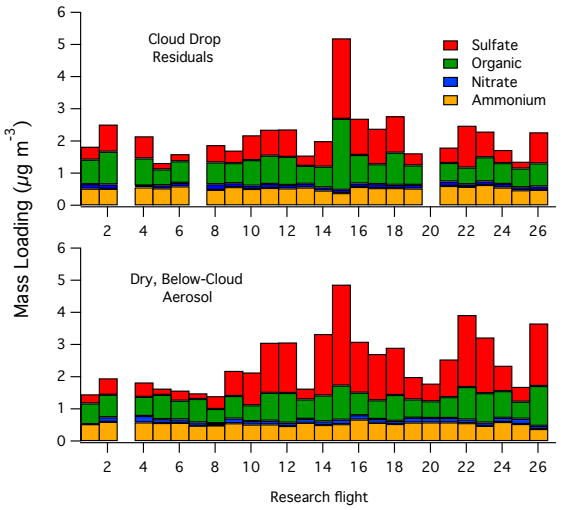

Fig. 2. Bulk AMS species measured in cloud drop residuals (top panel) and dry, below-cloud aerosol (bottom panel) over the course of the study. Only organic and sulfate vary significantly each day (variance of organic = 0.04, sulfate = 0.6 in below-cloud aerosol). Ammonium and nitrate exhibit variances that are at most 0.5 % of the variance of sulfate.

200 nm, which is the accumulation mode commonly observed in regions with marine stratocumulus (Hoppel et al., 1986, 1994; Frick and Hoppel, 2000), may be indicative of cloud processing. We note, however, that other sources can contribute to this mode. For example, Phinney et al. (2006) observed organic mass distributions during periods of direct ship fumigation with modes between 150–200 nm which may enhance number concentrations in this "cloud-processed" mode. However, given that most flights were conducted in the presence of marine stratocumulus, we suspect that cloud processing was a major contributor to aerosol in the accumulation mode.

During perturbed flights, the total aerosol volume concentration is approximately twice as large as that for clean flights. For example, the aerosol volume concentration for flights 16, 26 (perturbed) and 8, 20 (clean) are 2.24, 2.74 µm^3 cm^{-3} and 1.47, 0.47 µm^3 cm^{-3}, respectively. Representative size distributions of fresh ship exhaust from three ships (Fig. 3, bottom panel) exhibit a primary mode between 56–73 nm, which falls in the range of non cloud-processed aerosol. It is possible that ship emissions enhanced the number concentration of small mode aerosol during perturbed flights.

Cloud processing likely affected aerosol composition (Fig. 4), which is consistent with previous studies. Cloud scavenging and subsequent reaction of gaseous sulfur species lead to the accumulation of sulfate (Faloona (2009) and references therein). Under conditions of low acidity, some

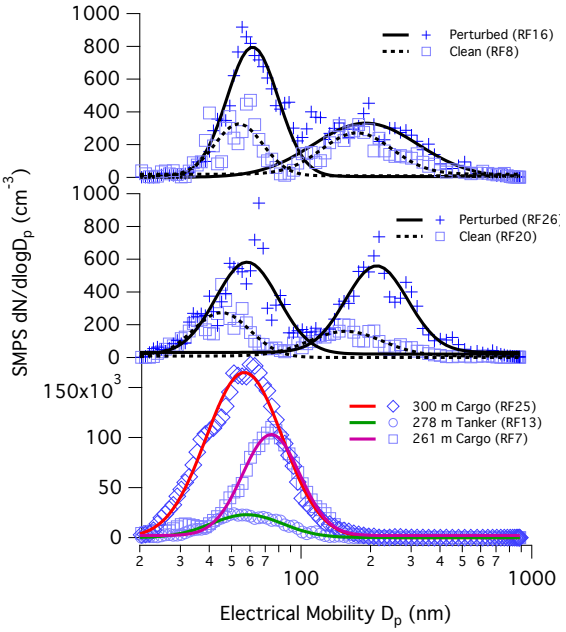

Fig. 3. Marine aerosol number size distributions of below-cloud aerosol measured during clean and perturbed flights (top and middle panels). Aerosol size distributions for the exhaust of three ships (bottom panel). Lines are log-normal fits.

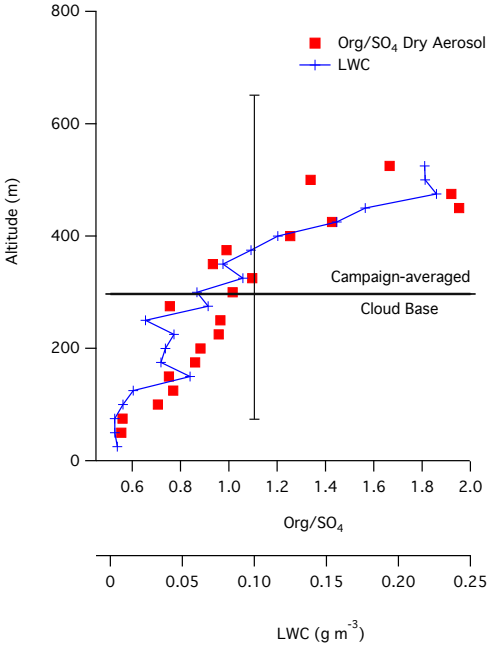

Fig. 4. Average organic:sulfate mass ratio of dry, unperturbed marine aerosol sampled in cloud-free air as a function of altitude. For clarity, standard deviations bars are omitted, however we note that variation increased with altitude. Average LWC is presented to illustrate the study-averaged, below-cloud top liquid water profile and show that cloud processing was prevalent at all altitudes. The campaign-average cloud base is shown with bars depicting the range of cloud bases and tops observed during the campaign. Cloud base altitudes were measured during aircraft soundings.

studies have shown that organics can also be formed from aqueous-phase processing. If the pH is high enough, the uptake and reaction of organic precursors (e.g., glyoxal and acetic acid) may exceed that of SO_2 (Ervens et al., 2003a,b; Sorooshian et al., 2007a) For example, Sorooshian et al. (2007a,b), showed that the ratio of oxalate:sulfate increases in cloud droplets with higher liquid water content (LWC). After the droplet evaporates, low volatility organics that may be formed by aqueous-phase chemistry remain in particle residuals (Sorooshian et al. (2007a) and references therein). Figure 4 shows the average out-of-cloud organic:sulfate ratio as a function of altitude. As observed by Sorooshian et al. (2007a), the ratio of organic:sulfate increases with altitude, a finding that is also coincident with an average increase in LWC. Though we suspect that this may be an indication of aqueous-phase chemistry, there are other processes that could affect the organic : sulfate ratio. During a typical flight, aerosol above cloud top exhibited high concentrations of organic. Previous studies have found that entrainment of air from the free troposphere into the marine boundary layer is a major source of aerosol number (Katoshevski et al., 1999; Kazil et al., 2011). If this aerosol were to be entrained into the cloud, this would elevate organic : sulfate ratios. Furthermore, it is possible that the dry aerosol shown in Fig. 4 did not result from evaporated cloud particles; rather, the aerosol could be the result of incomplete particle activation. Inorganic salts often increase the activation of organic aerosol particles (e.g. Bilde and Svenningsson, 2004). Thus, particles with higher amounts of sulfate may activate to cloud droplets first, therefore leaving behind interstitial aerosol with higher concentrations of organic. Despite these effects, it appears that cloud processing may have played a significant role controlling aerosol composition in the present study, which is consistent with the observation of a cloud-processed mode in the aerosol size distribution data (Fig. 3).

3.2 Cloud water chemistry

Figure 5 summarizes the trends in major cloud water ion and metal concentrations. These data are presented similarly to those reported by Straub et al. (2007) and Benedict et al. (2012), such that the present values can be easily compared. In this study, Cl^-, SO_4^{2-}, and NO_3^- are measured by IC and are therefore representative of soluble ions. Species such as Na, Ca, Mg and K are measured by ICP-MS. This analysis technique strictly gives information about the total metal content. In order to compare the results of the present study

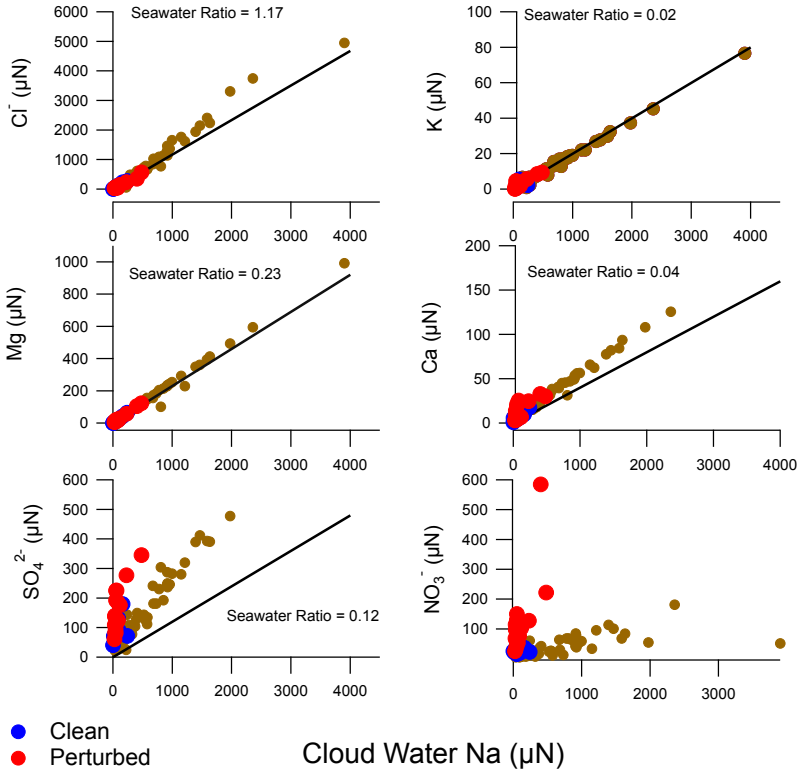

Fig. 5. Summary of major seawater species measured in marine cloud water. Data are presented analogously to those reported by Straub et al. (2007) and Benedict et al. (2012). In the present study, we assume that seawater species measured by ICP-MS (e.g., Na, K, Mg, Ca) reflect aqueous phase ions. The solid lines indicate the ion ratio typically observed in seawater. Each point represents a single cloud water measurement. Clean flights (RF 5–8) are colored in blue while perturbed flights (RF 14–18) are colored in red. The remainder of the flights are shown as brown circles.

to those by Straub et al. (2007) and Benedict et al. (2012), we assume that those species measured by ICP-MS originate from soluble seawater species and represent the ion content of each sample. Furthermore, to calculate concentrations in units of normality (μN), we assume that when present in the aqueous phase, these metals exist in their most stable valence state (for example, we assume that magnesium measured by ICP-MS exists as Mg^{2+}). If we assume that sodium concentrations reported in this study are representative of soluble sodium with +1 valence, then E-PEACE concentrations (0.7–3900 μN) are consistent with those observed by Straub et al. (2007) (36–2784 μN). Of all the common seawater species, Cl^{-}, Mg, and K exhibit a ratio with respect to Na that is consistent with the global average ratio found in seawater. Calcium is observed at a ratio slightly higher than typical seawater. Similar enhancements in calcium have been observed previously (e.g., Straub et al., 2007; Benedict et al., 2012) and may be the result of dissolved crustal minerals. The strong linear correlation with sodium, however, implies that the variation in calcium was primarily influenced by sea spray.

Of particular interest is the variation of seawater species between flights. Markers in Fig. 5 colored by blue and red indicate flights performed during clean (RF 5–8) and perturbed (RF 14–18) conditions, respectively. In general, the concentration of seawater species in marine cloud water is invariant during clean and perturbed flights. These species also appear to be present at lower concentrations during these flights than compared to all other flights performed during E-PEACE. It is reasonable, therefore, to neglect the mass contribution from seawater to the variation of sulfate observed in Table 3 and Fig. 2, given that clean and perturbed flights show little variation in sea-related species.

Sulfate and nitrate in the present study do not exhibit a strong linear relationship with sodium. These species are also enhanced during perturbed conditions (Fig. 5). In Sect. 3.4, we show that metals associated with shipping emissions (such as vanadium) are also enhanced during perturbed conditions and that their variation is coincident with higher

concentrations of sulfate in dry marine aerosol. It is possible that enhanced sulfate and nitrate in cloud water samples originated from ship-impacted air masses.

3.3 CCN measurements

Marine aerosol CCN measurements are summarized in Fig. 6. In the top panel, CCN activation spectra are compared for perturbed (red, RF 15) and clean (blue, RF 20) flights. In general, the fraction of activated particles at a given supersaturation is enhanced under perturbed conditions. For example, at 0.7 % supersaturation, 90 % of the particles measured during RF 15 activate in the CCN instrument. In contrast, only 60 % of the particles activate in the instrument during RF 20. If we fit a sigmoidal curve of the form $\mathrm{CCN/CN} = a_0/(1+(x/a_1)^{-a_2})$ (where a_0, a_1 and a_2 are fitted parameters) and take the inflection point to reflect the aerosol population ensemble critical supersaturation (Moore et al., 2011), we find that the critical supersaturation is lower for particles measured during RF 15 than those measured during RF 20 (0.23 % vs. 0.27 %). While this does not represent a significant difference in supersaturation, it appears that higher fractions of particles activate to CCN under perturbed conditions relative to clean conditions.

The bottom panel in Fig. 6 shows the fraction of activated particles at 0.15, 0.3, 0.5 and 0.7 % supersaturation for all dry aerosol measurements. Markers are colored by sulfate loading to illustrate the extent to which shipping emissions may have influenced the measurement. In general, a higher fraction of activated particles is coincident with elevated concentrations of sulfate. This is consistent with the averaged spectrum in Fig. 6 (top) which shows that more particles activated during perturbed flight RF 15 compared to clean flight RF 20. From Fig. 3, we see that the aerosol measured during RF 20 exhibited two modes that, when normalized by total aerosol number, have similar peak shape to aerosol measured during a perturbed flight (e.g., RF 16). The only observable difference in normalized number size distributions is that the small mode from RF 20 peaks at a smaller diameter (40 nm) than RF 16 (60 nm). While this may partially explain the increased fraction of CCN during perturbed conditions, the enhancement of activated particles may also result from elevated concentrations of sulfate (as shown in Fig. 6).

Enhanced CCN concentrations in the presence of anthropogenic pollution events has been previously observed in the Eastern Pacific (Hegg et al., 2009, 2010; Langley et al., 2010). Langley et al. (2010) found that anthropogenic pollution acted as condensation sites for sulfur species, resulting in an increase in CCN number concentrations. Hegg et al. (2010) deduced that 67 % of the CCN off the coast of California are anthropogenic in origin. The CCN concentrations reported in the present study are consistent with those results (see Table 3 comparison), suggesting that anthropogenic sources are major contributors to the CCN properties reported in Fig. 6. In Sect. 3.4, we show that increased

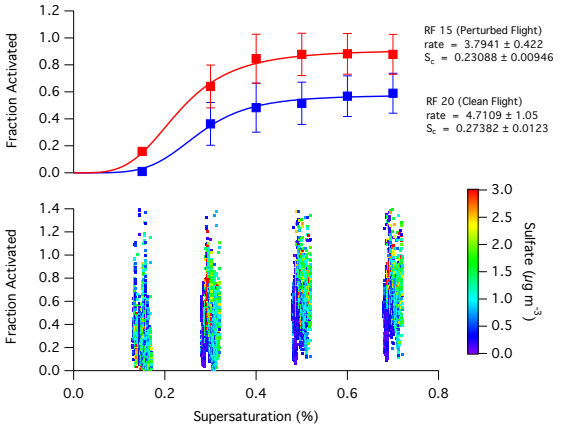

Fig. 6. CCN spectra showing the activation of particles at various supersaturations. The top panel is CCN data from a perturbed flight (red markers, RF 15) and clean flight (blue markers, RF 20) fitted to a sigmoidal curve of the form $\mathrm{CCN/CN} = a_0/(1+(x/a_1)^{-a_2})$ where a_0, a_1 and a_2 are fitted parameters. The error bars represent the measurement standard deviation. The bottom panel shows all CCN measurements made over the course of the campaign at 0.15, 0.3, 0.5 and 0.7 % supersaturation.

sulfate can be primarily linked to shipping emissions; thus, shipping emissions may have exerted a strong control on CCN properties during this study.

3.4 Relationship between marine aerosol and cloud droplet properties

In this study, sulfate is a major constituent of submicrometer marine aerosol (Fig. 2). Sulfate affects cloud water chemistry and cloud droplet number concentrations by lowering cloud water pH (via SO_2 oxidation) and increasing CCN concentrations (e.g., ship emissions, homogeneous nucleation of H_2SO_4 or MSA) (Hegg and Hobbs, 1986; Hoppel et al., 1994; Straub et al., 2007; Hegg et al., 2010; Langley et al., 2010). Sources of sulfate in the marine atmosphere include ship emissions, DMS, and continental pollution. Here, we relate sulfate measured below cloud to properties of cloud water chemistry and present evidence that elevated sulfate measured during perturbed flights was largely influenced by ship emissions. In the present discussion, we only compare trace metals such as iron and vanadium due to their links to shipping. Subsequent work will provide a more complete overview of cloud water chemistry during the E-PEACE campaign.

Figure 7 compares below-cloud sulfate with various cloud properties. Iron and vanadium were measured in cloud water samples using ICP-MS, while hydronium concentrations were calculated from cloud water pH. All data are presented in air equivalent units, which represents the mass of a species per unit volume of air (see Appendix A for details). We

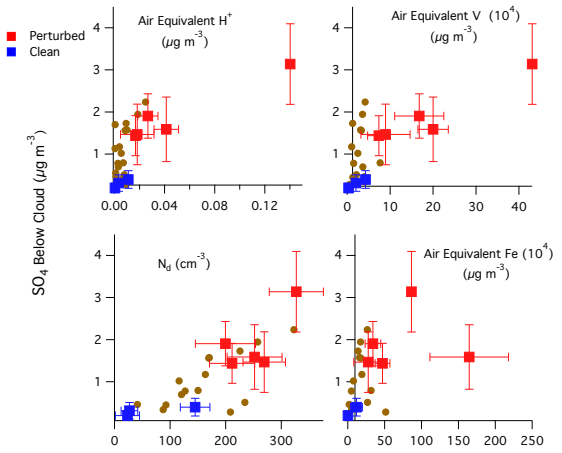

Fig. 7. Trends in below cloud sulfate vs. air equivalent H^+, cloud droplet number concentration (N_d), air equivalent V and air equivalent Fe. Iron and vanadium were measured in cloud water samples using ICP-MS. Hydronium concentrations were calculated based on cloud water sample pH. Air equivalent units are calculated as the product of the concentration of a species in a bulk cloud water sample and the average liquid water content measured during the cloud water collection period. Each point represents a single flight. Clean flights (RF 5–8) are colored blue while perturbed flights (RF 14–18) are colored red. Error bars show the standard deviation of each measurement. The remainder of the flights are shown as brown circles.

observe that sulfate in below-cloud aerosol correlates well with pH (not shown) and cloud droplet number concentration ($R^2 = -0.57$ and 0.64, respectively). This is consistent with observations of enhanced cloud water acidification and CCN in the presence of sulfate (e.g., Hoppel et al., 1994; Straub et al., 2007; Langley et al., 2010). Perturbed flights exhibit greater acidification in cloud water samples and higher concentrations of cloud droplets, vanadium, and iron as compared to clean flights. Of all the flights, the highest concentration of sulfate below cloud occurred during RF 15, which also exhibited the greatest amount of acidification, highest concentration of vanadium, highest concentration of cloud droplets, and second highest concentration of iron in cloud water samples. This enhancement is clearly seen in Table 3, where perturbed flights 14–18 exhibit 5–10 times higher concentrations of iron and vanadium than clean flights.

The hypothesis in the present study is that cloud water acidification results from the oxidation of SO_2 originating from ship emissions. This could occur by several mechanisms. SO_2 could be oxidized in the gas-phase to form sulfuric acid, which could then partition into cloud droplets or aerosol particles. If the aerosol particles were to activate, then this could subsequently lead to cloud droplet acidification. Alternatively, if exhaust were directly emitted into the cloud, then gas-phase SO_2 could partition into the cloud droplet and undergo aqueous-phase processing. The correlation with below-cloud sulfate suggests that enhanced sulfur emissions led to an decrease in pH. Even more suggestive of ship-influenced acidification is the correlation between cloud water vanadium and cloud water acidity ($R^2 = 0.8$, Fig. 8). Studies have shown that shipping emissions are the predominant source of vanadium in the marine atmosphere (Agrawal et al., 2008; Sholkovitz et al., 2009; Furutani et al., 2011). The strong correlation between vanadium and acidity and the enhancement of both during perturbed conditions implies that in the present study, shipping emissions largely contributed to cloud water acidification.

The variation in iron concentrations with below-cloud sulfate (Fig. 7) could result from a number of sources. While iron is often attributed to continental dust, recent studies suggest that iron also has significant sources from ship emissions. Using single particle mass spectrometry, Furutani et al. (2011) found that iron-containing aerosol from Asian outflows could be subdivided into several major iron-containing categories, one of which is iron associated with vanadium. Iron-containing aerosols constituted nearly 40 % of the total number of particles in the ship-associated vanadium category. While it is possible that shipping emissions enhanced iron concentrations during perturbed flights, it appears that elevated iron concentrations in the present study were largely due to continental dust. Figure 8 (bottom) shows the relationship between iron and manganese in cloud water samples. The strong correlation ($R^2 = 0.9$) suggests that the two are linked to a common source.

Manganese is primarily attributed to crustal minerals (Statham and Chester, 1988; Guieu et al., 1994; Ohta et al., 2006; Duvall et al., 2008). Iron and manganese concentrations were not strongly correlated to cloud water sulfate ($R^2 = 0.27$ and 0.29 for iron and manganese, respectively); therefore, the elevation of iron and manganese in cloud water during perturbed flights is likely indicative of air transported from continental sources. The contribution of below-cloud sulfate from continental sources is difficult to quantify given that iron and manganese are related to the transport of dust and are not directly linked to anthropogenic sources. We note, however, that iron and manganese are not strongly correlated with cloud water acidification (not shown, $R^2 = 0.36$) which we hypothesize resulted from SO_2 oxidation. Furthermore, we show in Sect. 3.5 that perturbed flights were largely affected by air masses that were transported through major shipping lanes and not by air masses that were transported directly over land. Though we cannot rule out continental sources as contributors to below-cloud sulfate, we presume that shipping emissions exerted a stronger impact on properties of marine aerosol over continental sources given that metals associated with shipping emissions, such as vanadium, are strongly correlated to other properties of cloud water chemistry such as acidification.

DMS as a major source of sulfate during perturbed flights can be ruled out in the measurements here based on the small variation of methanesulfonic acid (MSA, DMS oxidation

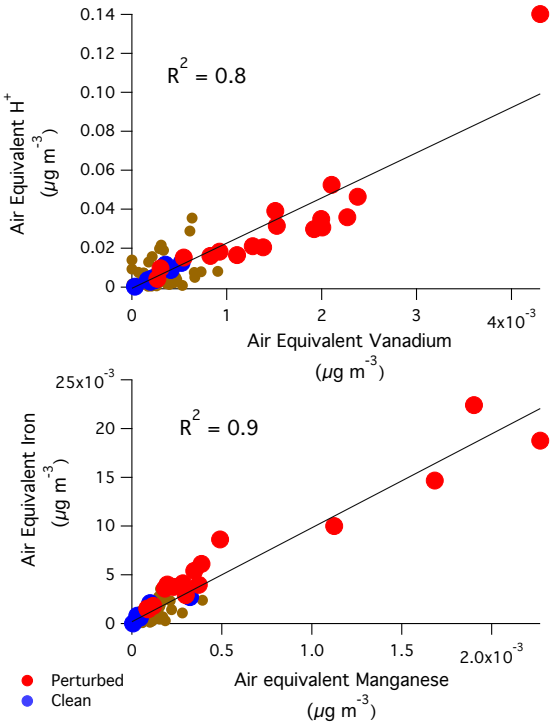

Fig. 8. Top – variation in air equivalent vanadium with respect to air equivalent hydronium concentrations for cloud water samples. Hydronium concentrations were calculated based on cloud water sample pH. Bottom – trend in manganese and iron concentrations in cloud water for measurements made during clean (blue) and perturbed (red) days, respectively.

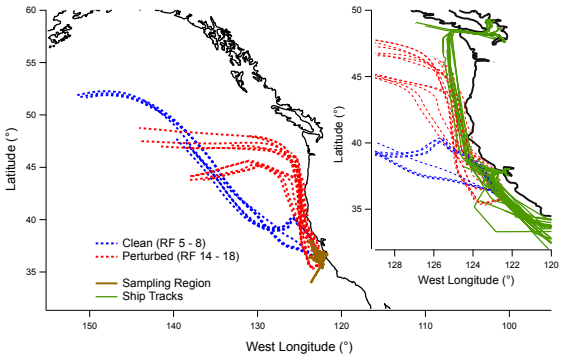

Fig. 9. Back-trajectories (72 h) of cloud water samples collected during clean (blue) and perturbed (red) flights. Back-trajectories were calculated using the NOAA HYSPLIT model (available at: http://www.arl.noaa.gov/ready/hysplit4.html). Simulations were initialized with trajectories ending at the time, location and altitude of cloud water sampling. Inset shows a closer perspective of the California coast. The green traces are the ship tracks of 15 cargo and tanker ships probed during the campaign and illustrate the general location of the shipping lanes north of Long Beach, CA.

product). Appendix Fig. A1 shows the variation of cloud water MSA and sulfate as measured by ion chromatography. The amount of MSA in cloud water was no different during perturbed flights when compared to clean or intermediate flights. We infer from these results and those from Figs. 7 and 8 that the primary source of below-cloud sulfate during perturbed flights originated from ship exhaust.

3.5 Back-trajectory comparisons

As discussed in Sect. 3.4, the variation of manganese and iron in cloud water samples is likely indicative of crustal minerals transported from continental sources. Based on these results, we presume that the enhancement in sulfate during perturbed flights was at least partly due to changes in meteorology. These inferences are supported by the 72 h (NOAA HYSPLIT) back-trajectories corresponding to cloud water samples collected during clean and perturbed flights (Fig. 9).

During clean flights, air was primarily transported across the remote ocean, which may explain the observation of low mass loadings in sulfate, organics, iron, and manganese (Table 3, Fig. 2). During flights in which there is strong evidence of anthropogenic influence, air was primarily transported along the coast and through some of the most heavily transited shipping lanes. This is consistent with the observation of enhanced vanadium (shipping influences), iron, and manganese (continental influence) in cloud water samples during perturbed flights (Figs. 7 and 8). We infer from Fig. 9 that changes in meteorology likely influenced the variation in aerosol and cloud properties and that the enhancement of sulfate below cloud during perturbed conditions is partly due to the transport of air masses through shipping lanes.

4 Ship impacts on marine aerosol and clouds

4.1 Organic aerosol mass spectra

In the following discussion, we compare organic aerosol spectra during clean and perturbed flights to investigate possible influences of ship emissions on the composition of cloud droplet residuals and dry, below-cloud marine aerosol (Fig. 10). Flight 9 (RF 9) was used as a basis for clean conditions, despite exhibiting slightly higher sulfate than most other flights categorized as clean, because in this flight, distinct ship tracks were observed next to unperturbed cloud. As shown in the column of spectra to the right of the dotted line in Fig. 10, we compare perturbed and unperturbed organic spectra of cloud droplet residuals to provide a reference to how the organic composition of cloud particles changes in the presence of ship emissions. These spectra can be compared to those from flight 15 (RF 15), which was found to have the highest concentrations of vanadium and sulfate

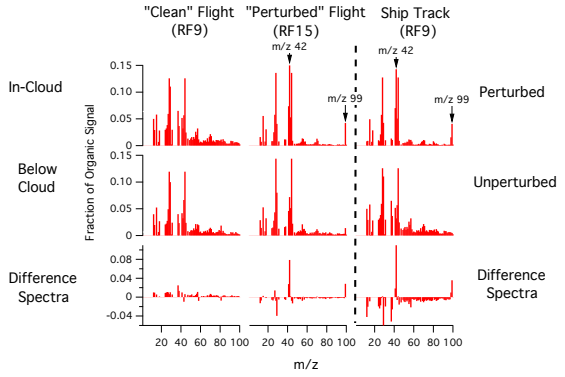

Fig. 10. Aerosol mass spectra comparing the organic signature of aerosol below and within cloud for a clean flight (RF 9) and perturbed flight (RF 15). To the right of the dotted line is a comparison of a ship track in cloud observed during RF 9 to the unperturbed, in-cloud background organics. The bottom row illustrates normalized difference spectra, which are the differences in the normalized (m/z mass/total mass) mass spectra of measurements presented in the top and middle rows. Positive values indicate a relative enhancement in masses observed in the top row spectra whereas negative values indicate a relative enhancement in masses observed in the middle row spectra.

within cloud and was the most likely to have been influenced by ship exhaust.

The top and middle rows in Fig. 10 are normalized organic mass spectra of cloud droplet residuals and dry, below-cloud aerosol, respectively. In general, aerosol and cloud residuals are highly oxidized, exhibiting strong signals at m/z 44 (CO_2^+). These spectra are consistent with marine aerosol measured by Murphy et al. (2009) and Phinney et al. (2006) and cloud droplet residuals measured by Lee et al. (2012). Jimenez et al. (2009) classified aerosol with similar mass spectra as low volatility, highly oxidized secondary organic aerosol (LV-OOA).

Many studies have shown that primary organic aerosol from ship and diesel exhaust exhibit reduced ions consistent with hydrocarbon-like organic aerosol (HOA) (e.g., Canagaratna et al., 2004; Murphy et al., 2009; Phinney et al., 2006). The prominent HOA peaks in fresh ship exhaust (m/z 55, 57, 69, 71, etc.) constitute less than 2 % of the mass in dry aerosol during perturbed flights. Murphy et al. (2009) attributed similar observations to dilution processes by comparing AMS measurements of fresh ship emissions to the organic spectrum of exhaust aged for 60 min. The authors showed that the organic fraction evolved to resemble the surrounding low volatility, unperturbed aerosol – the fraction of m/z 44 increased, while prominent HOA masses decreased. The authors note that this aging process could be explained primarily by dilution with unperturbed aerosol, however accumulation of low volatility organics may have also increased the fraction of oxidized mass.

The lack of prominent HOA masses in aged ship exhaust precludes the use of these peaks as tracers for ship emissions. Figure 10, however, provides evidence for a distinctive mass spectrum of ship emissions in perturbed cloud residuals. During RF 9, little difference existed between the organic signatures of cloud residuals and below-cloud aerosol (Fig. 10, bottom). In contrast, during RF 15, cloud residuals exhibited 8 and 3 % enhancements in masses at m/z 42 and 99 over dry, below-cloud aerosol. This enhancement in m/z 42 and 99 is also observed between the mass spectra of perturbed and unperturbed clouds (Fig. 10, third column), suggesting that m/z 42 and 99 may be linked to cloud-processed ship emissions.

The source of m/z 42 and 99 can be further investigated when considering the time series trend of m/z 99 across multiple flights. Figure 11 illustrates the variation of m/z 99, LWC, and bulk AMS traces for (1) RF 9 – moderately clean, cloudy (2) RF 16 – perturbed, cloudy (3) RF 27 – moderately clean, no clouds and (4) RF 28 – moderately clean, clouds. Flights RF 27 and RF 28 were additional experiments that were conducted outside the sampling area shown in Fig. 1. These flights were performed along the coastline starting in Monterey Bay and ending near the California/Oregon border. Figure 12 shows the flight paths of RF 27 and RF 28 in relationship to the sampling area shown in Fig. 1. Back-trajectories of samples measured in the middle of each flight show that air was transported from the same direction on both days.

Inspection of Fig. 11 reveals multiple trends consistent with the inferences drawn from Fig. 10. First, we note that the time series of m/z 99 varies with bulk AMS traces and is most prominent when measuring ship tracks and perturbed air masses. The time series of m/z 99 shows an enhancement in mass when ship tracks are detected (marked, Fig. 11), which is not observed in nearby unperturbed clouds. Also, we see that m/z 99 is highly variable both in and out of cloud and is coincident with variations of sulfate during a perturbed flight (RF 16). From these results, we infer that the source of m/z 99 is shipping exhaust.

The trends in Fig. 11 also imply that m/z 99 is linked to cloud processing. Among the flights presented, RF 27 was the only one performed under clear meteorological conditions. This is evident by the negligible LWC during vertical soundings. In addition, the larger mode in the aerosol size distribution (Fig. 11, top row) peaks at a lower diameter (77 nm) during clear conditions than during cloudy conditions (180–250 nm). This, along with the low LWC, possibly implies that cloud processing contributed less mass to below-cloud aerosol during RF 27 than other flights. The time series of m/z 99 during RF 27 shows little variation over the course of the flight. If we contrast this to RF 28, which was performed during a cloudy day and along a similar flight path (as illustrated in Fig. 12), we see that the variation of m/z 99

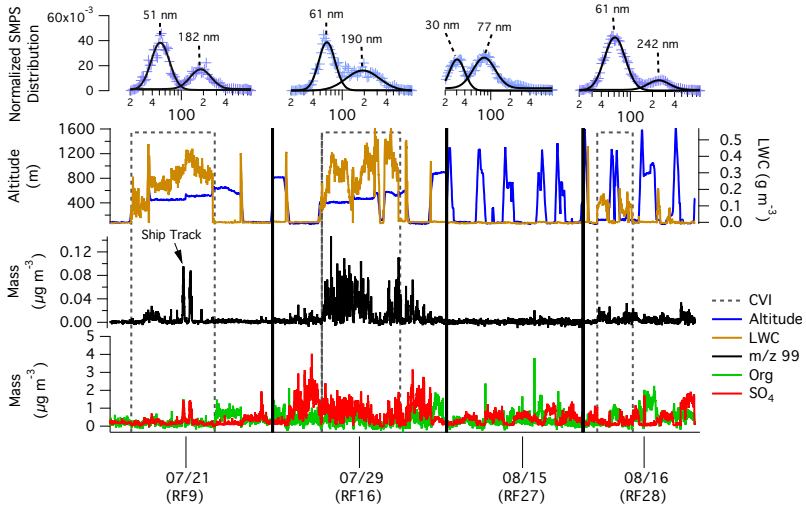

Fig. 11. Time series of organic, sulfate, organic m/z 99, LWC and altitude for research flights RF 9 (moderately clean, clouds), RF 16 (perturbed, clouds), and two additional flights that were performed outside the sampling region defined in Fig. 1, RF 27 (moderately clean, no clouds) and RF 28 (moderately clean, clouds). The top row of normalized aerosol number distributions ($\mathrm{d}N/\mathrm{d}\log D_\mathrm{p}$/(integrated loading)) show the distribution of marine aerosol below cloud for each flight. The dotted boxes show periods when samples were collected through the CVI inlet.

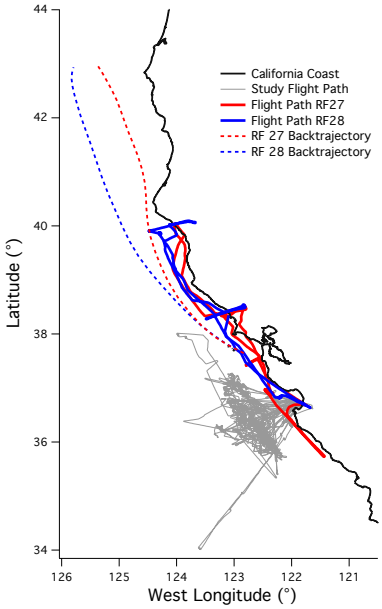

Fig. 12. Path of additional flights RF 27 (red) and RF 28 (blue) compared to the path of all other flights in the present study (grey). Dotted lines are back-trajectories (24 h) for air masses measured during the middle of each flight. RF 27 and RF 28 were coastal gradient flights conducted on clear (RF 27) and cloudy (RF 28) days.

is enhanced in and out of cloud. This evidence, along with the variation of m/z 99 in ship-impacted air masses, leads us to conclude that the variation of m/z 99 likely results from cloud processing of ship emissions.

4.2 Application of m/z 42 and 99 in evaluating ship-impacted airspace

Given the unit mass resolution of the C-ToF AMS, a number of masses could be responsible for the signals observed at m/z 42 and 99. The species $C_2H_2O^+$, $C_3H_6^+$, $C_2H_4N^+$ and $CHOCl_2^+$ are the non-isotopic ions present at m/z 42 while $C_8H_3^+$, $C_6H_{11}O^+$, $C_5H_7O_2^+$ and $C_7H_{15}^+$ are the non-isotopic ions present at m/z 99. Thus, the variation of m/z 42 and 99 in ship-impacted clouds could result from the fragmentation of aqueous-phase oxidation products ($C_2H_2O^+$, $C_5H_7O_2^+$, and $C_6H_{11}O^+$), alkane species ($C_7H_{15}^+$) or unsaturated carbon chains ($C_3H_6^+$, $C_8H_3^+$). High-resolution AMS measurements of marine aerosol performed onboard the R/V *Point Sur* suggests that the enhancements in masses at m/z 42 and 99 result from the increase in signal from $C_2H_2O^+$ and $C_5H_7O_2^+$ (see Sect. 4.3). This supports the presumption that the enhancement of m/z 42 and 99 in perturbed air masses result from aqueous-phase oxidation of ship emissions. We note that other masses, such as m/z 44, are prominent in the mass spectra of ship emissions measured in-cloud (see Fig. 10). We suspect that these masses also result from cloud-processed ship emissions. However, given that these masses also dominate surrounding unperturbed air masses,

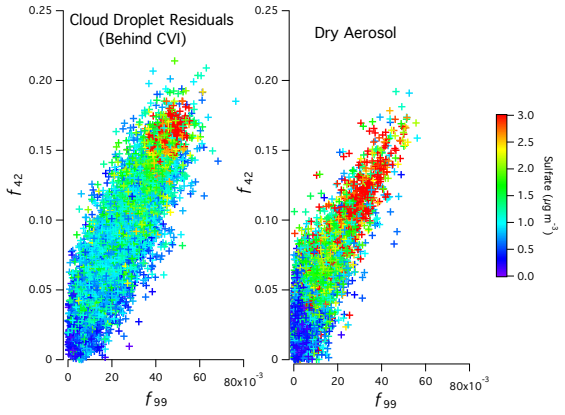

Fig. 13. Variation of the organic fraction of m/z 42 and m/z 99 (f_{42}, f_{99}) in the organic spectra of cloud water droplet residuals and dry aerosol. Markers are colored by sulfate loading to illustrate the potential impact of ships on each measurement.

we believe that using m/z 42 and 99 as tracers for cloud-processed ship emissions will help to delineate the source of subsequent marine aerosol measurements.

Given the large fraction of m/z 42 and 99 in perturbed air relative to clean air, we propose using these masses to indicate the degree to which shipping emissions affect marine aerosol. Figure 13 shows the relationship between the fractions of m/z 42 and 99 in the present study. Markers are colored by sulfate mass concentrations to illustrate the extent to which ships may have impacted each measurement. These plots show that the fraction of m/z 42 in the organic spectra strongly correlates with the fraction of m/z 99, with $R^2 = 0.72$ and 0.67 for measurements of cloud droplet residuals and dry aerosol, respectively. Also, higher fractions of m/z 42 and 99 are coincident with higher loadings of sulfate. Appendix Fig. A2 shows the Pearson R correlation spectrum relating the fraction of m/z 42 and 99 with sulfate loading (top) and the fraction of all other organic masses (middle, bottom). Of all the masses in the organic spectrum, m/z 42 and 99 have the strongest correlation with sulfate ($R = 0.58$ and 0.53, respectively). This correlation could result from simultaneous aqueous phase sulfur oxidation or from the presence of sulfate in shipping emissions. Similarly, these two ions appear to correlate only with each other and not with typical aerosol tracers (e.g., m/z 57 for HOA spectra and m/z 44 for OOA). The relationship between m/z 42 and 99 appears to be unique and strongly linked to ship emissions.

If we take the fraction of m/z 42 and m/z 99 to reflect the degree of cloud-processed ship emissions (as suggested by Figs. 10 and 11) and that ship emissions are coincident with elevated sulfate concentrations (as suggested by Fig. 7 and the observation of high sulfate during the heaviest ship-influenced flights), then we see that Fig. 13 illustrates the extent to which ship emissions influence marine aerosol. Therefore, we propose a metric by which one can evaluate the extent of ship-impacted air masses in the presence of clouds. Measurements of the organic fractions of m/z 42 (f_{42}) and 99 (f_{99}) scattering about the red markers in Fig. 13 ($f_{42} > 0.15$; $f_{99} > 0.04$) would imply heavy influence from shipping emissions. Measurements of m/z 42 and 99 scattering about the green markers ($0.05 < f_{42} < 0.15$; $0.01 < f_{99} < 0.04$) would imply moderate, but persistent, ship influences. Finally, measurements of m/z 42 and 99 scattering about the blue markers ($f_{42} < 0.05$; $f_{99} < 0.01$) would imply clean, non-ship-influenced air. If we apply these metrics to the data in the present study, this would imply that 72 % of the measurements made behind the CVI and 12 % of measurements of dry aerosol were at least moderately impacted by ship emissions.

Despite observing similar spectra from cloud-processed organics originating from many different ships during the E-PEACE campaign, we note that shipping emissions are highly variable. Thus, one cannot assume that all cloud-processed shipping emissions will exhibit the same mass spectra as those presented here. Furthermore, we were unable to determine an exact chemical source for the masses at m/z 42 and 99. Therefore, this proposed metric is subject to future identification of the exact source of these masses. We note that further investigations into the chemical origin of m/z 42 and 99 might also help to elucidate chemical processes not yet identified in current literature.

4.3 High resolution AMS analysis of ions at m/z 42 and 99

Additional aerosol properties were measured below cloud onboard the R/V *Point Sur* from 13–23 July. The R/V *Point Sur* was primarily deployed to generate controlled ship tracks for aerosol/cloud interaction studies (Russell et al., 2012); however, the high-resolution AMS onboard the R/V *Point Sur* continuously sampled marine aerosol. As shown in Table 3 and Fig. 2, the first half of the cruise (14–19 July) was coincident with the cleanest period of the study, whereas the latter half of the cruise (20–23 July) corresponded to periods of elevated sulfate. Investigating the variation of ions at m/z 42 and 99 during the latter half of the cruise is likely to provide information relevant to ship-impacted air masses.

Table 4 summarizes the fraction of the non-isotopic ions at m/z 42 and 99 during the R/V *Point Sur* cruise. Over the entire cruise (top), ions $C_2H_2O^+$ (m/z 42) and $C_5H_7O_2^+$ (m/z 99) constitute the majority (> 50 %) of the mass at their respective m/z. The contribution of these ions to the total signal increased during the latter half of the cruise. The fraction of other ions either decreased or increased little (< 3 %) during the period of elevated sulfate (bottom), implying that ions at m/z 42 and 99 other than $C_2H_2O^+$ and $C_5H_7O_2^+$ are not strongly associated with ship emissions.

Table 4. Fraction of each ion at m/z 42 and m/z 99 over the entire R/V *Point Sur* cruise (top) and during periods of high sulfate loading (bottom). Values in parenthesis are the variance in the measurement.

m/z 42 Average over entire cruise			m/z 99 Average over entire cruise		
Ion	Fraction of total organic signal	Fraction of signal at m/z 42	Ion	Fraction of total organic signal	Fraction of signal at m/z 99
$C_2H_2O^+$	0.014	0.57	$C_5H_7O_2^+$	4.22×10^{-4}	0.51
	(5.11×10^{-5})	(0.030)		(1.26×10^{-7})	(0.044)
$C_3H_6^+$	0.008	0.33	$C_7H_{15}^+$	2.42×10^{-4}	0.21
	(2.43×10^{-5})	(0.037)		(5.48×10^{-8})	(0.036)
$C_2H_4N^+$	0.002	0.08	$C_6H_{11}O^+$	1.84×10^{-4}	0.19
	(2.36×10^{-6})	(0.005)		(2.40×10^{-8})	(0.020)
$CHOCl_2^+$	4.01×10^{-4}	0.02	$C_8H_3^+$	7.81×10^{-5}	0.09
	(1.26×10^{-7})	(0.0004)		(9.21×10^{-9})	(0.008)
Average during period of elevated sulfate (19–23 Jul)			Average during period of elevated sulfate (19–23 Jul)		
Ion	Fraction of total organic signal	Fraction of signal at m/z 42	Ion	Fraction of total organic signal	Fraction of signal at m/z 99
$C_2H_2O^+$	0.020	0.72	$C_5H_7O_2^+$	6.72×10^{-4}	0.58
	(5.07×10^{-5})	(0.013)		(1.25×10^{-7})	(0.030)
$C_3H_6^+$	0.004	0.15	$C_7H_{15}^+$	2.23×10^{-4}	0.15
	(8.27×10^{-6})	(0.009)		(5.11×10^{-8})	(0.023)
$C_2H_4N^+$	0.003	0.11	$C_6H_{11}O^+$	2.23×10^{-4}	0.18
	(2.51×10^{-6})	(0.006)		(2.78×10^{-8})	(0.013)
$CHOCl_2^+$	2.92×10^{-4}	0.01	$C_8H_3^+$	1.08×10^{-4}	0.10
	(1.21×10^{-7})	(0.0004)		(1.17×10^{-8})	(0.007)

Based on Table 4, we presume that $C_2H_2O^+$ and $C_5H_7O_2^+$ are the major ions responsible for the variation in m/z 42 and 99 observed in Fig. 9. Even though the alkane ion at m/z 99 ($C_7H_{15}^+$) constituted approximately 20 % of the signal, this ion can be ruled out as a major contributor to the variation in m/z 99 because other major HOA-type ions (m/z 55, 57, 69, 71, etc.) were not observed to vary significantly with m/z 42 or 99 (see Appendix Fig. A2). $C_3H_6^+$ was also variable and constituted a significant fraction of the signal at m/z 42. Though the contribution of this ion decreased when averaged during the perturbed period, $C_3H_6^+$ is an unsaturated, reduced ion of the series $C_nH_{2n}^+$, which is likely alkene in nature (McLafferty, 1980), that could have originated from an HOA or aged organic source.

Appendix Fig. A3 shows the variation in the organic fraction of $C_2H_2O^+$ and $C_3H_6^+$ at m/z 42 versus the organic fraction of $C_5H_7O_2^+$ at m/z 99. Over the entire cruise, $C_2H_2O^+$ is better correlated with $C_5H_7O_2^+$ than with the reduced ion ($R^2 = 0.49$ versus $R^2 = -0.09$, respectively). The two oxidized ions also exhibit a positive correlation that is consistent with the variation of m/z 42 and m/z 99 observed in Fig. 13. The variation appears to be coincident with increasing sulfate, which is also similar to the trend observed in Fig. 13. Appendix Fig. A3 also shows the time series trends of each ion at m/z 42 and 99 during the clean and perturbed periods. During the clean period, there is little variation in the ions at their respective masses. In contrast, during the periods of inceased sulfate, the variations at m/z 42 and 99 are enhanced and are mostly attributable to $C_2H_2O^+$ and $C_5H_7O_2^+$. In conjunction with Table 5, Fig. A3 suggests that the variations in m/z 42 and 99 observed in C-ToF AMS measurements result from the enhancement of the oxidized ions $C_2H_2O^+$ and $C_5H_7O_2^+$, respectively.

5 Conclusions

A major finding of the present work is the identification of aerosol mass spectral peaks at m/z 42 and 99 as markers for cloud-processed ship emissions. The co-variation of m/z 42 and 99 in dry marine aerosol is unique and likely due to ship emissions that were processed by clouds and subsequently dried. Based on high-resolution AMS measurements, it appears that these masses were primarily due to variations in oxidized ions. In the present study, we are unable to link the variation of these ions to a specific chemical source. Therefore, until future studies can identify a specific compound that is linked to m/z 42 and 99, we must caution that not all cloud-processed shipping emissions may

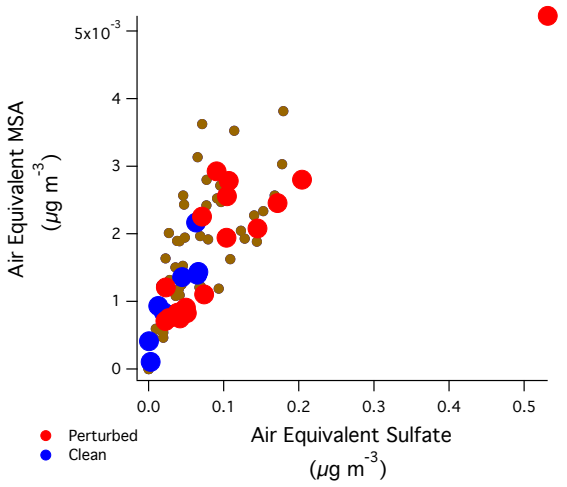

Fig. A1. Variation of air equivalent MSA and sulfate in cloud water droplets. Red markers represent measurements made during perturbed flights (RF 14–18), blue markers represent measurements made during clean flights (RF 5–8). Brown markers are all other measurements.

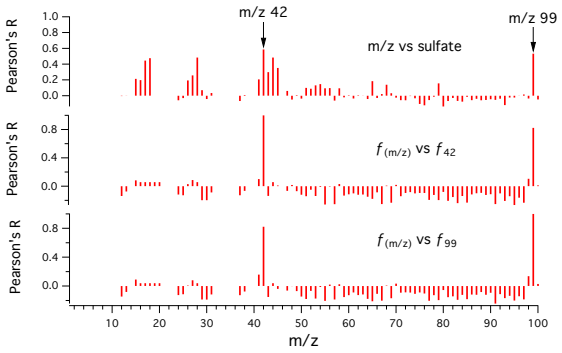

Fig. A2. Pearson R spectrum showing the variation of m/z concentrations vs. the concentration of sulfate (top), the variation of the fraction of m/z 42 (f_{42}) against the fraction of all other organic masses (middle), and the variation of the fraction of m/z 99 (f_{99}) against the fraction of all other organic masses (bottom). These correlations were calculated for measurements made outside of cloud.

exhibit enhancements in these ions. Further investigations into the source of these ions may provide information about the chemical transformations of shipping emissions in the marine atmosphere.

Though the exact chemical source remains uncertain, one can use the fractions of m/z 42 and m/z 99 as a proxy for determining the extent of ship influences on cloud and aerosol properties in the marine environment. Measurements of the organic fractions of m/z 42 (f_{42}) and 99 (f_{99}) falling within the range $f_{42} > 0.15$; $f_{99} > 0.04$ would imply heavy influence from shipping emissions. Measurements of m/z 42 and 99 in the range $0.05 < f_{42} < 0.15$; $0.01 < f_{99} < 0.04$ would imply moderate, but persistent influences from ships. Finally, measurements of m/z 42 and 99 in the range $f_{42} < 0.05$; $f_{99} < 0.01$ would imply clean, non-ship-influenced air. These proxies apply under the condition in which clouds have been impacted by ship emissions. The results from this study also suggest that shipping exhaust is a major contributor to marine aerosol in regions of heavy shipping. If we apply the proposed conditions for moderate shipping influences, we find that 72 % of the measurements illustrated in Fig. 13 are (at least) moderately perturbed cloud particles, while 12 % of the measurements are moderately perturbed evaporated cloud droplets. The marine atmosphere off the coast of Central California is likely seldom free from shipping influences and exhibits a persistent shipping signature on marine particles in the region defined between latitude 35.5–37.5° N and longitude 122–123.25° W.

Appendix A

Additional instrument information

A1 Physical properties of aerosol and cloud droplets

Cloud and aerosol properties were measured onboard the Twin Otter using a suite of wing-mounted probes and cabin-based size classifiers. Aerosol size and number concentrations were measured outside the aircraft using a passive cavity aerosol spectrometer probe (PCASP) (Particle Measuring Systems, Boulder, CO). Simultaneous measurements were performed behind the main aerosol inlet/CVI using a custom-built scanning mobility particle sizer (SMPS) consisting of a differential mobility analyzer (DMA, model 3081, TSI) coupled to a condensation particle counter (CPC 3010, TSI, Shoreview, MN). PCASP and SMPS were calibrated using polystyrene latex spheres.

Cloud droplet distributions were measured using a cloud, aerosol and precipitation spectrometer (CAS) (Droplet Measurement Technologies, Boulder, CO) and was calibrated using glass beads. Cloud droplet number concentrations presented in this study reflect integrated CAS distributions for particles with diameters 2–50 µm.

Cloud condensation nuclei (CCN) number concentrations were measured using a streamwise thermal-graident cloud condensation nuclei counter (CCNC, Droplet Measurement Technologies) (Lance et al., 2006; Roberts and Nenes, 2005). A flow orifice and active control system was used to maintain instrument pressure at 700 mb independent of ambient pressure. The instrument was mostly run in scanning flow CCN analysis (SCFA) mode (Moore and Nenes, 2009). SFCA produced CCN spectra over the range 0.15–0.85 % supersaturation every forty seconds. During zig-zag ship intercepts,

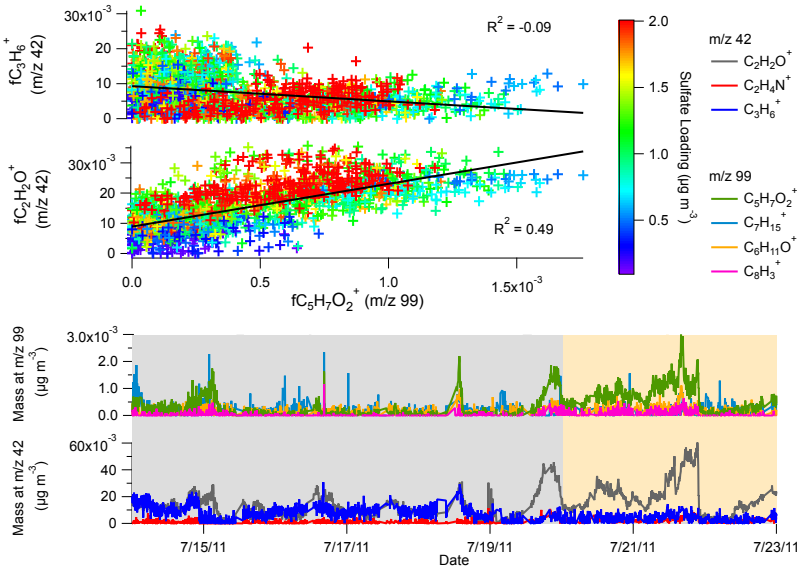

Fig. A3. Top – variation of $C_2H_2O^+$ and $C_3H_6^+$ at m/z 42 with $C_5H_7O_2^+$ at m/z 99. Markers are colored by sulfate loading. Bottom – time series trend showing the variation of the ions at m/z 42 and 99. Region shaded grey corresponds to the clean period of the cruise, region shaded light brown corresponds to the perturbed period of cruise.

CCNC operation was switched to conventional operation, maintaining a constant flow rate and constant 0.15 % supersaturation.

A2 Composition measurements by aerosol mass spectrometry

A compact time-of-flight (CToF) aerosol mass spectrometer (AMS, Aerodyne Research Inc., Billerica, MA) was used onboard the Twin Otter to measure bulk aerosol chemistry. A high-resolution time-of-flight AMS (HR-ToF-AMS) was used onboard the R/V *Point Sur* to characterize detailed aerosol chemistry. The AMS has been described elsewhere and only a brief description is given here (Jayne et al., 2000; Allan et al., 2004; Drewnick et al., 2005). The AMS measures the ensemble average mass spectra and chemically resolved size distribution of non-refractory particle phase organic and inorganic species. Spectra were analyzed in IGOR Pro (WaveMetrics, Inc., Lake Oswego, Oregon, USA) using the SQUIRREL v 1.51H and PIKA v 1.10H modules. Gas phase interferences were corrected using the fragmentation table developed by Allan et al. (2004) and Aiken et al. (2008).

Onboard the Twin Otter, MS mode was run for 8 s per saved run. A pressure-controlled inlet was used to maintain a flow rate of 1.4 $cm^{-3}\,s^{-1}$ to the AMS vacuum chamber. Prior to each flight, the AMS ionization efficiency (the ratio of the number of molecules ionized to the total number of molecules that enter the instrument) was calibrated using dried 350 nm NH_4NO_3 particles. Detection limits were taken to be twice the standard deviation of organic, sulfate, nitrate, ammonium and total mass measured during the filter period.

Composition dependent collection efficiencies (CE) were calculated based on the method by Middlebrook et al. (2012). Figure A4 compares aerosol mass concentrations measured by AMS to calculated aerosol mass concentrations from SMPS data before (left) and after (right) applying the CE correction factor. Volume concentrations measured by the SMPS were calculated by integrating SMPS data from 60–1000 nm. Volume concentrations were then converted to mass concentrations assuming a density of 1.6 g cm^{-3}, which is representative of a mixture of 60 % sulfuric acid ($\rho = 1.84$ g cm^{-3}) and 40 % organics ($\rho = 1.2$ g cm^{-3}) (Phinney et al., 2006). Before applying the CE correction, AMS and SMPS data scatter below the 1 : 1 line with a slope of 0.45. After applying the CE correction, AMS and SMPS data scatter close to the 1 : 1 line with a slope of 0.85. The bias towards higher aerosol mass concentrations calculated from SMPS data may result from a number of unknowns including overestimation of aerosol density, uncertainty of particle losses in the SMPS instrument and uncertainty in the amount of non-refractory material present in the aerosol. In general, however, the good agreement warrants use of the method developed by Middlebrook et al. (2012) in estimating the CE correction factor.

A3 Cloud water chemistry

Cloud water samples were collected using a modified Mohen slotted cloudwater collector (Hegg and Hobbs, 1986).

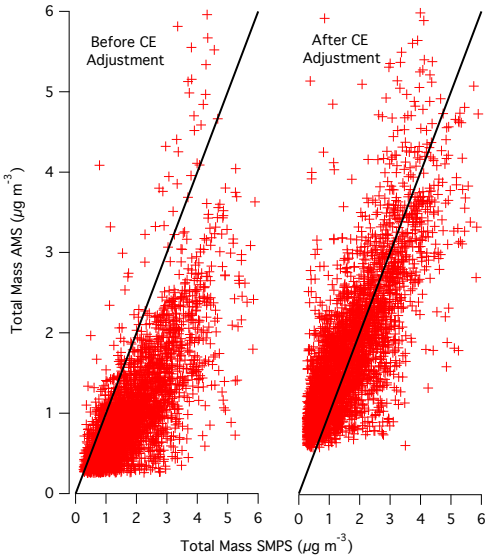

Fig. A4. Comparison of collection efficiency (CE) corrected AMS mass measurements to calculated total mass measured by SMPS. The plot on the left is the trend before CE correction (slope = 0.45), the plot on the right is the trend after CE correction (slope = 0.85). Volume concentration measured by SMPS was converted to mass concentration assuming a density of 1.6 g cm^{-3}, which is representative of a mixture of 60 % sulfuric acid ($\rho = 1.84$ g cm^{-3}) and 40 % organics ($\rho = 1.2$ g cm^{-3}) (Phinney et al., 2006).

Samples were collected at various altitudes and stored at 4 °C until chemical analysis could be performed. Trace metals were measured using inductively coupled plasma mass spectrometry (ICP-MS) and major ions were measured using ion chromatography (IC).

To compare cloud water chemistry measured by off-line analysis to below-cloud aerosol loading measured by AMS, cloud water sample concentrations (ppb) were converted to air equivalent concentrations (μg m^{-3}) as prescribed by (Straub et al., 2007). To achieve this conversion, the ion concentrations measured by ICP-MS and IC were multiplied by the average LWC recorded during sample collection. Measurements reported in air equivalent units reflect the total amount of material present per volume of air.

Acknowledgements. This work was funded by ONR grants N00014-11-1-0783, N00014-10-1-0200, and N00014-10-1-0811, and NSF grants AGS-1013381 and AGS-1008848. We acknowledge Dean Hegg for providing the cloud water collector.

Edited by: R. Krejci

References

Ackerman, A. S., Toon, O. B., and Hobbs, P. V.: Numerical modeling of ship tracks produced by injections of cloud condensation nuclei into marine stratiform clouds, J. Geophys. Res., 100, 7121–7133, 1995.

Agrawal, H., Malloy, Q. G. J., Welch, W. A., Wayne Miller, J., and Cocker III, D. R.: In-use gaseous and particulate matter emissions from a modern ocean going container vessel, Atmos. Environ., 42, 5504–5510, 2008.

Aiken, A. C., DeCarlo, P. F., Kroll, J. H., Worsnop, D. R., Huffman, J. A., Docherty, K. S., Ulbrich, I. M., Mohr, C., Kimmel, J. R., Sueper, D., Sun, Y., Zhang, Q., Trimborn, A., Northway, M., Ziemann, P. J., Canagaratna, M. R., Onasch, T. B., Alfarra, M. R., Prevot, A. S. H., Dommen, J., Duplissy, J., Metzger, A., Baltensperger, U., and Jimenez, J. L.: O/C and OM/OC ratios of primary, secondary, and ambient organic aerosols with high-resolution time-of-flight aerosol mass spectrometry, Environ. Sci. Technol., 42, 4478–4485, 2008.

Allan, J., Delia, A., Coe, H., Bower, K., Alfarra, M., Jimenez, J., Middlebrook, A., Drewnick, F., Onasch, T., and Canagaratna, M.: A generalised method for the extraction of chemically resolved mass spectra from aerodyne aerosol mass spectrometer data, J. Aerosol Sci., 35, 909–922, 2004.

Benedict, K. B., Lee, T., and Collett Jr., J. L.: Cloud water composition over the Southeastern Pacific Ocean during the VOCALS regional experiment, Atmos. Environ., 46, 104–114, 2012.

Bilde, M. and Svenningsson, B.:CCN activation of slightly soluble organics: the importance of small amounts of inorganic salt and particle phase, Tellus, 56B, 128–134, 2004.

Canagaratna, M. R., Jayne, J. T., Ghertner, D. A., Herndon, S., Shi, Q., Jimenez, J. L., Silva, P. J., Williams, P., Lanni, T., Drewnick, F., Demerjian, K. L., Kolb, C. E., and Worsnop, D. R.: Chase studies of particulate emissions from in-use New York City vehicles, Aerosol Sci. Tech., 38, 555–573, 2004.

Christensen, M. W. and Stephens, G. L.: Microphysical and macrophysical responses of marine stratocumulus polluted by underlying ships: Evidence of cloud deepening, J. Geophys. Res., 116, D03201, doi:10.1029/2010JD014638, 2011.

Coakley, J., Bernstein, R., and Durkee, P.: Effect of ship-stack effluents on cloud reflectivity, Science, 237, 1020–1022, 1987.

Corbett, J. J. and Fischbeck, P.: Emissions from ships, Science, 278, 823–824, 1997.

Cunningham, W. C. and Zoller, W. H.: The chemical composition of remote aerosols, J. Aerosol Sci., 12, 367–384, 1981.

Drewnick, F., Hings, S., DeCarlo, P., Jayne, J., Gonin, M., Fuhrer, K., Weimer, S., Jimenez, J., Demerjian, K., Borrmann, S., and Worsnop, D.: A new Time-Of-Flight Aerosol Mass Spectrometer (TOF-AMS) – instrument description and first field deployment, Aerosol Sci. Tech., 39, 637–658, 2005.

Durkee, P. A., Noone, K. J., and Bluth, R. T.: The Monterey area ship track experiment, J. Atmos. Sci., 57, 2523–2541, 2000.

Duvall, R. M., Majestic, B. J., Shafer, M. M., Chuang, P. Y., Simoneit, B. R. T., and Schauer, J. J.: The water-soluble fraction of carbon, sulfur, and crustal elements in Asian aerosols and Asian soils, Atmos. Environ., 42, 5872–5884, 2008.

Eyring, V., Kohler, H., van Aardenne, J., and Lauer, A.: Emissions from international shipping: 1. The last 50 years, J. Geophys. Res., 110, D17305, doi:10.1029/2004JD005619, 2005.

Ervens, B., Gligorovski, S. and Herrmann, H.:Temperature-dependent rate constants for hydroxyl radical reactions with organic compounds in aqueous solutions, Phys. Chem. Chem. Phys., 5, 1811–1824, 2003a.

Ervens, B., George, C., Williams, J.E., Buxton, G.V., Salmon, G.A., Bydder, M., Wilkinson, F., Dentener, F., Mirabel, P., Wolke, R., Herrmann, H.:CAPRAM 2.4 (MODAC mechanism): An extended and condensed tropospheric aqueous phase mechanism and its application, J. Geophys. Res., 108, 4426, doi:10.1029/2002JD002202, 2003b.

Faloona, I.: Sulfur processing in the marine atmospheric boundary layer: A review and critical assessment of modeling uncertainties, Atmos. Environ., 43, 2841–2854, 2009.

Frick, G. and Hoppel, W.: Airship measurements of ship's exhaust plumes and their effect on marine boundary layer clouds, J. Atmos. Sci., 57, 2625–2648, 2000.

Furutani, H., Jung, J., Miura, K., Takami, A., Kato, S., Kajii, Y., and Uematsu, M.: Single-particle chemical characterization and source apportionment of iron-containing atmospheric aerosols in Asian outflow, J. Geophys. Res., 116, D18204, doi:10.1029/2011JD015867, 2011.

Guieu, C., Duce, R., and Arimoto, R.: Dissolved input of manganese to the ocean: Aerosol source, J. Geophys. Res., 99, 18789–18800, 1994.

Hegg, D. A. and Hobbs, P. V.: Sulfate and nitrate chemistry in cumuliform clouds, Atmos. Environ., 20, 901–909, 1986.

Hegg, D. A., Covert, D. S., Rood, M. J., and Hobbs, P. V.: Measurements of aerosol optical properties in marine air, J. Geophys. Res., 101, 12893–12903, 1996.

Hegg, D.A., Covert, D.S., Jonsson, H., Covert, P.A.: Determination of the Transmission Efficiency of an Aircraft Aerosol Inlet, Aerosol Sci. Technol., 39, 966–971, 2005.

Hegg, D. A., Covert, D. S., and Jonsson, H. H.: Measurements of size-resolved hygroscopicity in the California coastal zone, Atmos. Chem. Phys., 8, 7193–7203, doi:10.5194/acp-8-7193-2008, 2008.

Hegg, D. A., Covert, D., Jonsson, H., and Woods, R.: Differentiating natural and anthropogenic cloud condensation nuclei in the California coastal zone, Tellus B, 61, 669–676, 2009.

Hegg, D. A., Covert, D. S., Jonsson, H. H., and Woods, R. K.: The contribution of anthropogenic aerosols to aerosol light-scattering and CCN activity in the California coastal zone, Atmos. Chem. Phys., 10, 7341–7351, doi:10.5194/acp-10-7341-2010, 2010.

Hersey, S. P., Sorooshian, A., Murphy, S. M., Flagan, R. C., and Seinfeld, J. H.: Aerosol hygroscopicity in the marine atmosphere: a closure study using high-time-resolution, multiple-RH DASH-SP and size-resolved C-ToF-AMS data, Atmos. Chem. Phys., 9, 2543–2554, doi:10.5194/acp-9-2543-2009, 2009.

Hoppel, W., Frick, G., and Larson, R.: Effect of nonprecipitating clouds on the aerosol size distribution in the marine boundary layer, Geophys. Res. Lett., 13, 125–128, 1986.

Hoppel, W., Frick, G., and Fitzgerald, J.: Marine boundary layer measurements of new particle formation and the effects nonprecipitating clouds have on aerosol size distribution, J. Geophys. Res., 99, 14443–14459, 1994.

Hudson, J. G., Garrett, T. J., Hobbs, P. V., Strader, S. R., Xie, Y., and Yum, S. S.: Cloud Condensation Nuclei and Ship Tracks, J. Atmos. Sci., 57, 2696–2706, 2000.

Jayne, J. T., Leard, D. C., Zhang, X., Davidovits, P., Smith, K. A., Kolb, C. E., and Worsnop, D. R.: Development of an aerosol mass spectrometer for size and composition analysis of submicron particles, Aerosol Sci. Tech., 33, 49–70, 2000.

Jimenez, J. L.,Canagaratna, M. R., Donahue, N. M.,Prévôt, A. S. H., Zhang, Q., Kroll, J. H., DeCarlo, P. F., Allan, J. D., Coe, H., Ng, N. L., Aiken, A. C., Docherty, K. S., Ulbrich, I. M., Grieshop, A. P., Robinson, A. L., Duplissy, J., Smith, J. D., Wilson, K. R., Lanz, V. A., Hueglin, C., Sun, Y. L., Tian, J., Laaksonen, A., Raatikainen, T., Rautiainen, J., Vaattovaara, P., Ehn, M., Kulmala, M., Tomlinson, J. M., Collins, D. R., Cubison, M. J., Dunlea, J., Huffman, J. A., Onasch, T. B., Alfarra, M. R., Williams, P. I., Bower, K., Kondo, Y., Schneider, J., Drewnick, F., Borrmann, S., Weimer, S., Demerjian, K., Salcedo, D., Cottrell, L., Griffin, R., Takami, A., Miyoshi, T., Hatakeyama, S., Shimono, A., Sun, J. Y., Zhang, Y. M., Dzepina, K., Kimmel, J. R., Sueper, D., Jayne, J. T., Herndon, S. C., Trimborn, A. M., Williams, L. R., Wood, E. C., Middlebrook, A. M., Kolb, C. E., Baltensperger, U., and Worsnop, D. R.:Evolution of Organic Aerosols in the Atmosphere, Science, 326, 1525–1529, 2009.

Katoshevski, D., Nenes, A., and Seinfeld, J. H.:A study of processes that govern the maintenance of aerosols in the marine boundary layer, J. Aerosol Sci., 30, 503–532, 1999.

Kazil, J., Wang, H., Feingold, G., Clarke, A. D., Snider, J. R., and Bandy, A. R.: Modeling chemical and aerosol processes in the transition from closed to open cells during VOCALS-REx, Atmos. Chem. Phys., 11, 7491–7514, doi:10.5194/acp-11-7491-2011, 2011.

Lance, S., Nenes, A., Medina, J., and Smith, J. N.: Mapping the operation of the DMT continuous flow CCN counter, Aerosol Sci. Techol., 40, 242–254, 2006.

Langley, L., Leaitch, W. R., Lohmann, U., Shantz, N. C., and Worsnop, D. R.: Contributions from DMS and ship emissions to CCN observed over the summertime North Pacific, Atmos. Chem. Phys., 10, 1287–1314, doi:10.5194/acp-10-1287-2010, 2010.

Lee, A. K. Y., Hayden, K. L., Herckes, P., Leaitch, W. R., Liggio, J., Macdonald, A. M., and Abbatt, J. P. D.: Characterization of aerosol and cloud water at a mountain site during WACS 2010: secondary organic aerosol formation through oxidative cloud processing, Atmos. Chem. Phys. Discuss., 12, 6019–6047, doi:10.5194/acpd-12-6019-2012, 2012.

Lu, M.-L., Sorooshian, A., Jonsson, H. H., Feingold, G., Flagan, R. C., and Seinfeld, J. H.: Marine stratocumulus aerosol-cloud relationships in the MASE-II experiment: Precipitation susceptibility in Eastern Pacific marine stratocumulus, J. Geophys. Res., 114, D24203, doi:10.1029/2009JD012774, 2009.

McInnes, L., Quinn, P., Covert, D., and Anderson, T.: Gravimetric analysis, ionic composition, and associated water mass of the marine aerosol, Atmos. Environ., 30, 869–884, 1996.

McInnes, L., Covert, D., and Baker, B.: The number of sea-salt, sulfate, and carbonaceous particles in the marine atmosphere, Tellus, 49, 300–313, 1997.

McLafferty, F.: Interpretation of Mass Spectra, University Science Books, 3rd Edn., 1980.

Middlebrook, A. M., Bahreini, R., Jimenez, J. L., and Canagaratna, M. R.: Evaluation of composition-dependent collection efficiencies for the aerodyne aerosol mass spectrometer using

field data, Aerosol Sci. Tech., 46, 258–271, 2012.

Moore, R. H. and Nenes, A.: Scanning flow CCN analysis – a method for fast measurements of CCN spectra, Aerosol Sci. Techol., 43, 1192–1207, 2009.

Moore, R. H., Bahreini, R., Brock, C. A., Froyd, K. D., Cozic, J., Holloway, J. S., Middlebrook, A. M., Murphy, D. M., and Nenes, A.: Hygroscopicity and composition of Alaskan Arctic CCN during April 2008, Atmos. Chem. Phys., 11, 11807–11825, doi:10.5194/acp-11-11807-2011, 2011.

Moore, R. H., Cerully, K., Bahreini, R., Brock, C. A., Middlebrook, A. M., and Nenes, A.: Hygroscopicity and composition of California CCN during summer 2010, J. Geophys. Res., 117, D00V12, doi:10.1029/2011JD017352, 2012.

Murphy, S. M., Agrawal, H., Sorooshian, A., Padró, L. T., Gates, H., Hersey, S., Welch, W. A., Jung, H., Miller, J. W., Cocker III, D. R., Nenes, A., Jonsson, H. H., Flagan, R. C., and Seinfeld, J. H.: Comprehensive simultaneous shipboard and airborne characterization of exhaust from a modern container ship at sea, Environ. Sci. Technol., 43, 4626–4640, 2009.

Noone, K., Ostrom, E., Ferek, R., Garrett, T., Hobbs, P., Johnson, D., Taylor, J., Russell, L., Flagan, R., Seinfeld, J. H., O'Dowd, C., Smith, M., Durkee, P., Nielsen, K., Hudson, J., Pockalny, R., De Bock, L., Van Grieken, R., Gasparovic, R., and Brooks, I.: A case study of ships forming and not forming tracks in moderately polluted clouds, Am. Meterol. Soc., 57, 2729–2747, 2000.

Ohta, A., Tsuno, H., Kagi, H., Kanai, Y., Nomura, M., Zhang, R., and Terashima, S.: Chemical compositions and XANES speciations of Fe, Mn and Zn from aerosols collected in China and Japan during dust events, Geochem. J., 40, 363–376, 2006.

Ovadnevaite, J., O'Dowd, C., Dall'Osto, M., Ceburnis, D., Worsnop, D.R., and Berresheim, H.: Detecting high contributions of primary organic matter to marine aerosol: A case study, Geophys. Res. Lett., 38, L02807, doi:10.1029/2010GL046083, 2011.

Phinney, L., Richard Leaitch, W., Lohmann, U., Boudries, H., Worsnop, D. R., Jayne, J. T., Toom-Sauntry, D., Wadleigh, M., Sharma, S., and Shantz, N.: Characterization of the aerosol over the sub-arctic North East Pacific Ocean, Deep-Sea Res. Pt. II, 53, 2410–2433, 2006.

Roberts, G. C. and Nenes, A.: A continuous-flow streamwise thermal-gradient CCN chamber for atmospheric measurements, Aerosol Sci. Techol., 39, 206–221, 2005.

Russell, L. M., Sorooshian, A., Seinfeld, J. H., Albrecht, B. A., Nenes, A., Ahlm, L., Chen, Y.-C., Coggon, M. M., Craven, J. S., Flagan, R. C., Frossard, A. A., Jonsson, H., Jung, E., Lin, J. J., Metcalf, A. R., Modini, R., Mulmenstadt, J., Roberts, G. C., Shingler, T., Song, S., Wang, Z., and Wonaschutz, A.: Eastern Pacific Emitted Aerosol Cloud Experiment (E-PEACE), B. Am. Meteorol. Soc., in press, 2012.

Shingler, T., Dey, S., Sorooshian, A., Brechtel, F. J., Wang, Z., Metcalf, A., Coggon, M., Mülmenstädt, J., Russell, L. M., Jonsson, H. H., and Seinfeld, J. H.: Characterisation and airborne deployment of a new counterflow virtual impactor inlet, Atmos. Meas. Tech., 5, 1259–1269, doi:10.5194/amt-5-1259-2012, 2012.

Sholkovitz, E. R., Sedwick, P. N., and Church, T. M.: Influence of anthropogenic combustion emissions on the deposition of soluble aerosol iron to the ocean: Empirical estimates for island sites in the North Atlantic, Geochim. Cosmochim. Ac., 73, 3981–4003, 2009.

Sorooshian, A., Lu, M.-L., Brechtel, F. J., Jonsson, H., Feingold, G., Flagan, R. C., and Seinfeld, J. H.: On the Source of Organic Acid Aerosol Layers above Clouds, Environ. Sci. Technol., 41, 4647–4654, 2007a.

Sorooshian, A., Ng, N. L., Chan, A. W. H., Feingold, G., Flagan, R. C., and Seinfeld, J. H.: Particulate organic acids and overall water-soluble aerosol composition measurements from the 2006 Gulf of Mexico Atmospheric Composition and Climate Study (GoMACCS), J. Geophys. Res., 112, D13201, doi:10.1029/2007JD008537, 2007b.

Sorooshian, A., Padró, L. T., Nenes, A., Feingold, G., McComiskey, A., Hersey, S. P., Gates, H., Jonsson, H. H., Miller, S. D., Stephens, G. L., Flagan, R. C., and Seinfeld, J. H.: On the link between ocean biota emissions, aerosol, and maritime clouds: Airborne, ground, and satellite measurements off the coast of California, Global Biogeochem. Cy., 23, GB4007, doi:10.1029/2009GB003464, 2009.

Statham, P. and Chester, R.: Dissolution of manganese from marine atmospheric particulates into seawater and rainwater, Geochim. Cosmochim. Ac., 52, 2433–2437, 1988.

Straub, D. J., Lee, T., and Collett Jr., J. L.: Chemical composition of marine stratocumulus clouds over the Eastern Pacific Ocean, J. Geophys. Res., 112, D04307, doi:10.1029/2006JD007439, 2007.

Ulbrich, I. M., Canagaratna, M. R., Zhang, Q., Worsnop, D. R., and Jimenez, J. L.: Interpretation of organic components from Positive Matrix Factorization of aerosol mass spectrometric data, Atmos. Chem. Phys., 9, 2891–2918, doi:10.5194/acp-9-2891-2009, 2009.

Yan, F., Winijkul, E., Jung, S., Bond, T. C., and Streets, D. G.: Global emission projections of particulate matter (PM): I. Exhaust emissions from on-road vehicles, Atmos. Environ., 45, 4830–4844, 2011.

Chapter 4

Hygroscopic Properties of Smoke-generated Organic Aerosol Particles Emitted in the Marine Atmosphere

Atmos. Chem. Phys., 13, 9819–9835, 2013
www.atmos-chem-phys.net/13/9819/2013/
doi:10.5194/acp-13-9819-2013

Atmospheric Chemistry and Physics Open Access

Hygroscopic properties of smoke-generated organic aerosol particles emitted in the marine atmosphere

A. Wonaschütz[1], M. Coggon[2], A. Sorooshian[3,4], R. Modini[5,*], A. A. Frossard[5], L. Ahlm[5,], J. Mülmenstädt[5], G. C. Roberts[5,6], L. M. Russell[5], S. Dey[7], F. J. Brechtel[7], and J. H. Seinfeld[2]**

[1]University of Vienna, Faculty of Physics, Vienna, Austria
[2]Department of Chemical Engineering, California Institute of Technology, Pasadena, California, USA
[3]Department of Chemical and Environmental Engineering, University of Arizona, Tucson, AZ, USA
[4]Department of Atmospheric Sciences, University of Arizona, Tucson, AZ, USA
[5]Scripps Institution of Oceanography, University of California, San Diego, CA, USA
[6]Centre National de la Recherche Scientifique – Groupe d'études de l'Atmosphère Météorologique, Toulouse, France
[7]Brechtel Manufacturing, Inc., Hayward, CA, USA
[*]now at: Ecole Polytechnique Federale de Lausanne, Lausanne, Switzerland
[**]now at: Department of Applied Environmental Science, Stockholm University, Stockholm, Sweden

Correspondence to: A. Sorooshian (armin@email.arizona.edu)

Received: 15 April 2013 – Published in Atmos. Chem. Phys. Discuss.: 6 May 2013
Revised: 12 August 2013 – Accepted: 13 August 2013 – Published: 7 October 2013

Abstract. During the Eastern Pacific Emitted Aerosol Cloud Experiment (E-PEACE), a plume of organic aerosol was produced by a smoke generator and emitted into the marine atmosphere from aboard the R/V *Point Sur*. In this study, the hygroscopic properties and the chemical composition of the plume were studied at plume ages between 0 and 4 h in different meteorological conditions. In sunny conditions, the plume particles had very low hygroscopic growth factors (GFs): between 1.05 and 1.09 for 30 nm and between 1.02 and 1.1 for 150 nm dry size at a relative humidity (RH) of 92 %, contrasted by an average marine background GF of 1.6. New particles were produced in large quantities (several 10 000 cm^{-3}), which lead to substantially increased cloud condensation nuclei (CCN) concentrations at supersaturations between 0.07 and 0.88 %. Ratios of oxygen to carbon (O : C) and water-soluble organic mass (WSOM) increased with plume age: from < 0.001 to 0.2, and from 2.42 to 4.96 µg m^{-3}, respectively, while organic mass fractions decreased slightly (∼ 0.97 to ∼ 0.94). High-resolution aerosol mass spectrometer (AMS) spectra show that the organic fragment m/z 43 was dominated by $C_2H_3O^+$ in the small, new particle mode and by $C_3H_7^+$ in the large particle mode. In the marine background aerosol, GFs for 150 nm particles at 40 % RH were found to be enhanced at higher organic mass fractions: an average GF of 1.06 was observed for aerosols with an organic mass fraction of 0.53, and a GF of 1.04 for an organic mass fraction of 0.35.

1 Introduction

The interaction of atmospheric aerosol particles with water is a crucial factor affecting their evolution in the atmosphere. By taking up water, particles grow in size and experience modifications to their refractive index, which changes their ability to interact with solar radiation. Activation into cloud droplets is a determining factor in the atmospheric lifetime of particles. Furthermore, cloud droplets and water in deliquesced aerosol particles provide an aqueous medium for chemical reactions, which can lead to a change in the chemical composition of the particles (Hegg, 1985; Blando and Turpin, 2000; El Haddad et al., 2009; Bateman et al., 2011; Ervens et al., 2011).

Organic compounds can have a profound impact on the water-uptake properties of particles. An increase in the organic mass fraction of aerosol particles can reduce water uptake at relative humidities (RH) above the deliquescence RH (DRH) of salts, while simultaneously enabling hygroscopic

growth at RHs below the DRH (e.g., Dick et al., 2000; Hersey et al., 2009; Meyer et al., 2009). In the atmosphere, aging processes affect hygroscopic properties of the organic fraction of aerosols (commonly referred to as organic aerosols, OA). Organic components in fresh aerosols have been observed to decrease water uptake, but in aged aerosols, they can have the opposite effect (Saxena et al., 1995). Aging of aerosols broadly encompasses any change in their chemical composition and physical properties during their lifetime in the atmosphere. For OA, important aging processes include the addition of organic mass through secondary production via gas-to-particle conversion and aqueous-phase production (e.g., George et al., 2007; El Haddad et al., 2009; Ervens et al., 2011), as well as the continuing oxidation during photochemical and cloud processing (Jimenez et al., 2009). The transition from less oxidized to more oxidized organic compounds in OA increases hygroscopic growth factors ($GF = d_{p,RH}/d_{p,dry}$) (Massoli et al., 2010; Duplissy et al., 2011). The conversion of hydrophobic primary OA to hydrophilic particles has been shown to be rapid during the daytime in an urban environment (Wang et al., 2010).

Hygroscopic growth and cloud condensation nuclei (CCN) activity are often described in terms of a single parameter connecting the hygroscopicity of particles in the sub- and the supersaturated regime (Petters and Kreidenweis, 2007; Wex et al., 2008; Dusek et al., 2011). However, observations of several aerosol types, including biomass burning aerosol (Petters et al., 2009; Dusek et al., 2011), laboratory-generated secondary organic aerosol (SOA) (Wex et al., 2009), primary marine organic aerosol (Ovadnevaite et al., 2011a), and urban ambient aerosol (Hersey et al., 2013), have shown conflicting behavior in the form of reduced hygroscopic growth factors with simultaneous enhancements in CCN activity. The role of organic compounds in changing water-uptake properties of aerosols is not fully understood.

The marine environment is well suited to study the aging of organic aerosols. In continental locations, with numerous anthropogenic and natural aerosol sources, fresh and aged organic aerosols are often found in the same air mass. Over the ocean, sources of organic aerosols are more limited. Continental outflow is often the most important source of OA (Hawkins et al., 2010); however, primary and secondary marine sources can be relevant (Gantt and Meskhidze, 2013). An important marine primary organic aerosol source is bubble bursting, which transfers dissolved or film-forming organic substances from the ocean surface into the particle phase in the atmosphere (e.g., Middlebrook et al., 1998; O'Dowd et al., 2004; Cavalli et al., 2004; Leck and Bigg, 2005; Facchini et al., 2008a; Russell et al., 2010; Modini et al., 2010; Ovadnevaite et al., 2011b). Proposed marine sources of SOA include biogenic amines (Facchini et al., 2008b; Sorooshian et al., 2009; Dall'Osto et al., 2012), isoprene oxidation above phytoplankton blooms (Meskhidze and Nenes, 2006; O'Dowd and de Leeuw, 2007), and aqueous-phase production in marine stratus clouds (Crahan et al., 2004; Sorooshian et al., 2010). In the absence of such sources, marine background aerosol typically shows a hygroscopic mode with growth factors around 1.6–1.79 at 90 % RH (Swietlicki et al., 2008, and references therein). Less hygroscopic and hydrophobic modes are encountered in continental outflow (e.g., Hawkins et al., 2010; Hegg et al., 2010), free tropospheric air masses, and during episodes of fresh biogenic aerosol production (Swietlicki et al., 2008; Allan et al., 2009; Hersey et al., 2009; Mochida et al., 2011). Hygroscopic growth factors and the activation ratio (the ratio of CCN at a given supersaturation to the total measured particle number concentration, CCN / CN) have been shown to increase with the age of the continental air mass (Massling et al., 2007; Furutani et al., 2008). Anthropogenic disturbances such as emissions from ship traffic and oil spills constitute further sources of organic aerosols in the marine atmosphere. The injection of container ship exhaust, which includes particles consisting of a mix of hydrocarbon-like organic aerosol and sulfate (Murphy et al., 2009), is a persistent anthropogenic impact on atmospheric composition (Eyring et al., 2009). During the Deepwater Horizon oil spill, hydrocarbon-like SOA was found to derive from intermediate volatility organic compounds evaporated from the oil surface (de Gouw et al., 2011). Most of these particles acted as CCN at supersaturations exceeding 0.3 %, but were characterized by low hygroscopicity in the subsaturated regime (Moore et al., 2012).

This study aims to improve the process-level understanding of changes in water-uptake properties of organic aerosol by investigating a rare "hybrid experiment" between laboratory and field conditions: a well-defined organic aerosol is artificially generated in large quantities and exposed to the real marine atmosphere. We report measurements of hygroscopic growth factors and CCN concentrations in this organic plume, and compare its aging and its hygroscopic properties in both cloudy and sunny conditions.

2 Methods

2.1 The E-PEACE field campaign

The Eastern Pacific Emitted Aerosol Cloud Experiment (E-PEACE) was a field campaign conducted off the coast of California in July and August of 2011. Its general aim was to study aerosol–cloud–radiation interactions through the controlled emission of known aerosols into the marine stratocumulus deck and the measurement of its effects from ship, aircraft, and satellite observational platforms. A detailed description of the experiment and its first results are given by Russell et al. (2013). The location of the experiment is shown in Fig. 1. In this study, we investigate an organic plume produced on and emitted from the R/V *Point Sur* on a 12-day research cruise (12–23 July). To create the plume, refurbished battleship smoke generators were operated at the ship's stern:

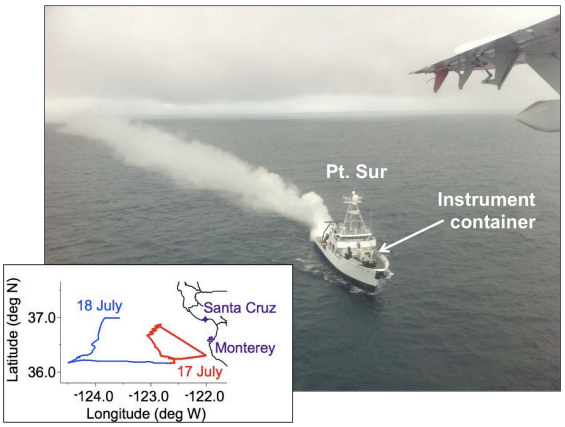

Fig. 1. Smoke generation on the R/V *Point Sur* (photo taken from CIRPAS Twin Otter). Insert: General area of the E-PEACE field campaign off the coast of California. The ship's course is shown for the days that are the focus of this study.

pulse jet engines operated with standard gasoline pumped and heated a paraffin-type oil, which vaporized at a temperature of about 150 °C, without igniting. Upon emission into the marine atmosphere through three nozzles, the oil condensed into a thick smoke of oil droplets and vapor ("organic plume", Fig. 1). More details on the oil production can be found in Russell et al. (2013). The properties of the organic plume and its interactions with the marine environment were measured from two platforms: the Center for Interdisciplinary Remotely-Piloted Aircraft Studies (CIRPAS) Twin Otter aircraft, and an instrument container on the R/V *Point Sur* itself. This study focuses on measurements from the R/V *Point Sur*.

2.2 Instruments

A complete list of all instruments located on the two platforms is given by Russell et al. (2013). The instruments onboard the R/V *Point Sur* whose data are used for this study are summarized in Table 1. The R/V *Point Sur* instrument container was located at the ship's bow. A common vertical inlet, which was shielded from spray, sampled ambient aerosol up to several micrometers in diameter. The aerosol was dried in diffusion driers before distribution to the instruments. Submicrometer particle size distributions were measured with a scanning electrical mobility spectrometer (SEMS Model 138 2002, Brechtel Manufacturing Inc.). Size distributions of larger particles were measured with an aerodynamic particle sizer (APS 3321, TSI Inc., size range 0.5–20 µm) and an optical particle sizer (OPS 330, TSI Inc., size range 0.3–10 µm). A condensation particle counter (CPC 3010, TSI Inc.) measured total particle number concentration.

Hygroscopic growth factors were measured using a humidified tandem differential mobility analyzer (HTDMA Model 3002, Brechtel Manufacturing Inc.) (Sorooshian et al., 2012). The system consisted of a dry DMA (DMA 1, RH < 8 %) selecting particles with dry diameters of 30, 75, 150, and 300 nm; a humidifier, in which the dry particles were exposed to RHs of 40, 70, 85, and 92 %; and a second, humidified DMA (DMA 2), which measured the number size distribution after hygroscopic growth. CCN concentrations for supersaturations (S) ranging between 0.07 and 0.88 % were measured using a CCN counter (custom design, miniaturized after Roberts and Nenes, 2005).

Submicrometer particles, separated from larger particles with a cyclone, were analyzed with a high-resolution time-of-flight aerosol mass spectrometer (AMS, Aerodyne Research Inc.) (DeCarlo et al., 2006) to measure the nonrefractory, inorganic (ammonium, sulfate, nitrate, chloride), and organic chemical composition. Submicrometer particles were also collected on 37 mm Teflon filters and scanned using Fourier transform infrared (FTIR) spectroscopy (Tensor 27, Bruker Optics, Inc.) (Russell et al., 2009; Frossard and Russell, 2012). I addition, samples of the ship diesel and smoke oil that were used during the E-PEACE cruise were atomized (atomizer, TSI Inc.), collected on Teflon filters, and scanned using FTIR spectroscopy.

Water-soluble organic carbon (WSOC) mass concentrations were quantified with a particle-into-liquid sampler (PILS, Brechtel Manufacturing Inc.) coupled to a total organic carbon analyzer (Sievers, Model 800) (Sullivan et al., 2006; Wonaschuetz et al., 2011). Black carbon (BC) concentrations were obtained from a single-particle soot photometer (SP2, Droplet Measurement Technologies Inc.). Meteorological conditions, including ambient temperature, wind direction and speed (corrected for the ship's movement), and RH, were measured routinely on the R/V *Point Sur*, along with ship-specific data such as heading and speed. Additional visual observations (e.g., fog, other ships) were noted in deck logs.

Mass concentrations of oxalate and glyoxylate are reported in this work for the smoke-sampling events (described in Sect. 2.6). PM_{10} was collected on prebaked 47 mm quartz fiber filters that were stored in a freezer prior to chemical analysis. The filter extraction procedure consisted of ultrasonication (15 min) of filter halves with 18.2 MΩ Milli-Q water. Syringe filters (Acrodisc filter, 25 µm) were used to remove any remaining insoluble matter from the extracts after ultrasonication. Ion chromatography analysis (IC – Thermo Scientific Dionex ICS-5000 anion system with an AS11-HC 2 mm column) was conducted using a 38 min multi-step gradient program with sodium hydroxide eluent (1 mM from 0 to 8 min, 1 mM to 30 mM from 8 to 28 min, 30 mM to 60 mM from 28 to 38 min).

Table 1. Instruments on the R/V *Point Sur.*

Measurement	Instrument	Size range	Time resolution
Particle size distribution	APS	0.5–20 µm	2 min
	OPS	0.3–50 µm	2 min
	SEMS	10–946 nm	5 min
Number concentration	CPC	>10 nm	1 s
Water uptake	CCN counter		9 s
	HTDMA (hygroscopic growth)	30, 75, 150, 300 nm	∼ 5 min
Chemical composition	AMS	<1 µm	4 min
	PILS – TOC (water-soluble organic carbon)	<1 µm	6 min
	SP2 (black carbon)	80–300 nm	10 s
	Filters scanned with FTIR spectroscopy	<1 µm	20 min–4 h

2.3 Data processing and quality control

For the HTDMA data, an important source of uncertainty is the variability of RH in DMA 2 (Swietlicki et al., 2008). For quality control, temperature and RH in DMA 2 and their variability in time (over the duration of a scan) and space (along the DMA 2 column) were calculated from measurements of flow rates, temperatures, and RH in the sample flow out of the humidifier and the sheath flow in DMA 2 at the beginning of the DMA 2 column (these two flows were humidified separately), and of temperature in the excess flow at the end of the DMA 2 column. Scans were accepted if they fulfilled the following criteria: (i) flow rates were within 25 % of the set point, (ii) combined humidifier and sheath air RH variability over the time of a scan did not exceed ±1.5 % RH, and (iii) the temperature gradient over the length of the DMA 2 did not exceed ±1 °C. Based on these criteria, 75 % of all scans were accepted. The raw count data from DMA 2 were inverted to produce the growth factor distributions: raw counts were shifted in time to correct for particle transit time between the DMA column and particle counter and desmeared to correct for a finite particle counter response time. The desmeared data were finally inverted using the diffusing form of the DMA transfer function (Stolzenburg, 1988) and assuming a single charge. Correcting only for a single charge (i.e., inverting for DMA 2 only, rather than the combined TDMA system) will accurately recover GF values and the relative fractions of growth factor populations, with some limitations on the resolution of the distribution shape (Gysel et al., 2009). Growth factors were estimated by fitting a lognormal function to the growth factor distributions, assuming mono-modal distributions as a first-order estimate and advancing to multi-peak fits when needed (Sect. 3.5).

The GF uncertainty was estimated using modeled GF values for selected inorganic salts (ammonium sulfate and sodium chloride) and malonic acid from a thermodynamic model of particle water uptake (Brechtel and Kreidenweis, 2000a, b; Sorooshian et al., 2008). Over the course of the HTDMA measurements, the change in mean RH in DMA 2 from one scan to the next rarely exceeded 1 % RH. The measurement GF uncertainty was therefore estimated by calculating the change in GF for a change in RH of 1 % (RH) around the set-point RH for pure particles of the three model substances. The maximum GF uncertainty for a RH set point of 40 % is estimated to be 0.010 (malonic acid particles; the RH set point of 40 % is below the efflorescence point for ammonium sulfate and sodium chloride). For the RH set point of 92 %, the maximum GF uncertainty is 0.185 (sodium chloride). Since the three model substances are among the most hygroscopic inorganic and organic compounds, these changes in RH represent upper limits on the uncertainty in the measured GF of the ambient particles, which are likely an internal mixture of more and less hygroscopic compounds, or on plume particles, which, as will be outlined, contained a large fraction of nonhygroscopic organics.

The SEMS, OPS, and APS each use a different operating principle to size aerosol particles. Total aerosol size distributions were created by merging the distributions over the nominal diameter range 0.01–20 µm using an algorithm based on Khlystov et al. (2004). For the AMS data, a collection efficiency of 0.5 and a detection limit of 0.01 µg m^{-3} were applied. Total nonrefractory mass concentrations were calculated as the sum of organic and inorganic concentrations. Size distributions of the nonrefractory mass components were calculated from the AMS measurements (DeCarlo et al., 2004, 2006). Since the measured masses were close to the detection limit, the size distributions were smoothed over 11 size bins, resulting in a smoothed size distribution between 21 and 946 nm. The AMS V-mode measurements were used to calculate the ratio of oxygen to carbon (O : C) in the measured organic particles (Aiken et al., 2007). For the WSOC measurements, the detection limit was 0.1 µg C m^{-3}. WSOC concentrations were converted into water-soluble organic matter (WSOM) concentrations using two different conversion factors based on literature values (Turpin and Lim, 2001): 1.4 for the R/V *Point Sur* organic plume, and

1.8 for the marine background aerosol. Water-insoluble organic matter (WIOM) was calculated as the difference between AMS organic and WSOM. The FTIR functional group composition was determined using an automated algorithm that includes baselining, peak fitting, and integrating at specific wavenumbers associated with major carbon bond types (Russell et al., 2009; Takahama et al., 2012). The functional groups that were quantified include hydroxyl, alkane, amine, carbonyl, and carboxylic acid groups.

2.4 Auxiliary data

Three-day HYSPLIT back trajectories (Draxler and Rolph, 2012) ending at the ship's location and at an altitude of 50 m were calculated for every third hour of the R/V *Point Sur* cruise. GOES visible satellite images (every 15 min) were collected and overlaid onto plots of the R/V *Point Sur*'s course to confirm and complement the visual observations of clouds from the R/V *Point Sur*. To analyze synoptic weather conditions, maps of surface temperature, wind, pressure, and 500 mb geopotential height were obtained from the website of the NOAA/OAR/ESRL Physical Science Division (http://www.esrl.noaa.gov/psd/data/composites/day/).

2.5 Synoptic conditions

Synoptic conditions during the cruise were characterized by two different regimes, as determined by the 500 mb geopotential height charts: the first ("Regime 1", 12–19 July) was governed by a midlatitude trough north of the cruise region; the second ("Regime 2", 20–23 July) was characterized by the reestablishment of a seasonally typical subtropical ridge to the south. Regime 1 was characterized by lower surface temperatures. HYSPLIT back trajectories show that during Regime 1, air masses arrived from the NW (Fig. 2). During the regime change (18–19 July), hereinafter termed "Transition", an episode of back trajectories from the west is apparent, in conjunction with a surface low-pressure center just north of the cruise area. Back trajectories parallel to the coast were dominant during Regime 2.

2.6 Plume tracking

During the majority of the cruise, ambient aerosol was measured. Background measurements are defined as time periods with CPC particle number concentrations $< 1000\,\mathrm{cm}^{-3}$. On several occasions the R/V *Point Sur* turned into the freshly generated plume and tracked it downwind. Plume tracking was limited by the ship's maximum speed, which was slower than typical wind speeds on most days. The ship was able to catch up with and track the plume on three days (16, 17, and 18 July, green shading in Fig. 3). The plume was tracked both by visually following the plume and by monitoring CPC particle number concentrations in real time. The ship's course was changed when needed to follow the highest concentrations. For this study, two plume tracking periods on 17 and 18 July were chosen for comparison. Plume characterization thus took place in air masses that were less influenced by coastal air (Regime 1 and Transition). The R/V *Point Sur* stack exhaust was sampled on one occasion on 22 July (yellow shading in Fig. 3).

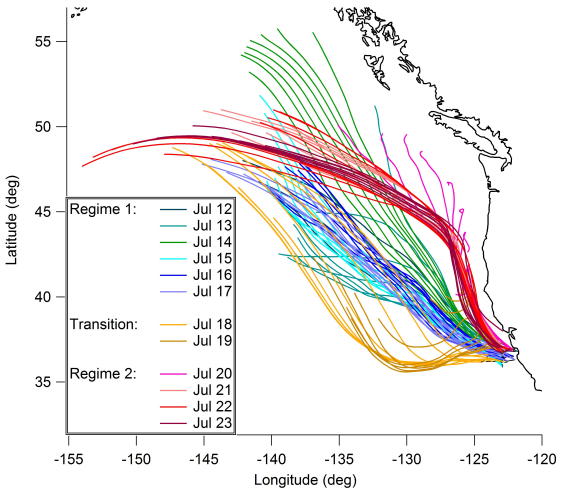

Fig. 2. Three-day HYSPLIT back trajectories (every three hours, ending altitude: 50 m) show air mass origins during the cruise. Three distinct groups of trajectories governed by synoptic conditions are apparent: back trajectories pertaining to Regime 1 (blue, green), Transition (orange), and Regime 2 (red).

During the cruise, 17 July was one of only two cloud-free days (Fig. 3, panel 3). GOES visible images show that clouds were present in the early morning but started to dissipate around 10:00 (this and all times hereinafter are local time, LT). The general area around the R/V *Point Sur's* location was cloud-free by 13:00. Relative humidity dropped from 91 % around sunrise (05:54) to 80 % at noon and further to an all-cruise minimum of 70 % by 18:00. Ambient temperature in the same time frame ranged between 13.6 and 15.7 °C. Smoke production on the R/V *Point Sur* began at 6:45 and ended at 11:15. The wind direction measured on the R/V *Point Sur* during smoke production and tracking was between 300° and 350°, with an average wind speed of $3.7 \pm 0.9\,\mathrm{m\,s}^{-1}$. The low wind speed on 17 July allowed for plume tracking by the R/V *Point Sur* for several hours. Figure 4a shows the ship's course as the plume was sampled. Smoke properties were measured during the time periods 11:20–11:32 (A1, fresh plume), 11:36–13:01 (A2, somewhat aged plume), and 15:02–15:20 (A3, aged plume). The plume was also encountered between 13:20 and 14:00, but it is likely that sampling occurred at the edge rather than the center of the plume. Therefore, this time period was not included in this analysis. The age of the plume encountered during tracking was estimated using the average wind speed and calculating the transport time from the location of the

last smoke production to the ship's locations during the three time periods of plume sampling. This estimate of plume age represents a lower boundary as the smoke encountered at a particular point may have been produced at a time earlier than the last smoke production. The lower bounds of the plume ages during the three time periods of interest were estimated to be A1 ≈ 6 min, A2 ≈ 1.6 h, and A3 ≈ 4.2 h.

On 18 July, it remained cloudy throughout the day. In addition, thick fog was noted in the deck logs (the ship's fog horn was used) from 04:00 to noon. RH remained close to 100 % during most of the morning and only dropped below 95 % at 12:25. Ambient temperature ranged between 14.6 and 16.4 °C. The R/V *Point Sur*'s course during smoke sampling is shown in Fig. 4b. Smoke was produced in two stages, from 06:45 to 07:40 and again from 09:00 to 09:30. Intermittent smoke sampling at the plume's edge occurred between 06:15 and 08:30; see also Fig. 5b (B1). The center of the plume was tracked successfully between 09:35 and 10:45; see also Fig. 5b (B2). The typical wind speed during smoke production and plume tracking was $5.4 \pm 1.3\,\mathrm{m\,s^{-1}}$, with a direction between 190 and 240°. The estimated plume ages were A1 ≈ 2 min and A2 ≈ 37 min.

During the plume tracking events (green shading in Fig. 3), the organic mass fraction (AMS organic mass : total AMS mass) in the fresh plume (plume age A1) was ≥ 97 %, as also found by Russell et al. (2013). The primary plume particles were created at a rate of 10^{11}–$10^{13}\,\mathrm{s^{-1}}$, and ranged between 100 nm and 8 µm in diameter (Russell et al., 2013). The high organic mass fraction distinguished the plume from other cargo ship exhaust plumes, which typically contain ∼ 50 % sulfate (Russell et al., 2013), and the background marine aerosol, which was found to contain between 40 and 60 % organic. The average ratio of organic : sulfate mass encountered in the background aerosol was 1.15 ± 0.80, and exceeded 5.0 in only a couple measurements during the entire campaign. Therefore, the plume was identified through AMS measurements for which the ratio of organic : sulfate exceeded 5.0. R/V *Point Sur* stack emissions also had very high organic mass fractions (around 90–95 %), but were characterized by higher BC concentrations ($> 6\,\mathrm{ng\,m^{-3}}$) and lower overall mass concentrations (yellow shading in Fig. 3). Using BC as an indicator, we find that stack emissions influenced the plume measurements only on rare occasions. For both plume tracking events, the total volume concentrations of the plume during tracking (A2) were comparable (see also "large mode volume" in Fig. 9), suggesting that the attempt to track the center of the plume was successful.

3 Results

3.1 Background aerosol

AMS measurements show that the nonrefractory, submicrometer fraction of the background aerosol is dominated by sulfate and organics (Fig. 3). During Regime 1, wind speeds generally stayed below $10\,\mathrm{m\,s^{-1}}$. In Regime 2, wind speeds were frequently higher than $10\,\mathrm{m\,s^{-1}}$, but rarely exceeded $15\,\mathrm{m\,s^{-1}}$. Externally mixed sea salt starts to become an important contributor to marine aerosol at wind speeds exceeding 6–$10\,\mathrm{m\,s^{-1}}$ (Ovadnevaite et al., 2012; Swietlicki et al., 2008, and references therein). A mode of particle volume in the 400 nm–1 µm range (Fig. 3, top panel) was observed during Regime 2 and likely had its origin in bubble-bursting processes, but constituted only a minor contribution to the background aerosol. The plume measurements, which were conducted at low wind speeds during Regime 1, found that plume particle concentrations were much higher than the background particle concentrations. For these reasons, we do not expect sea salt to have a controlling influence on the plume measurements. BC concentrations during Regime 1 were lower ($1.03 \pm 1.06\,\mathrm{ng\,m^{-3}}$) than during Regime 2 ($1.8 \pm 1.01\,\mathrm{ng\,m^{-3}}$, the difference is statistically significant at the 99 % confidence level), but short spikes in BC concentrations were observed in both regimes, confirming that the aerosol encountered during Regime 1 was still far from pristine. This is consistent with other work in the region showing a persistent influence of anthropogenic sources (Hegg et al., 2010; Coggon et al., 2012).

Hygroscopic growth factors at lower RH (40 and 70 %), below the deliquescence RH of most common inorganic salts, differed by meteorological regime. Table 2 shows that for a particle dry size of 150 nm, the growth factors averaged over Regime 2 were significantly lower (95 % confidence level in a two-sample z test) than those averaged over Regime 1. Hygroscopic growth at a RH below the deliquescence RH of most inorganic salts is at least partly enabled by the presence of organics (e.g., Hersey et al., 2009). It is unlikely that previous hygroscopic growth of inorganic components caused the observed growth as the aerosol was dried to RH < 8 % before the growth factor measurements, well below the efflorescence RH of most salts. The lower growth factors observed in Regime 2 at 40 and 70 % RH could have been caused by the higher BC concentrations (if internally mixed) and/or by a lower organic mass fraction: the average submicrometer organic mass fraction was 0.53 ± 0.11 in Regime 1 and 0.35 ± 0.10 in Regime 2. Additionally, the organic fraction in Regime 1, with trajectories from the sea rather than from coastal regions, may have been more aged and therefore more hygroscopic. At a RH above the deliquescence of most pure salts (92 and 85 %), there was no significant difference in growth factors between Regimes 1 and 2. In previous studies, lower growth factors at high RH have been observed in continentally influenced air masses,

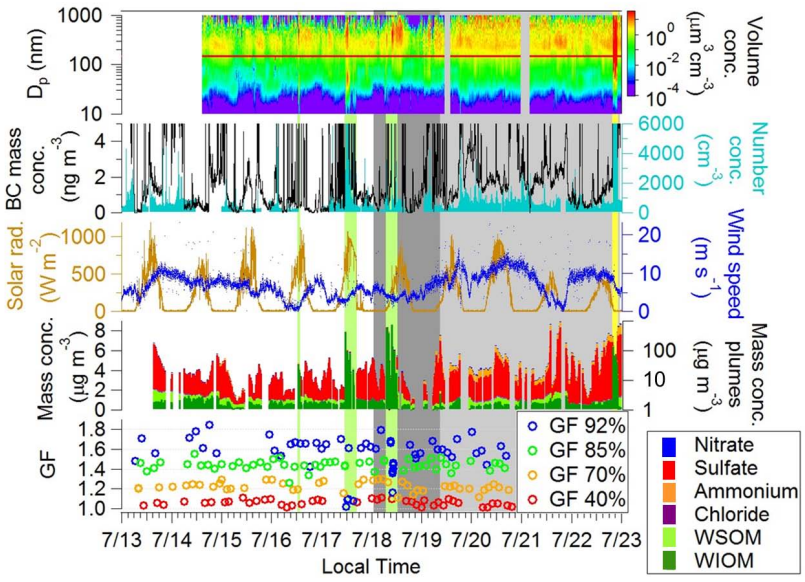

Fig. 3. Submicrometer volume distributions (SEMS), total number concentrations $< 6000\,\mathrm{cm}^{-3}$ (CPC), black carbon concentrations < 5 ng m^{-3} (SP2), chemical composition (AMS and PILS), and hygroscopic growth factors (HTDMA) for a dry particle size of 150 nm (indicated in the volume distribution (top panel) by the red line) and four different RHs as a function of time over the entire research cruise. Green shading: plume; yellow shading: ship stack exhaust; no shading: Regime 1; dark-gray shading: Transition; light-gray shading: Regime 2. Mass concentrations for AMS and PILS in green or yellow shading (plumes) pertain to the right *y* axis. Refer to Sect. 3.1 for more details.

referring to back trajectories originating over the continent (e.g., Massling et al., 2007; Allan et al., 2009; Hersey et al., 2009). This type of back trajectory was not encountered during this campaign (Fig. 2), explaining the lack of a more striking difference in growth factors by air mass origin at higher RH. Over the entire campaign, growth factors at 92 % RH (particle dry diameter of 150 nm) ranged between 1.43 and 1.96, with an average of 1.64 ± 0.11. These values compare well with the "more hygroscopic modes" observed in marine accumulation-mode aerosol in other studies (Massling et al., 2007; Swietlicki et al., 2008, and references therein; Allan et al., 2009; Mochida et al., 2011), and are associated with internally mixed aerosols containing sulfate, aged sea salt, and organic matter (Swietlicki et al., 2008). Higher growth factors are expected for fresh/pure sea-salt particles, and were found in the background aerosol of 18 July (Sect. 3.5).

3.2 Secondary organic aerosol formation in the plume

The most striking difference between the two plume tracking events (17 July, sunny, and 18 July, foggy) can be seen in the particle number concentrations in the aged plume (black/white marker boundaries in Fig. 4). On 18 July (Fig. 4b), number concentrations initially showed a short spike of $30\,000\,\mathrm{cm}^{-3}$, but dropped below $5000\,\mathrm{cm}^{-3}$ within five minutes and soon approached levels only about 40 % above the background. On 17 July (Fig. 4a), in contrast, particle number concentrations of $> 10\,000\,\mathrm{cm}^{-3}$ (a lower limit, as the CPC has substantial coincidence errors at concentrations $> 10\,000\,\mathrm{cm}^{-3}$ and does not report values exceeding $40\,000\,\mathrm{cm}^{-3}$) were observed for several hours at ages A2 and A3. These high particle concentrations, hours after the plume production stopped, are consistent with new particle formation successfully competing with dilution and coagulation. The temporal coincidence of these high number concentrations with the chemical signature of the plume (organic : sulfate > 5) and the absence of comparably high concentrations at any other time during the cruise make it highly

Table 2. Hygroscopic growth factors (150 nm dry diameter) averaged over the two meteorological regimes. For the bold values, the difference of the means between Regime 1 and Regime 2 is statistically significant (95 % confidence level). "σ" denotes standard deviations.

150 nm	Regime 1		Regime 2	
RH	mean	σ	mean	σ
40 %	**1.06**	**0.03**	**1.04**	**0.03**
70 %	**1.24**	**0.04**	**1.21**	**0.03**
85 %	1.44	0.05	1.44	0.05
92 %	1.66	0.12	1.60	0.10

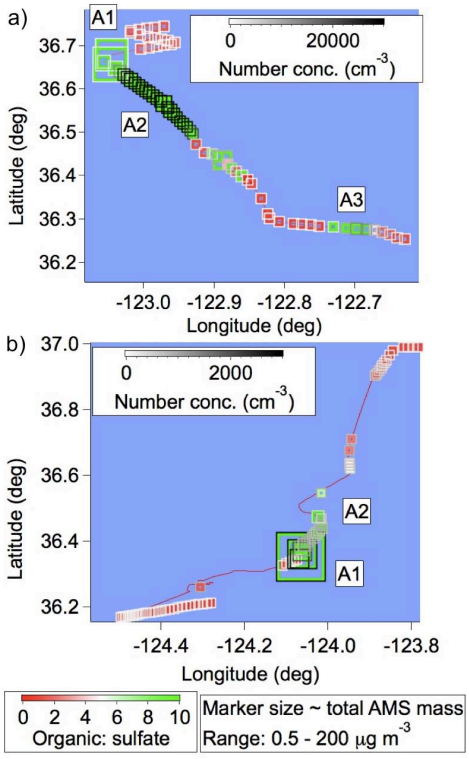

Fig. 4. R/V *Point Sur* ship trace during plume sampling on 17 July **(a)** and 18 July **(b)**. The plume location is identified by values of organic : sulfate > 5 (green markers). Black borders indicate high particle number concentrations. A1, A2, and A3 designate the three plume ages described in Sect. 2.6.

unlikely that the particles derived from any source other than the R/V *Point Sur* plume.

Figure 5 shows number and volume distributions for the plume events measured by the SEMS (10–500 nm) and the merged APS/OPS data (500 nm–2 µm). On 17 July, a "banana plot" typical of new particle formation and subsequent growth is visible (Fig. 5a, age A2, 11:36 to 13:01). Volatile organic compounds (VOCs) were emitted in the gas phase, along with the primary particles from the generators, and may have condensed after dilution and cooling, or underwent oxidation to form SOA in the aging plume. Alternatively, VOCs may have evaporated from primary plume particles, and formed SOA after photooxidation, in a process similar to that shown in the laboratory chamber experiments by Robinson et al. (2007). Figure 5c shows initial plume particles in a size range of 500 nm–1 µm approximately 5 min before the onset of new particle formation, and a subsequent decrease of both total volume and the modal size of the volume distribution, potentially indicating evaporation of plume particles.

A similar development potentially signifying evaporation of primary plume particles is also visible on 18 July (Fig. 5d). However, no new particle formation and growth was observed. It is conceivable that different parts of the plume with different particle size characteristics were sampled on the two days. Due to the reduced visibility on 18 July, it was difficult to follow the plume in an identical manner as on 17 July. The higher concentrations of large particles observed in the fresh plume on 18 July, as compared to the fresh plume on 17 July, indicate that a somewhat denser and fresher part of the plume was sampled initially. However, the plume was produced identically on both days, and, as described in Sect. 2.6, care was taken to follow the highest particle number concentrations. The most obvious difference distinguishing 18 July from 17 July was the presence of fog and clouds, and the associated diminished solar radiation (Fig. 3, middle panel). There are at least two explanations for the absence of a nucleation and growth event: (i) VOCs may have partitioned onto existing surfaces (e.g., fog droplets) instead of forming new particles – at least parts of the plume were able to enter the liquid phase, as evidenced by observations of the organic signature of the plume in cloud droplet residual particles (Shingler et al., 2012); and (ii) if photooxidation of plume VOCs was responsible for SOA formation on 17 July, cloud and fog shading may have suppressed such processes on 18 July.

3.3 Chemical composition

On 17 July (Fig. 6a), the maximum concentrations of AMS total organic mass and WSOM in the fresh plume (A1) were 885.67 and 4.16 µg m^{-3}, respectively. The decrease of AMS organic mass with plume age is attributable to dilution as the ship moved farther away from the location of the last smoke production, and potentially also to evaporation of organic mass from primary plume particles (Sect. 3.2). An interesting aspect is the increase of absolute concentrations of WSOM during A2: from 3.44 µg m^{-3} at 11:38 to 4.96 µg m^{-3} at 12:32. Since the typical background WSOM concentrations were below 1 µg m^{-3}, mixing of the plume with background aerosol cannot explain this increase. Rather, it is likely that WSOM formed in the plume, potentially contributing to the observed growth of newly formed particles. In the most aged part of the plume (A3), WSOM and AMS total organic concentrations still reached 3.4 and 48.4 µg m^{-3}, respectively, showing that SOA production largely compensated for plume dilution.

On both days, the O : C ratio and the relative contribution of WSOM to AMS total organic concentration increased as the plume aged, indicating a change in the functionality of the organic aerosol. Since the chemical measurements are mass based, the chemical composition data for plume age A1 are most representative of the larger, primary plume particles, which dominated the volume distribution (Fig. 5c, A1). The primary plume particles had low O : C ratios (< 0.001) and few water-soluble components (WSOM : Org ∼ 0.002)

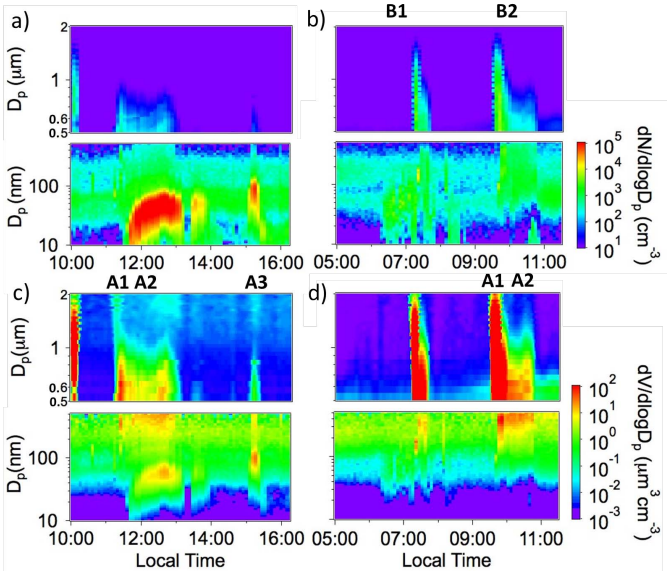

Fig. 5. Number **(a, b)** and volume **(c, d)** size distributions (SEMS and APS/OPS) of the plume particles on 17 July **(a, c)** and 18 July **(b, d)**. A particle formation and growth event is observed on 17 July, which contributes substantial aerosol mass to the plume. Only large plume particles were detected on 18 July.

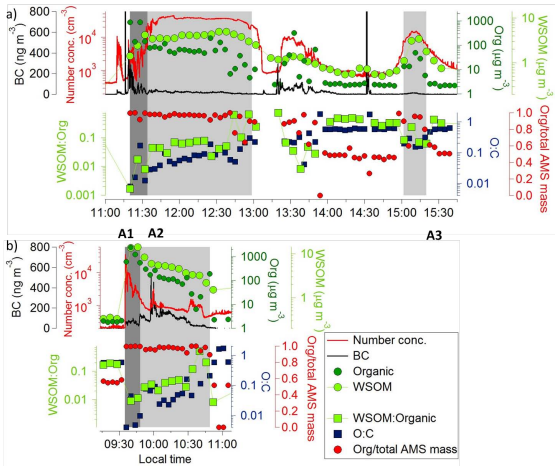

Fig. 6. Plume chemical composition measured by AMS for the three plume ages (A1, A2, A3) and marine background aerosol on 17 July **(a)** and 18 July **(b)**. Light-gray shading designates plume ages A2 and A3, and dark-gray shading represents the fresh plume (A1). The ratios O : C and WSOM : Org increase with plume age both days, and an absolute increase of WSOM is observed on 17 July.

(Fig. 6a, A1). At plume age A3, accumulation-mode particles, which likely had grown out of the nucleation mode, were dominant in the volume distribution (Fig. 5c, A3). Ratios of O : C and WSOM : Org at A3 were approximately 0.2 and 0.07, respectively (Fig. 6a, A3), showing that the organic fraction of the small-mode aerosol was more oxidized than that of the large mode. During A2, the volume was more evenly distributed over the primary and secondary plume particles (Fig. 5c, A2). For this plume age, it is not obvious whether the increasing O : C ratio and the observed production of WSOM (Fig. 6a, A2) were mostly properties of the new, growing particles or a result of the aging of the primary particles, or both. On 18 July, new particle formation was not observed, and the volume distribution was at all times dominated by particles with diameters > 100 nm (Fig. 5d). An increase in O : C and WSOM : Org was observed, suggesting that a chemical transformation to more oxidized and more water-soluble compounds occurred in the primary plume particles (Fig. 6b).

Figure 7 shows a comparison of the FTIR spectra of plume particles sampled during ages A1 and A2 ("A1+A2") on 17 and 18 July, and aged particles sampled during A3 on 17 July, as well as the spectrum of particles directly emitted from the ship stack. For comparison, the spectra of laboratory samples of the oil used for smoke generation and the diesel fuel for the ship's engine are shown as well. The spectra all show absorbance at 3000–2800 cm^{-1}, which is indicative of alkane functional groups. The individual peaks at 2920 and 2850 cm^{-1} indicate the presence of methylene groups (Pavia et al., 2001). An increase in hydroxyl functional groups (3700–3100 cm^{-1}) can be observed in the spectrum of the ship stack emissions (black line, upper panel, Fig. 7) compared to the laboratory spectrum of the ship diesel

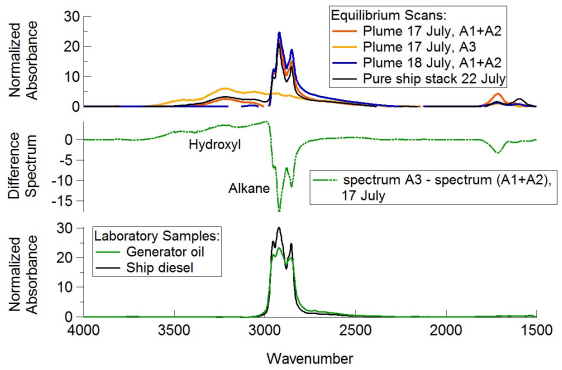

Fig. 7. FTIR spectra of the plume for a filter sample over ages A1 and A2 ("A1+A2"), and a sample for age A3 (upper panel) and their difference (middle panel). Spectra of the pure ship stack emissions (sampled on 22 July) as well as the smoke oil and the ship diesel fuel are shown for comparison (lower panel). Hydroxyl functional groups are detected in the aged smoke plume, but much less so in the fresh smoke and the laboratory samples.

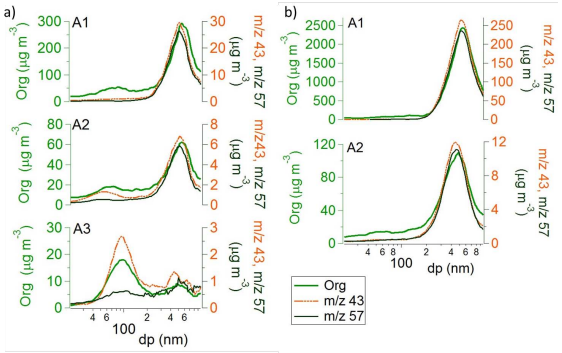

Fig. 8. Size-resolved concentrations of AMS organic, and the organic markers m/z 57 and m/z 43 for 17 July **(a)** and 18 July **(b)**. The small particle mode is clearly visible on 17 July. The marker m/z 57 only appears in the large particle mode, the marker m/z 43 in both modes.

(black line, lower panel, Fig. 7). Similarly, the spectra of the smoke plume (orange, yellow, and blue lines, upper panel, Fig. 7) show higher peaks in hydroxyl than the spectrum of the generator oil (green line, lower panel, Fig. 7). These relative increases in hydroxyl functional groups are indicative of oxidization of the alkane groups in the emissions that contributed to the particle formation. In the aged particles (A3) on 17 July, an increase in hydroxyl and a decrease in alkane functional groups are evident, implying increased oxidation with increased aging. This increase in hydroxyl functional groups with the age of particles is consistent with the increase in O : C observed by the AMS. For plume age A3, the hydroxyl peaks are a large feature. The concurrent low ratios of WSOM : Org (0.07) reflect the fact that WSOM and hydroxyl groups are not directly correlated.

Size-resolved AMS measurements of organic mass (Fig. 8) clearly show the larger fresh plume mode in the size range 500–800 nm for both plume sampling events, the newly emerging particle mode at A2, and the grown particles at A3 on 17 July (Fig. 8a). The organic marker m/z 57, which is associated with aliphatic organics ($C_4H_9^+$) and serves as a tracer for hydrocarbon-like organic aerosol (Zhang et al., 2005), was strongly related to the larger aerosol particles in the plume on both days, and did not appear in the smaller emerging mode. High-resolution AMS data show that $C_4H_9^+$ was the dominant fragment in m/z 57 in the fresh plume. The marker m/z 44, dominated by acid-like oxygenates, did not contribute substantially to any of the two modes. The organic marker m/z 43 was a component of both the larger and the smaller mode. Two fragments govern m/z 43: $C_3H_7^+$ from alkyl groups and $C_2H_3O^+$ from nonacid oxygenates (Ng et al., 2011). In ambient aerosols, the organic marker m/z 43 is expected to be dominated by nonacid oxygenates (Ng et al., 2010), which have also been found to be a major component in laboratory-generated SOA from primary anthropogenic sources (Heringa et al., 2012). When examining the temporal behavior of the fragments $C_2H_3O^+$ and $C_3H_7^+$ together with the integrated aerosol volumes for the small (particle diameter < 100 nm) and the large (particle diameter > 100 nm) mode (Fig. 9), it is obvious that on both days, $C_3H_7^+$ traces the large-mode volume. $C_2H_3O^+$, in contrast, traces the small particle volume on 17 July. The correlations between $C_3H_7^+$ and the large mode are significant on both days, whereas $C_2H_3O^+$ only shows a significant correlation with the small-mode volume on 17 July (Table 3). This indicates that the small mode comprised more oxygenated compounds than the large mode.

3.4 CCN concentrations

The temporal development of CCN concentrations and activation ratios during the plume sampling periods is shown in Fig. 10. On both days, CCN concentrations at the lower supersaturation (S) of 0.07–0.08 % were largely unaffected by the presence of the plume. At medium ($0.24 < S < 0.26$ %) and high ($0.87 < S < 0.88$ %) S, a substantial number of particles activated. Supersaturations in the stratocumulus deck are generally estimated to be in the range of 0.1–0.4 % (Hoppel et al., 1996; Feingold et al., 1998; Thouron et al., 2012). During E-PEACE, in-cloud supersaturations of 0.09 and 0.25 were estimated during two Twin Otter flights on 16 July and 10 August (Russell et al., 2013). As reported by Russell et al. (2013), the amount of CCN created in the plume was sufficient to create a track in the marine stratocumulus deck that was visible via satellite remote sensing. The primary plume particles were large enough to activate without the presence

of soluble ions, but it is possible that some of the newly formed particles acted as CCN as well.

On 17 July (Fig. 10a), the onset of new particle formation at 11:32 was accompanied by a dramatic reduction in the activation ratio. The use of the CCN activation ratio as a proxy for hygroscopicity requires caution when there is a high variability in the aerosol size distribution, as was clearly the case here: the drop in activation ratio is a result of the order of magnitude increase in condensation nuclei (CN) concentrations between A1 and A2. As the plume aged, CCN concentrations increased and eventually reached over 4000 cm^{-3} at high S. Changes in the size distribution are often the primary driver for CCN concentrations (Roberts et al., 2002; McFiggans et al., 2006), and probably explain most of the increase in the CCN concentrations at the high S observed here: the newly formed particles were too small to act as CCN, but grew into the relevant size ranges (Fig. 5a, A2, after 12:00) as the plume aged. However, as the primary plume particles were shown to become more oxidized, and therefore also more hygroscopic, it is likely that they contributed as well. At plume age A3, the secondary particles had grown into the accumulation mode (Fig. 5a), and CCN concentrations reached 637 and 9910 cm^{-3} at the medium and high S, respectively.

On 18 July (Fig. 10b), activation ratios were only initially suppressed, and increased steadily as CN concentrations decreased. The absolute CCN concentration at high S increased with increasing plume age, from 151 cm^{-3} at 09:33 to a peak value of 424 cm^{-3} at 10:13, a far lower concentration than on 17 July. Since there was no such dramatic change in the size distribution as on 17 July, the increase in CCN concentration on 18 July was likely driven by chemical transformations and the condensation of hydrophilic organics on the existing particles. Very short aging times (no more than a few hours) to convert hydrophobic particles into CCN have been observed in laboratory experiments (Tritscher et al., 2011) and suggested for atmospheric particles, particularly in daytime conditions with photochemical production of secondary aerosol mass (Wang et al., 2010). The CCN activity at high supersaturations can also be explained without invoking organic transformation: even trace amounts of hygroscopic material (e.g., sulfate) deposited at the surface of the particle can lead to activation and droplet growth. Such inorganic trace components would be hard to detect by the mass-sensitive online chemical measurement methods.

The activation diameter for medium and high S was estimated by integrating the merged APS/OPS and SEMS size distributions from the largest to smaller sizes to match the observed CCN concentrations. On 17 July, the estimated activation diameter (d_{act}) was smaller than the Kelvin diameter (d_K) at both supersaturations ($d_K = 0.81$ µm for $S = 0.26$ % and $d_K = 0.24$ µm for $S = 0.88$ %) and at all plume ages. This implies that plume particles smaller than the Kelvin diameter activated due to the probable presence of soluble ions and a certain degree of hygroscopicity. On 18 July, the estimated activation diameter was larger than the Kelvin diameter for both supersaturations at age A1. For medium S, d_{act} was lower than d_K at plume age A2; for high S, d_{act} stayed above d_K. An activation diameter larger than the Kelvin diameter can occur if a subpopulation of particles does not activate even at high S. Instances of $d_{act} > d_K$ thus point to the presence of an external mixture (Burkart et al., 2012). As discussed in Sect. 3.2, a fresher part of the plume was likely sampled on 18 July. Thus, the external mixture may comprise both large plume particles that did not activate and more aged plume particles, that activated at a size below d_K. Bulk measurements of CCN are prone to uncertainties in externally mixed aerosols; thus, future work should aim to measure size-resolved CCN concentrations. A decreasing trend in estimated d_{act} was observed at both supersaturations and on both days, and is indicative of a chemical transformation of CCN-inactive to CCN-active particles (e.g., Furutani et al., 2008).

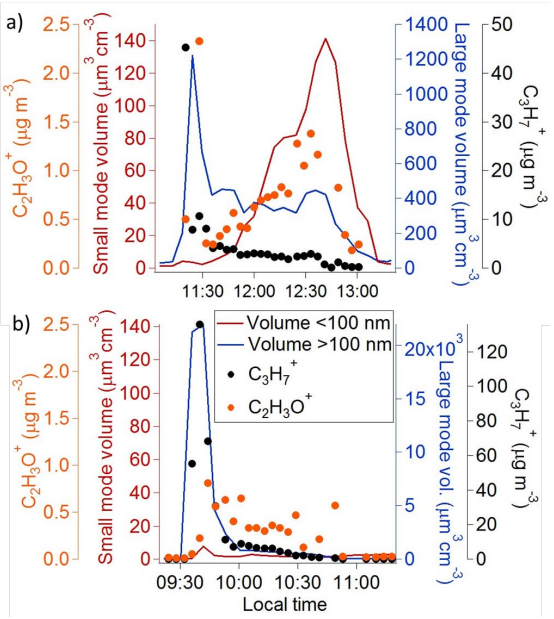

Fig. 9. Volume concentrations in the large (particle diameter >100 nm) and the small (particle diameter < 100 nm) modes, and concentrations of $C_2H_3O^+$ and $C_3H_7^+$ on 17 July **(a)** and 18 July **(b)**. The large-mode volume concentration decreases with plume age on both days. On 17 July, the volume concentration in the small mode increases as the plume ages, while on 18 July, no such dramatic increase is observed. $C_2H_3O^+$ covaries with the small particle mode on 17 July, while $C_3H_7^+$ covaries with the large particle volume on both days.

3.5 Hygroscopic growth factors

As opposed to the CCN measurements, which were not size resolved, the GFs were measured for specific sizes, thus

Table 3. Correlations (a = intercept; b = slope; n = number of samples) between the fragments $C_2H_3O^+$ and $C_3H_7^+$ and particle volume for the large and the small mode. Bold: correlation is statistically significant at the 99 % level. $C_3H_7^+$ correlates with the large mode on both days; $C_2H_3O^+$ correlates with the small mode on 17 July.

Day	Mode	$C_3H_7^+$				$C_2H_3O^+$			
		a	b	r^2	n	a	b	r^2	n
17 July	volume >100 nm	**−0.459**	**0.009**	**0.77**	**24**	0.270	0.001	0.16	22
	volume <100 nm	2.881	−0.016	0.10	24	**0.247**	**0.006**	**0.39**	**22**
18 July	volume > 100 nm	**1.525**	**0.003**	**0.86**	**42**	0.247	1.418	0.01	41
	volume <100 nm	3.765	0.859	0.03	42	0.275	−0.003	0.00	41

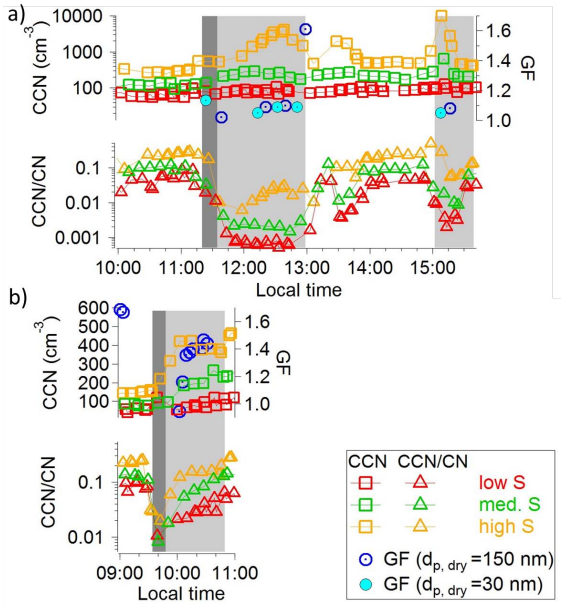

Fig. 10. Hygroscopic growth factors for 30 and 150 nm dry size at 92 % RH, and time series of CCN concentrations and activation ratios at three supersaturations: $0.07 < S < 0.08$ % (red, low), $0.24 < S < 0.26$ % (green, medium), and $0.87 < S < 0.88$ % (yellow, high) for the plume sampling events on 17 July **(a)** and 18 July **(b)**. Dark-gray shading represents plume age A1, and light-gray shading plume ages A2 and A3. Refer to Sect. 3.4 for more details.

giving direct insight into the hygroscopic properties of the smaller and the larger mode particles. The bulk chemical composition measurements cannot be assumed to be representative of the chemical composition of smaller particle sizes (30, 75, and 150 nm), for which the hygroscopic growth factors were measured.

Hygroscopic growth factors in the plume on 17 July at age A2 and A3 (Fig. 10a) were very low: for particles with a dry size of 30 nm (representative of the newly formed particles), GFs (RH = 92 %) ranged between 1.05 and 1.09. Those with a dry size of 150 nm (representative of larger plume particles) had GFs between 1.02 and 1.10. The high GFs shown at the very beginning and the very end of the plume period are representative of background marine aerosol, as evidenced by low number concentrations in the respective GF distributions (about a factor of 2 lower than those observed within the plume). Particles with a dry size of 75 nm did not grow at any plume age. The 75 nm particles are representative of the particles contributing most to the CCN concentrations, as the particle number concentration in the plume at ages A2 and A3 was dominated by particles in the size range below 100 nm (Fig. 5a). The very low to negligible GFs are not in contradiction with the observed increase in CCN concentrations: trace amounts of inorganic compounds contribute little to hygroscopic growth, which is sensitive to volume fractions of hygroscopic material. Similarly, insoluble but wettable organic substances would result in little or no hygroscopic growth, while allowing for activation as CCN.

While the measured GF change (1–1.1) is within the upper estimate of GF measurement uncertainty based on sodium chloride given in Sect. 2.3, the measured O : C ratios and GFs compare well with a chamber study on aging diesel exhaust, in which O : C ratios were observed to increase from 0.1 to 0.19 within < 2 h, while simultaneously, GFs increased from 1 to 1.1 (95 % RH, 100 nm dry particle diameter) (Tritscher et al., 2011). The organic aerosol formed in the plume underwent an overall chemical transformation leading to higher O : C ratios, from < 0.001 in the fresh plume to values around 0.2 in the plume at age A3 (Fig. 6a). Additionally, size-resolved measurements of the AMS organic concentrations at the center of the two modes of the plume (the primary mode at 500–800 nm and the emerging mode of ∼ 100 nm at plume age A3) indicate that a more oxygenated form of organic aerosol was present in the growing small mode as compared to the large primary mode (Sect. 3.3), potentially giving rise to modest hygroscopic growth.

On 18 July, in contrast, GFs increased significantly with increasing plume age (Fig. 10b). For particles with a dry size of 30 and 75 nm, the GF distributions (not shown) were bimodal, showing a mode with negligible hygroscopic growth

and a background mode with GFs between 1.5 and 1.7. For 150 nm particles, the GF distributions were mono-modal, but very broad, suggesting the presence of several overlapping peaks that are not readily distinguishable. In order to gain more insight, the distributions were approximated with a fit of three lognormal modes. In the background aerosol (i.e., an average over all scans of 18 July that were uninfluenced by local particle sources), two higher GF modes were found and yielded GFs of 1.60 and 2.09. One of these modes (GF = 1.60) corresponds to the "more hygroscopic mode" of the marine background (Sect. 3.1), the other (GF = 2.09) potentially to a pure sea-salt mode (Swietlicki et al., 2008). These two modes were assumed to be present and invariant throughout plume sampling. With this constraint, a lognormal mode was fitted that best explained the remainder of the GF distribution. This mode was still wider than the GF distributions for plume particles observed on 17 July, and thus the possibilities that additional modes were present, or that the background during plume tracking may differ from the all-day average, cannot be excluded. The GFs shown in the gray-shaded area in Fig. 10b pertain to the modeled lower GF mode. Within eight consecutive scans, the GF increased from 0.94 to 1.47, a much larger increase than on 17 July. While these GF values seem to approach background values, it has to be noted that number concentrations in all GF scans were at least 36 % higher than those in background GF distributions, and organic mass fractions were above 91 % (Fig. 6b), thus sampling occurred well within the plume.

O : C and WSOM : Org increases for 18 July are comparable to those of 17 July and do not explain the range of GFs (up to 1.47). Based on the findings of Jimenez et al. (2009), for a purely organic particle, an O : C ratio of 0.55–0.6 is required to result in a GF of 1.5. Such levels were not reached during plume sampling in this study. However, in the absence of a newly emerging mode, mass concentrations below about 200 nm were very low. Bulk chemical measurements may not be representative of particles with a 150 nm dry size, and size-resolved AMS measurements close to the detection limit are less reliable. We suggest the following explanations for the increasing GF on 18 July: (i) internal mixing with inorganic compounds, in particular sulfate. On 17 July, the 150 nm particles likely grew out of smaller particles through condensation of VOCs (assuming higher VOC levels on the sunny than on the foggy day), and may therefore have contained higher organic mass fractions than those on 18 July. (ii) Aqueous-phase processing of organics towards more hygroscopic organic species, as has been documented before in the region (e.g., Crahan et al., 2004; Sorooshian et al., 2007). The expected higher O : C ratios resulting from aqueous-phase processing may not be reflected in the bulk measurement of O : C, for the reasons stated above. Filter samples show that two particulate species that are tracers for cloud-processing the region (Crahan et al., 2004; Sorooshian et al., 2007) were observed in PM_{10} samples of the smoke on 18 July but not on 17 July: oxalate (236 ng m^{-3}) and glyoxylate (79 ng m^{-3}). Oxalate is also associated with coarse crustal matter (e.g., Wang et al., 2012); however, its simultaneous detection with glyoxylate only on 18 July suggests that aqueous-phase processing was an important factor on that day. Another, more speculative explanation is that surface organic films may have prevented water uptake on 17 July and formed a kinetic barrier, which may have been "broken" by the higher RH on 18 July. However, the timescales over which such a barrier would operate are not known (McFiggans et al., 2006).

4 Conclusions

We have shown substantial differences in hygroscopic growth and CCN activity of smoke-generated organic particles emitted in the marine atmosphere under different meteorological conditions. In sunny conditions, new particle formation occurred and originated from VOCs emitted together with or evaporated from larger primary plume particles. The organic fragment m/z 43 appeared both in the large plume particles and in the newly emerging mode, but with differing dominant fragments: $C_3H_7^+$ (alkyl groups) was dominant in the large particle mode, while $C_2H_3O^+$ (nonacid oxygenates) was dominant in the smaller mode, showing that the newly formed particles consisted of more oxygenated organic compounds. No growth of newly formed particles was observed in the aged plume in foggy conditions. Most likely, photooxidation of plume VOCs leading to new particle formation was less efficient due to the reduced solar flux. Additionally, the fog droplets may have acted as a sink for VOCs and small particles due to the large surface area they provide for diffusive deposition.

Meteorological conditions have a profound impact on size distributions and CCN yield of the plume particles. The majority of the plume particles did not act as CCN. However, the newly formed particles activated as CCN initially after growing into the appropriate size ranges and CCN concentrations reached very high numbers (> 4000 cm^{-3}) at high supersaturations ($S = 0.8$ %). Newly formed particles, consisting largely of SOA, can thus provide high concentrations of CCN, as was found in other studies (Hennigan et al., 2012). In the foggy conditions without new particle formation, the number concentration of CCN produced by the plume was lower by an order of magnitude.

In sunny conditions, plume particles with a dry size of 30 and 150 nm showed very limited hygroscopic growth (GF = 1.02–1.10 at RH = 92 %), while those with a dry size of 75 nm did not grow at all. Mixing with inorganic components, or aging of the organic fraction, which was reflected in increasing ratios of O : C and WSOM : Org, can cause hygroscopic growth. While the increase in O : C from < 0.001 to ∼ 0.2 is below what has been observed to influence GFs in ambient organic aerosols (Jimenez et al., 2009), both the range of O : C and that of GFs are consistent with a

chamber study of aging primary organic aerosol (Tritscher et al., 2011). This shows that the aging time to transform a pure hydrocarbon-like aerosol of the kind emitted in this experiment into a hygroscopic organic aerosol of the kind found in many ambient measurements is longer than the 1–4 h that were available in this study in clean marine conditions. The aging time for the same particles to act as CCN, in contrast, is much shorter (< 1 h). On the foggy day, GFs of 150 nm particles increased to up to 1.47 as the plume aged. A different degree of internal mixing with hygroscopic inorganic compounds and/or aqueous-phase processing are suggested as possible explanations for this behavior.

Acknowledgements. This work was funded by ONR grants N00014-11-1-0783, N00014-10-1-0200, and N00014-10-1-0811, and NSF grants AGS-1013381, AGS-10131423, and AGS-1008848. The measurements at sea were made possible by the support of the R/V *Point Sur* crew and staff. We acknowledge NOAA/OAR/ESRL PSD, Boulder, Colorado, USA, for providing weather maps from their website at http://www.esrl.noaa.gov/psd/. The authors gratefully acknowledge the NOAA Air Resources Laboratory (ARL) for the provision of the HYSPLIT transport and dispersion model and READY website (http://ready.arl.noaa.gov) used in this publication. Regina Hitzenberger is acknowledged for helpful comments and suggestions.

Edited by: M. C. Facchini

References

Aiken, A. C., DeCarlo, P. F., and Jimenez, J. L.: Elemental analysis of organic species with electron ionization high-resolution mass spectrometry, Anal. Chem., 79, 8350–8358, doi:10.1021/ac071150w, 2007.

Allan, J. D., Topping, D. O., Good, N., Irwin, M., Flynn, M., Williams, P. I., Coe, H., Baker, A. R., Martino, M., Niedermeier, N., Wiedensohler, A., Lehmann, S., Müller, K., Herrmann, H., and McFiggans, G.: Composition and properties of atmospheric particles in the eastern Atlantic and impacts on gas phase uptake rates, Atmos. Chem. Phys., 9, 9299–9314, doi:10.5194/acp-9-9299-2009, 2009.

Bateman, A. P., Nizkorodov, S. A., Laskin, J., and Laskin, A.: Photolytic processing of secondary organic aerosols dissolved in cloud droplets, Phys. Chem. Chem. Phys., 13, 12199–12212, doi:10.1039/c1cp20526a, 2011.

Blando, J. D. and Turpin, B. J.: Secondary organic aerosol formation in cloud and fog droplets: a literature evaluation of plausibility, Atmos. Environ., 34, 1623–1632, doi:10.1016/S1352-2310(99)00392-1, 2000.

Brechtel, F. J. and Kreidenweis, S. M.: Predicting Particle Critical Supersaturation from Hygroscopic Growth Measurements in the Humidified TDMA. Part I: Theory and Sensitivity Studies, J. Atmos. Sci. 57, 1854–1871, doi:10.1175/1520-0469(2000)057<1854:PPCSFH>2.0.CO;2, 2000a.

Brechtel, F. J. and Kreidenweis, S. M.: Predicting Particle Critical Supersaturation from Hygroscopic Growth Measurements in the Humidified TDMA. Part II: Laboratory and Ambient Studies, J. Atmos. Sci. 57, 1872–1887, doi:10.1175/1520-0469(2000)057<1872:PPCSFH>2.0.CO;2, 2000b.

Burkart, J., Hitzenberger, R., Reischl, G., Bauer, H., Leder, K., and Puxbaum, H.: Activation of "synthetic ambient" aerosols – Relation to chemical composition of particles <100 nm, Atmos. Environ., 54, 583–591, doi:10.1016/j.atmosenv.2012.01.063, 2012.

Cavalli, F., Facchini, M. C., Decesari, S., Mircea, M., Emblico, L., Fuzzi, S., Ceburnis, D., Yoon, Y. J., O'Dowd, C. D., Putaud, J.-P., and Dell'Acqua, A.: Advances in characterization of size-resolved organic matter in marine aerosol over the North Atlantic, J. Geophys. Res., 109, D24215, doi:10.1029/2004JD005137, 2004.

Coggon, M. M., Sorooshian, A., Wang, Z., Metcalf, A. R., Frossard, A. A., Lin, J. J., Craven, J. S., Nenes, A., Jonsson, H. H., Russell, L. M., Flagan, R. C., and Seinfeld, J. H.: Ship impacts on the marine atmosphere: insights into the contribution of shipping emissions to the properties of marine aerosol and clouds, Atmos. Chem. Phys., 12, 8439–8458, doi:10.5194/acp-12-8439-2012, 2012.

Crahan, K. K., Hegg, D., Covert, D. S., and Jonsson, H.: An exploration of aqueous oxalic acid production in the coastal marine atmosphere, Atmos. Environ., 38, 3757–3764, doi:10.1016/j.atmosenv.2004.04.009, 2004.

Dall'Osto, M., Ceburnis, D., Monahan, C., Worsnop, D. R., Bialek, J., Kulmala, M., Kurtén, T., Ehn, M., Wenger, J., Sodeau, J., Healy, R., and O'Dowd, C.: Nitrogenated and aliphatic organic vapors as possible drivers for marine secondary organic aerosol growth, J. Geophys. Res., 117, D12311, doi:10.1029/2012JD017522, 2012.

DeCarlo, P. F., Slowik, J. G., Worsnop, D. R., Davidovits, P., and Jimenez, J. L.: Particle morphology and density characterization by combined mobility and aerodynamic diameter measurements. Part 1: Theory, Aerosol Sci. Technol., 38, 1180–1205, doi:10.1080/027868290903907, 2004.

DeCarlo, P. F., Kimmel,J. R., Trimborn, A., Northway, M. J., Jayne, J. T., Aiken, A. C., Gonin, M., Fuhrer, K., Horvath, T., Docherty, K. S., Worsnop, D. R., and Jimenez, J. L.: Field-deployable, high-resolution, time-of-flight aerosol mass spectrometer, Anal. Chem., 78, 8281–8289, doi:10.1021/ac061249n, 2006.

de Gouw, J., Middlebrook, A. M., Warneke, C., Ahmadov, R., Atlas, E. L., Bahreini, R., Blake, D. R., Brock, C. A., Brioude, J., Fahey, D. W., Fehsenfeld, F. C., Holloway, J. S., Le Henaff, M., Lueb, R. A., McKeen, S. A., Meagher, J. F., Murphy, D. M., Paris, C., Parrish, D. D., Perring, A. E., Pollack, I. B., Ravishankara, A. R., Robinson, A. L., Ryerson, T. B., Schwarz, J. P., Spackman, J. R., Srinivasan, A., and Watts, L. A.: Organic aerosol formation downwind from the Deepwater Horizon oil spill, Science, 331, 1295–1299, doi:10.1126/science.1200320, 2011.

Dick, W. D., Saxena, P., and McMurry, P. H.: Estimation of water uptake by organic compounds in submicron aerosols measured during the Southeastern Aerosol and Visibility Study, J. Geophys. Res., 105, 1471–1479, doi:10.1029/1999JD901001, 2000.

Draxler, R. R. and Rolph, G. D.: HYSPLIT (HYbrid Single-Particle Lagrangian Integrated Trajectory) Model, access via NOAA ARL READY Website, available at: http://ready.arl.noaa.gov/HYSPLIT.php (last access: August 2012), NOAA Air Resources Laboratory, Silver Spring, MD, 2012.

Duplissy, J., DeCarlo, P. F., Dommen, J., Alfarra, M. R., Metzger, A., Barmpadimos, I., Prevot, A. S. H., Weingartner, E., Tritscher, T., Gysel, M., Aiken, A. C., Jimenez, J. L., Canagaratna, M. R., Worsnop, D. R., Collins, D. R., Tomlinson, J., and Baltensperger, U.: Relating hygroscopicity and composition of organic aerosol particulate matter, Atmos. Chem. Phys., 11, 1155–1165, doi:10.5194/acp-11-1155-2011, 2011.

Dusek, U., Frank, G. P., Massling, A., Zeromskiene, K., Iinuma, Y., Schmid, O., Helas, G., Hennig, T., Wiedensohler, A., and Andreae, M. O.: Water uptake by biomass burning aerosol at sub- and supersaturated conditions: closure studies and implications for the role of organics, Atmos. Chem. Phys., 11, 9519–9532, doi:10.5194/acp-11-9519-2011, 2011.

El Haddad, I., Yao Liu, Nieto-Gligorovski, L., Michaud, V., Temime-Roussel, B., Quivet, E., Marchand, N., Sellegri, K., and Monod, A.: In-cloud processes of methacrolein under simulated conditions – Part 2: Formation of secondary organic aerosol, Atmos. Chem. Phys., 9, 5107–5117, doi:10.5194/acp-9-5107-2009, 2009.

Ervens, B., Turpin, B. J., and Weber, R. J.: Secondary organic aerosol formation in cloud droplets and aqueous particles (aqSOA): a review of laboratory, field and model studies, Atmos. Chem. Phys., 11, 11069–11102, doi:10.5194/acp-11-11069-2011, 2011.

Eyring, V., Isaksen, I. S. A., Berntsen, T., Collins, W. J., Corbett, J. J., Endresen, O., Grainger, R. G., Moldanova, J., Schlager, H., and Stevenson, D. S.: Transport impacts on atmosphere and climate: shipping, Atmos. Environ., 44, 4735–4771, doi:10.1016/j.atmosenv.2009.04.059, 2009.

Facchini, M. C., Rinaldi, M., Decesari, S., Carbone, C., Finessi, E., Mircea, M., Fuzzi, S., Ceburnis, Flanagan, R., Nilsson, E. D., de Leeuw, G. D., Martino, M., Woeltjen, J., and O'Dowd, C.: Primary submicron marine aerosol dominated by insoluble organic colloids and aggregates, Geophys. Res. Lett., 35, L17814, doi:10.1029/2008GL034210, 2008a.

Facchini, M. C., Decesari, S., Rinaldi, M., Carbone, C., Finessi, E., Mircea, M., Fuzzi, S., Moretti, F., Tagliavini, E., Ceburnis, D., and O'Dowd, C.: Important source of marine secondary organic aerosol from biogenic amines, Environ. Sci. Technol., 42, 9116–9121, doi:10.1021/es8018385, 2008b.

Feingold G., Walko, R. L., Stevens, B., and Cotton, W. R.: Simulations of marine stratocumulus using a new microphysical parameterization scheme, Atmos. Res., 47–48, 505–528, doi:10.1016/S0169-8095(98)00058-1, 1998.

Frossard, A. A. and Russell, L. M.: Removal of sea salt hydrate water from seawater-derived samples by dehydration, Environ. Sci. Technol., 46, 13326–13333, doi:10.1021/es3032083, 2012.

Furutani, H., Dall'Osto, M., Roberts, G. C., and Prather, K. A.: Assessment of the relative importance of atmospheric aging on CCN activity derived from field observations, Atmos. Environ., 42, 3130–3142, doi:10.1016/j.atmosenv.2007.09.024, 2008.

Gantt, B. and Meskhidze, N.: The physical and chemical characteristics of marine primary organic aerosol: a review, Atmos. Chem. Phys., 13, 3979–3996, doi:10.5194/acp-13-3979-2013, 2013.

George, I. J., Vlasenko, A., Slowik, J. G., Broekhuizen, K., and Abbatt, J. P. D.: Heterogeneous oxidation of saturated organic aerosols by hydroxyl radicals: uptake kinetics, condensed-phase products, and particle size change, Atmos. Chem. Phys., 7, 4187–4201, doi:10.5194/acp-7-4187-2007, 2007.

Gysel, M., McFiggans, G. B., and Coe, H.: Inversion of tandem differential mobility analyser (TDMA) measurements, J. Aerosol Sci., 40, 134–151, doi:10.1016/j.jaerosci.2008.07.013, 2009.

Hawkins, L. N., Russell, L. M., Covert, D. S., Quinn, P. K., and Bates, T. S.: Carboxylic acids, sulfates and organosulfates in processed continental organic aerosol over the Southern Pacific Ocean during VOCALS-Rex 2008, J. Geophys. Res., 115, D13201, doi:10.1029/2009JD013276, 2010.

Hegg, D. A.: The importance of liquid phase oxidation of SO_2 in the atmosphere, J. Geophys. Res., 90, 3773–3779, doi:10.1029/JD090iD02p03773, 1985.

Hegg, D. A., Covert, D. S., Jonsson, H. H., and Woods, R. K.: The contribution of anthropogenic aerosols to aerosol light-scattering and CCN activity in the California coastal zone, Atmos. Chem. Phys., 10, 7341–7351, doi:10.5194/acp-10-7341-2010, 2010.

Hennigan, C. J., Westervelt, D. M., Riipinen, I., Engelhart, G. J., Lee, T., Collett, J. L., Pandis, S. N., Adams, P. J., and Robinson, A. L.: New particle formation and growth in biomass burning plumes: An important source of cloud condensation nuclei, Geophys. Res. Lett., 39, L09805, doi:10.1029/2012GL050930, 2012.

Heringa, M. F., DeCarlo, P. F., Chirico, R., Tritscher, T., Clairotte, M., Mohr, C., Crippa, M., Slowik, J. G., Pfaffenberger, L., Dommen, J., Weingartner, E., Prévôt, A. S. H., and Baltensperger, U.: A new method to discriminate secondary organic aerosols from different sources using high-resolution aerosol mass spectra, Atmos. Chem. Phys., 12, 2189–2203, doi:10.5194/acp-12-2189-2012, 2012.

Hersey, S. P., Sorooshian, A., Murphy, S. M., Flagan, R. C., and Seinfeld, J. H.: Aerosol hygroscopicity in the marine atmosphere: a closure study using high-time-resolution, multiple-RH DASH-SP and size-resolved C-ToF-AMS data, Atmos. Chem. Phys., 9, 2543–2554, doi:10.5194/acp-9-2543-2009, 2009.

Hersey, S. P., Craven, J. S., Metcalf, A. R., Lin, J., Lathem, T., Suski, K., Cahill, J., Duong, H., Sorooshian, A., Jonsson, H. H., Nenes, A., Prather, K. A., Flagan, R. C., and Seinfeld, J. H.: Composition and Hygroscopicity of the Los Angeles Aerosol: CalNex, J. Geophys. Res., 118, 3016–3036, 2013.

Hoppel W. A., Frick, G. M., and Fitzgerald, J. W.: Deducing droplet concentration and supersaturation in marine boundary layer clouds from surface aerosol measurements, J. Geophys. Res., 101, 26553–26565, doi:10.1029/96JD02243, 1996.

Jimenez, J. L., Canagaratna, M. R., Donahue, N. M., Prevot, A. S. H., Zhang, Q., Kroll, J. H., DeCarlo, P. F., Allan, J. D., Coe, H., Ng, N. L., Aiken, A. C., Docherty, K. S., Ulbrich, I. M., Grieshop, A. P., Robinson, A. L., Duplissy, J., Smith, J. D., Wilson, K. R., Lanz, V. A., Hueglin, C., Sun, Y. L.,. Tian, J, Laaksonen, A., Raatikainen, T., Rautiainen, J., Vaattovaara, P., Ehn, M., Kulmala, M., Tomlinson, J. M., Collins, D. R., Cubison, M. J., Dunlea, E. J., Huffman, J. A., Onasch, T. B., Alfarra, M. R., Williams, P. I., Bower, K., Kondo, Y., Schneider, J., Drewnick, F., Borrmann, S., Weimer, S., Demerjian, K., Salcedo, D., Cottrell, L., Griffin, R., Takami, A., Miyoshi, T., Hatakeyama, S., Shimono, A., Sun, J. Y., Zhang, Y. M., Dzepina, K., Kimmel, J. R., Sueper, D., Jayne, J. T., Herndon, S. C., Trimborn, A. M., Williams, L. R., Wood, E. C., Middlebrook, A. M., Kolb, C. E., Baltensperger, U., and Worsnop, D. R.: Evolution of organic aerosols in the atmosphere, Science, 326, 1525–1529, doi:10.1126/science.1180353, 2009.

Khlystov A., Stanier, C., and Pandis, S. N.: An algorithm for combining electrical mobility and aerodynamic size distributions data when measuring ambient aerosol, Aerosol Sci. Technol., 38, 229–238, doi:10.1080/02786820390229543, 2004.

Leck, C. and Bigg, E. K.: Source and evolution of the marine aerosol—A new perspective, Geophys. Res. Lett., 32, L19803, doi:10.1029/2005GL023651, 2005.

Massling, A., Leinert, S., Wiedensohler, A., and Covert, D.: Hygroscopic growth of sub-micrometer and one-micrometer aerosol particles measured during ACE-Asia, Atmos. Chem. Phys., 7, 3249–3259, doi:10.5194/acp-7-3249-2007, 2007.

Massoli, P., Lambe, A.T., Ahern, A. T., Williams, L. R., Ehn, M., Mikkilä, J., Canagaratna, M. R., Brune, W. H., Onasch, T. B., Jayne, J. T., Petäjä, T., Kulmala, M., Laaksonen, A., Kolb, C. E., Davidovits, P., and Worsnop, D. R.: Relationship between aerosol oxidation level and hygroscopic properies of laboratory generated secondary organic aerosol (SOA) particles, Geophys. Res. Lett., 37, L24801, doi:10.1029/2010GL045258, 2010.

McFiggans, G., Artaxo, P., Baltensperger, U., Coe, H., Facchini, M. C., Feingold, G., Fuzzi, S., Gysel, M., Laaksonen, A., Lohmann, U., Mentel, T. F., Murphy, D. M., O'Dowd, C. D., Snider, J. R., and Weingartner, E.: The effect of physical and chemical aerosol properties on warm cloud droplet activation, Atmos. Chem. Phys., 6, 2593–2649, doi:10.5194/acp-6-2593-2006, 2006.

Meskhidze, N. and Nenes, A.: Phytoplankton and cloudiness in the Southern Ocean, Science, 314, 1419, doi:10.1126/science.1131779, 2006.

Meyer, N. K., Duplissy, J., Gysel, M., Metzger, A., Dommen, J., Weingartner, E., Alfarra, M. R., Prevot, A. S. H., Fletcher, C., Good, N., McFiggans, G., Jonsson, Å. M., Hallquist, M., Baltensperger, U., and Ristovski, Z. D.: Analysis of the hygroscopic and volatile properties of ammonium sulphate seeded and unseeded SOA particles, Atmos. Chem. Phys., 9, 721–732, doi:10.5194/acp-9-721-2009, 2009.

Middlebrook, A. M., Murphy, D. M., and Thomson, D. S.: Observations of organic material in individual marine particles at Cape Grim during the First Aerosol Characterization Experiment (ACE 1), J. Geophys. Res., 103, 16475–16483, doi:10.1029/97JD03719, 1998.

Mochida, M., Nishita-Hara, C., Furutani, H., Miyazaki, Y., Jung, J., Kawamura, K., and Uematsu, M.: Hygroscopicity and cloud condensation nucleus activity of marine particles over the western North Pacific, J. Geophys. Res., 116, D06204, doi:10.1029/2010JD014759, 2011.

Modini, R. L., Harris, B., and Ristovski, Z. D.: The organic fraction of bubble-generated, accumulation mode Sea Spray Aerosol (SSA), Atmos. Chem. Phys., 10, 2867–2877, doi:10.5194/acp-10-2867-2010, 2010.

Moore, R. H., Raatikainen, T., Langridge, J. M., Bahreini, R., Brock, C. A., Holloway, J. S., Lack, D. A., Middlebrook, A. M., Perring, A. E., Schwarz, J. P., Spackman, J. R., and Nenes, A.: CCN spectra, hygroscopicity, and droplet activation kinetics of secondary organic aerosol resulting from the 2010 Deepwater Horizon oil spill, Environ. Sci. Technol., 46, 3093–3100, doi:10.1021/es203362w, 2012.

Murphy, S. M., Agrawal, H., Sorooshian, A., Padro, L. T., Gates, H., Hersey, S., Welch, W. A., Jung, H., Miller, J. W., Cocker, D. R., Nenes, A., Jonsson, H. H., Flagan, R. C., and Seinfeld, J. H.: Comprehensive simultaneous shipboard and airborne characterization of exhaust from a modern container ship at sea, Environ. Sci. Technol., 43, 4626–4640, doi:10.1021/es802413j, 2009.

Ng, N. L., Canagaratna, M. R., Zhang, Q., Jimenez, J. L., Tian, J., Ulbrich, I. M., Kroll, J. H., Docherty, K. S., Chhabra, P. S., Bahreini, R., Murphy, S. M., Seinfeld, J. H., Hildebrandt, L., Donahue, N. M., DeCarlo, P. F., Lanz, V. A., Prévôt, A. S. H., Dinar, E., Rudich, Y., and Worsnop, D. R.: Organic aerosol components observed in Northern Hemispheric datasets from Aerosol Mass Spectrometry, Atmos. Chem. Phys., 10, 4625–4641, doi:10.5194/acp-10-4625-2010, 2010.

Ng, N. L., Canagaratna, M. R., Jimenez, J. L., Chhabra, P. S., Seinfeld, J. H., and Worsnop, D. R.: Changes in organic aerosol composition with aging inferred from aerosol mass spectra, Atmos. Chem. Phys., 11, 6465–6474, doi:10.5194/acp-11-6465-2011, 2011.

O'Dowd, C. D. and de Leeuw, G.: Marine aerosol production: a review of the current knowledge, Philos. Trans. R. Soc. A, 365, 1753–1774, doi:10.1098/rsta.2007.2043, 2007.

O'Dowd, C. D., Maria Cristina Facchini, M. C., Cavalli, F., Ceburnis, D., Mircea, M., Decesari, S., Fuzzi, S., Yoon Y. J., and Putaud, J.-P.: Biogenically driven organic contribution to marine aerosol, Nature, 431, 676–680, doi:10.1038/nature02959, 2004.

Ovadnevaite, J., Ceburnis, D., Martucci, G., Bialek, J., Monahan, C., Rinaldi, M., Facchini, M. C., Berresheim, H., Worsnop, D. R., and O'Dowd, C.: Primary marine organic aerosol: A dichotomy of low hygroscopicity and high CCN activity, Geophys. Res. Lett., 38, L21806, doi:10.1029/2011GL048869, 2011a.

Ovadnevaite, J., O'Dowd, C., Dall'Osto, M., Ceburnis, D., Worsnop, D. R., and Berresheim, H.: Detecting high contributions of primary marine organic matter to marine aerosol: A case study, Geophys. Res. Lett., 38, L02807, doi:10.1029/2010GL046083, 2011b.

Ovadnevaite, J., Ceburnis, D., Canagaratna, M., Berresheim, H., Bialek, J., Martucci, G, Worsnop, D., and O'Dowd, C.: On the effect of wind speed on submicron sea salt mass concentrations and source fluxes, J. Geophys. Res., 117, D16201, doi:10.1029/2011JD017379, 2012.

Pavia, D. L., Lapman, G. M., and Kriz, G. S.: Introduction to spectroscopy, Third Ed., Brooks/Cole, 2001.

Petters, M. D. and Kreidenweis, S. M.: A single parameter representation of hygroscopic growth and cloud condensation nucleus activity, Atmos. Chem. Phys., 7, 1961–1971, doi:10.5194/acp-7-1961-2007, 2007.

Petters, M. D., Carrico, C. M., Kreidenweis, S. M., Prenni, A. J., DeMott, P. J., Collett, J. L., and Moosmuller, H.: Cloud condensation nucleation activity of biomass burning aerosol, J. Geophys. Res., 114, D22205, doi:10.1029/2009JD012353, 2009.

Roberts, G. C. and Nenes, A.: A continuous-flow streamwise thermal-gradient CCN chamber for atmospheric measurements, Aerosol Sci. Technol., 39, 206–221, doi:10.1080/027868290913988, 2005.

Roberts, G. C., Artaxo, P., Zhou, J. C., Swietlicki, E., and Andreae, M. O.: Sensitivity of CCN spectra on chemical and physical properties of aerosol: A case study from the Amazon basin, J. Geophys. Res., 114, doi:10.1029/2001JD000583, 2002.

Robinson, A. L., Donahue, N. M., Shrivastava, M. K., Weitkamp, E. A., Sage, A. M., Grieshop, A. P., Lane, T. E., Pierce, J. R., and Pandis, S. N.: Rethinking organic aerosols: semivolatile emissions and photochemical aging, Science, 315, 1259,

doi:10.1126/science.1133061, 2007.

Russell, L. M., Takahama, S. Liu, S., Hawkins, L. N., Covert, D. S., Quinn, P. K., and Bates, T. S.: Oxygenated fraction and mass of organic aerosol from direct emission and atmospheric processing measured on the R/V Ronald Brown during TEXAQS/GoMACCS 2006, J. Geophys. Res., 114, doi:10.1029/2008jd011275, 2009.

Russell, L. M., Hawkins, L. N., Frossard, A. A., Quinn, P. K., and Bates, T. S.: Carbohydrate-like composition of submicron atmospheric particles and their production from ocean bubble bursting, P. Natl. Acad. Sci. USA, 107, 15, 6652–6657, doi:10.1073/pnas.0908905107, 2010.

Russell, L. M., Sorooshian, A., Seinfeld, J. H., Albrecht, B. A., Nenes, A., Ahlm, L., Chen, Y. C., Coggon, M., Craven, J. S., Flagan, R. C., Frossard, A. A., Jonsson, H., Jung, E., Lin, J. J., Metcalf, A. R., Modini, R., Mülmenstädt, J., Roberts, G. C., Shingler, T., Song, S., Wang, Z., and Wonaschütz, A.: Eastern Pacific Emitted Aerosol Cloud Experiment (E-PEACE), B. Am. Meteorol. Soc., 94, 709–729, doi:10.1175/BAMS-D-12-00015, 2013.

Saxena, P., Hildemann, L., McMurry, P. H., and Seinfeld, J. H.: Organics alter hygroscopic behavior of atmospheric particles, J. Geophys. Res., 100, 18755–18770, doi:10.1029/95JD01835, 1995.

Shingler, T., Dey, S., Sorooshian, A., Brechtel, F. J., Wang, Z., Metcalf, A., Coggon, M., Mülmenstädt, J., Russell, L. M., Jonsson, H. H., and Seinfeld, J. H.: Characterisation and airborne deployment of a new counterflow virtual impactor inlet, Atmos. Meas. Tech., 5, 1259–1269, doi:10.5194/amt-5-1259-2012, 2012.

Sorooshian, A., Lu, M.-L., Brechtel, F. J., Jonsson, H., Feingold, G., Flagan, R. C., and Seinfeld, J. H., On the source of organic acid aerosol layers above clouds, Environ. Sci. Technol., 41, 4647–4654, doi:10.1021/es0630442, 2007.

Sorooshian, A., Hersey, S., Brechtel, F. J., Corless, A., Flagan, R. C., and Seinfeld, J. H.: Rapid, Size-Resolved Aerosol Hygroscopic Growth Measurements: Differential Aerosol Sizing and Hygroscopicity Spectrometer Probe (DASH-SP), Aerosol Sci. Technol. 42, 445–464, doi:10.1080/02786820802178506, 2008.

Sorooshian, A., Murphy, S. M., Hersey, S., Bahreini, R., Jonsson, H., Flagan, R. C., and Seinfeld, J. H.: Constraining the contribution of organic acids and AMS m/z 44 to the organic aerosol budget: On the importance of meteorology, aerosol hygroscopicity, and region, Geophys. Res. Lett., 37, L21807, doi:10.1029/2010GL044951, 2010.

Sorooshian, A., Csavina, J., Shingler, T., Dey, S., Brechtel, F., Sáez, E., and Betterton, E. A.: Hygroscopic and chemical properties of aerosols collected near a copper smelter: Implications for public and environmental health, Environ. Sci. Technol., 46, 9473–9480, doi:10.1021/es302275k, 2012.

Stolzenburg, M.: An ultra-fine aerosol size distribution measuring system, Ph.D. Thesis, University of Minnesota, Minneapolis, 1988.

Sullivan, A. P., Peltier, R. E., Brock, C. A., de Gouw, J. A, Holloway, J. S., Warneke, C., Wollny, A. G., and Weber, R. J.: Airborne measurements of carbonaceous aerosol soluble in water over northeastern united states: Method development and an investigation into water-soluble organic carbon sources, J. Geophys. Res., 111, D23S46, doi:10.1029/2006jd007072, 2006.

Swietlicki, E., Hansson, H.-C., Hämeri, K., Svenningsson, B., Massling, A., McFiggans, G., McMurry, P. H., Petäja, T., Tunved, P., Gysel, M., Topping, D., Weingartner, E., Baltensperger, U., Rissler, J., Wiedensohler, A., and Kulmala, M.: Hygroscopic properties of submicrometer atmospheric aerosol particles measured with H-TDMA instruments in various environments – a review, Tellus, 60B, 432–469, doi:10.1111/j.1600-0889.2008.00350.x, 2008.

Takahama, S., Johnson, A., and Russell, L. M.: Quantification of carboxylic and carbonyl functional groups in organic aerosol infrared absorbance spectra, Aerosol Sci. Technol., 47, 310–325, doi:10.1080/02786826.2012.752065, 2012.

Thouron, O., Brenguier, J.-L., and Burnet, F.: Supersaturation calculation in large eddy simulation models for prediction of the droplet number concentration, Geosci. Model Dev., 5, 761–772, doi:10.5194/gmd-5-761-2012, 2012.

Tritscher T., Juranyi, Z., Martin, M., Chirico, R., Gysel, M., Heringa, M. F., deCarlo, P. F., Sierau, B., Prevot, A. S. H., Weingartner, E., and Baltensperger, U.: Changes of hygroscopicity and morphology during ageing of diesel soot, Environ. Res. Lett., 6, 034026, doi:10.1088/1748-9326/6/3/034026, 2011.

Turpin, B. J. and Lim, H.-J: Species contributions to $PM_{2.5}$ mass concentrations: Revisiting common assumptions for estimating organic mass, Aerosol Sci. Technol., 35, 602–610, doi:10.1080/02786820152051454, 2001.

Wang, G., Kawamura, K., Cheng, C., Li, J., Cao, J., Zhang, R., Zhang, T., Liu, S., and Zhao, Z.: Molecular distribution and stable carbon isotopic composition of dicarboxylic acids, ketocarboxylic acids, and α-dicarbonyls in size-resolved atmospheric particles from Xi'an City, China, Environ. Sci. Technol., 46, 4783–4791, doi:10.1021/es204322c, 2012.

Wang, J., Cubison, M. J., Aiken, A. C., Jimenez, J. L., and Collins, D. R.: The importance of aerosol mixing state and size-resolved composition on CCN concentration and the variation of the importance with atmospheric aging of aerosols, Atmos. Chem. Phys., 10, 7267–7283, doi:10.5194/acp-10-7267-2010, 2010.

Wex, H., Stratmann, F., Hennig, T., Hartmann, S., Niedermeier, D., Nilsson, E., Ocskay, R., Rose, D., Salma, I., and Ziese, M.: Connecting hygroscopic growth at high humidities to cloud activation for different particle types, Environ. Res. Lett., 3 035004 doi:10.1088/1748-9326/3/3/035004, 2008.

Wex, H., Petters, M. D., Carrico, C. M., Hallbauer, E., Massling, A., McMeeking, G. R., Poulain, L., Wu, Z., Kreidenweis, S. M., and Stratmann, F.: Towards closing the gap between hygroscopic growth and activation for secondary organic aerosol: Part 1 – Evidence from measurements, Atmos. Chem. Phys., 9, 3987–3997, doi:10.5194/acp-9-3987-2009, 2009.

Wonaschütz, A., Hersey, S. P., Sorooshian, A., Craven, J. S., Metcalf, A. R., Flagan, R. C., and Seinfeld, J. H.: Impact of a large wildfire on water-soluble organic aerosol in a major urban area: the 2009 Station Fire in Los Angeles County, Atmos. Chem. Phys., 11, 8257–8270, doi:10.5194/acp-11-8257-2011, 2011.

Zhang Q., Alfarra, M. R., Worsnop, D. R., Allan, J. D., Doe, H., Canagaratna, M., and Jimenez, J. L.: Deconvolution and quantification of hydrocarbon-like and oxygenated organic aerosols based on aerosol mass spectrometry, Environ. Sci. Technol., 39, 4938–4952, doi:10.1021/es048568l, 2005.

Chapter 5

On the Mixing and Evaporation of Secondary Organic Aerosol Components

Environmental Science & Technology

Article

pubs.acs.org/est

On the Mixing and Evaporation of Secondary Organic Aerosol Components

Christine L. Loza,[†] Matthew M. Coggon,[†] Tran B. Nguyen,[‡] Andreas Zuend,[†,§] Richard C. Flagan,[†,¶] and John H. Seinfeld*[,†,¶]

[†]Division of Chemistry and Chemical Engineering, California Institute of Technology, Pasadena, California 91125, United States
[‡]Division of Geological and Planetary Sciences, California Institute of Technology, Pasadena, California 91125, United States
[¶]Division of Engineering and Applied Science, California Institute of Technology, Pasadena, California 91125, United States

ABSTRACT: The physical state and chemical composition of an organic aerosol affect its degree of mixing and its interactions with condensing species. We present here a laboratory chamber procedure for studying the effect of the mixing of organic aerosol components on particle evaporation. The procedure is applied to the formation of secondary organic aerosol (SOA) from α-pinene and toluene photooxidation. SOA evaporation is induced by heating the chamber aerosol from room temperature (25 °C) to 42 °C over 7 h and detected by a shift in the peak diameter of the SOA size distribution. With this protocol, α-pinene SOA is found to be more volatile than toluene SOA. When SOA is formed from the two precursors sequentially, the evaporation behavior of the SOA most closely resembles that of SOA from the second parent hydrocarbon, suggesting that the structure of the mixed SOA resembles a core of SOA from the initial precursor coated by a layer of SOA from the second precursor. Such a core-and-shell configuration of the organic aerosol phases implies limited mixing of the SOA from the two precursors on the time scale of the experiments, consistent with a high viscosity of at least one of the phases.

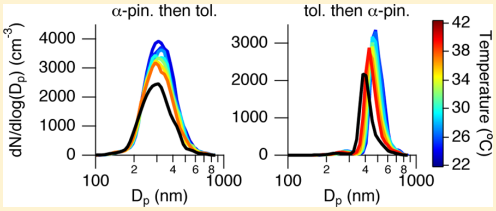

INTRODUCTION

Recent studies suggest that atmospheric organic aerosols may exist in an amorphous semisolid or amorphous solid (glassy) state.[1−9] The physical state of a particle affects its interaction with water and condensing organic compounds and its behavior upon heating or cooling.[10] It is difficult to observe the physical state of submicrometer particles directly; therefore, a number of indirect techniques have been used to probe the physical state of aerosols, typically at room temperature and low relative humidity (**RH**). Bounce of secondary organic aerosol (SOA) particles in an impactor was taken as indicative of a solid state.[1,8] Another study employed an amorphous protein substrate as a proxy for an amorphous, semisolid aerosol and showed that a model with finite, condensed-phase diffusion was necessary to reproduce ozone uptake by the substrate.[4] That the uptake of organic nitrates by α-pinene ozonolysis SOA did not follow absorptive equilibrium partitioning theory was taken, in another study, as indicative of nonliquid-like behavior.[7] Ammonia uptake of α-pinene ozonolysis SOA was larger under humid conditions (**RH** >94%) than under dry conditions (**RH** <5%), suggesting a transition from semisolid to liquid particles for increasing **RH**.[6] In other studies, α-pinene ozonolysis SOA exhibited slower evaporation kinetics than that expected for liquid droplets,[5] and pyrene evaporation from α-pinene ozonolysis SOA indicated a particle viscosity of approximately 10^8 Pa s, much greater than typical liquid viscosities of 10^{-2}–10^3 Pa s.[9] Based on the observation that α-pinene ozonolysis SOA partially evaporated in a thermodenuder without a change in particle chemical composition, it was concluded that particle-phase diffusional limitations prevented higher volatility compounds from evaporating preferentially.[3] The primary inference in each of these studies is that the retarded diffusion of compounds within the condensed phase can be attributed to highly viscous particle-phase behavior.

Others have studied particle mixing using controlled aerosol generation from two different sources. Laser ablation single-particle mass spectrometry data suggest that dioctyl phthalate and α-pinene ozonolysis SOA formed two separate phases when one type of aerosol was coated with the other type.[2] In another study,[11] SOA mass yields (ratio of mass of SOA formed to mass of parent hydrocarbon reacted) of sequentially formed α-pinene ozonolysis and labeled toluene photooxidation SOA showed that the SOA yield of the second precursor was consistent with partitioning to the combined SOA mass from the first and second precursors (pseudoideal mixing)[12−15] rather than partitioning to the SOA mass formed solely by the second precursor.

In this work, we present an experimental protocol designed to probe the mixing state of organic aerosols by observing the evaporation behavior of SOA formed sequentially from two different precursors in an environmental chamber. While oxidation products from the first precursor are present in the chamber throughout the experiment and can partition into the

Received: March 4, 2013
Revised: May 15, 2013
Accepted: May 20, 2013
Published: May 31, 2013

particle phase as more organic particle mass is formed from the second precursor, the second period of SOA formation is likely dominated by oxidation products from the second precursor. It is hypothesized that particle evaporation reflects the nature of SOA mixing. If a particle is well mixed, i.e. molecular diffusion time scales within the particle are the same order of magnitude or faster than evaporation time scales,[16] then volatile SOA components have essentially immediate access to the particle surface for evaporation. If diffusion time scales within the particle are much longer than evaporation time scales, evaporation of volatile components is inhibited.

Evaporation is induced by heating the chamber, run as a batch reactor, rather than using a thermodenuder, which is limited in the study of potential particle-phase mass transfer limitations due to its characteristic residence time (2 to 30 s).[17,18] Two drawbacks exist, however, to using chamber heating as a basis to infer aerosol evaporation behavior. First, the maximum chamber temperature, in the present case 50 °C, is substantially lower than that achieved in thermodenuders, ~400 °C. Second, condensable organic vapors are difficult to remove from a batch reactor without also removing the particles themselves. In a thermodenuder, the sample flows over a bed of activated carbon to remove vapors immediately after heating. Here, we dilute the chamber contents before heating to decrease the concentration of vapor-phase components and promote particle evaporation. Other studies have used chamber heating or dilution separately to evaluate the yield, volatility, reversibility of SOA formed from α-pinene ozonolysis[19−21] and *m*-xylene photooxidation;[22] we combine these procedures to study the mixing state of SOA.

EXPERIMENTAL SECTION

Experiments were performed in the Caltech indoor, dual 24-m^3 Teflon chambers. Prior to an experiment, the chamber was cleaned by flushing with air passed through beds of activated carbon, silica gel, Purafil SP Blend Media, and molecular sieves and a particle filter to achieve a particle background of <10 cm^{-3} and a relative humidity of <7%. The experiments were conducted under conditions of <5 ppbv NO_x and <7% relative humidity. Initial O_3 concentration was <5 ppbv, the instrument lower detection limit. While some O_3 formed during photooxidation, the major sink of both SOA precursors was reaction with OH. The temperature of the chamber enclosure was maintained initially at 25 ± 1 °C. Hydrogen peroxide (H_2O_2, 50% wt., Sigma Aldrich) was used as the OH radical source and was injected into the chamber by flowing purified air at 5 LPM over 280 μL of H_2O_2 in a glass bulb immersed in a 35 °C water bath. Photolysis of H_2O_2 by 350 nm-centered UV broadband lamps (40 W Sylvania 350BL, $j_{NO2} \sim 6 \times 10^{-3}$ s^{-1}) provided a constant source of OH radicals during the irradiation period at a concentration of about 3×10^6 molecules cm^{-3}, as inferred from the decrease in parent hydrocarbon concentration. Ammonium sulfate seed particles were added to the chamber by atomizing an aqueous solution of 0.015 M ammonium sulfate; particles dried upon contact with the dry air in the chamber. Toluene (99.8% purity, Sigma Aldrich) and/or α-pinene (99+ % purity, Sigma Aldrich) were added to the chamber by flowing purified air at 5 LPM over a measured liquid volume. After injections, the chamber contents were allowed to mix for 1 h before irradiation.

During sequential precursor experiments, the second precursor was added in the same manner as the first after SOA growth from the first precursor stabilized. After 17−24 h, the irradiation period ended, and the lights were turned off, halting OH production, which was confirmed by a leveling of the concentration of unreacted toluene. Approximately 100 ppbv of cyclohexane, used as a dilution tracer, was added to the chamber using the same method as the hydrocarbon injections. Once the cyclohexane concentration stabilized, the chamber contents were diluted by a factor of 2−3 with purified air. After dilution, the temperature of the dark chamber enclosure was ramped linearly over 7 h from 25 to 45 °C to achieve a maximum chamber temperature of 40−42 °C. The chamber was maintained at the maximum temperature for 7 h.

A suite of instruments was used to study the evolution of the gas and particle phases. Toluene, α-pinene, and cyclohexane were measured using a gas chromatograph equipped with a flame ionization detector (GC/FID, Agilent, 6890N). Samples were collected by drawing chamber air through a 10 mL sample loop and were analyzed using a HP-5 column (15 m × 0.53 mm ID × 1.5 μm thickness, Agilent). The sample was injected onto the 60 °C column; after 1 min, the oven temperature was ramped at 40 °C min^{-1} to 250 °C and then held at 250 °C for 3 min. Relative humidity and temperature, NO and NO_x, and O_3 were continuously monitored using a Vaisala HMP 233, a chemiluminescence NO_x monitor (T200, Teledyne), and an O_3 monitor (APOA-360, Horiba), respectively.

The suspended aerosol size distribution and number concentration were measured continuously using a custom-built scanning mobility particle sizer consisting of a differential mobility analyzer (DMA, TSI, 3081) coupled to a condensation particle counter (CPC, TSI, 3010), henceforth referred to as the DMA. The DMA was operated in a closed-loop configuration with a recirculating sheath and excess flow of 2.67 L min^{-1} and a 5.4:1 ratio of sheath to aerosol flow rates, and column voltage was scanned from 15 to 9850 V over 45 s. DMA mobility (diameter) resolution, *R*, is defined as[23]

$$R = \frac{Z_p^*}{\Delta Z_p} \quad (1)$$

where Z_p^* is the mobility corresponding to the peak of the transfer function, and ΔZ_p is the full width of the transfer function at half-maximum. The resolution was calculated for each of the 106 mobility (diameter) bins using the transfer function given in Stolzenburg.[24] Because size distribution data are binned, a well-resolved change in mobility is deemed one in which a particle with any mobility in the first bin is resolved from a particle with any mobility in the second bin. At the DMA operating conditions in the present work, the DMA can resolve a 15−25% change in particle diameter. Here, particle diameter shifts are reported using the size bin median diameter. Real-time particle mass spectra were collected by an Aerodyne high-resolution time-of-flight aerosol mass spectrometer (AMS).[25,26] The AMS switched among the higher sensitivity, lower resolution "V-mode," Particle Time-of-Flight (PToF) mode, and the lower sensitivity, higher resolution "W-mode." AMS data were processed using "Squirrel," the ToF-AMS Unit Resolution Analysis Toolkit (http://cires.colorado.edu/jimenez-group/ToFAMSResources/ToFSoftware/index.html), in Igor Pro Version 6.22A (Wavemetrics, Lake Oswego, OR). "V-mode" and PToF data were analyzed using a fragmentation table to separate sulfate, ammonium, and organic spectra and to time-trace specific *m*/*z* ratios.[27] "V-mode" and "W-mode" data were analyzed using a separate high-resolution spectra toolbox PIKA (Peak Integration by Key Analysis) to determine the

chemical formulas contributing to distinct m/z ratios.[25] The signals of organic ions below m/z 141 were used to calculate elemental ratios. The ratio of particle-phase CO^+ to CO_2^+ was approximately equal to 1, and in "V-mode," the contribution of CO^+ to the organic signal was equated to that of particle-phase CO_2^+. The intensities of water-derived ions (H_2O^+, OH^+, and O^+) were calculated from particle-phase CO_2^+.[28] A relative ionization efficiency of 1.4 was applied to organic ion signals. AMS data reported in this work are averaged over 1-h intervals.

RESULTS AND DISCUSSION

Aerosol Size Distribution Evolution. Both evaporation and particle wall losses affect suspended particle size distributions in this study (Figure 1). Partial particle evaporation decreases particle size but does not affect the number concentration, whereas particle wall loss decreases the number concentration but does not change particle size.

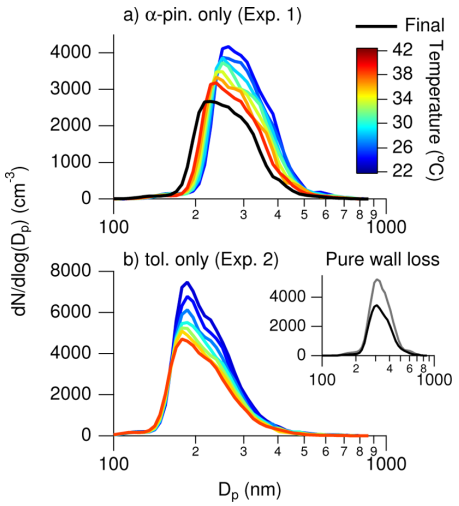

Figure 1. Evolution of the suspended particle size distribution of single-precursor SOA during heating of the chamber enclosure. The data shown are averaged over 1-h intervals. Abbreviations correspond to toluene (tol.) and α-pinene (α-pin.). The final aerosol size distribution for Experiment 2 is not reported due to inadvertent chamber irradiation (see Table 1). The inset in panel b shows the change in particle size distribution for pure wall loss observed in Experiment 7 (Table 1). The initial size distribution after dilution is in gray, and the final size distribution after 9 h is in black.

Particle wall loss rate constants in the Caltech chambers are size-dependent with a minimum occurring between 200 and 300 nm. Particle wall losses potentially change the shape of the size distribution as particles of certain diameters are lost faster than others. The inset of Figure 1b shows the evolution of a SOA size distribution generated from sequential photooxidation of toluene and then α-pinene in which the chamber contents were diluted but not heated (Table 1, Experiment 7), and only particle wall losses were observed. The diameter of the size distribution peak remained within the same size bin (300–319 nm) over 9 h of wall loss. In the size range of the present experiments, wall loss is not expected to affect the diameter of the size distribution peak, only its magnitude. Evaporation can shift the size distribution peak diameter to lower diameters and, due to the Kelvin effect, broaden the size distribution as vapors evaporating from smaller diameter particles condense onto larger diameter particles. For particle diameters in the present study (≥200 nm), the Kelvin effect is not expected to be significant, but the effect is admittedly difficult to isolate in the behavior of the particle size distributions.

SOA evaporation also can be observed as a decrease in bulk particle mass and volume; however, particle wall losses, in addition to evaporation, affect the bulk particle mass and volume and must be corrected for prior to assessing possible particle evaporation. One large uncertainty associated with particle wall loss corrections is the extent of gas-particle partitioning of deposited particles. SOA mass, calculated using the two gas-particle partitioning limiting assumptions (deposited particles undergo no gas-particle partitioning or the same gas-particle partitioning as suspended particles), can differ by almost 100% when comparing the lower and higher limits.[29] There are also uncertainties associated with quantifying particle wall loss rates necessary to wall-loss correct the DMA data, and AMS PToF data show that the organic-to-sulfate ratio is not constant across the mass distribution in the present experiments, which would necessitate the use of size-dependent wall loss rates to quantify particle wall losses for AMS data.[30] Given the uncertainties associated with particle wall loss corrections, it is advantageous to detect partial SOA evaporation as a shift in the size distribution peak diameter.

The evaporation of toluene and α-pinene SOA was first assessed individually (Experiments 1 and 2, see Table 1). SOA was photochemically formed and aged for 17–19.5 h before dark dilution and heating, and no particle nucleation was observed. In Experiment 1, all α-pinene was consumed before dilution, and in Experiment 2, 70% of the toluene reacted before dilution. Figure 1 shows the evolution of the hourly averaged, suspended particle size distributions during the 7-h

Table 1. Experimental Details

expt #	seed vol (μm^3 cm^{-3})	first precursor[a]	conc (ppbv)	second precursor[a]	conc (ppbv)	dilution ratio[b]	max temp (°C)
1	23.6 ± 7.1	α-pin.	67.1 ± 3.8	-	-	3.0	41 ± 2
2[c]	22.7 ± 6.8	tol.	98.8 ± 6.2	-	-	1.8	41 ± 2
3	95.0 ± 28.5	α-pin.	61.0 ± 3.5	tol.	90.4 ± 5.7	3.0	40 ± 2
4	42.8 ± 12.8	α-pin.	74.0 ± 4.2	tol.	75.3 ± 4.8	3.7	40 ± 2
5	34.6 ± 10.4	tol.	76.0 ± 4.8	α-pin.	80.7 ± 4.6	3.4	42 ± 2
6	116 ± 35	α-pin.[d]	58.0 ± 3.3	tol.[d]	100 ± 6	3.0	41 ± 2
7	65.3 ± 19.6	tol.	43.5 ± 2.8	α-pin.	47.0 ± 2.7	3.2	27 ± 2

[a]Abbreviations correspond to toluene (tol.) and α-pinene (α-pin.). [b]Ratio of cyclohexane concentration before and after dilution. [c]During Experiment 2, the chamber was inadvertently irradiated beginning approximately 1 h after the chamber reached 41 °C. The remaining 17 ppbv of toluene reacted with the OH produced, forming a small amount of SOA. [d]Both α-pinene and toluene were injected initially.

heating period after dilution. Particle evaporation is characterized by a significant shift, as determined by the DMA resolution, in the size distribution peak diameter to smaller diameters, behavior that is observed for α-pinene (Figure 1a) but not for toluene (Figure 1b). After the heating period, α-pinene SOA continued to evaporate while the chamber enclosure was held at an elevated temperature, indicated by the black size distribution in Figure 1a. For the initial α-pinene SOA size distribution, a shift in peak diameter of 36 nm was deemed significant, and a 47 nm peak shift was observed; the 9 nm peak shift observed for the toluene SOA size distribution was not considered significant. These observations suggest that α-pinene SOA is more volatile than toluene SOA. Previous studies have measured the volatility of SOA from α-pinene or toluene photooxidation using a thermodenuder and found that both types of SOA evaporated to some extent.[29,31,32] Notably, 55% of toluene SOA evaporated at 39 °C and 16.5 s residence time.[29] In that study, however, the SOA was produced at 11 °C. In the present study, SOA was produced at 27 °C. SOA yields increase as temperature decreases,[21,22,29] as partitioning of semivolatile species to the particle phase is facilitated at lower temperatures. SOA produced from a specific precursor at higher temperatures is expected to contain a higher fraction of low volatility components than that produced at lower temperatures.

The results from Experiments 1 and 2 show that α-pinene SOA evaporates partially, whereas toluene SOA does not evaporate significantly. By observing the evaporation behavior of combinations of α-pinene and toluene SOA, it is possible to determine whether particle-phase diffusion is rapid (i.e., evaporation of SOA components, presumably from α-pinene photooxidation, occurs regardless of the SOA formation sequence) or not.

Figure 2 shows irradiation, dilution, and heating stages and the evolution of the chamber contents during Experiment 4 in which SOA was produced sequentially, first from α-pinene and then from toluene. Similar particle growth, hydrocarbon decay, and temperature changes were observed for Experiments 3 and 5. In Experiment 6, both α-pinene and toluene were injected before irradiation, and the evolution of the chamber contents resembled that in Experiment 4, excluding the second SOA growth period (commencing at the black, vertical line). During Experiments 3–5, SOA growth from the first precursor stabilized before the second precursor was added; α-pinene and toluene growth stabilized after 8 and 17 h of irradiation, respectively. Although some toluene remained after 17 h, the next part of the experiment was begun at this point due to constraints imposed by particle wall losses. Particle nucleation was not observed in Experiments 3–6.

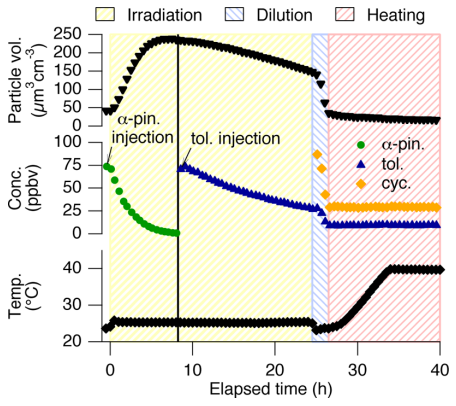

Figure 2. Experiment profile for SOA formation and evaporation when α-pinene and toluene were injected sequentially (Experiment 4). The suspended particle volume concentration, α-pinene (α-pin.), toluene (tol.), and cyclohexane (cyc.) concentrations (when above the limit of detection), and the chamber temperature are shown. Periods of irradiation, dilution, and heating are highlighted, and the toluene injection is denoted by the vertical, black line.

The evolution of the hourly averaged suspended particle size distributions during the heating period for Experiments 3–6 is shown in Figure 3. A significant shift of the size distribution peak diameter is observed only in Experiment 5 (panel c), in which toluene oxidation was followed by α-pinene oxidation. The peak shift observed was 98 nm, and a shift of at least 77 nm was deemed significant. Experiments 3 and 4 (panels a and b), in which SOA was produced in the reverse order, did not show significant changes in particle diameter due to heating. A significant shift in the peak diameter was considered to be at least 45 nm, but the peak diameter shifted 0 and 31 nm in Experiments 3 and 4, respectively. The size distribution behavior in Experiment 6, in which both precursors are present initially, is similar to that observed in Experiments 3 and 4. In Experiment 6, the diameter change of the peak, 33 nm, was also deemed insignificant (48 nm shift required). Because α-pinene reacts more rapidly with OH than does toluene (the OH reaction rate constants at 298 K are 5.3×10^{-11} cm^3 molec^{-1} s^{-1} and 5.6×10^{-12} cm^3 molec^{-1} s^{-1},[33,34] respectively), SOA formed initially in Experiment 6 likely was composed of α-pinene photooxidation products; toluene photooxidation products condensed later in the experiment, which resulted in SOA that was more similar to that in Experiments 3 and 4 than to that in Experiment 5.

The evaporation behavior in Experiments 3–6 suggests the extent of particle mixing. In Experiments 3–6, the evaporation behavior of the SOA most closely represents that of the SOA from the second parent hydrocarbon. This behavior suggests that the particle structure more closely resembles that of a core of SOA from the initial precursor coated by a layer of SOA from the second precursor rather than a single, homogeneous particle phase (aside from the solid ammonium sulfate seed). The evaporation behavior of particles in the present experiments is consistent with observations by Emanuelsson et al.,[32] who measured the volatility of mixed anthropogenic (toluene or *p*-xylene) and biogenic (α-pinene and limonene) SOA using a thermodenuder. The anthropogenic SOA was less volatile than the biogenic SOA. When anthropogenic SOA was formed on biogenic SOA particles, the volatility of the particles decreased, whereas when biogenic SOA was formed on anthropogenic SOA particles, the volatility of the particles increased. The proposed core-and-shell SOA configuration is inconsistent with results obtained by Hildebrandt et al.,[11] who found that SOA yields of α-pinene and toluene SOA indicated pseudoideal particle mixing. Uncertainties in the SOA mass calculations prevented the authors from making definitive conclusions about SOA mixing thermodynamic ideality. It is possible that the SOA in the present experiments does not exist as a strict core and shell but that long diffusion times cause SOA at the gas-particle interface to be poorly mixed with that in the particle interior.

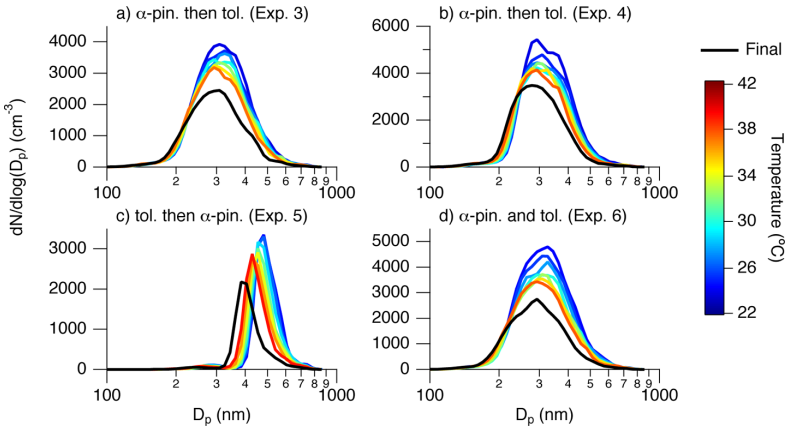

Figure 3. Evolution of the suspended particle size distribution of SOA from sequentially or simultaneously injected precursors during heating of the chamber enclosure. The data shown are averaged over 1-h intervals. Abbreviations correspond to toluene (tol.) and α-pinene (α-pin.).

For Experiments 3 and 4, in which SOA from α-pinene was coated with that of toluene and for which no evaporation was observed, it is possible to estimate the thickness of SOA from toluene condensed onto that from α-pinene and to obtain an upper bound on the diffusion coefficient for SOA components from α-pinene photooxidation in a matrix of those from toluene photooxidation, assuming that diffusional limitations prevented evaporation of SOA formed from α-pinene. The characteristic diffusion time in spherical coordinates, τ (s), is[35]

$$\tau = \frac{R_p^2}{\pi^2 D} \quad (2)$$

where R_p is distance in the radial direction (cm), and D is the diffusion coefficient ($cm^2\ s^{-1}$). Toluene SOA coating thicknesses in Experiments 3 and 4 were 2.2×10^{-6} and 2.9×10^{-6} cm, respectively, and significant evaporation was not observed in a 14-h period, providing a upper estimate of $D = 1 \times 10^{-17}$ $cm^2\ s^{-1}$, that of a semisolid.[4]

The initial concentrations of α-pinene and toluene differed among Experiments 1−6 by ∼25 ppbv (Table 1). In Experiment 5, the initial concentration of α-pinene, 81 ppbv, was the highest of all experiments in the present work. Partial SOA evaporation was observed in this case; however, partial evaporation was also observed in Experiment 1, in which SOA was formed from 67 ppbv α-pinene. This result indicates that within the range of α-pinene concentrations in the present work, no bias toward evaporation should be expected of SOA formed from higher initial α-pinene concentrations.

Because of the sequential protocol in Experiments 3−6, the second precursor and its photooxidation products were present in the chamber for less time than the first precursor and thus experienced lower OH exposure. SOA that partially evaporated (Experiment 5) contained products formed from 8 h of α-pinene photooxidation, whereas SOA that did not evaporate significantly (Experiments 3, 4, and 6) contained products formed from 23 h of α-pinene photooxidation. To investigate if increased oxidative aging affected particle evaporation, dilution and heating of solely α-pinene SOA (Experiment 1) was begun after 19.5 h of irradiation. The SOA partially evaporated (Figure 1) after experiencing OH exposures slightly less, i.e. shorter photooxidation time, than in experiments that did not show significant SOA evaporation (Experiments 3, 4, and 6). Similar results were observed by Lambe et al.,[36] who found that α-pinene photooxidation SOA evaporated partially in a thermodenuder regardless of the OH exposure used to produce it. It is unlikely that increased OH exposure under these laboratory settings would produce α-pinene SOA that is essentially nonvolatile.

Experiments 3 and 4 were conducted in the same manner, but different amounts of α-pinene and toluene were used to generate SOA in each experiment (Table 1). Although the size distribution peak diameter shifts were not significant upon heating in either experiment (0 and 31 nm for Experiments 3 and 4, respectively), a larger shift was observed in Experiment 4 than in Experiment 3. The initial α-pinene concentration in Experiment 4 was higher than that in Experiment 3, and the concentration of toluene added in Experiment 4 was lower than that in Experiment 3. At the end of the α-pinene SOA growth period, the size distribution peak diameters were similar for both experiments, but after toluene addition, the peak diameter of the size distribution in Experiment 3 increased by 43−73 nm, whereas the peak diameter increased by 14−43 nm in Experiment 4. If SOA from the second precursor coats the existing SOA from the first precursor, then the observed increase in size distribution peak diameter suggests that particles in Experiment 3 were more thickly coated with toluene SOA than those in Experiment 4. It is possible that a thicker toluene SOA coating would hinder evaporation of an α-pinene SOA core more than a thinner coating because species must diffuse farther through a thicker coating than through a thinner coating to reach the particle surface; however, this effect was not clearly detected in the present study with a 14-h evaporation period.

Aerosol Chemical Composition. One may expect to find a correlation between evaporation behavior and SOA chemical composition. If compounds with a range of volatilities exist within a particle and if mass transfer limitations do not exist, then species of higher volatility should evaporate before species of lower volatility. However, mass transfer limitations within a particle will impede evaporation of high volatility compounds. The extent to which such trends exist was evaluated using average carbon oxidation state, $\overline{OS}_C$ calculated from oxygen-to-carbon and hydrogen-to-carbon ratios (O:C, H:C) measured by the AMS.[37] It is important to note that the AMS measures

bulk particle chemical composition even if the SOA exists as a core-and-shell configuration. For example, as α-pinene SOA condenses onto toluene SOA, the bulk chemical composition of the particles may change; however, the condensing α-pinene SOA may not greatly affect the chemical composition of the pre-existing toluene SOA core. With the exception of small molecules and oligomers, volatility of a compound decreases with increasing O:C,[38] and thus $\overline{OS}_C$. Upon evaporation of higher volatility components, $\overline{OS}_C$ should increase in the remaining SOA.

The bulk chemical composition of SOA formed during all experiments is shown in Figure 4. During the SOA formation

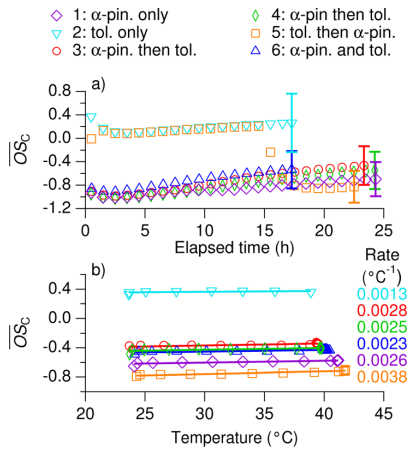

Figure 4. Evolution of aerosol oxidation state during formation (panel a) and dilution and heating (panel b). The error bars in panel a represent the uncertainty values for $\overline{OS}_C$, calculated from those for H:C and O:C, 10% and 31%, respectively,[28] at the end of the formation period. The rate of change of $\overline{OS}_C$ as a function of temperature for each experiment is listed in panel b. Abbreviations correspond to toluene (tol.) and α-pinene (α-pin.).

period (Figure 4a), $\overline{OS}_C$ increases, a trend generally observed during SOA growth,[31,39,40] with the exception of Experiment 5. In Experiment 5, the expected trend is observed during the initial formation of SOA from toluene, but once α-pinene is injected and α-pinene SOA condenses onto the toluene SOA, $\overline{OS}_C$ decreases abruptly. As α-pinene SOA continues to condense, the expected trend is repeated. SOA from α-pinene has lower $\overline{OS}_C$ than that from toluene, as observed in Experiments 1 and 2 and by others, reported separately as O:C and H:C.[31−40] The aromatic ring of toluene provides more sites for OH attack than does the structure of α-pinene, which contains only a single alkene functionality, and has a greater potential for producing highly oxygenated species. The vapor pressure of α-pinene is a factor of 10 lower than that of toluene,[41,42] and less oxygenation of α-pinene than of toluene is needed to produce condensable products. Because toluene contains fewer carbons than α-pinene, the addition of each oxygen atom to the molecule preferentially increases the O:C, and thus $\overline{OS}_C$, for toluene products more than for α-pinene products. SOA condenses within 30 min of α-pinene photooxidation, and because its chemical composition differs from that of toluene SOA, a sudden change in SOA chemical composition when α-pinene SOA condenses onto toluene SOA is not unexpected. A rough estimation of the volume fractions of SOA from α-pinene and toluene in Experiments 5 can be obtained from the change in size distribution peak diameter upon SOA condensation. Peak diameters for the seed, seed and SOA from toluene, and seed and SOA from toluene and α-pinene are 69, 162, and 482 nm, respectively. The ratio of SOA from α-pinene to that from toluene is approximately 25:1, and bulk SOA chemical composition is expected to reflect primarily α-pinene, even upon evaporation.

Bulk SOA chemical composition did not change drastically upon dilution and heating (Figure 4b). $\overline{OS}_C$ increased upon heating linearly with temperature, as shown in Figure 4b with the rate-of-change of $\overline{OS}_C$, $r\overline{OS}_C$, listed for each experiment on the right side of the panel. The largest $r\overline{OS}_C$ was observed for SOA from toluene coated with that from α-pinene (Experiment 5), and the smallest $r\overline{OS}_C$ was observed for SOA from toluene only (Experiment 2). All changes in $\overline{OS}_C$ during the heating period were small relative to the change in $\overline{OS}_C$ upon SOA formation, and the differences in $\overline{OS}_C$ among SOA generated in the different experiments. The lack of substantial chemical change during evaporation is consistent with results obtained by Cappa and Wilson[3] and Huffman et al.[43] when measuring the bulk chemical composition of thermodenuded α-pinene ozonolysis SOA. However, in other studies of α-pinene ozonolysis SOA evaporation, using either a thermodenuder or diluting particles suspended in a chamber, chemical changes were observed in the SOA upon evaporation.[19,44,45] The differences in the studies that lead to the contrasting results remain to be identified.

Correlations between bulk chemical composition and evaporation behavior were assessed using data collected immediately before the dilution and heating period, those with the largest elapsed time in Figure 4a. The data show that the SOA formed spans a range of $\overline{OS}_C$ values. A clear correlation of chemical composition with volatility is observed for the solely toluene SOA and the solely α-pinene SOA experiments. Toluene SOA, which has the highest $\overline{OS}_C$ of the systems studied, did not evaporate significantly. α-Pinene SOA exhibited lower $\overline{OS}_C$ than the toluene SOA and partially evaporated. From these two observations, it is possible to conclude that a transition from volatile to essentially non-volatile SOA occurs in the range of average $\overline{OS}_C$ observed in the present work for α-pinene and toluene SOA. However, for the combined α-pinene and toluene SOA, no distinct correlation between bulk chemical composition and evaporation behavior is observed. The bulk chemical composition of the two-precursor SOA more closely resembled that of α-pinene SOA than toluene SOA. SOA with lower $\overline{OS}_C$ than solely α-pinene SOA (formed from toluene then α-pinene) partially evaporated, whereas SOA with higher $\overline{OS}_C$ than solely α-pinene SOA (formed from α-pinene then toluene or α-pinene and toluene) did not significantly evaporate. However, the variance in the data for these SOA types, excluding solely toluene SOA, lies within the uncertainty of the measurements, represented by the error bars in Figure 4a. Even if SOA exists in a core-and-shell configuration, the bulk elemental composition reflects a combination of SOA from the two precursors and will not be indicative necessarily of the elemental composition of the phase at the gas-particle interface. While bulk chemical composition data correlate with volatility for SOA from a single parent hydrocarbon, the same correlation does not apply to SOA formed from multiple precursors. The present experiments

suggest that both particle composition and history can play a role in its physiochemical behavior.

AUTHOR INFORMATION

Corresponding Author

*E-mail: seinfeld@caltech.edu.

Present Address

[§]Institute for Atmospheric and Climate Science, ETH Zurich, Switzerland.

Notes

The authors declare no competing financial interest.

ACKNOWLEDGMENTS

This work was supported by the Office of Science (Biological and Environmental Research), US Department of Energy Grant DE-SC 0006626. We thank Jill Craven, Rebecca Schwantes, Lindsay Yee, and Xuan Zhang for experimental assistance, Andrew Metcalf and Manabu Shiraiwa for helpful discussions, and Yu Jun Leong and Robert Griffin for lending us their AMS power supply.

REFERENCES

(1) Virtanen, A.; Joutsensaari, J.; Koop, T.; Kannosto, J.; Yli-Pirilä, P.; Leskinen, J.; Mäkelä, J. M.; Holopainen, J. K.; Pöschl, U.; Kulmala, M.; Worsnop, D. R.; Laaksonen, A. An amorphous solid state of biogenic secondary organic aerosol particles. *Nature* **2010**, *467*, 824−827.

(2) Vaden, T. D.; Song, C.; Zaveri, R. A.; Imre, D.; Zelenyuk, A. Morphology of mixed primary and secondary organic particles and the adsorption of spectator organic gases during aerosol formation. *Proc. Natl. Acad. Sci. U.S.A.* **2010**, *107*, 6658−6663.

(3) Cappa, C. D.; Wilson, K. R. Evolution of organic aerosol mass spectra upon heating: Implications for OA phase and partitioning behavior. *Atmos. Chem. Phys.* **2011**, *11*, 1895−1911.

(4) Shiraiwa, M.; Ammann, M.; Koop, T.; Pöschl, U. Gas uptake and chemical aging of semisolid organic aerosol particles. *Proc. Natl. Acad. Sci. U.S.A.* **2011**, *108*, 11003−11008.

(5) Vaden, T. D.; Imre, D.; Beránek, J.; Shrivastava, M.; Zelenyuk, A. Evaporation kinetics and phase of laboratory and ambient secondary organic aerosol. *Proc. Natl. Acad. Sci. U.S.A.* **2011**, *108*, 2190−2195.

(6) Kuwata, M.; Martin, S. T. Phase of atmospheric secondary organic material affects its reactivity. *Proc. Natl. Acad. Sci. U.S.A.* **2012**, *109*, 17354−17359.

(7) Perraud, V.; Bruns, E. A.; Ezell, M. J.; Johnson, S. N.; Yu, Y.; Alexander, M. L.; Zelenyuk, A.; Imre, D.; Chang, W. L.; Dabdub, D.; Pankow, J. F.; Finlayson-Pitts, B. J. Nonequilibrium atmospheric secondary organic aerosol formation and growth. *Proc. Natl. Acad. Sci. U.S.A.* **2012**, *109*, 2836−2841.

(8) Saukko, E.; Lambe, A. T.; Massoli, P.; Koop, T.; Wright, J. P.; Croasdale, D. R.; Pedernera, D. A.; Onasch, T. B.; Laaksonen, A.; Davidovits, P.; Worsnop, D. R.; Virtanen, A. Humidity-dependent phase state of SOA particles from biogenic and anthropogenic precursors. *Atmos. Chem. Phys.* **2012**, *12*, 7517−7529.

(9) Abramson, E.; Imre, D.; Beranek, J.; Wilson, J.; Zelenyuk, A. Experimental determination of chemical diffusion within secondary organic aerosol particles. *Phys. Chem. Chem. Phys.* **2013**, *15*, 2983−2991.

(10) Koop, T.; Bookhold, J.; Shiraiwa, M.; Pöschl, U. Glass transition and phase state of organic compounds: Dependency on molecular properties and implications for secondary organic aerosols in the atmosphere. *Phys. Chem. Chem. Phys.* **2011**, *13*, 19238−19255.

(11) Hildebrandt, L.; Henry, K. M.; Kroll, J. H.; Worsnop, D. R.; Pandis, S. N.; Donahue, N. M. Evaluating the mixing of organic aerosol components using high-resolution aerosol mass spectrometry. *Environ. Sci. Technol.* **2011**, *45*, 6329−6335.

(12) Odum, J. R.; Hoffmann, T.; Bowman, F.; Collins, D.; Flagan, R. C.; Seinfeld, J. H. Gas/particle partitioning and secondary organic aerosol yields. *Environ. Sci. Technol.* **1996**, *30*, 2580−2585.

(13) Bowman, F. M.; Odum, J. R.; Seinfeld, J. H.; Pandis, S. N. Mathematical model for gasparticle partitioning of secondary organic aerosols. *Atmos. Environ.* **1997**, *31*, 3921−3931.

(14) Odum, J. R.; Jungkamp, T. P. W.; Griffin, R. J.; Flagan, R. C.; Seinfeld, J. H. The atmospheric aerosol-forming potential of whole gasoline vapor. *Science* **1997**, *276*, 96−99.

(15) Strader, R.; Lurmann, F.; Pandis, S. N. Evaluation of secondary organic aerosol formation in winter. *Atmos. Environ.* **1999**, *33*, 4849−4863.

(16) Shiraiwa, M.; Seinfeld, J. H. Equilibration timescale of atmospheric secondary organic aerosol partitioning. *Geophys. Res. Lett.* **2012**, *39*, L24801.

(17) An, W. J.; Pathak, R. K.; Lee, B.-H.; Pandis, S. N. Aerosol volatility measurement using an improved thermodenuder: Application to secondary organic aerosol. *J. Aerosol Sci.* **2007**, *38*, 305−314.

(18) Tritscher, T.; Dommen, J.; DeCarlo, P. F.; Gysel, M.; Barmet, P. B.; Praplan, A. P.; Weingartner, E.; Prévôt, A. S. H.; Riipinen, I.; Donahue, N. M.; Baltensperger, U. Volatility and hygroscopicity of aging secondary organic aerosol in a smog chamber. *Atmos. Chem. Phys.* **2011**, *11*, 11477−11496.

(19) Grieshop, A. P.; Donahue, N. M.; Robinson, A. L. Is the gas-particle partitioning in alphapinene secondary organic aerosol reversible? *Geophys. Res. Lett.* **2007**, *34*, L14810.

(20) Stanier, C. O.; Pathak, R. K.; Pandis, S. N. Measurements of the volatility of aerosols from α-piniene ozonolysis. *Environ. Sci. Technol.* **2007**, *41*, 2756−2763.

(21) Warren, B.; Austin, R. L.; Cocker, D. R., III Temperature dependence of secondary organic aerosol. *Atmos. Environ.* **2009**, *43*, 3548−3555.

(22) Qi, L.; Nakao, S.; Tang, P.; Cocker, D. R., III Temperature effect on physical and chemical properties of secondary organic aerosol from *m*-xylene photooxidation. *Atmos. Chem. Phys.* **2010**, *10*, 3847−3854.

(23) Zhang, S. H.; Flagan, R. C. Resolution of the radial differential mobility analyzer for ultrafine particles. *J. Aerosol Sci.* **1996**, *27*, 1179−1200.

(24) Stolzenburg, M. R. An ultrafine aerosol size distribution measuring system. Ph.D. Thesis, University of Minnesota, 1988.

(25) DeCarlo, P. F.; Kimmel, J. R.; Trimborn, A.; Northway, M. J.; Jayne, J. T.; Aiken, A. C.; Gonin, M.; Fuhrer, K.; Horvath, T.; Docherty, K. S.; Worsnop, D. R.; Jimenez, J. L. Field deployable, high-resolution, time-of-fight aerosol mass spectrometer. *Anal. Chem.* **2006**, *78*, 8281−8289.

(26) Canagaratna, M. R.; et al. Chemical and microphysical characterization of ambient aerosols with the aerodyne aerosol mass spectrometer. *Mass Spectrom. Rev.* **2007**, *26*, 185−222.

(27) Allan, J. D.; Delia, A. E.; Coe, H.; Bower, K. N.; Alfarra, M. R.; Jimenez, J. L.; Middlebrook, A. M.; Drewnick, F.; Onasch, T. B.; Canagaratna, M. R.; Jayne, J. T.; Worsnop, D. R. A generalised method for the extraction of chemically resolved mass spectra from Aerodyne aerosol mass spectrometer data. *J. Aerosol Sci.* **2004**, *35*, 909−922.

(28) Aiken, A. C.; et al. O/C and OM/OC ratios of primary, secondary, and ambient organic aerosols with high-resolution time-of-fight aerosol mass spectrometry. *Environ. Sci. Technol.* **2008**, *42*, 4478−4485.

(29) Hildebrandt, L.; Donahue, N. M.; Pandis, S. N. High formation of secondary organic aerosol from the photo-oxidation of toluene. *Atmos. Chem. Phys.* **2009**, *9*, 2973−2986.

(30) Loza, C. L.; Chhabra, P. S.; Yee, L. D.; Craven, J. S.; Flagan, R. C.; Seinfeld, J. H. Chemical aging of *m*-xylene secondary organic aerosol: Laboratory chamber study. *Atmos. Chem. Phys.* **2012**, *12*, 151−167.

(31) Lambe, A. T.; Onasch, T. B.; Massoli, P.; Croasdale, D. R.; Wright, J. P.; Ahern, A. T.; Williams, L. R.; Worsnop, D. R.; Brune, W. H.; Davidovits, P. Laboratory studies of the chemical composition and cloud condensation nuclei (CCN) activity of secondary organic

aerosol (SOA) and oxidized primary organic aerosol (OPOA). *Atmos. Chem. Phys.* **2011**, *11*, 8913−8928.
(32) Emanuelsson, E. U.; Hallquist, M.; Kristensen, K.; Glasius, M.; Bohn, B.; Fuchs, H.; Kammer, B.; Kiendler-Scharr, A.; Nehr, S.; Rubach, F.; Tillmann, R.; Wahner, A.; Wu, H.-C.; Mentel, T. F. Formation of anthropogenic secondary organic aerosol (SOA) and its influence on biogenic SOA properties. *Atmos. Chem. Phys. Discuss.* **2012**, *12*, 20311−20350.
(33) Atkinson, R.; Baulch, D. L.; Cox, R. A.; Crowley, J. N.; Hampson, R. F.; Hynes, R. G.; Jenkin, M. E.; Rossi, M. J.; Troe, J. IUPAC Subcommittee, Evaluated kinetic and photo-chemical data for atmospheric chemistry: Volume II - gas phase reactions of organic species. *Atmos. Chem. Phys.* **2006**, *6*, 3625−4055.
(34) Atkinson, R.; Arey, J. Atmospheric degradation of volatile organic compounds. *Chem. Rev.* **2003**, *103*, 4605−4638.
(35) Seinfeld, J. H.; Pandis, S. N. *Atmospheric Chemistry and Physics*, 2nd ed.; John Wiley and Sons, Inc.: Hoboken, NJ, 2006.
(36) Lambe, A. T.; Onasch, T. B.; Croasdale, D. R.; Wright, J. P.; Martin, A. T.; Franklin, J. P.; Massoli, P.; Kroll, J. H.; Canagaratna, M. R.; Brune, W. H.; Worsnop, D. R.; Davidovits, P. Transitions from functionalization to fragmentation reactions of laboratory secondary organic aerosol (SOA) generated from the OH oxidation of alkane precursors. *Environ. Sci. Technol.* **2012**, *46*, 5430−5437.
(37) Kroll, J. H.; Donahue, N. M.; Jimenez, J. L.; Kessler, S. H.; Canagaratna, M. R.; Wilson, K. R.; Altieri, K. E.; Mazzoleni, L. R.; Wozniak, A. S.; Bluhm, H.; Mysak, E. R.; Smith, J. D.; Kolb, C. E.; Worsnop, D. R. Carbon oxidation state as a metric for describing the chemistry of atmospheric organic aerosol. *Nat. Chem.* **2011**, *3*, 133−139.
(38) Jimenez, J. L.; et al. Evolution of organic aerosols in the atmosphere. *Science* **2009**, *326*, 1525−1529.
(39) Ng, N. L.; et al. Organic aerosol components observed in Northern Hemispheric datasets from Aerosol Mass Spectrometry. *Atmos. Chem. Phys.* **2010**, *10*, 4625−4641.
(40) Chhabra, P. S.; Ng, N. L.; Canagaratna, M. R.; Corrigan, A. L.; Russell, L. M.; Worsnop, D. R.; Flagan, R. C.; Seinfeld, J. H. Elemental composition and oxidation of chamber organic aerosol. *Atmos. Chem. Phys.* **2011**, *11*, 8827−8845.
(41) Hawkins, J.; Armstrong, G. Physical and thermodynamic properties of terpenes. III. The vapor pressures of α-pinene and β-pinene. *J. Am. Chem. Soc.* **1954**, *76*, 3756−3758.
(42) Pitzer, K. S.; Scott, D. W. The thermodynamics and molecular structure of benzene and its methyl derivatives. *J. Am. Chem. Soc.* **1943**, *65*, 803−829.
(43) Huffman, J. A.; Docherty, K. S.; Mohr, C.; Cubison, M. J.; Ulbrich, I. M.; Ziemann, P. J.; Onasch, T. B.; Jimenez, J. L. Chemically-resolved volatility measurements of organic aerosol from different sources. *Environ. Sci. Technol.* **2009**, *43*, 5351−5357.
(44) Docherty, K. S.; Wu, W.; Lim, Y. B.; Ziemann, P. J. Contributions of organic peroxides to secondary aerosol formed from reactions of monoterpenes with O_3. *Environ. Sci. Technol.* **2005**, *39*, 4049−4059.
(45) Kostenidou, E.; Lee, B.-H.; Engelhart, G. J.; Pierce, J. R.; Pandis, S. N. Mass spectra deconvolution of low, medium, and high volatility biogenic secondary organic aerosol. *Environ. Sci. Technol.* **2009**, *43*, 4884−4889.

Chapter 6

Organic Aerosol Formation from the Reactive Uptake of Isoprene Epoxydiols (IEPOX) onto Non-acidified Inorganic Seeds.

Atmos. Chem. Phys., 14, 3497–3510, 2014
www.atmos-chem-phys.net/14/3497/2014/
doi:10.5194/acp-14-3497-2014

Atmospheric Chemistry and Physics
Open Access

Organic aerosol formation from the reactive uptake of isoprene epoxydiols (IEPOX) onto non-acidified inorganic seeds

T. B. Nguyen[1], M. M. Coggon[2], K. H. Bates[2], X. Zhang[1], R. H. Schwantes[1], K. A. Schilling[2], C. L. Loza[2,*], R. C. Flagan[2,3], P. O. Wennberg[1,3], and J. H. Seinfeld[2,3]

[1]Division of Geological and Planetary Sciences, California Institute of Technology, Pasadena, California, USA
[2]Division of Chemistry and Chemical Engineering, California Institute of Technology, Pasadena, California, USA
[3]Division of Engineering and Applied Science, California Institute of Technology, Pasadena, California, USA
[*]currently at: 3M Environmental Laboratory, 3M Center, Building 0260-05-N-17, St. Paul, Minnesota, USA

Correspondence to: T. Nguyen (tbn@caltech.edu)

Received: 10 October 2013 – Published in Atmos. Chem. Phys. Discuss.: 28 October 2013
Revised: 8 February 2014 – Accepted: 18 February 2014 – Published: 8 April 2014

Abstract. The reactive partitioning of *cis* and *trans* β-IEPOX was investigated on hydrated inorganic seed particles, without the addition of acids. No organic aerosol (OA) formation was observed on dry ammonium sulfate (AS); however, prompt and efficient OA growth was observed for the *cis* and *trans* β-IEPOX on AS seeds at liquid water contents of 40–75 % of the total particle mass. OA formation from IEPOX is a kinetically limited process, thus the OA growth continues if there is a reservoir of gas-phase IEPOX. There appears to be no differences, within error, in the OA growth or composition attributable to the *cis* / *trans* isomeric structures. Reactive uptake of IEPOX onto hydrated AS seeds with added base (NaOH) also produced high OA loadings, suggesting the pH dependence for OA formation from IEPOX is weak for AS particles. No OA formation, after particle drying, was observed on seed particles where Na^+ was substituted for NH_4^+. The Henry's Law partitioning of IEPOX was measured on NaCl particles (ionic strength ∼9 M) to be 3×10^7 M atm^{-1} (−50 / +100 %). A small quantity of OA was produced when NH_4^+ was present in the particles, but the chloride (Cl^-) anion was substituted for sulfate (SO_4^{2-}), possibly suggesting differences in nucleophilic strength of the anions. Online time-of-flight aerosol mass spectrometry and offline filter analysis provide evidence of oxygenated hydrocarbons, organosulfates, and amines in the particle organic composition. The results are consistent with weak correlations between IEPOX-derived OA and particle acidity or liquid water observed in field studies, as the chemical system is nucleophile-limited and not limited in water or catalyst activity.

1 Introduction

A significant portion of the organic aerosol (OA) production from isoprene, a non-methane hydrocarbon emitted to the atmosphere in vast amounts, is attributed to the heterogeneous chemistry of isoprene epoxydiols (IEPOX) (Froyd et al., 2010; Chan et al., 2010; McNeill et al., 2012; Surratt et al., 2010; Hatch et al., 2011; Budisulistiorini et al., 2013; Pye et al., 2013). IEPOX, of which there are four isomeric forms (Scheme 1), is a second-generation low nitric oxide (NO) isoprene photooxidation product formed from the OH-oxidation of particular isomers of isoprene hydroxy hydroperoxides (Paulot et al., 2009b). The mechanism for OA production from IEPOX has been proposed as ring-opening of the epoxide group, activated by proton transfer from a strong acid such as sulfuric acid (H_2SO_4), followed by nucleophilic addition of available nucleophiles in the condensed phase, e.g., addition of water to produce tetrols, sulfate to produce organosulfates, and so on (Minerath et al., 2008; Eddingsaas et al., 2010; Surratt et al., 2010). This proposed mechanism has been corroborated by chamber investigations of particle acidity effects on OA formation (Surratt et al., 2007; Lin et al., 2012), wherein dry acidic seeds ($MgSO_4 : H_2SO_4$, 1 : 1) prompted strong reactive uptake behavior from epoxides (Paulot et al., 2009b), compared to negligible uptake for dry, non-acidified seeds.

Recent field data suggest that the story might be more complex than described above, as weak correlations between particle acidity and the abundance of IEPOX particle-phase tracer products were observed in Southeastern USA sites

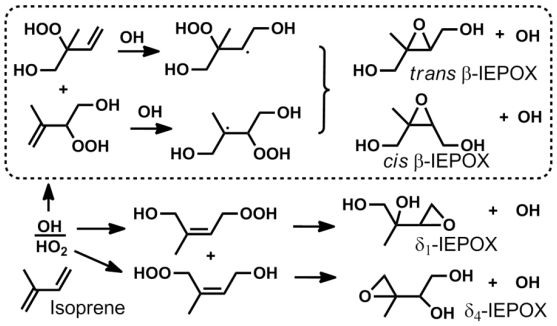

Scheme 1 Formation of IEPOX isomers, from relevant isoprene hydroxy hydroperoxide precursors, in the low-NO photooxidation of isoprene. The expected dominant pathway is shown inside the box. The naming convention is based on Paulot et al. (2009b).

(Lin et al., 2013; Budisulistiorini et al., 2013). It should be noted that the indirect definition of "particle acidity," which relies on charge balance of cations and anions, have several limitations and may not effectively represent the activity of H^+ in the aqueous phase of particles in some cases (Gregoire, 2013). Nevertheless, from the field observations, Lin and coworkers proposed that other factors may possibly modulate OA formation from IEPOX in conjunction with particle $[H^+]$. One important distinction between previous chamber investigations, which have all been conducted under dry conditions (relative humidity, RH < 5 %), and the Southeastern USA location is the prevalence of particle liquid water on the ammonium sulfate seeds. Water is a ubiquitous and abundant component of the atmosphere, therefore the effect of liquid water on the uptake of OA precursors has important implications for much of the globe. The crystalline ammonium sulfate seeds used in dry chamber experiments may not have adequate liquid water for IEPOX to partition into the aqueous phase, nor sufficient H^+, NH_4^+, and SO_4^{2-} activities to promote reactive uptake. Similarly, a particle with a large weight percent of H_2SO_4 may have a sizeable liquid water component, even at RH < 5 %, due to the strong hygroscopicity of H_2SO_4 (Xiong et al., 1998), and the difference in reactive uptake of IEPOX may be due either to the differences in particle liquid water or the particle free acidity. In contrast, high concentrations of liquid water may cause dilution of aqueous ions, i.e., changing the acidity or ionic strength, which has been demonstrated to change the effective Henry's Law partitioning coefficient of glyoxal (Kampf et al., 2013). Despite these important interactions, the effect of liquid water on OA formation from IEPOX has not been systematically explored in the laboratory.

We report here the reactive uptake of two isomers of IEPOX, the *cis* and *trans* β-IEPOX (Paulot et al., 2009b), which together comprise more than 97 % of the isomer distribution (Bates et al., 2014). We synthesized authentic standards and observed the dark OA growth onto non-acidified and hydrated inorganic seeds at several particle liquid water concentrations. In the atmosphere, ammonium ions (NH_4^+) are one of the most abundant components of aerosols and considerable IEPOX-derived OA are observed, even when a dominant portion of the aerosols are charge-balanced, e.g., $[NH_4^+] : 1/2 \times [SO_4^{2-}]$ or $[NH_4^+] : [NO_3^-] \sim 1$ (Lin et al., 2013). The aqueous NH_4^+ may possibly act as catalyst for OA formation, as has been shown for a number of atmospherically important reactions (Noziere et al., 2009; Sareen et al., 2010; Ervens and Volkamer, 2010; Yu et al., 2011). We study reaction with NH_4^+ as a potential rate-limiting mechanism for the IEPOX reaction. The role of cation and anion compositions in the seed for OA formation is studied by using ammonium sulfate, ammonium chloride, sodium sulfate, and sodium chloride seeds.

2 Materials and methods

2.1 Experimental procedures

This work utilized a newly constructed 24 m^3 FEP Teflon environmental chamber specifically reserved for low-NO_x applications. The walls have not been in contact with strong acids and the chamber was operated in batch mode. Experiments were performed at room temperature (23–24 °C) and in the dark. Prior to the start of experiments, the chamber was thoroughly flushed with dry, purified air until particle concentrations are < 0.01 µg m^{-3}. For humid experiments, water vapor was injected until the desired relative humidity (RH) was achieved in the chamber by flowing dry purified air over a Nafion membrane humidifier (FC200, Permapure LLC), which is kept moist by recirculating 27 °C ultrapurified (18 MΩ) water (Milli-Q, Millipore Corp). Temperature and RH were measured by a Vaisala HMM211 probe, calibrated with saturated salt solutions in the RH range of 11–95 %. For RH < 11 %, the water vapor content was quantified by chemical ionization mass spectrometry (Sect. 2.2.1).

Seed particles were injected by atomizing aqueous solutions (0.06 M) of ammonium sulfate ($(NH_4)_2SO_4$, AS), sodium chloride (NaCl), ammonium chloride (NH_4Cl), or sodium sulfate (Na_2SO_4) at 2100 hPa of air into the chamber through a ^{210}Po neutralizer and water trap. All inorganic seeds were injected through a 30 cm custom-built wet-wall denuder kept at 90 °C, such that the seed particles enter the chamber hydrated. Liquid water is expected to evaporate from the seed particles according to the salt's efflorescence behavior (Lee and Hsu, 2000) at the RH of the chamber, e.g., in a dry chamber it is expected that the hydrated particles will enter the chamber fully dried. Particles were allowed to equilibrate until their volume concentrations are stable prior to organic injections.

Two isomers of isoprene epoxydiols (*cis* and *trans* β-IEPOX) were synthesized via procedures adapted from

Zhang et al. (2012) and purified with normal-phase column chromatography until the estimated purity based on nuclear magnetic resonance (NMR) of the *cis* and *trans* β-IEPOX isomers are 99 % and > 92 %, respectively. Details of the synthesis and NMR spectra are reported in Bates et al. (2014). Although the mole fractions of the impurities are low, their high volatility may lead to an over-represented abundance in the gas phase. For the *cis* isomer, we detected experimental interference from the volatile 1,4-dihydroxy-2-methyl-2-butene (a precursor used in the synthesis), comprising ∼50 % of the vapor phase measured directly above a bulb of IEPOX droplets by chemical ionization mass spectrometry (CIMS, Sect. 2.2). In order to further purify before experiments were conducted, *cis* β-IEPOX droplets were purged with dry N_2, and combined with 60 °C heating for > 8 h until the measured impurity fraction dropped below 2 % (Fig. S1 in the Supplement). After the additional purification, IEPOX was injected into the chamber by flowing a 5–8 L min^{-1} stream of dry purified air past several droplets in a clean glass bulb heated to 60 °C for 2–4 h. The mixtures of IEPOX and seed aerosols were allowed to equilibrate for > 1 h. Most of the experimental conditions were repeated and were found to be reproducible within 15 %. We expect systematic error to dominate over the error of precision in this work.

2.2 Analytical methods

2.2.1 Chemical ionization mass spectrometry (CIMS)

Gas-phase IEPOX was measured with negative-ion chemical ionization mass spectrometry (CIMS) using CF_3O^- as the reagent ion, described in more detail previously (Crounse et al., 2006; Paulot et al., 2009a; St. Clair et al., 2010). The mass analyzer is a Varian triple-quadrupole spectrometer with unit mass resolution. Air is brought from the chamber using a 3 mm inner diameter perfluoroalkoxy (PFA) Teflon line with flow rate of 2.5 L min^{-1}. Of the total chamber flow, a 145 mL min^{-1} analyte flow was sampled orthogonally through a glass critical orifice into the CIMS. The analyte flow was further diluted by a factor of 12 with dry N_2 to minimize the interaction of water vapor from the chamber with the reagent ion in the ion-molecule flow region. The subsequent data analysis corrects for the dilution factor. The operational pressure and temperature were kept at 35.5 hPa and 35 °C, respectively. The CIMS operated in a scanning MS mode (m/z 50–250) and tandem MS mode (MSMS). In MSMS mode, collisionally induced dissociation (CID) with 2.6 hPa of N_2 fragments analyte ions into product ions in the second quadrupole, following the ejection of neutral species. The MS cluster ion $C_5H_{10}O_3 \cdot CF_3O^-$ (m/z 203) of IEPOX was used for quantification, due to the higher signal-to-noise (S / N) of this ion compared to MSMS ions. The MSMS product ion $C_5H_9O_3 \cdot CF_2O^-$ (m/z 203 → m/z 183), found to be unique to IEPOX in the isoprene OH-oxidation system, was used to differentiate IEPOX from the isobaric isoprene hydroperoxide (ISOPOOH), which has been documented to yield mainly m/z 63 and a negligible amount of m/z 183 upon CID (Paulot et al., 2009b). ISOPOOH (m/z 203 → m/z 63), was not expected, nor observed, during IEPOX injections.

CIMS calibrations of *cis* and *trans* β-IEPOX were performed by separately atomizing dilute (1–3 mM) solutions of each isomer with equimolar concentrations of hydroxyacetone, used as an internal standard, into the chamber through a 15 cm PFA Teflon transfer line for a few hours. During synthesis, NMR analysis showed that IEPOX was stable in water solution for many hours if no acid was present, so decay of IEPOX in the atomizer solution was not expected over the course of the calibration experiment. Toluene was used as a tracer to obtain the exact volume of the Teflon bag for each calibration experiment. A measured volume of toluene (6 µL) was injected into a clean glass bulb with a microliter syringe (Hamilton) and quantitatively transferred into the chamber with a 5 L min^{-1} stream of dry purified air. The gas-phase toluene was monitored by commercial gas chromatograph with flame-ionization detector (GC-FID, Hewlett-Packard 6890N) using a calibrated HP-5 column (15 m, 0.53 mm i.d.). The initial chamber temperature was 35 °C, and the temperature was ramped until 45 °C or until no increase of IEPOX signal was observed in the CIMS. The atomized solution was weighed before and after atomization. Each sensitivity determination was repeated at least twice. The sensitivities of the IEPOX isomers were calculated from the ratio of the normalized ion counts (with respect to the reagent ion signal) to the number of atomized moles. Small amounts of nucleated organic aerosols were observed in the chamber from the atomization, as measured by a scanning mobility particle sizer (Sect. 2.2.3) and that volume concentration was subtracted from the theoretical moles of IEPOX (corrections of < 1 %). Based on their calculated dipole moments and average polarizability, the *cis* isomer was expected to have a sensitivity of ∼1.6 times greater than the *trans* isomer (Paulot et al., 2009b), and we found the sensitivity of the *cis* isomer to be a factor of 1.8 greater than the *trans* isomer in the MS mode. The difference between the two ratios is within the error of the sensitivity determination.

Additionally, several mixing ratios of water vapor were introduced into the CIMS ion-molecule region to measure the water dependence of the IEPOX detection. Water vapor was quantified by Fourier-transform infrared spectroscopy (FT-IR, Nicolet Magna-IR 560) with a 19 cm pathlength quartz cell. Spectral fitting was performed using the HITRAN spectral database (Rothman et al., 2009) and the nonlinear fitting software NLM4 developed by Griffith (1996). In the low-RH range, outside the calibration limit of the membrane RH probe, the CIMS water ions $H_2O \cdot {}^{13}CF_3O^-$ (m/z 104) and $(H_2O)_2 \cdot CF_3O^-$ (m/z 121) were used to quantify water vapor concentration in the chamber after calibration of water vapor with FT-IR. These ions provide excellent sensitivity to water and linearity in the 20–3500 ppm range in the CIMS

ion molecule flow region (corresponding to 1–100 % RH in the chamber at 24 °C, before CIMS dilution). No water dependence in the detection of the IEPOX ions was observed within the range of water vapor observed by CIMS.

In order to quantify the gas-phase concentrations of IEPOX, the CIMS signal was corrected to account for the RH-dependent wall losses of IEPOX. The interactions of IEPOX with chamber walls have not been previously characterized, although those of its C_4 analog have been reported (Loza et al., 2010). IEPOX wall loss experiments were conducted at RH = 3 %, 46 %, and 69 %, as described in Section 2.1, continuously for 5–10 h. Figure S2 shows that the wall losses of IEPOX on non-acidic walls were negligibly small ($\sim$0.4 % h^{-1} at RH 69 %), within the error of CIMS measurements.

2.2.2 Aerosol mass spectrometry (AMS)

Online particle composition was measured with a high-resolution time-of-flight aerosol mass spectrometer (ToF-AMS, Aerodyne Research Inc.). The ToF-AMS was operated in V mode (R $\sim$2000 at m/z 200) and W mode (R $\sim$3000–4000 at m/z 200). Prior to experiments, the ToF-AMS ionization efficiency was calibrated using size-selected 350 nm ammonium nitrate particles. The ToF-AMS monitored the content of ammonium (NH_4^+), sulfate (SO_4^{2-}) and other non-refractory ions throughout the course of the experiment. The ammonium to sulfate ratio did not change over the course of the experiment. Gas interferences and elemental ratios were calculated using the fragmentation tables developed by Allan et al. (2004) and Aiken et al. (2008). Data were analyzed in IGOR Pro 6.31 (WaveMetrics, Inc.) using the SQUIRREL v 1.51H and PIKA v 1.10H analysis toolkits. Total concentration of organics (µg m^{-3}) was calculated by summing the nitrate-equivalent masses of each high-resolution ion correlated with the organic fraction from the V-mode data.

Particles were sampled through a 130 cm Nafion membrane diffusion drier (MD-110, Permapure LLC) to avoid flow obstructions from wet particles over time, at a flow rate of 0.084 L min^{-1}. It is expected that drying the particles may introduce particle or organic line losses in the drier tube and change the particle bounce characteristics on the AMS vaporizer plate. These perturbations may be corrected by applying a collection-efficiency (CE) factor. It was demonstrated that organic aerosol particles with higher water content have very low bounce probability, which corresponds to a CE of unity (Matthew et al., 2008; Docherty et al., 2013). Comparatively, dry particles have much lower CE ($\sim$0.25 for pure, dry AS) due to the high bounce rate. The CE of IEPOX-derived organic aerosol-coated particles was calculated by measuring the mass concentrations of organics, sulfate, and ammonium of the wet particles without a drier, wherein CE was assumed to be unity and line losses assumed to be negligible, and comparing with measurements made through a drier. We observe a CE of 0.75 for all conditions in this work, which is consistent with the collection efficiency of organic aerosols measured previously (Docherty et al., 2013). Further, it is expected that drying particles, relevant to the hydration/evaporation cycles of aerosols in nature, may lead to enhanced interactions between organic and inorganic compounds (De Haan et al., 2011; Nguyen et al., 2012), irreversibly forming OA.

2.2.3 Particle size and number concentration

Particle size and number concentrations were measured with a scanning mobility particle sizer (SMPS), comprised of a custom-built differential mobility analyzer (DMA) coupled to a commercial butanol-based condensation particle counter (CPC, TSI Inc.). The SMPS particle size measurement was calibrated with polystyrene latex (PSL) spheres. The particles entering the chamber have a static polydisperse distribution, with peak dry particle diameter distributions in the range of 50–100 nm. The sample air flow was not dried in humid experiments. Particle mass concentrations were corrected for RH- and size-dependent wall losses. The mass concentration of particles typically ranged from 65–90 µg m^{-3} for all experiments, using a particle density of 1.2 g cm^{-3}.

For AS-based experiments, the particle liquid water content was calculated based on the size-dependent hygroscopicity of AS (Biskos et al., 2006; Hu et al., 2010). For each particle diameter bin measured by SMPS, a theoretical dry diameter was calculated based on size-dependent literature growth factor data at the RH of the experiment. The difference in the wet (measured) and dry (calculated) integrated area of the mass distribution yielded the liquid water concentration in g m^{-3}. Similarly, the percent of liquid water content is calculated as % LWC = 100 % $\times$ (V_{wet}–V_{dry})/V_{wet}, using the predicted wet and dry diameters.

Particle wall loss characterizations were performed for AS seeds at RH = 3 %, 20 %, 50 %, and 80 % prior to the start of the experimental series to correctly quantify the mass concentrations of particles as a function of time. It was assumed that the loss rates of AS were representative for particles of different composition. Seed aerosols were atomized into the dry or humid chambers in the dark, allowed to stabilize, and particle size and number concentrations were measured for > 12 h. The particle correction method that accounts for wall loss has been discussed in detail previously (Loza et al., 2012).

2.2.4 Filter collection and analysis

Offline OA composition analysis was performed by ultra-high performance liquid chromatography time-of-flight electrospray ionization mass spectrometry (UPLC/ESI-ToFMS). Aerosol samples were collected onto Teflon membrane filters (Millipore, 1 µm pore), pulled at a 20 L min^{-1} flow through an activated charcoal denuder to remove the volatile and semivolatile components. Each filter was extracted with

methanol (Fisher, Optima grade, ≥ 99.9 %) by ultrasonication for 15 min in a 20 mL scintillation vial. The filtered extracts were blown dry under a gentle stream of ultra-high-purity N_2. The residue was reconstituted with 150 µL of 50 : 50 v / v acetonitrile (Fisher Optima grade, ≥ 99.9 %) and water (Milli-Q).

Extracts were analyzed by a Waters Xevo G2-S UPLC/ESI-ToF-MS equipped with an Acquity CSH C_{18} column (1.7 µm, 2.1 × 100 mm). The solvents used for gradient elution were acetonitrile (Fisher Optima grade, ≥ 99.9 %) and water with a 0.1 % formic acid spike (solvent "A"). The flow rate was held at 0.5 mL min^{-1}. Accurate mass correction was completed by a lock spray of leucine enkephalin (0.61 ng μL^{-1} in 50 : 50 v / v acetonitrile / water with 0.1 % formic acid). The ESI source was operated in negative mode, where most analytes are ionized by deprotonation and measured as $[M\text{-}H]^-$. Ionic molecular formulas were determined from accurate masses (mass resolution of 60 000 at m/z 400) using the elemental composition tool in Mass Lynx. Control filters (no particles) and laboratory controls (seeds only) were analyzed in the same manner.

3 Results and Discussion

3.1 Reactive uptake of *cis* and *trans* β-IEPOX onto ammonium sulfate seeds

3.1.1 Liquid water content of seeds

Figure 1 shows the time profile for the organic aerosol (OA) growth corresponding to reactive uptake of the *trans* β-IEPOX onto ammonium sulfate (AS) seeds at two RH conditions, dry (LWC ∼0 %) and RH 57 % (LWC ∼55 %). The traces shown in Fig. 1 are representative of uptake behavior for both isomers on the experimental timescale. For RH conditions above the ammonium sulfate (AS) efflorescence point tested in this work (E_{RH} ∼35 %, (Biskos et al., 2006)), prompt and efficient OA growth onto AS seeds was observed for both IEPOX isomers. No OA growth was observed when the AS seeds were dry, in good agreement with other reports (Lin et al., 2012, Surratt et al., 2010).

The OA growth from IEPOX did not halt after the end of the gas-phase injection period (Fig. 1, solid black line), even after periods of > 2 h (Fig. S3, top panel). This behavior is indicative of a non-equilibrium process, as the addition of nucleophiles is not reversible after the rate-limiting step of IEPOX activation (Eddingsaas et al., 2010). The formation of low-volatility compounds should continue as long as a reservoir of gas-phase IEPOX is available. The series of expected reactions leading to the formation of ring-opening products (ROP) is shown below, illustrated using a general proton donor (AH) and nucleophile (Nu).

$$\mathrm{IEPOX_{(g)} \leftrightarrows IEPOX_{(aq)}, K_H} \quad \text{(R1)}$$

$$\mathrm{IEPOX_{(aq)} + AH \leftrightarrows IEPOX - H^+ + A_{-H}, k_{AH}} \quad \text{(R2)}$$

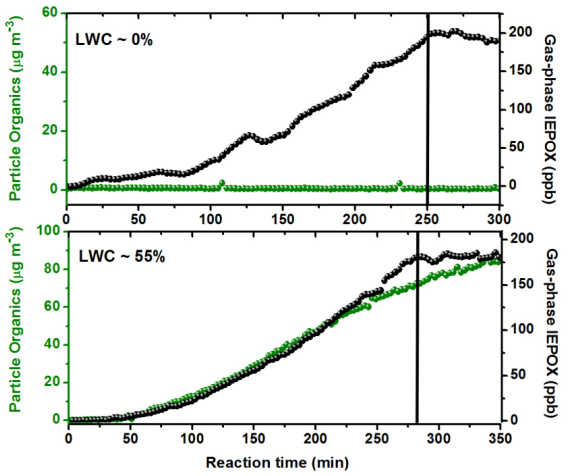

Fig. 1. Typical uptake experiment results as a function of time, shown for *trans* isomer, at dry (top) and humid (bottom) conditions with the corresponding percent of liquid water content (LWC). The solid black line indicates when IEPOX injection stopped and the mixture was allowed to equilibrate. Double *y* axes correspond to traces of the same color.

$$\mathrm{IEPOX - H^+ + Nu \rightarrow ROP - H^+, k_{Nu}} \quad \text{(R3)}$$

$$\mathrm{ROP - H^+ + A_{-H} \rightarrow ROP + AH, k_{neutral}} \quad \text{(R4)}$$

For a solution with low AH and Nu activity, the equilibrium accommodation of IEPOX into the aqueous phase, described by the Henry's Law coefficient of IEPOX (K_H), can be measured in isolation. Henry's Law may not be an appropriate description of the IEPOX reactive uptake experiments performed on the liquid water of suspended aerosols, as the aerosol water layers represent highly non-ideal solutions and the OA formation is kinetically limited. The OA formation mechanism may include contributions from reactions other than Reactions (1–4). To a first-order approximation, total OA mass formed from gas-phase reactive uptake of IEPOX will be a function of aqueous IEPOX concentration, nucleophile activity, and catalyst activity.

For the sake of comparison between experiments, it is useful to have a metric that includes the ratio of OA formed to gas-phase IEPOX injected and accounts for the variability in the size and number of injected seeds between experiments, which is reflected by the calculated aerosol water at different RH. We define here a reactive partitioning coefficient ($\Phi_{OA/IEPOX}$), calculated similarly to an effective Henry's Law coefficient, and thus having the same units (Seinfeld and Pandis, 2006):

$$\Phi_{OA/IEPOX} = (C_{OA} / C_{IEPOX}) / [10^{-6} \cdot R \cdot T \cdot P_{LWC}], \quad (1)$$

where (C_{OA}/C_{IEPOX}) is the mass concentration ratio of the IEPOX-derived organic aerosol (dried), measured by ToF-AMS, and the gas-phase IEPOX, measured by negative-ion

Table 1. Summary of results from representative reactive uptake experiments onto ammonium sulfate seeds. Mean results from Lin et al. (2012) are shown for comparison.

Exp. index	IEPOX isomer	Seed composition	RH (%)	Particle pH*	Seed ($\mu g\,m^{-3}$)	P_{LWC} ($g\,m^{-3}$)	C_{OA} / C_{IEPOX}	$\Phi_{OA/IEPOX}$ ($M\,atm^{-1}$)
1	cis	$(NH_4)_2SO_4$	3	–	70	$<1\times10^{-6}$	5.04×10^{-4}	–
2	cis	$(NH_4)_2SO_4$	42	3.67	91	3.74×10^{-5}	0.102	1.15×10^{8}
3	cis	$(NH_4)_2SO_4$	50	3.74	92	4.79×10^{-5}	0.118	1.01×10^{8}
4	cis	$(NH_4)_2SO_4$	86	3.90	81	5.68×10^{-5}	0.179	4.00×10^{7}
5	trans	$(NH_4)_2SO_4$	2	–	65	$<1\times10^{-6}$	4.74×10^{-4}	–
6	trans	$(NH_4)_2SO_4$	39	3.65	82	3.44×10^{-5}	0.090	1.06×10^{8}
7	trans	$(NH_4)_2SO_4$	57	3.77	89	4.64×10^{-5}	0.095	8.44×10^{7}
8	trans	$(NH_4)_2SO_4$	81	3.88	88	6.14×10^{-5}	0.115	7.66×10^{7}
9	trans	$(NH_4)_2SO_4$ + NaOH, pH = 7	70	∼5.5	84	5.33×10^{-5}	0.090	6.89×10^{7}
Lin et al. (2012)	cis	$MgSO_4$ + H_2SO_4 (1 : 1)	< 5	∼-10	48	1.62×10^{-5}**	0.058	1.47×10^{8}

* Modeled pH using E-AIM and AIOMFAC models (the value from (Lin et al., 2012) is $a_{molality}$-based pH), see text (Sect. 3.1.2).
** Based on hygroscopicity of H_2SO_4 at RH 5 %, assumed growth factor 1.15, Xiong et al. (1998).

CIMS, P_{LWC} is the liquid water content of the inorganic aerosols prior to IEPOX introduction ($g\,m^{-3}$), R is the ideal gas constant ($atm\,L\,mol^{-1}\,K^{-1}$), T is the temperature (K), and 10^{-6} is a conversion factor ($m^3\,cm^{-3}$). $\Phi_{OA/IEPOX}$ includes the contribution from Henry's Law equilibrium partitioning of IEPOX (Reaction R1), and thus is an upper limit for the effective Henry's Law constant.

We observe that $\Phi_{OA/IEPOX}$ was not time-dependent when both IEPOX and OA were increasing, as the ratio C_{OA}/C_{IEPOX} stabilized when OA grew in response to gas-phase IEPOX (Fig. S3) but increased after IEPOX injection stopped. The stabilized ratio is used for $\Phi_{OA/IEPOX}$ calculations to compare between experiments. P_{LWC} did not have a significant time dependence due to a stable particle volume distribution before IEPOX gas-phase injections. The uncertainties in the accuracy of the $\Phi_{OA/IEPOX}$ and K_H measurements were estimated to be −50 % and +100 %, compounded from the uncertainties in the calculated CIMS sensitivities, liquid water fraction, AMS organic mass determinations, and other measurements.

A summary of $\Phi_{OA/IEPOX}$ and other values is given in Table 1 for all AS-based uptake experiments. Figure 2 shows $\Phi_{OA/IEPOX}$, as a function of particle liquid water, for the *cis* and *trans* β-IEPOX uptake onto hydrated AS. A trend of decreasing $\Phi_{OA/IEPOX}$ with increasing LWC was reproducibly observed, despite the uncertainty range in the $\Phi_{OA/IEPOX}$ determinations. The suppression of $\Phi_{OA/IEPOX}$ as a function of added water is likely due to dilution. For example, high aerosol sulfate concentrations may cause a "salting-in" effect for IEPOX, or other water-soluble organic compounds (Kampf et al., 2013), which is inversely proportional to water content. Higher water may also reduce the $[H^+]$, although the dependence of the reaction on catalyst concentrations is not expected to be high. Additionally, higher P_{LWC} dilutes the aqueous IEPOX and nucleophile concentrations in the aerosol liquid water, which reduce the rate of the chemical reaction as these species are direct reagents. The dilution effect from increasing the pure water fraction at a fixed ion content (moles of NH_4^+ and SO_4^{2-}) is in contrast to a modeled increase in OA mass in areas with high "anthropogenic water", in other words, mixtures of water-soluble compounds found in urban regions (Carlton and Turpin, 2013). In the atmosphere, the partitioning of anthropogenic gases like NH_3 and SO_2 will simultaneously impact aqueous acidity and inorganic concentration and thus may lead to enhanced OA formation in areas with higher P_{LWC}.

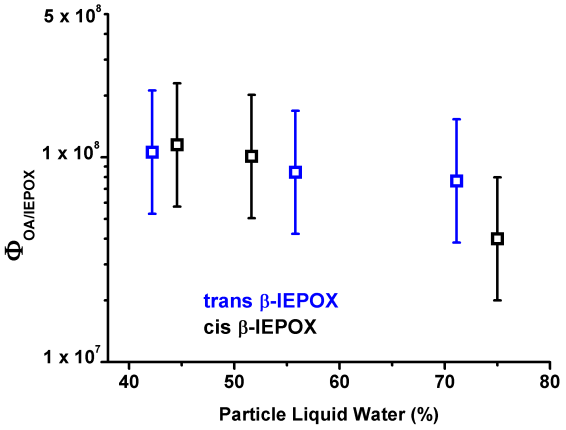

Fig. 2. Reactive partitioning coefficients ($\Phi_{OA/IEPOX}$) during the gas-phase IEPOX injection phase for the *trans* and *cis* isomers as a function of the particle liquid water concentration. Error bars indicate experimental uncertainty as described in the text.

3.1.2 Particle acidity

As the decrease of $\Phi_{OA/IEPOX}$ with increasing liquid water content may be due to more than one factor, an experiment was carried out to isolate the effect of pH. In experiment 9 (Table 1), the AS solution was neutralized with a strong base

(NaOH) until the atomizer solution reached pH = 7. Solutions of AS without additives had pH ∼5.5 before atomization because, although no strong acid was present, H^+ is expected to be present in small quantities based on the dissociation equilibria of inorganics, such as the bisulfate/sulfate dissociation, and dissolution of CO_2. An enhancement in the acidity of the particle may result from a smaller volume of water in the particle and/or through loss of NH_3 upon atomization. In the case of a fully hydrated AS particle, the pH in the particle is predicted to be pH ∼4 using the E-AIM Model (Clegg et al., 1998), and modeled pH values in the particle for all AS-based experiments are shown in Table 1. As the pH values of the particles in this work are derived using inorganic models, the values obtained may include any uncertainties inherent in the models, including uncertainties in the gas/particle partitioning of NH_3, hygroscopicity of salts, and/or acid dissociation equilibria. When the RH is below the deliquescence point of AS, the pH was estimated by calculating a concentration factor from the P_{LWC} at the lower RH. It is expected that atomization will also lead to slightly lower pH for the base-neutralized atomizer solution, so the particle may have pH < 7. However, adding NaOH above neutralization to counter this effect may induce side reactions such as base-catalyzed epoxide opening and OH^- nucleophilic addition (Solomons and Fryhle, 2004). NaOH is not explicitly treated in the E-AIM and AIOMFAC (Zuend et al., 2008) inorganic models, therefore, it was assumed that atomization of the AS + NaOH solution may lead to, at most, the same enhancement factor that occurred for the pH of the pure AS solutions.

Figure 3 shows that $\Phi_{OA/IEPOX}$ for the *trans* β-IEPOX + AS system decreases slightly as pH is increased, reaching a plateau above pH ∼4. We note that any perceived change is within the error of the measurement, however, it is clear that the trend of $\Phi_{OA/IEPOX}$ with pH is minor. These results differ from those of Eddingsaas et al. (2010), who observed a linear increase of epoxide reaction rate with H^+ activity. Eddingsaas et al. (2010) used H_2SO_4/Na_2SO_4 solutions, and thus the differences in observations may be entirely due to the high NH_4^+ activity in the AS particles employed in this work. The data suggest that when $[H^+]$ is small, NH_4^+ may activate reactions leading to OA formation, similarly to its catalytic activity toward glyoxal (Noziere et al., 2009), methylglyoxal (Sareen et al., 2010), and other carbonyls (Nguyen et al., 2013, Bones et al., 2010). Interestingly, pH > 4 is the range where NH_4^+ catalysis is most efficient. This is demonstrated by a stable reactivity of the NH_4^+-catalyzed reaction to generate brown carbon from limonene SOA at pH 4–9, but a sharp decline of reactivity below pH 4 (Nguyen et al., 2012). As the H^+ and NH_4^+ ions are reactive toward organics in low-moderate and moderate-high pH ranges, respectively, the resulting pH dependence may appear to be weak in AS-containing seeds. The dual reactivities of H^+ and NH_4^+ toward IEPOX is expected to be important in nature, as NH_4^+-based seeds are abundant.

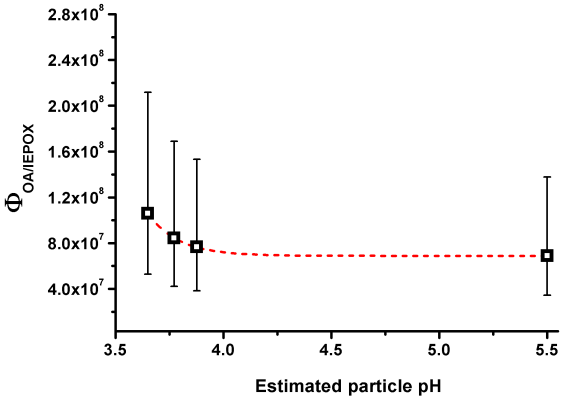

Fig. 3. $\Phi_{OA/IEPOX}$ for the *trans* β-IEPOX isomer as a function of the modeled particle pH.

In comparison, the $MgSO_4 : H_2SO_4$ particles at RH < 5 % in the work of Lin et al. (2012) are strongly acidic. These particles are predicted to have a non-negligible amount of water due to the large hygroscopicity of H_2SO_4 – and indeed, acidity in particles is not a useful concept if water is not present. At RH = 0–5 %, pure H_2SO_4 particles have a growth factor of 1.1–1.2 (Xiong et al., 1998). Assuming a growth factor of 1.15, and taking into consideration the inorganic seed mass concentration, we calculated P_{LWC} for the mean results in Lin et al. (2012), shown in Table 1. The AIOMFAC Model (Zuend et al., 2008; Zuend et al., 2011) was used to estimate the pH based on the molal activity of H^+ in the $MgSO_4$:H_2SO_4 (1 : 1) particle. The calculated pH is ~ -10 and the corresponding mean $\Phi_{OA/IEPOX}$ is $\sim 1.5 \times 10^8\,M\,atm^{-1}$ for *cis* β-IEPOX (the *trans* isomer was not studied). $\Phi_{OA/IEPOX}$ for the acidic $MgSO_4$ seeds is slightly higher than, but within the error of, the $\Phi_{OA/IEPOX}$ values for non-acidified AS seeds when a small amount of water is present (RH ∼40 %). This comparison is meant to be qualitative and subject to uncertainty because the experiments were not performed under the same conditions. Nevertheless, the comparison shows that a solution of high H^+ activity and a solution of high NH_4^+ activity may both lead to a relatively similar reactive uptake coefficient. As $[NH_4^+] \gg [H^+]$ in the particles in this work, a similar $\Phi_{OA/IEPOX}$ would also suggest that $k_{NH_4^+} \ll k_{H^+}$ if the observed rate coefficient for Reaction (2) is defined as $k_{obs} = k_{AH} \cdot [AH]$. Eddingsaas et al. (2010) estimated $k_{H^+} \sim 5 \times 10^{-2}\,M^{-1}\,s^{-1}$ and Cole-Filipiak et al. (2010) determined $k_{H^+} = 3.6 \times 10^{-2}\,M^{-1}\,s^{-1}$ for IEPOX.

3.2 Molecular picture of OA formation from IEPOX

3.2.1 Cation and anion substitutions

To further investigate the role of NH_4^+ in IEPOX ring-opening reactions at near-neutral conditions, NH_4^+ was replaced by a cation that cannot act as a proton donor (Na^+). As isomer structure appears to be unimportant for uptake, only the *trans* isomer was used for this portion of the study. Further, many nucleophiles present in the atmosphere are known to add to the protonated epoxide to give the beta-hydroxy ring-opening product, for example: H_2O (Solomons and Fryhle, 2004), SO_4^{2-} ions (Cavdar and Saracoglu, 2009), NH_3 or amines (Clayden et al., 2001), and halide ions (Clayden et al., 2001). Thus, SO_4^{2-} was substituted by Cl^- to study the anion (or nucleophile) effect.

Hydrated particles of AS ($(NH_4)_2SO_4$), sodium sulfate (Na_2SO_4), ammonium chloride (NH_4Cl), and sodium chloride (NaCl) were introduced into the chamber in separate experiments, followed by the introduction of *trans* β-IEPOX. The mixtures were allowed to equilibrate for 3.5–6 h. The RH range for these reactions is 60–85 %, chosen at a point well above their respective efflorescence RH (Martin, 2000), so that each seed would contain a considerable fraction of liquid water. The particle size distributions for each seed type were polydisperse and unimodal, with hydrated mobility diameters in the range of 15–600 nm and with 60–120 nm peak diameters. It is expected that the hydrated particles were spherical. The size-dependent hygroscopicities of AS and NaCl are well-studied, however, the calculations of liquid water content for other seed types are subject to error based on the method we described due to limited literature data. Therefore, we opt to present results based only on the C_{OA}/C_{IEPOX} for the comparison of inorganic seed compositions.

OA formation after particle drying, as detected by ToF-AMS, is negligible for both sodium salts (NaCl and Na_2SO_4). The OA mass did not grow in response to the addition of IEPOX for the Na^+-based particles (Fig. S4). Figure 4 shows the average stabilized ratios of OA formed with respect to *trans* β-IEPOX injected for the four inorganic salts used in this work. The atomizer solution pH for Na^+-based seeds was also ∼5.5, a typical pH for a water solution in equilibrium with CO_2 (Reuss, 1977). The large difference in reactivity of IEPOX on Na_2SO_4 vs. $(NH_4)_2SO_4$ seeds may be attributed primarily to NH_4^+ activity, although there will be some differences in [H+] for the NH_4^+-based and Na^+-based seeds due to the slight dissociation of $NH_4^+ \leftrightarrows NH_3$. Additionally, in light of the weak pH dependence for AS solutions, it appears likely that NH_4^+ activity is an important factor in suppressing OA formation on Na_2SO_4 seed particles. The results show that equilibrium partitioning of IEPOX, i.e., any condensed-phase mass formed from unreacted IEPOX, onto salty solutions is not competitive with reactive partitioning for OA formation.

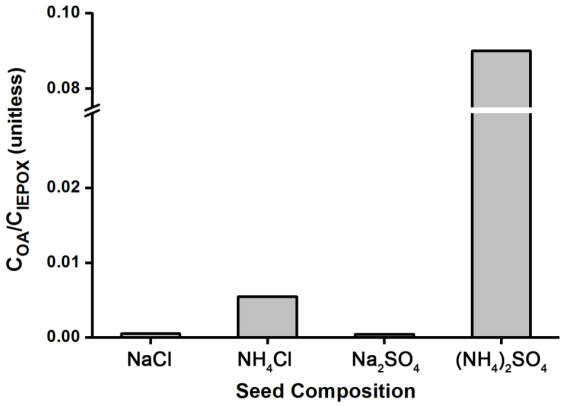

Fig. 4. Ratio of organic aerosol produced to gas-phase *trans* β-IEPOX injected for seeds of various compositions (RH 60–85 %).

For the ammonium salts, NH_4Cl produced an order of magnitude lower mean C_{OA}/C_{IEPOX} ratio than $(NH_4)_2SO_4$, after an approximate 2h delay (Fig. S4). The modeled pH, using E-AIM, for both ammonium salt systems is similar (pH ∼4–4.5), and thus, the difference in reactivity may be attributed to the nucleophilic activity of Cl^- compared to SO_4^{2-}. Interestingly, Minerath et al. (2009) showed that acid-catalyzed ring-opening products of an epoxide with Cl^- may be more efficient than SO_4^{2-}. In that study, sulfuric acid was added to the NaCl + epoxide aqueous solution, which provide sulfate and bisulfate ions to the solution. Therefore, the results may not be directly comparable to this work. If Cl^- can be a good nucleophile in aqueous solutions of IEPOX when coupled with NH_4^+ catalysis, we may expect to observe organochloride products. There was no evidence of organochloride-derived accurate mass fragments in ToF-AMS data for the NH_4Cl reactive uptake organics. Further, gas-phase organochlorides were not observed by the CIMS. It is possible that organochlorides are produced but are easily hydrolyzed in the aerosol liquid water due to the relatively good leaving group ability of Cl^-, i.e., the hydrolysis behavior of organochlorides is more similar to that of tertiary organonitrates than that of organosulfates (Darer et al., 2011). It is also possible that organochlorides are preferentially evaporated in the diffusion drier because they might be more volatile than organosulfates or polyols. In both situations, but more so the latter, the total organic mass from the NH_4Cl experiments would be underestimated by ToF-AMS. Although we did not quantify tetrols and other polyols in this work, it is expected that they are present in substantial quantities because they are the thermodynamically preferred products in the epoxide ring-opening reactions.

3.2.2 Henry's Law constant

Although ToF-AMS did not observe OA formation for experiments using sodium salts (NaCl and Na_2SO_4) after particle drying, the wall-loss-corrected SMPS data (not dried) showed a minor and stable change in particle volume upon injection of IEPOX into the chamber with hydrated NaCl or Na_2SO_4 seeds (Fig. S5a, shown for NaCl). It is likely that the dissolved but unreacted IEPOX was removed from the condensed phase upon particle drying, which would lead to no observed OA mass in the ToF-AMS data throughout the duration of the experiment. The reversibility OA formation on the hydrated seeds indicates equilibrium-partitioning of IEPOX into the aerosol liquid water. The ratio of dissolved OA to injected IEPOX (Fig. S5b) reached a steady-state value at the end of the IEPOX injection period. Because NH_4^+ is not present, and $[H^+]$ is not expected to be considerable in the aqueous phase, Reactions (R2) and (R4) are unimportant for this system. Further, in experiments using NaCl seeds, where the nucleophilicity of the solution is weaker, we are able to neglect the contribution of Reaction (R3), thereby isolating the equilibrium partitioning of IEPOX (Reaction R1).

We estimate the Henry's Law coefficient (K_H) for the equilibrium partitioning of IEPOX into a briny liquid (NaCl ∼9 M ionic strength) representative of atmospheric aerosol to be 3×10^7 $(-50/+100\,\%)\,\mathrm{M\,atm^{-1}}$. The K_H in a solution of NaCl may be different than the value in pure water, due to complex aqueous interactions of Cl^- and Na^+ with water-soluble organics. As an example, the Henry's Law constant for glyoxal was measured to be $K_H = (4.19 \pm 0.87) \times 10^5\,\mathrm{M\,atm^{-1}}$ in pure water, $1.90 \times 10^6\,\mathrm{M\,atm^{-1}}$ in a 0.05 M NaCl solution, and $8.50 \times 10^5\,\mathrm{M\,atm^{-1}}$ in a 4.0 M NaCl solution at 298 K (Ip et al., 2009). Ip et al. (2009) attributed the increase in K_H for NaCl solutions at low ionic strengths (compared to water) to hydrogen bonding interactions of Cl^- and OH groups and the decrease at high ionic strength to a "salting-out" effect. The K_H value for IEPOX has not been experimentally determined in the past; however, the range of K_H has been estimated using the HENRYWIN model (EPA, 2008) by several studies. For example, Eddingsaas et al. (2010) estimated $K_H = 2.7 \times 10^6\,\mathrm{M\,atm^{-1}}$ using a bond contribution method, and $K_H = 2.9 \times 10^{10}\,\mathrm{M\,atm^{-1}}$ using a group contribution method in version 4.0 of the model. The empirical K_H value reported here is within range of both estimations – closer to the bond contribution method estimate. These results provide a critical constraint in the partitioning coefficient, significantly decreasing the error associated with using K_H in a quantitative manner (from 4 orders of magnitude to a factor of two).

3.2.3 Organic composition

A full analysis of the OA composition is outside the scope of this work. The reader is referred elsewhere for a discussion of the formation of oxygenated hydrocarbons, for example, tetrols and alkenetriols and organosulfates in the aqueous reaction of IEPOX catalyzed by acidic sulfate (Eddingsaas et al., 2010, Surratt et al., 2010). Although strong acid is absent in the systems studied in this work, we observe many similarities in the IEPOX-derived OA composition compared to the existing chamber and field results. For example, organosulfate products are abundant when hydrated AS seeds are used. The dominant ion observed in negative ion mode UPLC/ESI-ToFMS for AS uptake was $C_5H_{11}SO_7^-$ (Fig. S6), corresponding to the ring-opening trihydroxy organosulfate product of IEPOX. Derivatization was not performed in this work to detect tetrols. Organosulfate fragments were also observed in ToF-AMS (CSO family of fragments, not shown).

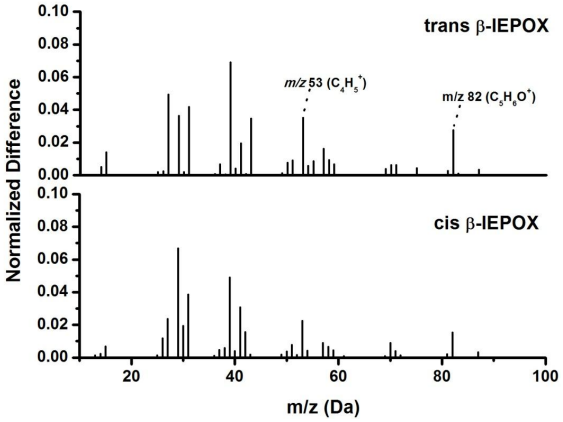

Fig. 5. ToF-AMS normalized difference spectra (composition at peak OA growth minus composition during seed injection), showing the organic composition of the OA produced by reactive uptake of the *trans* and *cis* isomers. Select nominal mass ions previously suggested to be IEPOX-derived OA tracers are labeled.

IEPOX-derived OA formed under near-neutral conditions in this work have ToF-AMS spectra similar to those of OA observed in the field. The suggested tracers for IEPOX-derived organics, m/z 53 (mostly $C_4H_5^+$) and m/z 82 (mostly $C_5H_6O^+$) (Lin et al., 2012, Robinson et al., 2011, Budisulistiorini et al., 2013), were observed in uptake experiments using both isomers. These mass fragments were proposed to originate from the electron-impact (EI) ionization of furan-derived molecules that were suggested to be formed from the acid-catalyzed rearrangement of IEPOX (Lin et al., 2013). Although mass fragments produced by EI may have multiple sources, in the pure system used in this study, m/z 82 was found to be a good tracer for IEPOX-derived OA. Figure 5 shows the difference between mass spectra at the end of the experiment and those at the time period prior to organic injection, corresponding to the organic fraction of the OA formed from the uptake of both isomers. The spectral ion distributions are very similar to each other

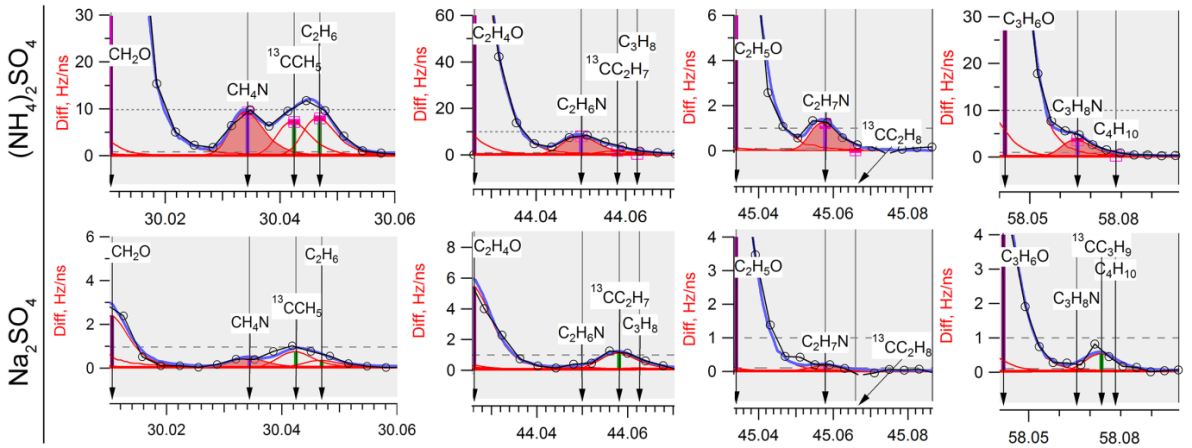

Fig. 6. ToF-AMS difference spectra (open minus closed chopper) showing organic nitrogen (amine) fragments from the reactive uptake of *trans* β-IEPOX onto AS vs. Na_2SO_4 seeds. Similar fragments were observed for *cis* β-IEPOX using NH_4^+-based seeds and not observed in Na^+-based seeds.

and m/z 53 and m/z 82 constituted a substantial fraction of the total ion intensity. The ion abundance of tracer fragments increased in accordance with the growth of OA mass (Fig. S7). As m/z 53 ($C_4H_5^+$) is a reduced fragment, it is also linked to hydrocarbon-like organics in chamber studies and may not be unique to IEPOX-derived OA. m/z 53 was observed in all experiments, including those that used Na^+-based seeds. However, m/z 82 is abundant only when NH_4^+-based seeds were used, supporting the suggestion that it can be formed though the EI fragmentation of an IEPOX-derived ring-opening product in ToF-AMS.

A unique aspect of the NH_4^+-catalyzed ring-opening reaction of IEPOX is the minor possibility of nucleophilic addition by NH_3, instead of reforming NH_4^+ after neutralizing the addition of another nucleophile. Figure 6 shows ion peaks for organic fragments containing C-N bonds observed in ToF-AMS data from the uptake of *trans* β-IEPOX onto AS vs. Na_2SO_4 seeds. The same C-N fragments were observed in *cis* β-IEPOX experiments using AS. These C-N fragments were not initially present in the AS seeds, and grow linearly following the introduction of IEPOX. Individual C-N fragments correlate well (Fig. S8, linear fit $R^2 = 0.69$–0.88) with the m/z 82 IEPOX-derived OA tracer fragment ($C_5H_6O^+$), suggesting that the reaction of IEPOX is responsible for the presence of these amines. Comparatively, C-N type fragments were negligible or non-existent in uptake experiments from Na^+-based seeds. The identification of amines is tentative; however, to the best of our knowledge, this is the first suggestion of amine formation from IEPOX. As organic nitrogen compounds also give rise to non-nitrogenous mass fragments in ToF-AMS, it is not possible to estimate a mass concentration for the amines in this work. However, the C-N family of fragments comprised approximately 10 % of the $C_5H_6O^+$ signal, an indication that amine formation may not be negligible. The formation of organic nitrogen from the IEPOX + NH_4^+ reaction has important implications in the atmosphere as the ring-opening reaction of epoxides with amines should be more efficient than with NH_3 (Azizi and Saidi, 2005). Further investigations may provide more insight on the source of organic nitrogen from the atmospheric reactions of epoxides.

4 Summary and atmospheric implications

It was demonstrated here that the conversion of IEPOX to organic aerosol (OA) depends on the coupled relationship between the inorganic composition and liquid water content of the particle (P_{LWC}). The inorganic composition governs the catalyst and nucleophile characteristics, and P_{LWC} provides a reaction medium for the partitioning of IEPOX and controls the activities of all the aqueous components. The weak dependence on pH and the strong dependence on nucleophile activity and particle liquid water suggest that the IEPOX reactions in hydrated ammonium salts are nucleophile-limited, rather than catalyst-limited.

We showed that the equilibrium partitioning (Reaction 1) and the rate-limiting step of IEPOX activation (Reaction 2) do not proceed in the absence of liquid water; however, increasing the pure water content does not necessarily increase the reactive partitioning coefficient due to various dilution effects. When the inorganic particle is hydrated, the OA conversion is then determined by the catalyst and nucleophile activities. The rate of OA formation incorporates both Reactions (R2) and (R3), as illustrated by the cation and anion substitution case studies. In the hydrated Na_2SO_4 experiment, there was high activity of a relatively

good nucleophile, but a good catalyst was absent. Therefore, the formation of OA, i.e., the ring-opening product, was not observed because the equilibrium of Reaction (R2) favors $IEPOX_{(aq)}$. The aqueous IEPOX mass that partitioned from the gas phase (K_H) onto the hydrated Na^+-based seeds was removed from the condensed phase following the evaporation of water. In the hydrated NH_4Cl experiment, there was high activity of a good catalyst but possibly a poorer nucleophile than sulfate ion. A smaller quantity of OA formed because the rate of Reaction (R3) was slow, which was further supported by the observed 2 h delay in OA formation. Only when P_{LWC}, NH_4^+ activity, and SO_4^{2-} activity are all significant, as in the case of hydrated $(NH_4)_2SO_4$ seeds, is the OA formation efficient and prompt. The OA mass formed from IEPOX uptake onto 1:1 $MgSO_4$:H_2SO_4 seeds (RH < 5 %) from previous studies may also be explained in terms of these conditions, as P_{LWC} (∼30 %), catalyst (H^+) activity and nucleophile (SO_4^{2-}) activity were all sufficiently high in the particle.

In the atmosphere, relationships of water-soluble OA with P_{LWC} may be different and more difficult to interpret compared to laboratory studies because an increase in the P_{LWC} of atmospheric particles is often accompanied by the co-partitioning of water-soluble organic and inorganic compounds. The abundance of water-soluble organic compounds in the Southeast USA has been observed to be proportional to the liquid water contents of particles (Hennigan et al., 2008, 2009, Carlton and Turpin, 2013). In contrast, a weak correlation of modeled P_{LWC} with the abundance of IEPOX-derived OA tracers has also been observed, in the same geographical region (Budisulistiorini et al., 2013). The results of this work may not be directly comparable to field observations, however, they do not necessarily conflict. Particles may experience multiple hydration/evaporation cycles in the atmosphere, and the majority of particles likely contain liquid water at some point during their long lifetimes. The OA produced from IEPOX reactive uptake onto AS is irreversible (not removed from particle drying in this work), and depending on whether it had been sampled in the atmosphere before or after an evaporation cycle, the apparent correlation of IEPOX-derived OA with P_{LWC} would be different. Consequently, systematic studies in the laboratory are important for elucidating observations from the field.

Our results offer an alternate explanation to the abundance of IEPOX-derived OA tracers when the free H^+ acidity in particles is modeled to be low (Lin et al., 2013). It has been suggested that the reason for the weak correlation with acidity is the reaction of an acidic seed particle with IEPOX to form organosulfates, which affects the particle acidity over time (Budisulistiorini et al., 2013). We show here that particle acidity does not appear to be important for the IEPOX + AS system if particle liquid water is present, in that highly acidic seeds and weakly acidic AS seeds both have high potential to form OA from IEPOX reactive partitioning. The apparent correlation between OA mass from IEPOX and P_{LWC},

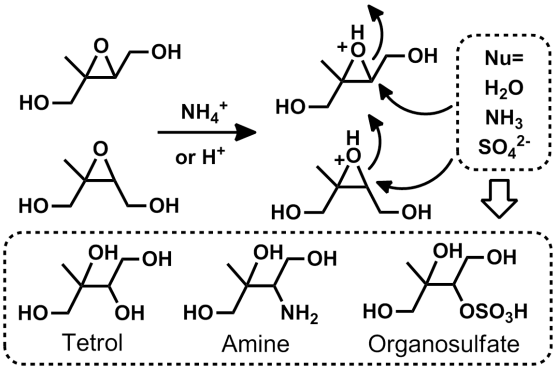

Scheme 2 Addition of weak nucleophiles in the aqueous NH_4^+ – and H^+-catalyzed ring opening of IEPOX to form low-volatility organic compounds.

ammonium or acidity may be weak whenever water or catalyst concentrations are not limited; thus, in regions with high AS loading and RH, there should be a higher correlation with sulfate. This result would suggest that the OA formation process from IEPOX is insensitive to changes in the degree of neutralization of the particles in many AS-dominated areas, including the Southeast USA. The typical $[NH_4^+]$ is several orders of magnitude larger than $[H^+]$ in atmospheric particles, making it very likely to activate the IEPOX ring-opening reaction. Current models consider only H^+ and HSO_4^- activity (McNeill et al., 2012, Pye et al., 2013), likely owing to the lack of experimental data describing the NH_4^+-initiated reaction with IEPOX, for example, kinetic coefficients like $k_{NH_4^+}$. Future experimental and modeling studies should consider the NH_4^+ activity of a particle, in addition to the H^+ and HSO_4^- activity, for a more-accurate representation of OA formation from IEPOX.

An updated reaction mechanism appears in Scheme 2, in which NH_4^+ and H^+ are shown to donate a proton to the epoxide oxygen, followed by nucleophilic addition to form oxygenated hydrocarbons, ammonia (or amines), and organosulfates. The ability of NH_4^+ to catalyze a nucleophilic addition reaction is not unprecedented, as NH_4^+ can protonate aldehydes to facilitate nucleophilic addition (Noziere et al., 2009), and the high ring strain of an epoxide should provide an even greater thermodynamic motivation for the reaction. Indeed, due to the strain of epoxides, ring opening is chemically facile and may be promoted by a wide range of aqueous chemical species and conditions common in atmospheric aerosols, in addition to H^+ and NH_4^+. For example, Lewis acids such as iron (Fe^{3+}) (Iranpoor and Salehi, 1994) and copper (Cu^{2+}) (Muzart and Riahi, 1992) ions may be even stronger catalysts. Furthermore, the reaction may proceed with no added catalyst, for example, in the presence

of amines (Azizi and Saidi, 2005) or even hot water (60 °C) (Wang et al., 2008). The nucleophiles for these reactions may be water, amines or ammonia, thiols, sulfate ions, nitrate ion, halide ions, carboxylic acids, and alcohols (Iranpoor et al., 1996, Jacobsen et al., 1997, Clayden et al., 2001). Because of the diversity in the composition of atmospheric aerosols and fog/cloud droplets (Graedel and Weschler, 1981), the distribution of IEPOX-derived products in nature may be more complex and varied than currently believed.

Supplementary material related to this article is available online at http://www.atmos-chem-phys.net/14/3497/2014/acp-14-3497-2014-supplement.pdf.

Acknowledgements. This research was supported by the National Science Foundation (NSF) grants AGS-1057183 and AGS-1240604. TBN acknowledges funding from the NSF Postdoctoral Research Fellowship program, award AGS-1331360, and from the Foster and Coco Stanback Postdoctoral Fellowship. We are grateful for research support provided by the Brian Stoltz Group at Caltech for the syntheses of the β-IEPOX isomers, with special acknowledgement to Dr. Nathan Bennett. We thank Dr. Nathan Dalleska, director of the Caltech Environmental Analysis Center (EAC), for his assistance with the UPLC/ESI-ToFMS analyses.

Edited by: V. F. McNeill

References

Aiken, A. C., Decarlo, P. F., Kroll, J. H., Worsnop, D. R., Huffman, J. A., Docherty, K. S., Ulbrich, I. M., Mohr, C., Kimmel, J. R., Sueper, D., Sun, Y., Zhang, Q., Trimborn, A., Northway, M., Ziemann, P. J., Canagaratna, M. R., Onasch, T. B., Alfarra, M. R., Prevot, A. S. H., Dommen, J., Duplissy, J., Metzger, A., Baltensperger, U., and Jimenez, J. L.: O/C and OM/OC ratios of primary, secondary, and ambient organic aerosols with high-resolution time-of-flight aerosol mass spectrometry, Environ. Sci. Technol., 42, 4478–4485, 2008.

Allan, J. D., Delia, A. E., Coe, H., Bower, K. N., Alfarra, M. R., Jimenez, J. L., Middlebrook, A. M., Drewnick, F., Onasch, T. B., and Canagaratna, M. R.: A generalised method for the extraction of chemically resolved mass spectra from aerodyne aerosol mass spectrometer data, J. Aerosol. Sci., 35, 909–922, 2004.

Azizi, N. and Saidi, M. R.: Highly chemoselective addition of amines to epoxides in water, Org. Lett., 7, 3649–3651, 2005.

Bates, K. H., Crounse, J. D., St. Clair, J. M., Bennett, N. B., Nguyen, T. B., Seinfeld, J. H., Stoltz, B. M., and Wennberg, P. O.: Gas phase production and loss of isoprene epoxydiols. J. Phys. Chem. A, 118, 1237–1246, doi:10.1021/jp4107958, 2014.

Biskos, G., Paulsen, D., Russell, L. M., Buseck, P. R., and Martin, S. T.: Prompt deliquescence and efflorescence of aerosol nanoparticles, Atmos. Chem. Phys., 6, 4633–4642, 10, http://www.atmos-chem-phys.net/6/4633/10/.5194/acp-6-4633-2006, 2006.

Bones, D. L., Henricksen, D. K., Mang, S. A., Gonsior, M., Bateman, A. P., Nguyen, T. B., Cooper, W. J., and Nizkorodov, S. A.: Appearance of strong absorbers and fluorophores in limonene-O_3 secondary organic aerosol due to NH_4^+-mediated chemical aging over long time scales, J. Geophys. Res., 115, D05203, doi:10.01029/02009jd012864, 2010.

Budisulistiorini, S. H., Canagaratna, M. R., Croteau, P. L., Marth, W. J., Baumann, K., Edgerton, E. S., Shaw, S. L., Knipping, E. M., Worsnop, D. R., Jayne, J. T., Gold, A., and Surratt, J. D.: Real-time continuous characterization of secondary organic aerosol derived from isoprene epoxydiols in downtown Atlanta, Georgia, using the Aerodyne aerosol chemical speciation monitor, Environ. Sci. Technol., 47, 5686–5694, 2013.

Carlton, A. G. and Turpin, B. J.: Particle partitioning potential of organic compounds is highest in the Eastern US and driven by anthropogenic water, Atmos. Chem. Phys., 13, 10203–10214, doi:10.5194/acp-13-10203-2013, 2013.

Cavdar, H., and Saracoglu, N.: Ring opening of epoxides with $NaHSO_4$: Isolation of β-hydroxy sulfate esters and an effective synthesis for trans-diols, Tetrahedron, 65, 985–989, 2009.

Chan, M. N., Surratt, J. D., Claeys, M., Edgerton, E. S., Tanner, R. L., Shaw, S. L., Zheng, M., Knipping, E. M., Eddingsaas, N. C., Wennberg, P. O., and Seinfeld, J. H.: Characterization and quantification of isoprene-derived epoxydiols in ambient aerosol in the southeastern united states, Environ. Sci. Technol., 44, 4590–4596, 2010.

Clayden, J., Greeves, N., Warren, S., and Wothers, P.: Organic chemistry, Oxford University Press, 386 pp., ISBN 978-380-319-850346-850340, 2001.

Clegg, S. L., Brimblecombe, P., and Wexler, A. S.: Thermodynamic model of the system H^+–NH_4^+–SO_4^{2-}–NO_3–H_2O at tropospheric temperatures, J. Phys. Chem. A, 102, 2137-2154, 1998.

Cole-Filipiak, N. C., O'Connor, A. E., and Elrod, M. J.: Kinetics of the hydrolysis of atmospherically relevant isoprene-derived hydroxy epoxides, Environ. Sci. Technol., 44, 6718–6723, 2010.

Crounse, J. D., McKinney, K. A., Kwan, A. J., and Wennberg, P. O.: Measurement of gas-phase hydroperoxides by chemical ionization mass spectrometry, Anal. Chem., 78, 6726–6732, 2006.

Darer, A. I., Cole-Filipiak, N. C., O'Connor, A. E., and Elrod, M. J.: Formation and dtability of stmospherically televant isoprene-derived organosulfates and organonitrates, Environ. Sci. Technol., 45, 1895–1902, 2011.

De Haan, D. O., Hawkins, L. N., Kononenko, J. A., Turley, J. J., Corrigan, A. L., Tolbert, M. A., and Jimenez, J. L.: Formation of nitrogen-containing oligomers by methylglyoxal and amines in simulated evaporating cloud droplets, Environ. Sci. Technol., 45, 984–991, 2011.

Docherty, K. S., Jaoui, M., Corse, E., Jimenez, J. L., Offenberg, J. H., Lewandowski, M., and Kleindienst, T. E.: Collection efficiency of the aerosol mass spectrometer for chamber-generated secondary organic aerosols, Aerosol Sci. Technol., 47, 294–309, 2013.

Eddingsaas, N. C., VanderVelde, D. G., and Wennberg, P. O.: Kinetics and products of the acid-catalyzed ring-opening of atmospherically relevant butyl epoxy alcohols, J. Phys. Chem. A, 114, 8106–8113, 2010.

EPA: Estimation programs interface for microsoft mindows xp v4.0, US EPA, 2008.

Ervens, B. and Volkamer, R.: Glyoxal processing by aerosol multiphase chemistry: towards a kinetic modeling framework of sec-

ondary organic aerosol formation in aqueous particles, Atmos. Chem. Phys., 10, 8219–8244, doi:10.5194/acp-10-8219-2010, 2010.

Froyd, K. D., Murphy, S. M., Murphy, D. M., de Gouw, J. A., Eddingsaas, N. C., and Wennberg, P. O.: Contribution of isoprene-derived organosulfates to free tropospheric aerosol mass, Proc. Natl. Acad. Sci., 107, 21360–21365, doi:10.1073/pnas.1012561107, 2010.

Graedel, T. E. and Weschler, C. J.: Chemistry within aqueous atmospheric aerosols and raindrops, Rev. Geophys., 19, 505–539, 1981.

Gregoire, P.: Implications of ambient ammonia on aerosol acidity and reactive nitrogen measurements, MS, Department of Chemistry, University of Toronto, Toronto, Ontario, Canada, 82 pp., 2013.

Griffith, D. W. T.: Synthetic calibration and quantitative analysis of gas-phase FT-IR spectra, Appl. Spectrosc., 50, 59–70, 1996.

Hatch, L. E., Creamean, J. M., Ault, A. P., Surratt, J. D., Chan, M. N., Seinfeld, J. H., Edgerton, E. S., Su, Y., and Prather, K. A.: Measurements of isoprene-derived organosulfates in ambient aerosols by aerosol time-of-flight mass spectrometry – Part 2: Temporal variability and formation mechanisms, Environ. Sci. Technol., 45, 8648–8655, 2011.

Hennigan, C. J., Bergin, M. H., Dibb, J. E., and Weber, R. J.: Enhanced secondary organic aerosol formation due to water uptake by fine particles, Geophys. Res. Lett., 35, L18801, doi:10.1029/2008GL035046, 2008.

Hennigan, C. J., Bergin, M. H., Russell, A. G., Nenes, A., and Weber, R. J.: Gas/particle partitioning of water-soluble organic aerosol in Atlanta, Atmos. Chem. Phys., 9, 3613–3628, doi:10.5194/acp-9-3613-2009, 2009.

Hu, D., Qiao, L., Chen, J., Ye, X., Yang, X., Cheng, T., and Fang, W.: Hygroscopicity of inorganic aerosols: Size and relative humidity effects on the growth factor, Aerosol. Air. Qual. Res., 10, 255–264, 2010.

Ip, H. S. S., Huang, X. H. H., and Yu, J. Z.: Effective henry's law constants of glyoxal, glyoxylic acid, and glycolic acid, Geophys. Res. Lett., 36, L01802, doi:10.1029/2008gl036212, 2009.

Iranpoor, N. and Salehi, P.: Highly efficient, regio-and stereoselective alcoholysis of epoxides catalyzed with iron (iii) chloride, Synthesis, 1994, 1152–1154, 1994.

Iranpoor, N., Tarrian, T., and Movahedi, Z.: $FeCl_3 \cdot 6H_2O$ supported on SiO_2 catalysed ring opening of epoxides with alcohols, acetic acid, water, chloride, bromide and nitrate ions, Synthesis, 1996, 1473–1476, 1996.

Jacobsen, E. N., Kakiuchi, F., Konsler, R. G., Larrow, J. F., and Tokunaga, M.: Enantioselective catalytic ring opening of epoxides with carboxylic acids, Tetrahedron Lett., 38, 773–776, 1997.

Kampf, C. J., Waxman, E. M., Slowik, J. G., Dommen, J., Pfaffenberger, L., Praplan, A. P., Prévôt, A. S. H., Baltensperger, U., Hoffmann, T., and Volkamer, R.: Effective Henry's law partitioning and the salting constant of glyoxal in aerosols containing sulfate, Environ. Sci. Technol., 47, 4236–4244, 2013.

Lee, C.-T. and Hsu, W.-C.: The measurement of liquid water mass associated with collected hygroscopic particles, J. Aerosol. Sci., 31, 189–197, 2000.

Lin, Y.-H., Zhang, Z., Docherty, K. S., Zhang, H., Budisulistiorini, S. H., Rubitschun, C. L., Shaw, S. L., Knipping, E. M., Edgerton, E. S., Kleindienst, T. E., Gold, A., and Surratt, J. D.: Isoprene epoxydiols as precursors to secondary organic aerosol formation: Acid-catalyzed reactive uptake studies with authentic compounds, Environ. Sci. Technol., 46, 250–258, 2012.

Lin, Y.-H., Knipping, E. M., Edgerton, E. S., Shaw, S. L., and Surratt, J. D.: Investigating the influences of SO2 and NH3 levels on isoprene-derived secondary organic aerosol formation using conditional sampling approaches, Atmos. Chem. Phys., 13, 8457–8470, doi:10.5194/acp-13-8457-2013, 2013.

Loza, C. L., Chan, A. W. H., Galloway, M. M., Keutsch, F. N., Flagan, R. C., and Seinfeld, J. H.: Characterization of vapor wall loss in laboratory chambers, Environ. Sci. Technol., 44, 5074–5078, 2010.

Loza, C. L., Chhabra, P. S., Yee, L. D., Craven, J. S., Flagan, R. C., and Seinfeld, J. H.: Chemical aging of m-xylene secondary organic aerosol: laboratory chamber study, Atmos. Chem. Phys., 12, 151–167, doi:10.5194/acp-12-151-2012, 2012.

Martin, S. T.: Phase transitions of aqueous atmospheric particles, Chem. Rev., 100, 3403–3453, 2000.

Matthew, B. M., Middlebrook, A. M., and Onasch, T. B.: Collection efficiencies in an Aerodyne aerosol mass spectrometer as a function of particle phase for laboratory generated aerosols, Aerosol. Sci. Technol., 42, 884–898, 2008.

McNeill, V. F., Woo, J. L., Kim, D. D., Schwier, A. N., Wannell, N. J., Sumner, A. J., and Barakat, J. M.: Aqueous-phase secondary organic aerosol and organosulfate formation in atmospheric aerosols: A modeling study, Environ. Sci. Technol., 46, 8075–8081, 2012.

Minerath, E. C., Casale, M. T., and Elrod, M. J.: Kinetics feasibility study of alcohol sulfate esterification reactions in tropospheric aerosols, Environ. Sci. Technol., 42, 4410–4415, 2008.

Minerath, E. C., Schultz, M. P., and Elrod, M. J.: Kinetics of the reactions of isoprene-derived epoxides in model tropospheric aerosol solutions, Environ. Sci. Technol., 43, 8133–8139, 2009.

Muzart, J. and Riahi, A.: Palladium- and light-enhanced ring-opening of oxiranes by copper chloride, J. Organomet. Chem., 433, 323–336, 1992.

Nguyen, T. B., Lee, P. B., Updyke, K. M., Bones, D. L., Laskin, J., Laskin, A., and Nizkorodov, S. A.: Formation of nitrogen- and sulfur-containing light-absorbing compounds accelerated by evaporation of water from secondary organic aerosols, J. Geophys. Res., 117, D01207, doi:10.01029/02011JD016944, 2012.

Nguyen, T. B., Laskin, A., Laskin, J., Nizkorodov, S. A., Brown carbon formation from ketoaldehydes of biogenic monoterpenes, Faraday Discuss., 165, 473–494, 2013.

Noziere, B., Dziedzic, P., and Cordova, A.: Products and kinetics of the liquid-phase reaction of glyoxal catalyzed by ammonium ions (NH_4^+), J. Phys. Chem. A, 113, 231–237, 2009.

Paulot, F., Crounse, J. D., Kjaergaard, H. G., Kroll, J. H., Seinfeld, J. H., and Wennberg, P. O.: Isoprene photooxidation: new insights into the production of acids and organic nitrates, Atmos. Chem. Phys., 9, 1479–1501, doi:10.5194/acp-9-1479-2009, 2009a.

Paulot, F., Crounse, J. D., Kjaergaard, H. G., Kurten, A., St. Clair, J. M., Seinfeld, J. H., and Wennberg, P. O.: Unexpected epoxide formation in the gas-phase photooxidation of isoprene, Science, 325, 730–733, 2009b.

Pye, H. O. T., Pinder, R. W., Piletic, I. R., Xie, Y., Capps, S. L., Lin, Y.-H., Surratt, J. D., Zhang, Z., Gold, A., Luecken, D. J., Hutzell, W. T., Jaoui, M., Offenberg, J. H., Kleindienst, T. E., Lewandowski, M., and Edney, E. O.: Epoxide pathways improve

model predictions of isoprene markers and reveal key role of acidity in aerosol formation. Environ. Sci. Technol., 47, 11056–11064, 2013.

Reuss, J.: Chemical and biological relationships relevant to the effect of acid rainfall on the soil-plant system, Water Air Soil Pollut., 7, 461–478, 1977.

Robinson, N. H., Hamilton, J. F., Allan, J. D., Langford, B., Oram, D. E., Chen, Q., Docherty, K., Farmer, D. K., Jimenez, J. L., Ward, M. W., Hewitt, C. N., Barley, M. H., Jenkin, M. E., Rickard, A. R., Martin, S. T., McFiggans, G., and Coe, H.: Evidence for a significant proportion of Secondary Organic Aerosol from isoprene above a maritime tropical forest, Atmos. Chem. Phys., 11, 1039–1050, doi:10.5194/acp-11-1039-2011, 2011.

Rothman, L. S., Gordon, I. E., Barbe, A., Benner, D. C., Bernath, P. F., Birk, M., Boudon, V., Brown, L. R., Campargue, A., and Champion, J.-P.: The HITRAN 2008 molecular spectroscopic database, J. Quant. Spectrosc. Rad. Transf., 110, 533–572, 2009.

Sareen, N., Schwier, A. N., Shapiro, E. L., Mitroo, D., and McNeill, V. F.: Secondary organic material formed by methylglyoxal in aqueous aerosol mimics, Atmos. Chem. Phys., 10, 997-1016, doi:10.5194/acp-10-997-2010, 2010.

Seinfeld, J. H. and Pandis, S. N.: Atmospheric chemistry and physics: From air pollution to climate change, Wiley, 2006.

Solomons, T. W. G. and Fryhle, C. B.: Organic chemistry, 8 ed., John Wiley & Sons, Inc., Hoboken, NJ, 1255 pp., 2004.

St. Clair, J. M., McCabe, D. C., Crounse, J. D., Steiner, U., and Wennberg, P. O.: Chemical ionization tandem mass spectrometer for the in situ measurement of methyl hydrogen peroxide, Rev. Sci. Instrum., 81, 094102–094106, 2010.

Surratt, J., Chan, A. W. H., Eddingsaas, N. C., Chan, M., Loza, C. L., Kwan, A. J., Hersey, S. P., Flagan, R. C., Wennberg, P. O., and Seinfeld, J. H.: Reactive intermediates revealed in secondary organic aerosol formation from isoprene, Proc. Natl. Acad. Sci., 107, 6640–6645, 2010.

Surratt, J. D., Lewandowski, M., Offenberg, J. H., Jaoui, M., Kleindienst, T. E., Edney, E. O., and Seinfeld, J. H.: Effect of acidity on secondary organic aerosol formation from isoprene, Environ. Sci. Technol., 41, 5363–5369, 2007.

Wang, Z., Cui, Y.-T., Xu, Z.-B., and Qu, J.: Hot water-promoted ring-opening of epoxides and aziridines by water and other nucleopliles, J. Org. Chem., 73, 2270–2274, 2008.

Xiong, J. Q., Zhong, M., Fang, C., Chen, L. C., and Lippmann, M.: Influence of organic films on the hygroscopicity of ultrafine sulfuric acid aerosol, Environ. Sci. Technol., 32, 3536–3541, 1998.

Yu, G., Bayer, A. R., Galloway, M. M., Korshavn, K. J., Fry, C. G., and Keutsch, F. N.: Glyoxal in aqueous ammonium sulfate solutions: Products, kinetics and hydration effects, Environ. Sci. Technol., 45, 6336–6342, 2011.

Zhang, Z., Lin, Y. H., Zhang, H., Surratt, J. D., Ball, L. M., and Gold, A.: Technical note: Synthesis of isoprene atmospheric oxidation products: Isomeric epoxydiols and the rearrangement products cis- and trans-3-methyl-3,4-dihydroxytetrahydrofuran, Atmos. Chem. Phys., 12, 8529–8535, doi:10.5194/acp-12-8529-2012, 2012.

Zuend, A., Marcolli, C., Luo, B. P., and Peter, T.: A thermodynamic model of mixed organic-inorganic aerosols to predict activity coefficients, Atmos. Chem. Phys., 8, 4559–4593, doi:10.5194/acp-8-4559-2008, 2008.

Zuend, A., Marcolli, C., Booth, A. M., Lienhard, D. M., Soonsin, V., Krieger, U. K., Topping, D. O., McFiggans, G., Peter, T., and Seinfeld, J. H.: New and extended parameterization of the thermodynamic model aiomfac: Calculation of activity coefficients for organic-inorganic mixtures containing carboxyl, hydroxyl, carbonyl, ether, ester, alkenyl, alkyl, and aromatic functional groups, Atmos. Chem. Phys., 11, 9155–9206, doi:10.5194/acp-11-9155-2011, 2011.

Chapter 7

Reactive Uptake and Photo-Fenton Oxidation of Glycolaldehyde in Aerosol Liquid Water

Environmental Science & Technology

Article

pubs.acs.org/est

Reactive Uptake and Photo-Fenton Oxidation of Glycolaldehyde in Aerosol Liquid Water

T. B. Nguyen,*[,†] M. M. Coggon,[‡] R. C. Flagan,[‡,§] and J. H. Seinfeld[‡,§]

[†]Division of Geological and Planetary Sciences, [‡]Division of Chemistry and Chemical Engineering, and [§]Division of Engineering and Applied Science, California Institute of Technology, Pasadena, California, United States

Supporting Information

ABSTRACT: The reactive uptake and aqueous oxidation of glycolaldehyde were examined in a photochemical flow reactor using hydrated ammonium sulfate (AS) seed aerosols at RH = 80%. The glycolaldehyde that partitioned into the aerosol liquid water was oxidized via two mechanisms that may produce aqueous OH: hydrogen peroxide photolysis ($H_2O_2 + h\nu$) and the photo-Fenton reaction ($Fe_{(II)} + H_2O_2 + h\nu$). The uptake of 80 (±10) ppb glycolaldehyde produced 2−4 wt % organic aerosol mass in the dark ($k_H^* = (2.09–4.17) \times 10^6$ M atm^{-1}), and the presence of an OH source increased the aqueous uptake by a factor of 4. Although the uptake was similar in both OH-aging mechanisms, photo-Fenton significantly increased the degree of oxidation (O/C = 0.9) of the aerosols compared to H_2O_2 photolysis (O/C = 0.5). Aerosol organics oxidized by photo-Fenton and H_2O_2 photolysis resemble ambient "aged" and "fresh" OA, respectively, after the equivalent of 2 h atmospheric aging. No uptake or changes in particle composition occurred on dry seed aerosol. This work illustrates that photo-Fenton chemistry efficiently forms highly oxidized organic mass in aerosol liquid water, providing a possible mechanism to bridge the gap between bulk-phase experiments and ambient particles.

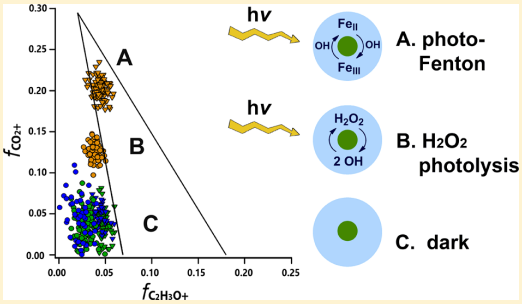

INTRODUCTION

Organic aerosols (OA) found in the atmosphere are often more oxidized[1,2] and contain higher organic mass[3,4] than those generated in the laboratory. To account for the under-predicted organic mass and oxidation state, aqueous-phase oxidation has been suggested as an important mechanism contributing to OA production and aging in the ambient environment.[5−11] Most laboratory investigations of aqueous-phase chemistry focus on bulk phase oxidation or "cloud processing", e.g., aging of model water-soluble organic compounds (e.g., glyoxal, methylglyoxal, pyruvic acid, etc.)[10,12−23] or OA extracts[24−26] in beaker-scale experiments.

It has been suggested that the aqueous phase of particles (aerosol liquid water) may be an even more efficient medium for aqueous chemistry because the smaller volume of aerosol water allows for greater concentrations of organic compounds, oxidants, and inorganic ions as compared to clouds.[10,11] Precursors of the OH radical in cloudwater, e.g., Fe ions (Fenton reactions),[27−29] hydrogen peroxide (H_2O_2),[30,31] and nitrate ion,[32] are expected to occur in higher concentration in aerosol water. In addition, there is evidence that aqueous chemistry in aerosol water may be very different from that in the bulk phase. For example, the mechanism of OH oxidation, initiated by H_2O_2 photolysis, in aqueous water/organic mixtures changes with water content,[33] which has implications for concentrated vs dilute aqueous solution chemistry.[22] Furthermore, the formation of organosulfates and oligomers may be more important in aerosol water compared to clouds.[12,34] In this work, we investigate aqueous chemistry in the liquid water of suspended aerosols, with particular focus on hydrogen peroxide (H_2O_2) photolysis and Fenton and photo-Fenton chemistry as oxidation mechanisms for particle-phase organic matter. Fenton and photo-Fenton are redox reactions of iron ($Fe_{(II)}/Fe_{(III)}$) with H_2O_2, producing aqueous OH and other oxidizing agents in either the dark or photolytic conditions, respectively. Fenton mechanisms are powerful in the bulk cloudwater-phase application,[35−40] and are often utilized for wastewater treatment of organic pollutants;[41,42] however, they have yet to be demonstrated as OH sources in the liquid water of suspended aerosol.

This work also investigates the reactive uptake of a model atmospheric organic compound, glycolaldehyde ($C_2H_4O_2$), onto the liquid water of inorganic seed aerosol. Reactive uptake onto wet particles has been studied for a few representative atmospheric organic compounds, resulting in significant mass gain;[43−48] however, the heterogeneous chemical behavior of glycolaldehyde has not yet been investigated. Glycolaldehyde is an important atmospheric compound, observed with mixing ratios up to 3 ppbv in a

Received: February 2, 2013
Revised: April 2, 2013
Accepted: April 4, 2013
Published: April 4, 2013

forested region,[49] that may efficiently partition into the aqueous phase (k_H in pure water = 4.14 × 10^5 M atm^{-1}).[50,51] Glycolaldehyde is formed in substantial yield from the gas-phase OH oxidation of isoprene (yield = 25−42%),[52,53] methyl vinyl ketone (MVK, 40−42%),[52] and 2-methyl-3-butenol (MBO, 28−79%),[54−58] and is also emitted from biomass burning.[59,60] The bulk aqueous oxidation of glycolaldehyde, from H_2O_2 photolysis, has also been recently reported to form OA.[20,61]

EXPERIMENTAL SECTION

An abridged version of the experimental section is given here. The full version can be found in the Supporting Information (SI). Experiments were performed in a 16 L glass photochemical tubular flow reactor at low Reynolds number flow (Re < 5) housed in a 0.6 m^3 enclosure at room temperature, under dry (relative humidity, RH < 10%) and humid (RH ∼ 80%) conditions (Figure S1.) The residence times of the aerosols vary from 30 to 60 min. Variable RH was achieved in the reactor by mixing dry zero air with humid injection air (RH > 90%) past a water trap. Temperature and RH were measured by a Vaisala HMM211 probe, calibrated prior to use in the RH range of 11−95% with saturated salt solutions. Seed aerosols were mixed with the air stream in a 200 cm^3 glass mixing tube and pulled through the flow reactor at ∼450 std. cm^3 per minute (sccm).

Dilute aqueous ammonium sulfate (AS) solutions (Acros −0.012 M) were atomized to produce seed aerosols, either alone or with 200 μM H_2O_2 (Aldrich) and ferrous sulfate hexahydrate ($Fe(SO_4)·7H_2O$, Macron) added immediately prior to atomization such that the initial [$Fe_{(II)}$] = 5 wt % of the inorganic mass.[28,29] Upon atomization at RH = 80%, the contents of the atomizer solution are concentrated in the aerosol by 2 orders of magnitude; however, the Fe mass ratio is not expected to change. Gas-phase H_2O_2 that may be produced from atomization was not detected by chemical ionization mass spectrometry (CIMS) during dry and humid atomization of AS + H_2O_2 solutions (Figure S2). Especially under dry conditions, H_2O_2 may be lost to metal tubing or the Nafion membrane of the drier prior to particles reaching the flow reactor. Therefore, gas-phase OH formation was likely negligible during the course of the experiments and results are attributed to aqueous-phase oxidation. Four seed compositions were used for experiments: AS, AS + H_2O_2, AS + Fe, and AS + Fe + H_2O_2. In the humid experiments, the aerosols were atomized wet and enter the flow reactor at RH ∼ 80%, such that the aerosols retain significant amounts of liquid water. In the dry experiments, the seed aerosols were dried with a Nafion membrane diffusion drier before entering the flow reactor set at RH < 10%.

Glycolaldehyde (23147−58−2, Fluka, >98% purity) was injected with a 55 sccm stream of dry air at 76 °C. For uptake experiments, particles reached a steady state before glycolaldehyde injection. The gas-phase concentration of glycolaldehyde was monitored by chemical ionization mass spectrometry (CIMS) coupled to a Varian triple-quadrupole spectrometer with unit mass resolution and 2−5 min time resolution, using CF_3O^- as the reagent ion.[62−64] The CIMS signal for glycolaldehyde (m/z 145), which corresponded to a steady-state mixing ratio of 80 (±10) ppb in experiments, was calibrated in the operational RH range prior to measurements.

Photochemistry within the flow reactor is initiated by UV−B broadband lamps (310 nm peak, Phillips, 40W T12-UVB). The lamp photon flux spectrum (Figure S3) is compared with a modeled ground-level solar flux[65] at solar zenith angle = 0°. From calculated photolysis rates of H_2O_2 (J_{H2O2} = 3.2 × 10^{-5} s^{-1} in the flow reactor and J_{H2O2} = 9.2 × 10^{-6} s^{-1} in the atmosphere), we estimate that 1 h photolytic aging in the flow reactor equals up to 3.5 h under atmospheric clear sky tropical noon conditions with 300 DU ozone column. Aging time scales reported here have not been converted to atmospheric values.

Control experiments showed that temperature differences (∼5 °C) between dark and photolytic conditions did not significantly affect the results (Figure S4 and associated discussion). Aerosol composition data were corrected to the ratio of aerosol liquid water content (R_{LWC}) at the operational temperature (27−32 °C) in relation to the LWC at room temperature, e.g., org wt% = $(mass)_{org}/[(mass)_{total}·R_{LWC}]$. The resulting values correspond to the wt% of organics in LWC of deliquesced AS particles at RH 80% and T = 27 °C. LWC was calculated based on hygroscopicity measurements of ultrafine AS.[66] The flow reactor was thoroughly flushed between each series of experiments. The exit flow was dried with a Nafion diffusion drier before particle composition characterization.

Particle size and number concentrations were measured with a custom-built column and radial mobility analyzer (CARMA) coupled to a butanol condensation particle counter (CPC). The CARMA-CPC was calibrated with polystyrene latex (PSL) spheres. The particles entering the flow reactor were polydisperse, with a peak diameter at D_p ∼ 40 nm (Figure S5). The mass concentration of AS particles typically ranged from 5 to 25 μg m^{-3} for all experiments. All composition measurements are normalized to the total particle mass.

Particle composition was measured with an aerosol mass spectrometer using a high-resolution time-of-flight mass analyzer (ToF-AMS, Aerodyne Research Inc.) in V mode (resolution ∼3000−4000 at m/z 200). Data were analyzed in Igor Pro (WaveMetrics, Inc.) using the Squirrel v 1.51H and Pika v 1.10H analysis toolkits. Gas interferences and elemental ratios were calculated using the fragmentation table developed by Allan et al.[67] and Aiken et al.[68] Prior to experiments, the ToF-AMS ionization efficiency was calibrated using 350 nm ammonium nitrate particles. CHO^+ (m/z 29) and CH_4O^+ (m/z 32), two peaks with strong interferences from common air species, were omitted in our analysis due to possible errors in the fitting calculation (Figure S6 and associated discussion). Consequently, the O/C ratios of organics may be biased low. The elemental ratios reported in this work are used primarily as a metric for comparison between different oxidation mechanisms.

RESULTS AND DISCUSSION

Composition Analysis. Difference mass spectra, where the positive scale shows enhancement and the negative scale shows depletion due to a chemical change, for the uptake and aqueous oxidation experiments are shown in Figure 1. Aerosol-phase glycolaldehyde (and its derivatives) from uptake onto AS (Figure 1b) and AS + Fe (Figure 1e) seeds was confirmed by the CH_3O^+ mass fragment (CH_3O^+, m/z 31), the dominant peak in the electron impact spectrum of glycolaldehyde (Figure 1a),[69] and the molecular ion ($C_2H_4O_2^+$, m/z 60). As glycolaldehyde is the only source of carbon in the system, the total organic concentration is expected to be due entirely to glycolaldehyde and its aqueous-phase derivatives. CH_3O^+ was used as the primary tracer for glycolaldehyde because of its high signal-to-noise. The AMS tracer for amines/imines, CH_4N^+,[70] is enhanced in the particles from glycolaldehyde injection

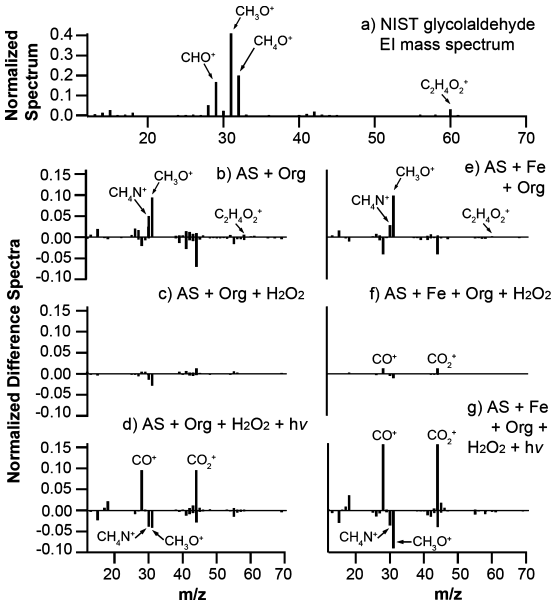

Figure 1. Electron impact mass spectra of (a) glycolaldehyde from the NIST mass spectral database, and the AMS difference mass spectra between (b) exp i and particle blank, (c) exp ii and exp i, (d) exp iii and exp ii, (e) exp iv and particle blank, (f) exp v and exp iv, and (g) exp vi and exp v, as listed in Table 1. "Org" = gas-phase injection of glycolaldehyde. Note: the CHO^+ and CH_4O^+ peaks were omitted in this work due to strong air interferences (Figure S6).

(Figure 1b and e), indicating that the dark reaction of aqueous NH_4^+ with aldehydes generates organic nitrogen (amines, imines and N-heterocyclic compounds) in the hydrated particles,[71,72] especially if followed by evaporation.[25,73] A good correlation exists between CH_4N^+ and CH_3O^+ (Figure S7), indicating that glycolaldehyde may be the dominant source of the organic nitrogen in this system.

The introduction of H_2O_2 to the AS seeds produced little change in organic composition, e.g., no significant enhancements or depletion (Figure 1c). However, when H_2O_2 was added to AS + Fe seeds (Figure 1f), the dark Fenton reaction occurs to some degree, producing small traces of CO^+ and CO_2^+, which are indicative of oxidized organics. The irradiation of the AS + Org + H_2O_2 sample (Figure 1d) enhanced oxidized organics (CO^+/CO_2^+) and decreased the concentrations of glycolaldehyde (CH_3O^+) and amine/imine (CH_4N^+). Irradiation of the AS + Fe + org + H_2O_2 sample (Figure 1g), which initiated the photo-Fenton reaction, led to the largest enhancement in oxidized organics and highest loss of glycolaldehyde and organic nitrogen.

Glycolaldehyde Reactive Uptake. Figure 2a shows that particle-phase glycolaldehyde concentration in the hydrated aerosols (f_{CH3O+}) grows in response to the injection of gas-phase glycolaldehyde. This uptake behavior is nonexistent in experiments with dry seed aerosol (dashed lines). Dark aqueous reactions of glycolaldehyde that may produce OA after evaporation include formation of the geminal diol (hydration),[74] hemiacetals,[75] and amines/imines as discussed earlier. Figure 2b shows that the total aerosol organic mass mirrors the behavior of f_{CH3O+}, and increases up to a maximum of 4 wt %. In the dry experiment, the concentration of particle-phase

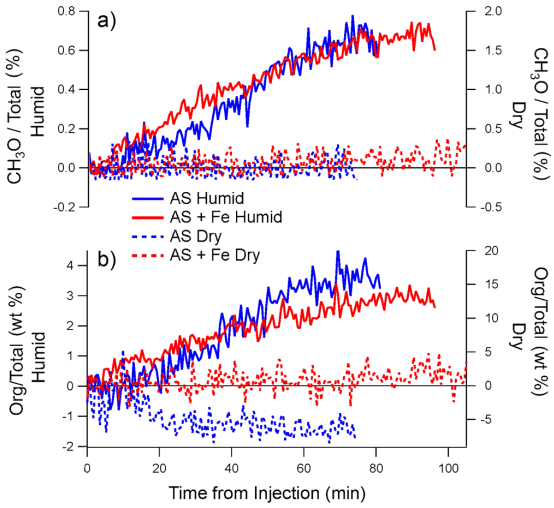

Figure 2. Time profile of the uptake of glycolaldehyde onto dry and hydrated seed particles, monitored by AMS (a) tracer mass fragment CH_3O^+ (m/z 31, not calibrated to wt %) and (b) total organic mass.

organics from injection of glycolaldehyde is either zero, within error, or negative. We note that the error in organic mass in dry experiments is higher because of the lower signal-to-noise in detected peaks.

The degree of oxidation, C=C unsaturation, and organic nitrogen content in organic particles are typically parametrized by the oxygen-to-carbon (O/C), hydrogen-to-carbon (H/C), and nitrogen-to-carbon ratios, respectively.[68,76] Figure 3a shows the time profiles of the elemental ratios (O/C, H/C, and N/C) of aerosols in humid experiments. The experiment identification labels and ensemble-average organic mass values and elemental ratios are reported in Table 1. The aerosol composition is relatively insensitive to seed composition in

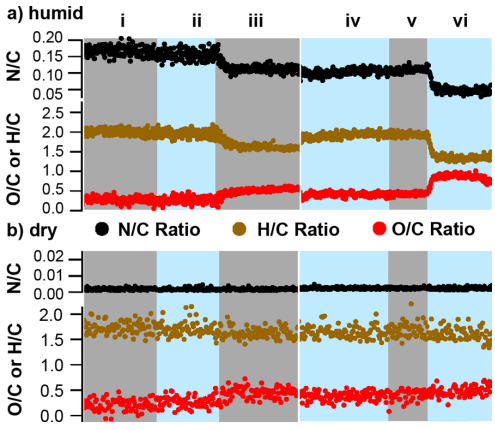

Figure 3. N/C, H/C, and O/C ratios from experiments at (a) RH 80% and (b) RH < 10%. Experimental regimes shown correspond to (i) AS + org; (ii) AS + org + H_2O_2; (iii) AS + org + H_2O_2 + $h\nu$; (iv) AS + Fe(II) + org; (v) AS + Fe(II) + org + H_2O_2; and (vi) AS + Fe(II) + org + H_2O_2 + + $h\nu$, where "org" = gas-phase injection of glycolaldehyde. Experimental data correspond to time scales greater than 30 min.

dx.doi.org/10.1021/es400538j | Environ. Sci. Technol. 2013, 47, 4307−4316

Table 1. Average Weight Percent and Elemental Ratios for Aerosol Organics, from the Uptake of 80 (±10) ppb Gas-Phase Glycolaldehyde ("org") onto 5–25 $\mu g\ m^{-3}$ of Hydrated Inorganic Seeds[a]

#	experiment	net org. (wt %)	⟨H/C⟩	⟨O/C⟩	⟨N/C⟩
ii	AS + H_2O_2 + org	2.4 (±0.5)	1.9	0.3	0.15
i	AS + org	3.5 (±0.5)	2.0	0.3	0.16
iii	AS + H_2O_2 + org + $h\nu$	12.6 (±0.5)	1.6	0.5	0.11
iv	AS + Fe(II) + org	2.9 (±0.5)	1.9	0.4	0.11
v	AS + Fe(II) + H_2O_2 + org	2.8 (±0.5)	1.9	0.4	0.11
vi	AS + Fe(II) + H_2O_2 + org + $h\nu$	12.2 (±0.5)	1.3	0.9	0.04

[a]Seed water contents for these experiments were 165–200% of the dry seed mass. The organic "background" of seed blanks, shown in Figure 3, has been subtracted from organic weight percent. Dry (seed water <5%) results are shown in Table S1.

the dark experiments (exp i–ii and iv–v), but changes significantly from the initiation of photochemistry (exp iii and vi). In the absence of light, organic growth and composition are similar, with or without the addition of H_2O_2 or Fe. Under dry conditions, no changes are observable within error (Figure 3b), indicating that oxidation reactions occur exclusively in the aerosol liquid water. Compared to dark uptake, the presence of an OH source increases the organic accommodation into the aqueous phase by a factor of 4 (i.e., ∼3 wt % uptake in the dark vs 12–13 wt % with light). The enhanced uptake is likely due to the photoinduced reactions of glycolaldehyde, in addition to aforementioned dark reactions. Both photochemical OH sources produce similar amounts of aerosol organics despite changes in the degree of oxidation. This may be due to the simultaneous decrease in N/C and H/C ratios as O/C ratios increase (Figure 3a), thus conserving the total organic mass within the error of the measurements.

It is expected that the high ionic strength[77] and organic–inorganic interactions[78] in hydrated AS aerosols may significantly increase the Henry's law constant of glycolaldehyde as compared to its value in pure water ($k_H = 4.14 \times 10^5$ M atm^{-1})[50] Based on the mass fraction of glycolaldehyde for AS particles ($f_A = C_{aq.}/C_{gas}$), the effective Henry's law constant is calculated as $k_H^* = f_A/[10^{-6}RTL]$, where f_A is the fraction of mass in the aqueous phase vs the gas phase, R is the ideal gas constant, T is the temperature in K, L is the liquid water content in g m^{-3}, and 10^{-6} is a unit conversion factor.[79] We estimate the effective Henry's law constant for glycolaldehyde uptake onto AS particles (either pure or doped with H_2O_2 and Fe) at RH 80% to be $k_H^* = (2.09–4.17) \times 10^6$ M atm^{-1} in the dark. The k_H^* values for glycolaldehyde are high for a typical atmospheric volatile compound,[79] but more than an order of magnitude lower than that of glyoxal.[80,81] However, given that glycolaldehyde may be found at high mixing ratios relative to glyoxal in a typical forested environment,[51,60,82,83] the aqueous processing of these C_2 aldehydes may be similarly important.

Oxidation in Aerosol Liquid Water. Although the glycolaldehyde uptake is similar for the photolytic periods (exp iii and vi), the degree of oxidation of the aerosol organics is highly dependent on the OH source. H_2O_2 photolysis increases the O/C by 0.2 and decreases the H/C by 0.3–0.4 compared to dark uptake, an unequivocal indication of chemical evolution of the OA mass. The changes in elemental ratio due to photo-Fenton are more substantial, approximately a factor of 2 greater than H_2O_2 photolysis ($\Delta O/C = 0.5$ and $-\Delta H/C = 0.6$). The O/C of organics aged by photo-Fenton chemistry approach the O/C observed in ambient "aged" OA (O/C = 0.9–1.0), while in comparison, the O/C of organics aged by H_2O_2 photolysis most closely resembles "fresh" OA (O/C = 0.5–0.6).[68] We will discuss subsequently the chemistry underlying this difference in oxidation state.

The increase in oxidation appears to be more abrupt for photo-Fenton chemistry, as evidenced by a sharper change in elemental ratios. As both particles and gas-phase organics stabilize before lights are turned on, the photoinduced changes in particle composition were witnessed with only a minor time delay, i.e., the few minutes it takes to reach aerosol instrumentation. Therefore, the rate of increase in oxidation state tracks the oxidant production rate. The observed changes in O/C occur and stabilize on the order of 5 min in the photo-Fenton oxidation. Even when corrected to atmospheric time scales (∼20 min), the mechanism can be considered fast compared to a typical aerosol lifetime (hours to days).

The oxidative changes are conveniently viewed in either a "triangle" diagram (Figure 4a) where the fraction of the ToF-

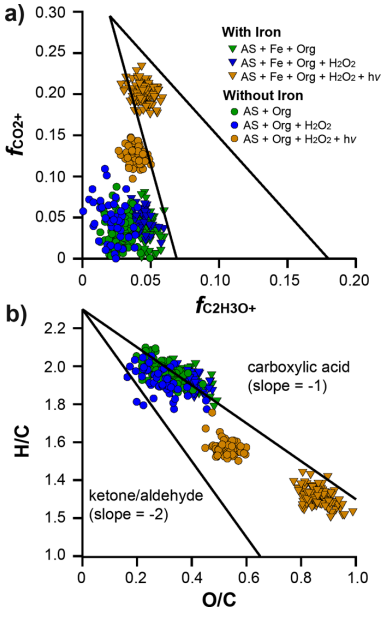

Figure 4. High-resolution AMS (a) f_{CO2+} vs f_{C2H3O+} plot of particulate organics from glycolaldehyde uptake and oxidation at RH = 80%, superimposed on the ambient triangle space from Ng et al.[2] and (b) Van Krevelen diagram with slopes corresponding to formation of carboxylic acids and ketones/aldehydes. Photo-induced oxidation was significantly enhanced in the presence of Fe(II). No trends were observed in dry experiments, shown in Figure S8.

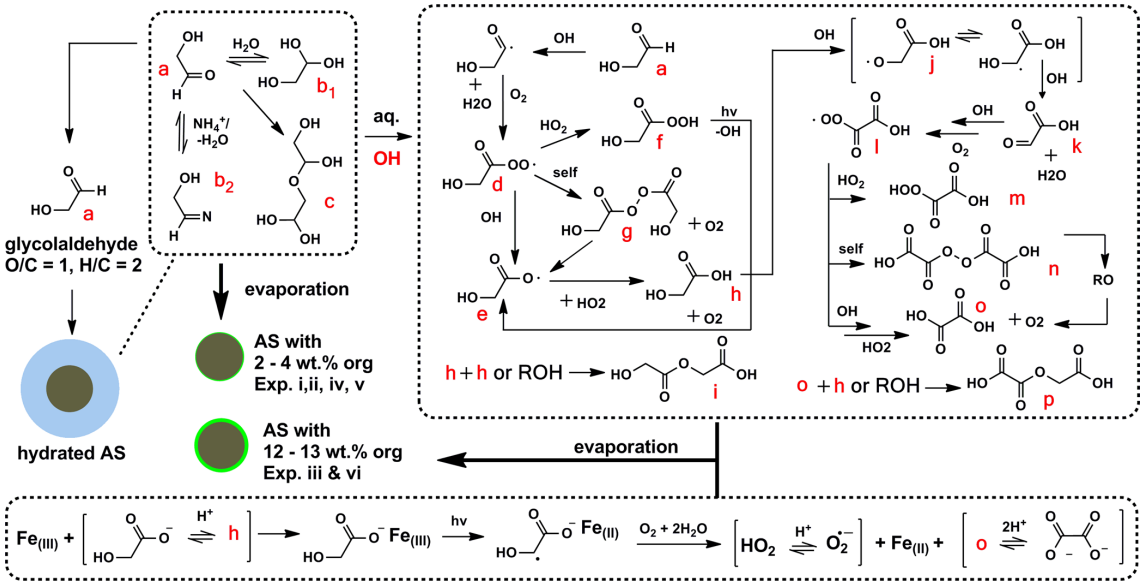

Figure 5. Proposed scheme of reactions occurring in the glycolaldehyde uptake and aqueous photooxidation onto hydrated AS seeds.

AMS mass fragment CO_2^+ (f_{CO2+}) is plotted against that of $C_2H_3O^+$ (f_{C2H3O+}), and in which the triangular region designates the mass space that encompasses a majority of ambient aerosol data[2] or a Van Krevelen (VK) diagram (Figure 4b), where the H/C is plotted against O/C. An advantage of the triangle space is that the normalization vanishes ($f_{CO2+}/f_{C2H3O+} = (m_{CO2+}/M)/(m_{C2H3O+}/M)$, where $M = [m_{total} \cdot R_{LWC}]$). Furthermore, as the triangle diagram was developed specifically to illustrate "aged" and "fresh" aerosols, it does not suffer from AMS underestimation of O/C and overestimation of H/C.[84] Data from the dry experiments (Figure S8) show only scattered points. Data points from dark uptake experiments onto hydrated AS seeds cluster in the lower left region of the diagram outside the triangle space, corresponding to semi-volatile oxygenated organic aerosols (OOA), unlike those found in the ambient environment. Organic mass aged by aqueous H_2O_2 photolysis moves vertically up the diagram, with a distinctly higher average f_{CO2+} than unaged aerosols. Finally, photo-Fenton oxidation dramatically enhances the average f_{CO2+} of the organic aerosol, moving the data cluster toward the apex of the triangle, where low-volatility OOA (LV-OOA) are typically found in the atmosphere. The VK diagram shows that the oxidation of organics advances the O/C ratio toward 1, constrained by either the carboxylic acid or ketone/aldehyde trajectories.[85] The elemental ratios of the H_2O_2/$h\nu$-oxidized organics lay between the carboxylic and ketone/aldehyde slope in the VK space. The photo-Fenton-oxidized organics are more oxidized at a given time and have a trajectory corresponding to carboxylic acid formation, which typically describes the trajectory of ambient aerosol aging.[85] In short, both representations show that photo-Fenton aging produces organic aerosol more closely resembling ambient LV-OOA than aqueous H_2O_2 photolysis within the timescale of the experiment.

Comparison of Aqueous Oxidation Mechanisms. The mechanisms of H_2O_2 photolysis (reactions 1−2), dark Fenton,[86] and photo-Fenton[87−89] reactions are discussed below. We note that the mechanism of photo-Fenton is highly pH-dependent, and the identities of oxidants involved under different conditions are still subject to debate.[89,90] In the liquid water of AS-seeded aerosols, iron forms an array of complexes with sulfate, water, and organics with pH-dependent speciation.[91] We only consider complexes that contribute to Fenton photochemistry. At lower pH (<3.5), OH appears to be the predominant oxidant, as the introduction of OH scavengers quenches the Fenton reaction; however at pH 6−8, OH scavengers are found to be ineffective.[92] A different oxidant is likely formed at near-neutral pH, possibly an $Fe_{(IV)}$ species.[89,93] From pH 3.5 to 6, more than one oxidant may be active. The dilute AS + $Fe_{(II)}$ atomizer solutions used here are initially pH ∼ 5.3 and acidify over time from reaction. In the absence of consensus for the neutral pH mechanism, and the expectation that acidity is more concentrated in the particles than in the atomizer solution, we focus on the OH-dominated mechanisms that control the early stages of oxidation:

$$H_2O_2 + h\nu \rightarrow 2OH\cdot \quad (1)$$

$$H_2O_2 + OH\cdot \rightarrow HO_2\cdot + H_2O \quad (2)$$

$$Fe^{2+} + H_2O_2 \rightarrow OH\cdot + OH^- + Fe^{3+} \quad (3)$$

$$Fe^{3+} + H_2O_2 \rightarrow Fe^{2+} + HO_2\cdot + H^+ \quad (4)$$

$$Fe^{3+} + H_2O \rightarrow Fe(OH)^{2+} + H^+ \quad (5)$$

$$Fe(OH)^{2+} + h\nu \rightarrow OH\cdot + Fe^{2+} \quad (6)$$

In the initial step of Fenton chemistry, the addition of H_2O_2 to Fe^{2+} produces Fe^{3+} and OH (reaction 3). However, the regeneration of Fe^{2+} by H_2O_2 in dark Fenton (reaction 4) is in competition with the formation of iron hydroxide complexes, e.g., $Fe_{(III)} = [Fe^{3+} + Fe(OH)^{2+} + Fe(OH)_2^+ + ...]$.[91] In this concentration regime and pH range, $Fe(OH)^{2+}$ is expected to be the species most responsible for oxidation photochemistry.[91] Upon addition of H_2O_2, the pH of the atomizer solution drops

to 3.4 due to the hydrolysis of Fe^{3+} (e.g., reaction 5). Also, a soluble yellow−orange product is immediately observed that is consistent with the absorption spectrum of $Fe(OH)^{2+}$,[94] perhaps with some contribution from $Fe(O_2H)^{2+}$.[89] After ∼40 min in solution, the pH decreases further to pH 2.8 in solution (lower in the aerosol water). These mechanisms may be dominant until the production of organic acid ligands for $Fe_{(III)}$.

Under our experimental conditions, dark Fenton chemistry becomes ineffective within a relatively short time (a few minutes) due to the irreversible loss of Fe^{2+}, consistent with other accounts of low $[Fe^{2+}]$ in dark Fenton.[94] However, in photo-Fenton, $Fe(OH)^{2+}$ photodegrades to regenerate Fe^{2+} and another OH radical.[94] Over time, the efficacy of the photo-Fenton reaction diminishes (Figure 3a (exp vi)), as evident by the slowly decreasing O/C ratio of the aerosol after approximately 40 min. This is likely due to the aforementioned differences in iron speciation with decreasing pH that may produce fewer photochemically active species that can recycle Fe^{2+} or through precipitation of insoluble iron oxides

$$Fe_{(III)} + H_2O \rightarrow Fe(OH)_{3\downarrow} + 3H^+ \quad (7)$$

This precipitation reaction is observed to form over the course of hours in the atomizer solution and inhibits both dark and photo-Fenton mechanisms at pH > 1.5.[91]

Figure 5 shows an abridged, but unifying, diagram of the uptake and OH-initiated reactions discussed in this work, in addition to Fe-mediated oxidation. Competition from direct photolysis is estimated to be minor (SI section II). Glycolaldehyde partitions into the aerosol liquid water and undergoes dark reactions that increase the particle-phase organic concentration to 2−4 wt % upon particle evaporation, i.e., hydration to the geminal diol (Figure 5, b1), formation of an imine (b2), and oligomerization via hemiacetal formation (c). The equilibrium amount of unreacted glycolaldehyde is able to repartition into the gas phase. The introduction of OH sources in exp iii and vi provides photolytic loss processes for glycolaldehyde, perturbing the dark uptake equilibrium and resulting in higher aerosol mass accommodation and lower revolatilization.

The glycolaldehyde OH-oxidation is believed to be initiated mainly by abstraction of the aldehydic hydrogen.[95] Addition of oxygen generates an acylperoxy radical ($RC(O)O_2$, d) that may undergo a variety of reactions. Reaction with the hydroperoxy radical (HO_2) will likely result in the formation of a peracid (f). $RC(O)O_2$ self-reactions may produce an diacyl peroxide (RC(O)OO(O)CR), analogous to reactions of alkylperoxy radicals.[79,96] Similar peroxides were found to be efficient OA precursors in isoprene nitrate-initiated oxidation.[97] The acyloxy radical pathway ($2RC(O)O_2 \rightarrow 2RC(O)O + O_2$) is also viable,[98] and may be a large source of RC(O)O radicals (e) that react with HO_2 to form organic acids like glycolic acid (h). The product hydroxyacids may react with themselves or with an alcohol group to form oligomer esters, which have been demonstrated to increase the OA mass.[23,34,99−101] Because many of the oxidation products of glycolaldehyde are lower-volatility than the parent, it is possible that the removal of glycolaldehyde is the most important step in increasing the OA mass. The steps following glycolaldehyde loss will change the OA composition but not necessarily the uptake, consistent with our observation that the two OH sources studied yield the same OA mass but very different OA compositions.

The observed difference in degree of oxidation may be due to the following reasons: (1) the production of Fe-org complexes that are photoactive, (2) variation in HO_2 concentrations; and (3) changes in the OH formation from the different oxidation mechanisms. First, after production of organic acids from reactions shown in Figure.5, Fe-organic complexes may be present in solution. These Fe-organic complexes are photochemically active both under our lamps and in sunlight. [94] The complexation of organic acid, like glycolic acid (h), conjugate bases with an $Fe_{(III)}$ species will undergo a photoinduced 1-electron transfer to $Fe_{(III)}$ to produce $Fe_{(II)}$ bound to an anion radical (Figure 5, lower panel).[37,102] In the presence of oxygen, oxidation of the anion radical forms oxalate, superoxide, and their conjugate acids (oxalic acid and HO_2, respectively). This mechanism may supplement the OH-initiated mechanisms to enhance the oxidative power of photo-Fenton compared to H_2O_2 photolysis.

Second, the production of HO_2 from the H_2O_2 + OH reaction (R1b, $k_{298} = 1.8 \times 10^{-12}$ cm^3 $molec^{-1}$ s^{-1})[103] is likely more prominent in the H_2O_2 photolysis system. This OH + H_2O_2 reaction is competitive with the OH-oxidation of organic constituents. The modeled HO_2/OH ratio for H_2O_2 photolysis ranges from 10^2 to 10^3. Estimated values are not available for photo-Fenton, although the ratio is expected to be significantly lower because, in the presence of $Fe_{(II)}$ at ∼8 times the molar concentration of H_2O_2 in the atomizer solution, most of the H_2O_2 may have reacted with $Fe_{(II)}$ before atomized aerosols reach the flow reactor. Although the C_2-peracids formed from the reaction of $RC(O)O_2$ with HO_2 have high O/C, they are still volatile enough to partition into the gas phase.[104] In contrast, the reaction of $RC(O)O_2$ with OH eventually produces glycolic acid (h), glyoxylic acid (k), and oxalic acid (o),[20,105] which may form low-volatility salts,[106] oligomers,[17] and complexes with iron, so the highly oxidized compounds remain in the aerosol phase upon evaporation.

Third, the OH production is enhanced in Fenton photochemistry. We estimate the aqueous photolysis of H_2O_2 in the presence of 1 μg m^{-3} of particle-phase glycolaldehyde (from organic wt% under photolytic conditions) may produce an OH steady-state concentration of approximately 8×10^{-13} M in the aerosol liquid water, based on a simplified mechanism of glycolaldehyde aqueous chemistry,[20] the photon flux from the flow reactor lamps (Figure S1), and the assumption that all H_2O_2 remains dissolved upon humid atomization. The modeled organics include only glycolaldehyde in solution, and not its oligomers, hydrates, or oxidation products; therefore, calculated OH values are upper-limit estimations only. This OH concentration is within the range modeled for cloudwater (10^{-13}−10^{-12} M)[107] but much greater than concentrations measured in fog droplets (10^{-16}−10^{-15} M).[108] Typical OH concentrations in aerosol liquid water are unknown. Higher [OH] is expected for photo-Fenton due to the larger UV absorption cross section of $Fe(OH)^{2+}$ ($\sigma = 3.03 \times 10^{-18}$ cm^2 at 310 nm)[87,109] compared to H_2O_2 ($\sigma = 3.74 \times 10^{-21}$ cm^2 at 310 nm),[103] despite the higher OH quantum yield expected for the H_2O_2 photolysis system.[30,87,88]

Although the aqueous equilibria of the Fe and H_2O_2 in this work are complex, the results still represent a simple model system, in that other metals, photosensitizers, and organic ligands commonly found in clouds, fogs, and aerosol water are not present.[110−112] We expect differences in the chemical behavior of atmospheric aqueous solutions. For example, the majority of soluble iron in natural waters may be bound to

organic ligands.[113] As discussed earlier, these Fe-organic complexes promote both the photo-Fenton and dark Fenton reactions compared to $Fe(OH)^{2+}$ because of a larger overlap of their absorption cross sections with natural sunlight[94] and an increased dark OH yield from R2a, [114] respectively. Additionally, photosensitizers like humic-like substances (HULIS) may further enhance the efficiency of iron-mediated reactions in the atmosphere.[38] It is possible that the present work underpredicts the oxidative power of Fenton chemistry in atmospheric aerosols.

This work offers some important insights: (a) photo-Fenton chemistry may occur in the liquid water of atmospheric aerosols, and not just in the aqueous bulk, (b) photo-Fenton is a more powerful oxidation mechanism for organic aerosols compared to the photolysis of atmospherically relevant concentrations of H_2O_2, and (c) the reactive uptake of glycolaldehyde onto hydrated AS seed aerosol is substantially more efficient than predicted by its pure-water Henry's law constant. In atmospheric aerosol water, multiple OH sources may be simultaneously responsible for aged OA, including OH uptake from the gas phase, which may be the dominant source of OH. These findings suggest that photo-Fenton may be another important source of OH, and may help explain previous discrepancies between aerosols studied in the laboratory and those found in the atmosphere, as the OA aged with photo-Fenton is very similar to ambient low-volatility oxygenated organic aerosols (LV-OOA). Given the complexity of atmospheric cloud, fog and aerosol water composition, more research is needed to elucidate the role of metals, inorganic ions, acidity, and anthropogenic compounds in the production and aging of organic aerosols.

■ ASSOCIATED CONTENT

Supporting Information

Section S1: experimental details, Section S2: possible competition from direct photolysis, Table S1: elemental ratios for dry experiments, Figure S1: diagram of flow reactor, Figure S2: CIMS mass spectra for atomization blanks, Figure S3: lamp flux inside the reactor, Figure S4: temperature of experiments, Figure S5: particle size distribution, Figure S6: AMS peak interferences, Figure S7: correlation of CH_4N^+ and CH_3O^+, Figure S8: "triangle" plots of dry and humid data. This material is available free of charge via the Internet at http://pubs.acs.org.

■ AUTHOR INFORMATION

Corresponding Author

*E-mail: T. B. Nguyen, tbn@caltech.edu.

Author Contributions

T.B.N. and M.M.C. contributed equally.

Notes

The authors declare no competing financial interest.

■ ACKNOWLEDGMENTS

This research was supported by the National Science Foundation grant AGS-1057183. T. B. Nguyen acknowledges funding from the Coco and Foster Stanback Postdoctoral Fellowship in Global Environmental Science. We are grateful to Prof. S. A. Nizkorodov (UC Irvine) for his contribution of a portion of the equipment used in this work. We thank Prof. P. O. Wennberg and Prof. M. R. Hoffman for helpful discussions.

■ REFERENCES

(1) Lambe, A. T.; Onasch, T. B.; Croasdale, D. R.; Wright, J. P.; Martin, A. T.; Franklin, J. P.; Massoli, P.; Kroll, J. H.; Canagaratna, M. R.; Brune, W. H.; Worsnop, D. R.; Davidovits, P. Transitions from Functionalization to Fragmentation Reactions of Laboratory Secondary Organic Aerosol (SOA) Generated from the OH Oxidation of Alkane Precursors. *Environ. Sci. Technol.* **2012**, *46* (10), 5430−5437.

(2) Ng, N. L.; Canagaratna, M. R.; Zhang, Q.; Jimenez, J. L.; Tian, J.; Ulbrich, I. M.; Kroll, J. H.; Docherty, K. S.; Chhabra, P. S.; Bahreini, R.; Murphy, S. M.; Seinfeld, J. H.; Hildebrandt, L.; Donahue, N. M.; DeCarlo, P. F.; Lanz, V. A.; Prévôt, A. S. H.; Dinar, E.; Rudich, Y.; Worsnop, D. R. Organic aerosol components observed in Northern Hemispheric datasets from Aerosol Mass Spectrometry. *Atmos. Chem. Phys.* **2010**, *10* (10), 4625−4641.

(3) Heald, C. L.; Ridley, D. A.; Kreidenweis, S. M.; Drury, E. E. Satellite observations cap the atmospheric organic aerosol budget. *Geophys. Res. Lett.* **2010**, *37* (24), L24808 DOI: 10.1029/2010GL045095.

(4) De Gouw, J.; Jimenez, J. L. Organic Aerosols in the Earth's Atmosphere. *Environ. Sci. Technol.* **2009**, *43* (20), 7614−7618.

(5) Blando, J. D.; Turpin, B. J. Secondary organic aerosol formation in cloud and fog droplets: a literature evaluation of plausibility. *Atmos. Environ.* **2000**, *34* (10), 1623−1632.

(6) Chen, J.; Griffin, R. J.; Grini, A.; Tulet, P. Modeling secondary organic aerosol formation through cloud processing of organic compounds. *Atmos. Chem. Phys.* **2007**, *7* (20), 5343−5355.

(7) Carlton, A. G.; Turpin, B. J.; Altieri, K. E.; Seitzinger, S. P.; Mathur, R.; Roselle, S. J.; Weber, R. J. CMAQ Model Performance Enhanced When In-Cloud Secondary Organic Aerosol is Included: Comparisons of Organic Carbon Predictions with Measurements. *Environ. Sci. Technol.* **2008**, *42* (23), 8798−8802.

(8) Fu, T. M.; Jacob, D. J.; Heald, C. L. Aqueous-phase reactive uptake of dicarbonyls as a source of organic aerosol over eastern North America. *Atmos. Environ.* **2009**, *43* (10), 1814−1822.

(9) Ervens, B.; Carlton, A. G.; Turpin, B. J.; Altieri, K. E.; Kreidenweis, S. M.; Feingold, G. Secondary organic aerosol yields from cloud-processing of isoprene oxidation products. *Geophys. Res. Lett.* **2008**, *35* (2), L02816 DOI: 10.1029/2007GL031828.

(10) Ervens, B.; Turpin, B. J.; Weber, R. J. Secondary organic aerosol formation in cloud droplets and aqueous particles (aqSOA): a review of laboratory, field and model studies. *Atmos. Chem. Phys* **2011**, *11* (8), 11069−11102.

(11) Ervens, B.; Volkamer, R. Glyoxal processing by aerosol multiphase chemistry: towards a kinetic modeling framework of secondary organic aerosol formation in aqueous particles. *Atmos. Chem. Phys* **2010**, *10* (17), 8219−8244.

(12) Lim, Y. B.; Tan, Y.; Perri, M. J.; Seitzinger, S. P.; Turpin, B. J. Aqueous chemistry and its role in secondary organic aerosol (SOA) formation. *Atmos. Chem. Phys* **2010**, *10* (21), 10521−10539.

(13) Lee, A. K. Y.; Zhao, R.; Gao, S. S.; Abbatt, J. P. D. Aqueous-phase OH oxidation of glyoxal: application of a novel analytical approach employing aerosol mass spectrometry and complementary off-line techniques. *J. Phys. Chem. A* **2011**, *115* (38), 10517−10526.

(14) Tan, Y.; Perri, M. J.; Seitzinger, S. P.; Turpin, B. J. Effects of Precursor Concentration and Acidic Sulfate in Aqueous Glyoxal-OH Radical Oxidation and Implications for Secondary Organic Aerosol. *Environ. Sci. Technol.* **2009**, *43* (21), 8105−8112.

(15) Carlton, A. G.; Turpin, B. J.; Altieri, K. E.; Seitzinger, S.; Reff, A.; Lim, H.-J.; Ervens, B. Atmospheric oxalic acid and SOA production from glyoxal: Results of aqueous photooxidation experiments. *Atmos. Environ.* **2007**, *41* (35), 7588−7602.

(16) Tan, Y.; Carlton, A. G.; Seitzinger, S. P.; Turpin, B. J. SOA from methylglyoxal in clouds and wet aerosols: Measurement and prediction of key products. *Atmos. Environ.* **2010**, *44* (39), 5218−5226.

(17) Altieri, K. E.; Carlton, A. G.; Lim, H. J.; Turpin, B. J.; Seitzinger, S. P. Evidence for Oligomer Formation in Clouds: Reactions of Isoprene Oxidation Products. *Environ. Sci. Technol.* **2006**, *40* (16), 4956−4960.

(18) Carlton, A. G.; Turpin, B. J.; Lim, H. J.; Altieri, K. E.; Seitzinger, S. Link between isoprene and secondary organic aerosol (SOA): Pyruvic acid oxidation yields low volatility organic acids in clouds. *Geophys. Res. Lett.* **2006**, *33* (6), L06822 DOI: 10.1029/2005gl025374.
(19) Guzman, M. I.; Colussi, A. J.; Hoffmann, M. R. Photoinduced Oligomerization of Aqueous Pyruvic Acid. *J. Phys. Chem. A* **2006**, *110* (10), 3619−3626.
(20) Perri, M. J.; Seitzinger, S.; Turpin, B. J. Secondary organic aerosol production from aqueous photooxidation of glycolaldehyde: Laboratory experiments. *Atmos. Environ.* **2009**, *43* (8), 1487−1497.
(21) Rincon, A. G.; Guzman, M. I.; Hoffmann, M. R.; Colussi, A. J. Thermochromism of Model Organic Aerosol Matter. *J. Phys. Chem. Lett.* **2010**, *1* (1), 368−373.
(22) Yasmeen, F.; Sauret, N.; Gal, J.-F.; Maria, P.-C.; Massi, L.; Maenhaut, W.; Claeys, M. Characterization of oligomers from methylglyoxal under dark conditions: a pathway to produce secondary organic aerosol through cloud processing during nighttime. *Atmos. Chem. Phys.* **2010**, *10* (8), 3803−3812.
(23) Altieri, K. E.; Seitzinger, S. P.; Carlton, A. G.; Turpin, B. J.; Klein, G. C.; Marshall, A. G. Oligomers formed through in-cloud methylglyoxal reactions: Chemical composition, properties, and mechanisms investigated by ultra-high resolution FT-ICR mass spectrometry. *Atmos. Environ.* **2008**, *42* (7), 1476−1490.
(24) Lee, A. K. Y.; Herckes, P.; Leaitch, W. R.; Macdonald, A. M.; Abbatt, J. P. D. Aqueous OH oxidation of ambient organic aerosol and cloud water organics: Formation of highly oxidized products. *Geophys. Res. Lett.* **2011**, *38* (11), L11805 DOI: 10.1029/2011gl047439.
(25) Nguyen, T. B.; Lee, P. B.; Updyke, K. M.; Bones, D. L.; Laskin, J.; Laskin, A.; Nizkorodov, S. A. Formation of nitrogen- and sulfur-containing light-absorbing compounds accelerated by evaporation of water from secondary organic aerosols. *J. Geophys. Res.* **2012**, *117* (D1), D01207 DOI: 10.1029/2011JD016944.
(26) Liu, Y.; Monod, A.; Tritscher, T.; Praplan, A.; DeCarlo, P.; Temime-Roussel, B.; Quivet, E.; Marchand, N.; Dommen, J.; Baltensperger, U. Aqueous phase processing of secondary organic aerosol from isoprene photooxidation. *Atmos. Chem. Phys* **2012**, *12*, 5879−5895.
(27) Arakaki, T.; Faust, B. C. Sources, sinks, and mechanisms of hydroxyl radical (•OH) photoproduction and consumption in authentic acidic continental cloud waters from Whiteface Mountain, New York: The role of the Fe(r) (r = II, III) photochemical cycle. *J. Geophys. Res.* **1998**, *103* (D3), 3487−3504.
(28) Hoffmann, P.; Dedik, A.; Ensling, J.; Weinbruch, S.; Weber, S.; Sinner, T.; Gütlich, P.; Ortner, H. Speciation of iron in atmospheric aerosol samples. *J. Aerosol. Sci.* **1996**, *27* (2), 325−337.
(29) Dedik, A.; Hoffmann, P.; Ensling, J. Chemical characterization of iron in atmospheric aerosols. *Atmos. Environ.* **1992**, *26* (14), 2545−2548.
(30) Arellanes, C.; Paulson, S. E.; Fine, P. M.; Sioutas, C. Exceeding of Henry's Law by Hydrogen Peroxide Associated with Urban Aerosols. *Environ. Sci. Technol.* **2006**, *40* (16), 4859−4866.
(31) Wang, Y.; Arellanes, C.; Curtis, D. B.; Paulson, S. E. Probing the Source of Hydrogen Peroxide Associated with Coarse Mode Aerosol Particles in Southern California. *Environ. Sci. Technol.* **2010**, *44* (11), 4070−4075.
(32) Zellner, R.; Exner, M.; Herrmann, H. Absolute OH quantum yields in the laser photolysis of nitrate, nitrite and dissolved H2O2 at 308 and 351 nm in the temperature range 278−353 K. *J. Atmos. Chem.* **1990**, *10* (4), 411−425.
(33) Livingston, R.; Zeldes, H. Paramagnetic Resonance Study of Liquids during Photolysis. III. Aqueous Solutions of Alcohols with Hydrogen Peroxide1. *J. Am. Chem. Soc.* **1966**, *88* (19), 4333−4336.
(34) Noziere, B.; Ekstrom, S.; Alsberg, T.; Holmstrom, S. Radical-initiated formation of organosulfates and surfactants in atmospheric aerosols. *Geophys. Res. Lett.* **2010**, *37*, 6.
(35) Gelencser, A.; Hoffer, A.; Kiss, G.; Tombacz, E.; Kurdi, R.; Bencze, L. In-situ Formation of Light-Absorbing Organic Matter in Cloud Water. *J. Atmos. Chem.* **2003**, *45* (1), 25−33.
(36) Holmes, B.; Petrucci, G. Oligomerization of levoglucosan by Fenton chemistry in proxies of biomass burning aerosols. *J. Atmos. Chem.* **2007**, *58* (2), 151−166.
(37) Siefert, R. L.; Pehkonen, S. O.; Erel, Y.; Hoffmann, M. R. Iron photochemistry of aqueous suspensions of ambient aerosol with added organic acids. *Geochim. Cosmochim. Acta* **1994**, *58* (15), 3271−3279.
(38) Moonshine, M.; Rudich, Y.; Katsman, S.; Graber, E. R. Atmospheric HULIS enhance pollutant degradation by promoting the dark Fenton reaction. *Geophys. Res. Lett.* **2008**, *35*, L20807/1−L20807/4.
(39) Chevallier, E.; Jolibois, R. D.; Meunier, N.; Carlier, P.; Monod, A. "Fenton-like" reactions of methylhydroperoxide and ethylhydroperoxide with Fe2+ in liquid aerosols under tropospheric conditions. *Atmos. Environ.* **2004**, *38*, 921−933.
(40) Nomi, S. N.; Kondo, H.; Sakugawa, H. Photoformation of OH radical in water-extract of atmospheric aerosols and aqueous solution of water-soluble gases collected in Higashi-Hiroshima, Japan. *Geochem. J.* **2012**, *46*, 21−29.
(41) Kavitha, V.; Palanivelu, K. The role of ferrous ion in Fenton and photo-Fenton processes for the degradation of phenol. *Chemosphere* **2004**, *55* (9), 1235−1243.
(42) Ghaly, M. Y.; Härtel, G.; Mayer, R.; Haseneder, R. Photochemical oxidation of p-chlorophenol by UV/H2O2 and photo-Fenton process. A comparative study. *Waste Manage.* **2001**, *21* (1), 41−47.
(43) Liggio, J.; Li, S. M.; McLaren, R. Reactive uptake of glyoxal by particulate matter. *J. Geophys. Res.* **2005**, *110* (D10), D10304.
(44) Galloway, M. M.; Chhabra, P. S.; Chan, A. W. H.; Surratt, J. D.; Flagan, R. C.; Seinfeld, J. H.; Keutsch, F. N. Glyoxal uptake on ammonium sulphate seed aerosol: reaction products and reversibility of uptake under dark and irradiated conditions. *Atmos. Chem. Phys.* **2009**, *9* (10), 3331−3345.
(45) Trainic, M.; Abo Riziq, A.; Lavi, A.; Flores, J. M.; Rudich, Y. The optical, physical and chemical properties of the products of glyoxal uptake on ammonium sulfate seed aerosols. *Atmos. Chem. Phys.* **2011**, *11* (18), 9697−9707.
(46) Liggio, J.; Li, S.-M.; McLaren, R. Heterogeneous reactions of glyoxal on particulate matter: identification of acetals and sulfate esters. *Environ. Sci. Technol.* **2005**, *39* (6), 1532−1541.
(47) Lloyd, J. A.; Heaton, K. J.; Johnston, M. V. Reactive Uptake of Trimethylamine into Ammonium Nitrate Particles. *J. Phys. Chem. A* **2009**, *113* (17), 4840−4843.
(48) Iinuma, Y.; Boge, O.; Kahnt, A.; Herrmann, H. Laboratory chamber studies on the formation of organosulfates from reactive uptake of monoterpene oxides. *Phys. Chem. Chem. Phys.* **2009**, *11* (36), 7985−7997.
(49) Lee, Y. N.; Zhou, X.; Kleinman, L. I.; Nunnermacker, L. J.; Springston, S. R.; Daum, P. H.; Newman, L.; Keigley, W. G.; Holdren, M. W.; Spicer, C. W.; Young, V.; Fu, B.; Parrish, D. D.; Holloway, J.; Williams, J.; Roberts, J. M.; Ryerson, T. B.; Fehsenfeld, F. C. Atmospheric chemistry and distribution of formaldehyde and several multioxygenated carbonyl compounds during the 1995 Nashville/Middle Tennessee Ozone Study. *J. Geophys. Res.* **1998**, *103* (D17), 22449−22462, DOI: 10.1029/98jd01251.
(50) Betterton, E. A.; Hoffmann, M. R. Henry's law constants of some environmentally important aldehydes. *Environ. Sci. Technol.* **1988**, *22* (12), 1415−1418.
(51) Matsunaga, S.; Mochida, M.; Kawamura, K. Variation on the atmospheric concentrations of biogenic carbonyl compounds and their removal processes in the northern forest at Moshiri, Hokkaido Island in Japan. *J. Geophys. Res.* **2004**, *109* (D4), D04302.
(52) Galloway, M. M.; Huisman, A. J.; Yee, L. D.; Chan, A. W. H.; Loza, C. L.; Seinfeld, J. H.; Keutsch, F. N. Yields of oxidized volatile organic compounds during the OH radical initiated oxidation of isoprene, methyl vinyl ketone, and methacrolein under high-NOx conditions. *Atmos. Chem. Phys.* **2011**, *11* (21), 10779−10790.
(53) Paulson, S. E.; Flagan, R. C.; Seinfeld, J. H. Atmospheric photooxidation of isoprene part I: The hydroxyl radical and ground

state atomic oxygen reactions. *Int. J. Chem. Kinet.* **1992**, *24* (1), 79−101.
(54) Chan, A. W. H.; Galloway, M. M.; Kwan, A. J.; Chhabra, P. S.; Keutsch, F. N.; Wennberg, P. O.; Flagan, R. C.; Seinfeld, J. H. Photooxidation of 2-Methyl-3-Buten-2-ol as a Potential Source of Secondary Organic Aerosol. *Environ. Sci. Technol.* **2009**, *43* (21), 8470−8470.
(55) Fantechi, G.; Jensen, N. R.; Hjorth, J.; Peeters, J. Mechanistic studies of the atmospheric oxidation of methyl butenol by OH radicals, ozone and NO3 radicals. *Atmos. Environ.* **1998**, *32* (20), 3547−3556.
(56) Ferronato, C.; Orlando, J. J.; Tyndall, G. S. Rate and mechanism of the reactions of OH and Cl with 2-methyl-3-buten-2-ol. *J. Geophys. Res.* **1998**, *103* (D19), 25579−25586.
(57) Alvarado, A.; Tuazon, E. C.; M. Aschmann, S.; Arey, J.; Atkinson, R. Products and mechanisms of the gas-phase reactions of OH radicals and O3 with 2-methyl-3-buten-2-ol. *Atmos. Environ.* **1999**, *33* (18), 2893−2905.
(58) Carrasco, N.; Doussin, J.; O'Connor, M.; Wenger, J.; Picquet-Varrault, B.; Durand-Jolibois, R.; Carlier, P. Simulation chamber studies of the atmospheric oxidation of 2-methyl-3-buten-2-ol: Reaction with hydroxyl radicals and ozone under a variety of conditions. *J. Atmos. Chem.* **2007**, *56* (1), 33−55.
(59) Christian, T.; Kleiss, B.; Yokelson, R.; Holzinger, R.; Crutzen, P.; Hao, W.; Saharjo, B.; Ward, D. Comprehensive laboratory measurements of biomass-burning emissions: 1. Emissions from Indonesian, African, and other fuels. *J. Geophys. Res* **2003**, *108* (4719), 1−4719.
(60) Kawamura, K.; Okuzawa, K.; Aggarwal, S. G.; Irie, H.; Kanaya, Y.; Wang, Z. Determination of gaseous and particulate carbonyls (glycolaldehyde, hydroxyacetone, glyoxal, methylglyoxal, nonanal and decanal) in the atmosphere at Mt. Tai. *Atmos. Chem. Phys. Discuss.* **2013**, *13* (1), 2725−2758.
(61) Ortiz-Montalvo, D. L.; Lim, Y. B.; Perri, M. J.; Seitzinger, S. P.; Turpin, B. J. Volatility and Yield of Glycolaldehyde SOA Formed through Aqueous Photochemistry and Droplet Evaporation. *Aerosol. Sci. Technol.* **2012**, *46* (9), 1002−1014.
(62) Crounse, J. D.; McKinney, K. A.; Kwan, A. J.; Wennberg, P. O. Measurement of Gas-Phase Hydroperoxides by Chemical Ionization Mass Spectrometry. *Anal. Chem.* **2006**, *78* (19), 6726−6732.
(63) St. Clair, J. M.; McCabe, D. C.; Crounse, J. D.; Steiner, U.; Wennberg, P. O. Chemical ionization tandem mass spectrometer for the in situ measurement of methyl hydrogen peroxide. *Rev. Sci. Instrum.* **2010**, *81* (9), 094102−6.
(64) Paulot, F.; Crounse, J. D.; Kjaergaard, H. G.; Kroll, J. H.; Seinfeld, J. H.; Wennberg, P. O. Isoprene photooxidation: new insights into the production of acids and organic nitrates. *Atmos. Chem. Phys.* **2009**, *9*, 1479−1501.
(65) Tie, X.; Madronich, S.; Walters, S.; Zhang, R.; Rasch, P.; Collins, W. Effect of clouds on photolysis and oxidants in the troposphere. *J. Geophys. Res.* **2003**, *108* (D20), 4642 DOI: 10.1029/2003JD003659.
(66) Hameri, K.; Vakeva, M.; Hansson, H.-C.; Laaksonen, A. Hygroscopic growth of ultrafine ammonium sulphate aerosol measured using an ultrafine tandem differential mobility analyzer. *J. Geophys. Res.* **2000**, *105* (D17), 22231−22242.
(67) Allan, J. D.; Delia, A. E.; Coe, H.; Bower, K. N.; Alfarra, M. R.; Jimenez, J. L.; Middlebrook, A. M.; Drewnick, F.; Onasch, T. B.; Canagaratna, M. R. A generalised method for the extraction of chemically resolved mass spectra from Aerodyne aerosol mass spectrometer data. *J. Aerosol. Sci.* **2004**, *35* (7), 909−922.
(68) Aiken, A. C.; Decarlo, P. F.; Kroll, J. H.; Worsnop, D. R.; Huffman, J. A.; Docherty, K. S.; Ulbrich, I. M.; Mohr, C.; Kimmel, J. R.; Sueper, D.; Sun, Y.; Zhang, Q.; Trimborn, A.; Northway, M.; Ziemann, P. J.; Canagaratna, M. R.; Onasch, T. B.; Alfarra, M. R.; Prevot, A. S. H.; Dommen, J.; Duplissy, J.; Metzger, A.; Baltensperger, U.; Jimenez, J. L. O/C and OM/OC ratios of primary, secondary, and ambient organic aerosols with high-resolution time-of-flight aerosol mass spectrometry. *Environ. Sci. Technol.* **2008**, *42* (12), 4478−4485.
(69) Ptasińska, S.; Denifl, S.; Scheier, P.; Märk, T. D. Electron impact ionization of glycolaldehyde. *Int.. J. Mass Spectrom.* **2005**, *243* (2), 171−176.
(70) Marcolli, C.; Canagaratna, M. R.; Worsnop, D. R.; Bahreini, R.; de Gouw, J. A.; Warneke, C.; Goldan, P. D.; Kuster, W. C.; Williams, E. J.; Lerner, B. M.; Roberts, J. M.; Meagher, J. F.; Fehsenfeld, F. C.; Marchewka, M.; Bertman, S. B.; Middlebrook, A. M. Cluster Analysis of the Organic Peaks in Bulk Mass Spectra Obtained During the 2002 New England Air Quality Study with an Aerodyne Aerosol Mass Spectrometer. *Atmos. Chem. Phys.* **2006**, *6* (12), 5649−5666.
(71) Yu, G.; Bayer, A. R.; Galloway, M. M.; Korshavn, K. J.; Fry, C. G.; Keutsch, F. N. Glyoxal in Aqueous Ammonium Sulfate Solutions: Products, Kinetics and Hydration Effects. *Environ. Sci. Technol.* **2011**, *45* (15), 6336−6342.
(72) Noziere, B.; Dziedzic, P.; Cordova, A. Products and Kinetics of the Liquid-Phase Reaction of Glyoxal Catalyzed by Ammonium Ions (NH(4)(+)). *J. Phys. Chem. A* **2009**, *113* (1), 231−237.
(73) De Haan, D. O.; Hawkins, L. N.; Kononenko, J. A.; Turley, J. J.; Corrigan, A. L.; Tolbert, M. A.; Jimenez, J. L. Formation of Nitrogen-Containing Oligomers by Methylglyoxal and Amines in Simulated Evaporating Cloud Droplets. *Environ. Sci. Technol.* **2011**, *45* (3), 984−991.
(74) Collins, G. C. S.; George, W. O. Nuclear magnetic resonance spectra of glycolaldehyde. *J. Chem. Soc. B* **1971**, *0* (0), 1352−1355.
(75) Barsanti, K. C.; Pankow, J. F. Thermodynamics of the formation of atmospheric organic particulate matter by accretion reactions - Part 1: aldehydes and ketones. *Atmos. Environ.* **2004**, *38* (26), 4371−4382.
(76) van Krevelen, D. W. Graphical-statistical method for the study of structure and reaction processes of coal. *Fuel* **1950**, *29*, 269−84.
(77) Kroll, J. H.; Ng, N. L.; Murphy, S. M.; Varutbangkul, V.; Flagan, R. C.; Seinfeld, J. H. Chamber studies of secondary organic aerosol growth by reactive uptake of simple carbonyl compounds. *J. Geophys. Res.* **2005**, *110* (D23), D23207 DOI: 10.1029/2005JD006004.
(78) Zhang, R.; Wang, L.; Khalizov, A. F.; Zhao, J.; Zheng, J.; McGraw, R. L.; Molina, L. T. Formation of nanoparticles of blue haze enhanced by anthropogenic pollution. *Proc. Natl. Acad. Sci. U.S.A.* **2009**, *106* (42), 17650−17654.
(79) Seinfeld, J. H.; Pandis, S. N., *Atmospheric Chemistry and Physics: From Air Pollution to Climate Change*; 1998.
(80) Kroll, J. H.; N, L. N.; Murphy, S. M.; Flagan, R. C.; Seinfeld, J. H. Secondary organic aerosol formation from isoprene photooxidation under high-NO x conditions. *Geophys. Res. Lett.* **2005**, *32*, L18808 DOI: 10.1029/2005GL023637.
(81) Volkamer, R.; Ziemann, P.; Molina, M. Secondary Organic Aerosol Formation from Acetylene (C2H2): seed effect on SOA yields due to organic photochemistry in the aerosol aqueous phase. *Atmos. Chem. Phys* **2009**, *9* (6), 1907−1928.
(82) Spaulding, R. S.; Schade, G. W.; Goldstein, A. H.; Charles, M. J. Characterization of secondary atmospheric photooxidation products: Evidence for biogenic and anthropogenic sources. *J. Geophys. Res.* **2003**, *108* (D8), 4247 DOI: 10.1029/2002jd002478.
(83) Lee, Y. N.; Zhou, X.; Hallock, K. Atmospheric carbonyl compounds at a rural. *J. Geophys. Res.* **1995**, *100* (D12), 25,933−25,944.
(84) Farmer, D. K.; Matsunaga, A.; Docherty, K. S.; Surratt, J. D.; Seinfeld, J. H.; Ziemann, P. J.; Jimenez, J. L. Response of an aerosol mass spectrometer to organonitrates and organosulfates and implications for atmospheric chemistry. *Proc. Natl. Acad. Sci. U.S.A.* **2010**, *107* (15), 6670−6675.
(85) Heald, C. L.; Kroll, J. H.; Jimenez, J. L.; Docherty, K. S.; DeCarlo, P. F.; Aiken, A. C.; Chen, Q.; Martin, S. T.; Farmer, D. K.; Artaxo, P. A simplified description of the evolution of organic aerosol composition in the atmosphere. *Geophys. Res. Lett.* **2010**, *37* (8), L08803 DOI: 10.1029/2010gl042737.
(86) Fenton, H. LXXIII.—Oxidation of tartaric acid in presence of iron. *J. Chem. Soc. Trans.* **1894**, *65*, 899−910.
(87) Faust, B. C.; Hoigné, J. Photolysis of Fe (III)-hydroxy complexes as sources of OH radicals in clouds, fog and rain. *Atmos. Environ.* **1990**, *24* (1), 79−89.

(88) David, F.; David, P. G. Photoredox chemistry of iron(III) chloride and iron(III) perchlorate in aqueous media. A comparative study. *J. Phys. Chem.* **1976**, *80* (6), 579−583.
(89) Pignatello, J. J.; Liu, D.; Huston, P. Evidence for an Additional Oxidant in the Photoassisted Fenton Reaction. *Environ. Sci. Technol.* **1999**, *33* (11), 1832−1839.
(90) Ma, J.; Ma, W.; Song, W.; Chen, C.; Tang, Y.; Zhao, J.; Huang, Y.; Xu, Y.; Zang, L. Fenton Degradation of Organic Pollutants in the Presence of Low-Molecular-Weight Organic Acids: Cooperative Effect of Quinone and Visible Light. *Environ. Sci. Technol.* **2005**, *40* (2), 618−624.
(91) Butler, J. N. *Ionic Equilibrium: Solubility and pH Calculations*, 2nd ed.; Wiley-Interscience, 1998; p 576.
(92) Hug, S. J.; Canonica, L.; Wegelin, M.; Gechter, D.; von Gunten, U. Solar Oxidation and Removal of Arsenic at Circumneutral pH in Iron Containing Waters. *Environ. Sci. Technol.* **2001**, *35* (10), 2114−2121.
(93) Hug, S. J.; Leupin, O. Iron-Catalyzed Oxidation of Arsenic(III) by Oxygen and by Hydrogen Peroxide: pH-Dependent Formation of Oxidants in the Fenton Reaction. *Environ. Sci. Technol.* **2003**, *37* (12), 2734−2742.
(94) Zuo, Y.; Hoigne, J. Formation of hydrogen peroxide and depletion of oxalic acid in atmospheric water by photolysis of iron(III)-oxalato complexes. *Environ. Sci. Technol.* **1992**, *26* (5), 1014−1022.
(95) Magneron, I.; Mellouki, A.; Le Bras, G.; Moortgat, G. K.; Horowitz, A.; Wirtz, K. Photolysis and OH-Initiated oxidation of glycolaldehyde under atmospheric conditions. *J. Phys. Chem. A* **2005**, *109* (20), 4552−4561.
(96) Finlayson-Pitts, B. J.; Pitts, J. N. *Chemistry of the Upper and Lower Atmosphere: Theory, Experiments, and Applications*; Academic Press: San Diego, 2000.
(97) Ng, N. L.; Kwan, A. J.; Surratt, J. D.; Chan, A. W. H.; Chhabra, P. S.; Sorooshian, A.; Pye, H. O. T.; Crounse, J. D.; Wennberg, P. O.; Flagan, R. C.; Seinfeld, J. H. Secondary organic aerosol (SOA) formation from reaction of isoprene with nitrate radicals (NO3). *Atmos. Chem. Phys.* **2008**, *8* (14), 4117−4140.
(98) Stockwell, W. R.; Milford, J. B.; Gao, D.; Yang, Y. J. The effect of acetyl peroxy-peroxy radical reactions on peroxyacetyl nitrate and ozone concentrations. *Atmos. Environ.* **1995**, *29* (14), 1591−1599.
(99) Surratt, J. D.; Murphy, S. M.; Kroll, J. H.; Ng, N. L.; Hildebrandt, L.; Sorooshian, A.; Szmigielski, R.; Vermeylen, R.; Maenhaut, W.; Claeys, M.; Flagan, R. C.; Seinfeld, J. H. Chemical composition of secondary organic aerosol formed from the photooxidation of isoprene. *J. Phys. Chem. A* **2006**, *110* (31), 9665−9690.
(100) Nguyen, T. B.; Laskin, J.; Laskin, A.; Nizkorodov, S. A. Nitrogen containing organic compounds and oligomers in secondary organic aerosol formed by photooxidation of isoprene. *Environ. Sci. Technol.* **2011**, *45*, 6908−6918.
(101) Chan, A. W. H.; Chan, M. N.; Surratt, J. D.; Chhabra, P. S.; Loza, C. L.; Crounse, J. D.; Yee, L. D.; Flagan, R. C.; Wennberg, P. O.; Seinfeld, J. H. Role of aldehyde chemistry and NOx concentrations in secondary organic aerosol formation. *Atmos. Chem. Phys.* **2010**, *10*, 7169−7188.
(102) Zuo, Y.; Hoigné, J. Photochemical decomposition of oxalic, glyoxalic and pyruvic acid catalysed by iron in atmospheric waters. *Atmos. Environ.* **1994**, *28* (7), 1231−1239.
(103) Sander, S. P.; Friedl, R. R.; Golden, D. M.; Kurylo, M. J.; Moortgat, G. K.; Wine, P. H.; Ravishankara, A. R.; Kolb, C. E.; Molina, M. J.; Finlayson-Pitts, B. J.; Huie, R. E.; Orkin, V. L. *Chemical Kinetics and Photochemical Data for Use in Stratospheric Modeling: Evaluation Number 15*. JPL Publication 06−2 ed.; Jet Propulsion Laboratory: Pasedena, CA, 2006.
(104) Lind, J. A.; Kok, G. L. Henry's law determinations for aqueous solutions of hydrogen peroxide, methylhydroperoxide, and peroxyacetic acid. *J. Geophys. Res.* **1986**, *91* (D7), 7889−7895.
(105) Ervens, B.; Feingold, G.; Frost, G. J.; Kreidenweis, S. M. A modeling study of aqueous production of dicarboxylic acids: 1. Chemical pathways and speciated organic mass production. *J. Geophys. Res.* **2004**, *109* (D15), n/a−n/a.
(106) Lim, H. J.; Carlton, A. G.; Turpin, B. J Isoprene forms secondary organic aerosol through cloud processing: model simulations. *Environ. Sci. Technol.* **2005**, *39*, 4441−4446.
(107) Ervens, B.; George, C.; Williams, J. E.; Buxton, G. V.; Salmon, G. A.; Bydder, M.; Wilkinson, F.; Dentener, F.; Mirabel, P.; Wolke, R.; Herrmann, H. CAPRAM 2.4 (MODAC mechanism): An extended and condensed tropospheric aqueous phase mechanism and its application. *J. Geophys. Res.* **2003**, *108* (D14), 4426.
(108) Anastasio, C.; McGregor, K. G. Chemistry of fog waters in California's Central Valley: 1. In situ photoformation of hydroxyl radical and singlet molecular oxygen. *Atmos. Environ.* **2001**, *35* (6), 1079−1089.
(109) Benkelberg, H. J.; Warneck, P. Photodecomposition of iron (III) hydroxo and sulfato complexes in aqueous solution: Wavelength dependence of OH and SO4-quantum yields. *J. Phys. Chem.* **1995**, *99* (14), 5214−5221.
(110) Collett, J. L.; Bator, A.; Sherman, D. E.; Moore, K. F.; Hoag, K. J.; Demoz, B. B.; Rao, X.; Reilly, J. E. The chemical composition of fogs and intercepted clouds in the United States. *Atmos. Res.* **2002**, *64* (1−4), 29−40.
(111) Cappiello, A.; De Simoni, E.; Fiorucci, C.; Mangani, F.; Palma, P.; Trufelli, H.; Decesari, S.; Facchini, M. C.; Fuzzi, S. Molecular Characterization of the Water-Soluble Organic Compounds in Fogwater by ESIMS/MS. *Environ. Sci. Technol.* **2003**, *37* (7), 1229−1240.
(112) Fisak, J.; Tesar, M.; Rezacova, D.; Elias, V.; Weignerova, V.; Fottova, D. Pollutant concentrations in fog and low cloud water at selected sites of the Czech Republic. *Atmos. Res.* **2002**, *64* (1−4), 75−87.
(113) Wu, J.; Boyle, E.; Sunda, W.; Wen, L.-S. Soluble and Colloidal Iron in the Oligotrophic North Atlantic and North Pacific. *Science* **2001**, *293* (5531), 847−849.
(114) Zepp, R. G.; Faust, B. C.; Hoigne, J. Hydroxyl radical formation in aqueous reactions (pH 3−8) of iron(II) with hydrogen peroxide: the photo-Fenton reaction. *Environ. Sci. Technol.* **1992**, *26* (2), 313−319.

Chapter 8

Conclusions and Future Work

This work is a synthesis of studies aimed at characterizing the formation and chemio-physical properties of organic aerosol. An overview of this work and its relationship to this theme is provided in Chapter 1; therefore, I conclude with a discussion of unanswered questions and recommendations for future work.

8.1 Field Studies

The E-PEACE and NiCE field campaigns were opportunities to study the impact of various sources on marine aerosol properties. Chapters 2 and 3 discussed contributions from ship and continental emissions, yet there remain questions about the role of other sources on the particle budget. A major uncertainty is the modulation of aerosol properties due to biological activity. Mesocosm experiments in wave channels have demonstrated that phytoplankton blooms strongly influence aerosol properties; however, the amount of aerosol emitted is strongly dependent on the microbial population growth dynamics (e.g., Wang et al. 2015). In the field, biological activity has been shown to enhance primary organic aerosol as well as secondary components such as sulfate derived from emissions of dimethyl sulfide (DMS, Sorooshian et al. 2009, Ovadnevaite et al. 2011); however, these emissions vary greatly depending on environmental conditions like wind speed. Given the number of factors that dictate bioaerosol strength, predicting its contribution to marine aerosol properties is challenging.

In Chapter 3, we conclude that a large fraction of sulfate observed in the shipping lanes was attributed to shipping activity. Much of the sulfate we observed was correlated with masses at m/z 42 and 99 (linked to cloud-processed ship emissions); however, there were periods when sulfate loadings were high and contribution from these markers were low. These periods are either indicative of a) ship emissions that have yet to be processed by clouds b) continental emissions or c) methanesulfonic acid (MSA) resulting from the oxidation of DMS. The AMS employed during this study lacked high mass-resolving power, and thus the unambiguous identification of sulfate source

via mass spectral markers is difficult (e.g., identifying contributions of MSA based on its fragmentation pattern with high fractions of m/z 79 [$CH_3SO_2^+$] or m/z 96 [$CH_3SO_3H^+$]). Employing a high-resolution AMS in conjunction with other composition instruments (e.g., particle into liquid sampler, chemical ionization mass spectrometer) may provide a better constraint on the biological contribution to background sulfate in the California coastal zone.

In addition to quantifying secondary sources, there is a need to understand primary bioaerosol. Bioaerosol have been shown to efficiently act as CCN and ice nuclei (IN) due to their size and, in some species, because of unique properties associated with membrane proteins (DeLeon-Rodriguez et al. 2013, Despres et al. 2012). Few studies have investigated these particles in situ and very little is known about how these particles behave in the California coastal zone. Using specialized particle counters such as the Waveband Integrated Bioaerosol Sensor (WIBS) and bulk aerosol collection via filter sampling, one could count and speciate the types of bioaerosol contributing to marine aerosol (DeLeon-Rodriguez et al. 2013, Toprak and Schnaiter, 2013). Measurements of bioaerosol behind the counter-flow virtual impactor (CVI) may help to quantify bioaerosol CCN properties. Such measurements would provide a clearer picture of how, and to what extent, these particles impact marine stratocumulus microphysics.

8.2 Iron Chemistry

In Chapter 7, we investigated the reactive uptake of glycolaldehdye onto ammonium sulfate seed doped with iron and hydrogen peroxide. We found that iron enhanced the O/C of glycolaldehyde SOA relative to particles only containing ammonium sulfate. These observations was attributed to enhanced OH production associated with the Fenton and photo-Fenton reactions (Reactions 8.1 - 8.3).

$$Fe^{2+} + H_2O_2 \rightarrow Fe^{3+} + {}^{\cdot}OH + OH^- \tag{8.1}$$

$$F^{3+} + H_2O \leftrightarrow FeOH^{2+} + H^+ \tag{8.2}$$

$$FeOH^{2+} + hv \rightarrow Fe^{2+} + {}^{\cdot}OH \tag{8.3}$$

While subsequent laboratory studies have confirmed the effectiveness of Fenton chemistry in aqueous SOA production (e.g., Daumit et al. 2014), the significance of these reactions on OH concentrations in real atmospheric systems remains debated. Fenton and photo-Fenton chemistry is highly sensitive to a number of environmental factors. The photo-Fenton reaction (Reaction 8.3) is most favorable with high iron concentration, high actinic flux, pH values between 3 and 4, and

low concentrations of complexing species (Deguillaume et al. 2005). Likewise, the Fenton reaction (Reaction 8.1) is suggested to be a series of reactions involving intermediate species such as the superoxide anion ($O_2^{-\cdot}$) and the $HO_2^{\cdot}$ radical (Deguillaume et al. 2005).

$$Fe^{2+} + {}^{\cdot}OH \rightarrow Fe^{3+} + OH^{-} \tag{8.4}$$

$$Fe^{2+} + O_2^{-\cdot}(+2H^{+}) \rightarrow Fe^{3+} + H_2O_2 \tag{8.5}$$

$$Fe^{2+} + HO_2^{\cdot}(+H^{+}) \rightarrow Fe^{3+} + H_2O_2 \tag{8.6}$$

$$H_2O_2 + {}^{\cdot}OH \rightarrow HO_2^{\cdot} + H_2O \tag{8.7}$$

$$Fe^{3+} + O_2^{-\cdot} \rightarrow Fe^{2+} + O_2 \tag{8.8}$$

$$Fe^{3+} + HO_2^{\cdot} \rightarrow Fe^{2+} + O_2 + H^{+} \tag{8.9}$$

With excess Fe^{2+}, the dominant pathway would be the formation of Fe^{3+} and OH radicals (Reactions 8.4, 8.5, 8.6, 8.1). With excess H_2O_2, hydrogen peroxide oxidation by OH increases reactive species such as $HO_2^{\cdot}$ (Reaction 8.7) which may reduce Fe^{3+} to Fe^{2+} and form molecular oxygen (Reactions 8.8, 8.9). The latter Fenton pathway would reduce the efficacy of OH generation (Deguillaume et al. 2005). Consequently, further investigations are needed to determine the conditions for which Fenton and photo-Fenton chemistry enhances particle-phase oxidation in real atmospheric systems.

The role of iron in SOA chemistry is not limited to the Fenton reactions. Iron is known to complex with organic species such as oxalic, pyruvic, glyoxylic, and succinc acid to form photochemically active iron-carboxylate complexes (Zuo and Hoigne 1992, Faust and Zepp 1993, Sedlak and Hoigne 1993, Zuo and Deng 1997, Johnson and Meskhidze 2013, Weller et al. 2014). The most common ligand, iron-oxalate, has been shown to degrade quickly in atmospheric waters after exposure to UV radiation (Reaction 8.10, Zuo and Hoigne 1992). A recent modeling study by Weller et al. (2014) demonstrates that iron complexation is a major sink for carboxylic acids in typical atmospheric waters. Upon implementation of measured photolysis rates for a suite of iron-carboxylate complexes into the chemical aqueous-phase radical mechanism (CAPRAM 3.0, Herrmann et al. 2005), Weller et al. (2014) estimate that of all the possible sinks of tartonate, pyruvate, and oxalate by typical atmospheric oxidants (e.g., OH, NO_3, SO_4, Fe), 46, 40, and 99% of the degradation can be attributed

to complex iron chemistry. Recent field measurements by Sorooshian et al. (2013) qualitatively support these findings as the authors observed dramatic reduction in oxalate content in cloud water samples containing iron.

The studies outlined above demonstrate that iron chemistry is a major sink of typical aqSOA products such as oxalate and pyruvate. This chemistry is also a means of producing reactive oxidants. Zuo and Hoigne (1992) found that iron-oxalate chemistry generates reactive intermediate species that ultimately lead to the formation of H_2O_2(Reactions 8.10 - 8.15).

$$Fe(C_2O_4)_2^- + h\nu \rightarrow Fe^{2+} + C_2O_4^{2-} + C_2O_4^{-\cdot} \tag{8.10}$$

$$C_2O_4^{-\cdot} \rightarrow CO_2 + CO_2^{-\cdot} \tag{8.11}$$

$$C_2O_4^{-\cdot} + O_2 \rightarrow 2CO_2 + O_2^{-\cdot} \tag{8.12}$$

$$O_2^{-\cdot} + H^+ \leftrightarrow HO_2^{\cdot} \tag{8.13}$$

$$HO_2^{\cdot} + HO_2^{\cdot} \rightarrow H_2O_2 \tag{8.14}$$

$$H_2O_2 + h\nu \rightarrow OH + OH \tag{8.15}$$

In systems where carboxylic acids are formed at high yields, it is possible that this chemistry would enhance the oxidation of bystander organic compounds due the production of reactive oxidants such as $O_2^{-\cdot}$ and OH. For example, the aqueous oxidation of glycolaldehyde produces carboxylic acids such as glycolic, glyoxylic, oxalic, succinc, and malonic acid at aqSOA yields upwards of 40% (Perri et al. 2009). As these acids are produced, Reactions 8.10 - 8.15 might lead to the regeneration of reactive oxidants that would sustain particle oxidation. A schematic outlining this potential cycling is illustrated in Fig. 8.1.

Ultimately, particle-phase iron may simultaneously act to enhance and consume SOA. Few laboratory studies have explored iron's impact on SOA yield, yet there is evidence that iron (and other transition metals) has large effects. For example, Chu et al. (2012) observed upwards of 60% reduction in SOA yield from toluene and α-pinene oxidation when seed aerosol was composed of $FeSO_4$. While the iron concentrations employed by Chu et al. (2012) were substantially higher than that found in ambient particles, iron's catalytic properties may help to drive this chemistry at lower concentrations. Future studies exploring SOA formation as a function of iron fraction within the

particle might help constrain its overall importance in SOA yield.

8.3 Flow Tube

In Chapter 7, we describe experiments conducted with the use of a photooxidation flow reactor. This system was a prototype intended to serve as an alternative research platform to the environmental chamber. Upon completion of this project, it was clear that a permanent flow tube reactor would complement the research conducted in the teflon chamber. Currently, the new reactor has been constructed and efforts have been made to characterize the flow and model the kinetics of simple gas-phase reactions. A publication describing the design and characterizing the physical and chemical behavior of the tube is forthcoming. Here, I focus on the types of projects that could be performed using the Caltech Photooxidation Tube (CPOT).

A schematic of the new flow tube reactor is presented in Fig. 8.2. The CPOT consists of two 1.22 m x 15 cm ID cylindrical quartz tubes flanged together with clamps and chemically resistant o-rings. To maintain an even temperature profile and minimize convective mixing due to heating, the reactors are fitted with quartz cooling jackets and a low-pressure chiller recirculates a 50/50 water/glycol mixture. At the ends of the reactors are two Pyrex cones designed to smoothly transition between the injection and sampling tubing. The entire system is housed within a box containing 16 UV lamps.

The CPOT is well-suited to study gas and particle-phase chemistry and allows one to perform kinetic studies under various environmental conditions. The tube may be operated at a range of temperatures (10-35°C) and relative humidities (0-100%); thus, one could conceivably design experiments to investigate particle-phase reactions as a function of aerosol phase. Lignell et al. (2014) demonstrated that the photolysis rate constant of 2,4-dinitrophenol mixed in bulk secondary organic material varied by 2 orders of magnitude when photolyzed at temperatures ranging between 300- 277 K. Similar behavior was observed in an identical experiment consisting of 2,4-dinitrophenol and octanol, which is known to exhibit significant phase transitions in this temperature range. The behavior suggests that phase (liquid, semi-solid, solid) can play a large role in dictating heterogeneous photochemistry.

The aforementioned study was conducted in non-suspended organic material. In the CPOT, atmospherically relevant studies with mixtures of gases and particles could be conducted to probe the impact of organic phase on heterogeneous chemistry. Since aerosol phase is also a function of liquid water content (e.g., Shiraiwa et al. 2013), experiments may be conducted at a range of relative humidities to investigate the role of organic/aqueous mixtures on photochemical reactivity.

The CPOT is an ideal apparatus to target specific gas and particle-phase reactions since less material is needed relative to that used in an environmental chamber study. One application may

be to investigate the influence of autoxidation reactions on SOA composition. Crounse et al. (2013) proposed that autoxidation plays an important role in atmospheric chemistry of low-NO_x systems. This intramolecular chemistry requires the formation of hydroperoxy radicals; thus, it is dependent on the presence of O_2. One could perform experiments on model compounds (similar to 3-pentanone studied by Crounse et al. 2013) under O_2 and N_2-rich environments to study the extent to which autoxidation contributes to organic oxidation. Furthermore, one could tailor the levels of NO_x to determine the regimes at which NO reactions compete with autoxidation.

Another benefit to the CPOT over typical environmental chambers is its ease of maintenance. Accordingly, one can study systems involving contaminating species (such as transition metals) that would be difficult to clean from a large teflon chamber. As discussed in Section 8.2, there is a need to study transition metal impacts on aqueous-phase oxidation, yet most studies have been conducted in bulk solutions. Experiments conducted with atmospherically-relevant, mixed-phase systems would provide more representative conditions and likely improve understanding of how these species influence VOC uptake and SOA formation.

Finally, the flow tube is well-suited to study advanced oxidation processes. Comparable reactors, such as the Potential Aerosol Mass reactor (PAM) described by Lambe et al. (2011), generate OH exposures on the order of 10^{10} - 10^{12} molec cm^{-3} s (equivalent to 0.2 - 14 days of atmospheric oxidation), which is significantly higher than the OH exposures attainable by environmental chambers ($<$ 10^{11} molec cm^{-3} s). While the current CPOT design enables OH exposures equivalent to that of an environmental chamber, the system can be outfitted with lower wavelength lights to achieve higher OH concentrations. Such modifications would allow for the study of week-long photooxidation.

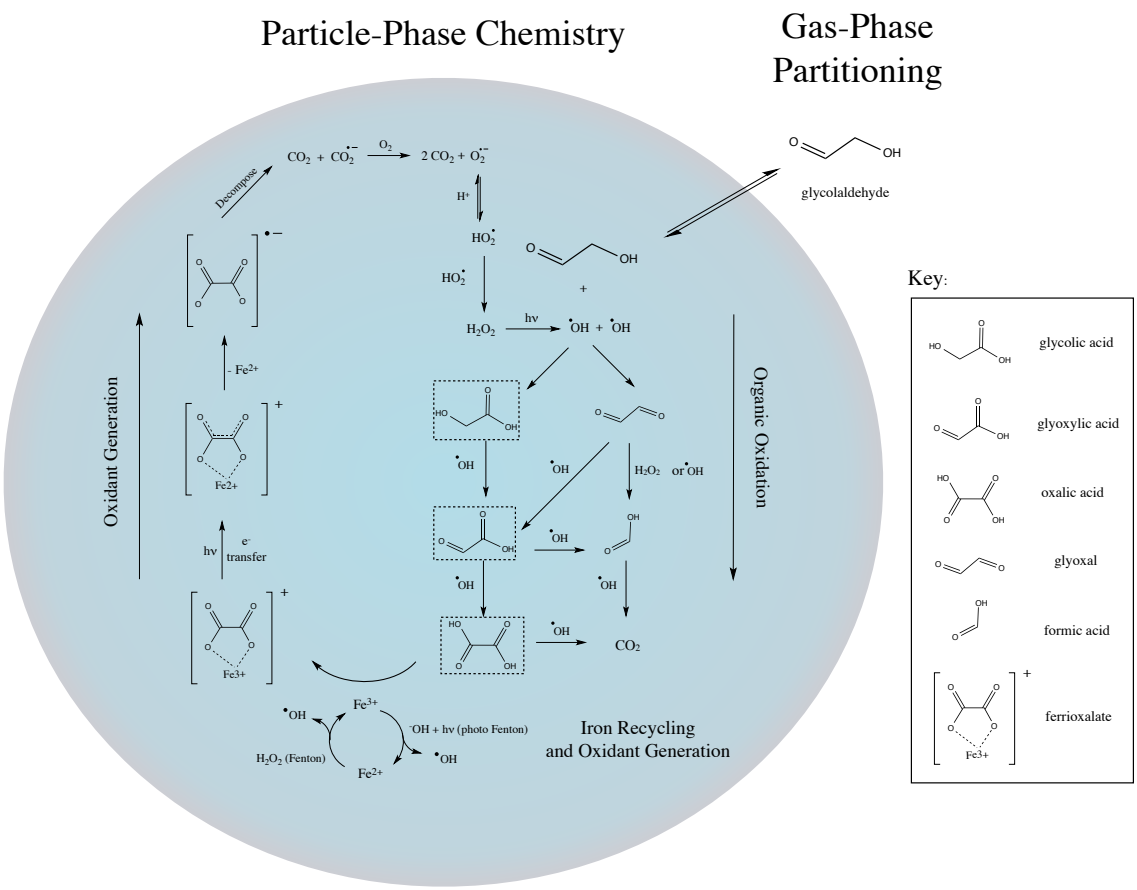

Figure 8.1: Scheme for the production of oxidation species from iron-carboxylate chemistry based on literature review. The mechanism for glycolaldehyde oxidation by OH is described by Perri et al. (2009); the mechanism for H_2O_2 production is described by Zuo and Hoigne (1992).

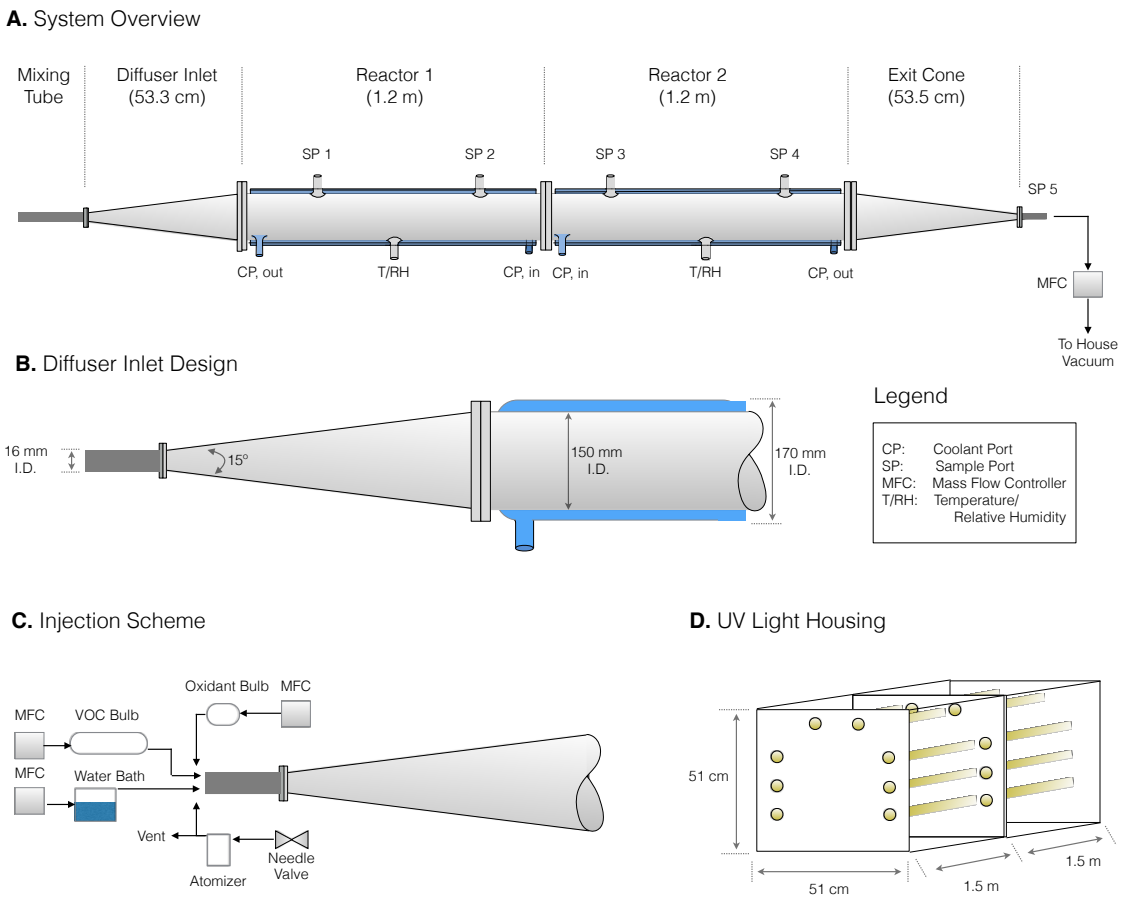

Figure 8.2: Schematic of the Caltech Photooxidation Tube.

8.4 References

1. Chu, B., Hao, J., Takekawa, H., Li, J., Wang, K., and Jian, J. (2012). The remarkable effect of $FeSO_4$ seed aerosols on secondary organic aerosol formation from photooxidation of a-pinene/NO_x and toluene/NO_x. *Atmos. Environ.* 55, 26-34. DOI: 10.1016/j.atmosenv.2012.03.006

2. Crounse, J.D., Nielsen, L.B., Jorgensen, S., Kjaergaard, H.G., and Wennberg, P.O. (2013). Autoxidation of organic compounds in the atmosphere. *J. Phys. Chem. Lett.* 4, 3513-3520. DOI: 10.1021/jz4019207

3. Daumit, K.E., Carrasquillo, A.J., Hunter, J.F., and Kroll, J.H. (2014). Laboratory studies of the aqueous-phase oxidation of polyols: sub micron particles vs. bulk aqueous solution. *Atmos. Chem. Phys.* 14, 10773-10784. DOI: 10.5194/acp-14-10773-2014

4. DeLeon-Rodriguez, N., Lathen, T.L., Rodriguez-R, L.M., Barazesh, J.M., Anderson, B.E.,

Beyersdorf, A.J., Ziemba, L.D., Bergin, M., Nenes, A., and Konstantinidis, K.T. (2013). Microbiome of the upper troposphere: Species composition and prevalence, effects of tropical storms, and atmospheric implications. *Proc. Nat. Acad. Sci* 110 (7), 2575-2580. DOI: 10.1073/pnas.1212089110

5. Deguillaume, L., Leriche, M., Desboeufs, K., Mailhot, G., George, C., and Chaumerliac, N. (2005). Transition metals in atmospheric liquid phases: sources, reactivity, and sensitive parameters. *Chem. Rev.* 105, 3388-3431. DOI: 10.1021/cr040649c

6. Despres, V.R., Huffman, J.A., Burrows, S.M., Hoose, C., Safatov, A.S., Buryak, Gl., Frohlich-Nowoisky, J., Elbert, W., Andrea, M.O., Poschl, Ul, and Jaenicke, R. (2012). Primary biological aerosol particles in the atmosphere: a review. *Tellus B.* 64, 15598. DOI: 10.3402/tellusb.v64i0.15598

7. Faust, B.C. and Zepp, R.G. (1993). Photochemistry of aqueous iron(III)-polycarboxylate complexes: roles in the chemistry of atmospheric and surface waters. *Environ. Sci. Technol.* 27, 2517-2522.

8. Herrmann, H., Tilgner, A., Barzaghi, P., Majdik, Z., Gilgorovski, S., Poulain, L., and Monod, A. (2005). Towards a more detailed description of tropospheric aqueous phase organic chemistry: CAPRAM 3.0. *Atmos. Environ.* 39, 4351-4363. DOI: 10.1016/j.atmosenv.2005.02.016

9. Johnson, M.S., and Meskhidze, N. (2013). Atmospheric dissolved iron deposition to the global oceans: effects of oxalate-promoted Fe dissolution, photochemical redox cycling, and dust mineralogy. *Geoci. Model Devl.* 6, 1137-1155. DOI: 10.5194/gmd-6-1137-2013

10. Lambe, A.T., Ahern, A.T., Williams, L.R., Slowik, J.G., Wong, J.P.S., Abbatt, J.P.D., Brune, W.H., Ng, N.L., Wright, J.P., Croasdale, D.R., Worsnop, D.R., Davidovits, P., and Onasch, T.B. (2011). Characterization of aerosol photooxidation flow reactors: Heterogeneous oxidation, secondary organic aerosol formation and cloud condensation nucleus (CCN) activity measurements. *Atmos. Meas. Tech.* 4, 445-461. DOI:10.5194/amt-4-445-2011

11. Lignell, H., Hinks, M.L., and Nizkorodov, S.A. (2014). Exploring matrix effects on photochemistry of organic aerosols. *Proc. Nat. Acad. Sci.* 111 (38), 13780-13785. DOI: 10.1073/pnas.1322106111

12. Ovadnevaite, J., O'Dowd, Dall'Osto, M., Ceburnis, D., Worsnop, D.R., and Berresheim, H. (2011). Detecting high contributions of primary organic matter to marine aerosol: A case study. *Geophy. Res. Lett.* 38, L02807. DOI: 10.1029/2010GL046083

13. Perri, M.J., Seitzinger, S., and Turpin, B.J. (2009). Secondary organic aerosol production from aqueous photooxidation of glycolaldehyde: Laboratory experiments. *Atmos. Environ.* 43, 1487-1497. DOI:10.1016/j.atmosenv.2008.11.037

14. Sedlak, D.L. and Hoigne, J. (1993). The role of copper and oxalate in the redox cycling of iron in atmospheric waters. *Atmos. Environ.* 27A (14), 2173-2185.

15. Sorooshian, A., Padro, L.T., Nenes, A., Feingold, G., McComiskey, A., Hersey, S.P., Gates, H., Jonsson, H.H., Miller, S.D., Stephens, G.L., Flagan, R.C., and Seinfeld, J.H. (2009). On the link between ocean biota emissions, aerosol, and maritime clouds: Airborne, ground, and satellite measurements off the coast of California. *Glob. Biogeochem. Cyc.* 23, GB4007. DOI: 10.1029/2009GB003464

16. Sorooshian, A., Wang, Z., Coggon, M.M., Haflidi, J., Erven, B. (2013). Observations of Sharp Oxalate Reductions in Stratocumulus Clouds at Variable Altitudes: Organic Acid and Metal Measurements During the 2011 E-PEACE Campaign. *Environ. Sci. Technol.* 47, 14, 77477756. DOI: 10.1021/es4012383.

17. Shiraiwa, M., Zuend, A., Bertram, A.K., and Seinfeld, J.H. (2013). Gas-particle partitioning of atmospheric aerosols: interplay of physical state, non-ideal mixing and morphology. *Phys. Chem. Chem. Phys.*, 15, 11441-11453. DOI: 10.1039/c3cp51595h.

18. Toprak, E. and Schnaiter, M. (2013). Fluorescent biological aerosol particles measured the Waveband Integrated Bioaerosol Sensor WIBS-4: laboratory combined with a one year field study. *Atmos. Chem. Phys.* 13, 225-243. DOI: 10.5194/acp-13-225-2013.

19. Wang et al. (2015). Microbial control of sea spray aerosol composition: A tale of two blooms. *ACS Cent. Sci.* 1 (3), 124-131. DOI: 10.1021/acscentsci.5b00148

20. Weller, C., Tilgner, A., Brauer, P., and Herrmann, H. (2014). Modeling the impact of iron-carboxylate photochemistry on radical budget and carboxylate degradation in cloud droplets and particles. *Environ. Sci. Technol.* 48 (10), 5652-5659. DOI: 10.1021/es4056643

21. Zuo, Y. and Hoigne, J. (1992). Formation of hydrogen peroxide and depletion of oxalic acid in atmospheric water by photolysis of iron(III)-oxalato complexes. *Environ. Sci. Technol.* 26, 1014-1022

22. Zuo, Y.G. and Deng, Y.W. (1997). Iron(II)-catalyzed photochemical decomposition of oxalic acid and generation of H2O2 in atmospheric liquid phases. *Chemosphere* 35 (9), 2051-2058.

Appendix

The following citations reference additional work not included as principal chapters of this thesis.

1. Krechmer, J.E., Coggon, M.M., Massoli, P., Hu, W., Day, D.A., Henze, D.K., Nowak, J.B., Kimmel, J.R., Mauldin, R.L., Stark, H., Jayne, J.T., Sipila, M., Junninen, H., Nguyen, T.B., Crounse, J.D., St. Clair, J., Zhang, X., Brune, W.H., Wennberg, P.O., Seinfeld, J.H., Worsnop, D.R., and Jimenez, J.L. Formation of low volatility organic compounds and secondary organic aerosol from isoprene hydroxyhydroperoxide low-NO oxidation. *Env. Sci. Technol.*. in prep.

2. Crosbie, E., Wang, Z., Sorooshian, A., Chuang, P.Y., Craven, J.S., Coggon, M.M., Brunke, M., Zeng, Xubin, Jonsson, H.H., Woods, R.K., Flagan, R.C., Seinfeld, J.H. (2015). Stratocumulus cloud clearings and notable thermodynamic and aerosol contrasts across the clear-cloudy interface. *Atmos. Sci.* accepted

3. Schwantes, R.H., Teng, A.P., Nguyen, T.B., Coggon, M.M., Crounse, J.D., St. Clair, J.M, Zhang, X., Schilling, K.A., Seinfeld, J.H., Wennberg, P.O. (2015). Isoprene NO_3 oxidation products from RO_2 + HO_2 pathway. submitted.

4. Zhang, X., Schwantes, R.H., McVay, R., Lignell, H., Coggon, M.M., Flagan, R.C., Seinfeld, J.H. (2014). Vapor wall deposition in Teflon chambers. *Atmos. Chem. Phys. Discuss.* 14, 26765-26802.

5. Schilling Fahnestock, K., Yee, L.D., Loza, C.L., Coggon, M.M., Schwantes, R., Zhang, X., Dalleska, N.F., Seinfeld, J.H. (2014). Secondary Organic Aerosol Composition from C_{12} Alkanes. *J. Phys. Chem. A.*. DOI: 10.1021/jp501779w

6. Prabhakar, G., Ervens, B., Wang, Z., Maudlin, L., Coggon, M.M., Jonsson, H.H., Seinfeld, J.H., Sorooshian, A. (2014). Sources of Nitrate in Stratocumlus Cloud Water: Airborne Measurements during the 2011 E-PEACE and 2013 NiCE Studies. Atmos. Environ., 97, 166–173. DOI: 10.1016/ j.atmosenv.2014.08.019.

7. Wang, Z., Prabhakar, G., Maudlin, L.C., Coggon, M.M., Jonsson, H.H., Sorooshian, A. (2013) Impact of Emissions from Shipping, Land, and the Ocean on Stratocumulus Cloud Water

Elemental Composition During the 2011 E-PEACE Field Campaign. *Atmos. Environ.*, 89, 570–580, DOI: 10.1016/ j.atmosenv.2014.01.020.

8. Zhang, X., Schwantes, R., Coggon, M.M., Loza, C., Schilling, K., Flagan, R.C., Seinfeld, J.H. (2013). Role of ozone in SOA formation from alkane photooxidation. *Atmos. Chem. Phys.*, 14, 1,733-1,753, DOI:10.5194/acp-14-1733-2014.

9. Loza, C.L., Craven, J.S., Yee, L.D., Coggon, M.M., Schwantes, R.H., Shiraiwa, M., Zhang, X., Schilling, K.A., Ng, N.L., Canagaratna, M.R., Ziemann, P.J., Flagan, R.C., Seinfeld, J.H. (2013). Secondary organic aerosol yields of 12-carbon alkanes. *Atmos. Chem. Phys.*, 13, 20677-20727. DOI: 10.5194/acpd-13-20677-2013

10. Yee, L.D., Kautzman, K.E., Loza, C.L., Schilling, K.A., Coggon, M.M., Chhabra, P.S., Chan, M.N., Chan, A.W.H, Hersey, S.P., Crounse, J.D., Wennberg, P.O., Flagan, R.C., and Seinfeld, J.H. (2013). Secondary organic aerosol formation from biomass burning intermediates: phenol and methoxyphenols. *Atmos. Chem. Phys*, 13, 8019-8043. DOI: 10.5194/acp-13-8019-2013

11. Sorooshian, A., Wang, Z., Coggon, M.M., Haflidi, J., Erven, B. (2013). Observations of Sharp Oxalate Reductions in Stratocumulus Clouds at Variable Altitudes: Organic Acid and Metal Measurements During the 2011 E-PEACE Campaign. *Environ. Sci. Technol.* 47, 14, 77477756. DOI: 10.1021/es4012383.

12. Metcalf, A.R., Loza, C.L., Coggon, M.M., Craven, J.S., Jonsson, H.H., Flagan, R.C., Seinfeld, J.H. (2012). Secondary Organic Aerosol Coating Formation and Evaporation: Chamber Studies Using Black Carbon Seed Aerosol and the Single-Particle Soot Photometer. *Aerosol Sci. Technol.*, 47, 3, 326-347. DOI: 10.1080/02786826.2012.750712.

13. Russell, L.M., Sorooshian, A., Seinfeld, J.H., Albrecht, B.A., Nenes, A., Ahlm, L., Chen, Y.C., Coggon, M., Craven, J.S., Flagan, R.C., Frossard, A.A., Jonsson, H., Jung, E., Lin, J.J., Metcalf, .R., Modini, R., Mulmenstadt, J., Roberts, G.C., Shingler, T., Song, S., Wang, Z., Wonaschutz, A. (2012) Eastern Pacific Emitted Aerosol Cloud Experiment (E-PEACE), *Bull. Amer. Met. Soc.*, 94, 709-729. DOI: 10.1175/BAMS-D-12-00015.1.

14. Shingler, T., Dey, S., Sorooshian, A., Brechtel, F.J., Wang, Z., Metcalf, A., Coggon, M.M., Mulmenstadt, J., Russell, L.M., Jonsson, H.H., Seinfeld, J.H. (2012). Characterization and airborne deployment of a new counterflow virtual impactor inlet. *Atmos. Meas. Tech.*, 5 (6), 1259-1269. DOI:10.5194/amt-5-1259-2012